Spectral Analysis and Parameter Estimation in Fibre Levitated Optomechanics

Swansea University
Prifysgol Abertawe

Author:
Chris Dawson
[redacted]

Supervisors:
Dr. J. Bateman
Prof. M. Charlton

Submitted to Swansea University in fulfilment of the requirements for the Degree of Doctor of Philosophy

Department of Physics
College of Science
Swansea University

1st March 2020

Declaration

This work has not previously been accepted in substance for any degree and is not being concurrently submitted in candidature for any degree.

Signed . . [redacted] . . . . (candidate)

Date . . . . 01 / 03 / 2020 . . . .

Statement 1

This thesis is the result of my own investigations, except where otherwise stated. Other sources are acknowledged by giving explicit references in the form of a bibliography.

Signed . . [redacted] . . . . (candidate)

Date . . . . 01 / 03 / 2020 . . . .

Statement 2

I hereby give consent for my thesis, if accepted, to be available for photocopying and for inter-library loan, and for the title and summary to be made available to outside organisations.

Signed . . [redacted] . . . . (candidate)

Date . . . . 01 / 03 / 2020 . . . .

Abstract

In levitated optomechanics, nano-scale objects are optically trapped so that their motion can be studied. These trapped nanoparticles are held in a 3D quadratic potential and act as damped harmonic oscillators; they are thermally and mechanically decoupled from the apparatus and their position is measured interferometrically to picometre accuracy. These systems are well suited to sensing and metrology applications, as any external disturbance of the particle can be observed using the scattered trapping light.

When examining the motion of a levitated nanoparticle, it's position is recorded and used to estimate a power spectral density (PSD), from which state parameters can be estimated. In this thesis an experimental setup is presented, optimised for maximum collection of particle position information in 1D, using a fibre-based parabolic mirror trap and heterodyne measurement system in order to produce spectra with minimal noise and unwanted artefacts.

A novel application of the Middleton expansion from RF engineering is used to generate a complete power spectrum that depends on the physical parameters of the system. This method treats the particle as a stochastic harmonic oscillator, phase modulated by a Gaussian random process with known PSD. We reproduce the PSD of intensity at a detector, a quantity that is sinusoidally dependent on particle position. This technique generates a single, full PSD using modified Bessel functions, and does not depend on assumptions about the relative phases of the interfered fields, highlighting the non-linear dependence of measured signal on position. Theoretical spectra are fitted to a measured PSD and the phase modulation depth is extracted; this is used to calculate the particle oscillation amplitude and, by an equipartition argument, the centre of mass temperature to mass ratio. State parameters are tracked as environmental conditions change and an increase in centre of mass temperature as a function of decreasing background gas pressure is observed.

Acknowledgements

Nobody finishes, or even starts a PhD without support. I am incredibly privileged to have had an amazing network of people around me and I am so grateful to them all. Below are just some of the people that have had an impact on me and this project.

I only had the opportunity to do a PhD because a young academic decided to uproot his new family and move to south Wales; fortunately for me, he seemed to think I was alright at physics and asked me to follow him over. Having never had a PhD student before, the last 3 years have been a process of discovery for both of us, and James, you has been everything I could have asked for in a supervisor and more. I think it's fair to say we both got lucky with the pairing, as few others could tolerate our hour-long discussions about how best to make a door communicate with a laser, how to make a vacuum chamber out of cling-film, and whether or not tea bags count as emergency lab supplies. In all seriousness, you have been patient when I haven't understood, willing to teach when I needed help, ready to listen when I had suggestions, and happy to just let me get on with it when I wanted to try something new. Thanks for being more like a best mate than a boss, and good luck with science, life and working out where anything is in the lab.

The phrase "there for me every step of the way" is somewhat of a cliché, but I have absolutely no trouble assigning it to my parents. They have shown me love, support, interest, patience, generosity and exactly the right amount of nagging when I needed it. Mum, Dad, you helped me become a scientist, an engineer, a (semi) grown up and a better human. You spent years helping me with homework, taking me to museums, tolerating me taking things apart, and encouraging me to work hard when I was too young and short-sighted to see the benefits. I want you to know I appreciate it all and, just so you have it in writing, you were right all along... I know I made it hard at times, but I know I absolutely would not be where I am today without you, and I will always be grateful. Kids don't come with an instruction manual, but somehow you did an amazing job anyway; thank you for everything.

Mike, you're my oldest best friend and little-big brother; thank you for 24 years of complete nonsense. Years of playing with lego, talking about the world, trying to beat video games together and quoting videos from the internet have turned us into worryingly similar people, but I know I am better off for it. You've been a great influence on me, and I'm proud of all that you have, and will achieve; even if you did turn out to be an engineer...

Hannah, you've shown the patience of a saint over the last 4 years, not only because you've listened to me talk about floating glass balls, lasers and Raspberry Pis constantly, but because you accepted that I wanted to move to a city 3 hours away by train to do something that I loved. You have been the person I could vent to when nothing worked, the one I could chatter excitedly to when it did, and you've supported me through it all. It's been made all the better by knowing that you can appreciate how doing a PhD feels, and being with a girl as strong and smart as you has made me strive to do the best job I can, and be the best person I can be. Thank you for putting up with me, here's to no more long distance!

Swansea University Physics department, thank you for a great 3 years filled with weird discussions, board games, poker nights and avocado plants. A particular thanks has to go out to the original 406/609 boys: Rhys, Connor, Alex and Liam; with the later accidental addition of Stan. Thank you for hours of discussions about physics, maths and programming, and for help with my project. Sorry I couldn't fix your code.

A big thanks as well to Hugh, Julian and Phil for help with manufacturing parts for the experiment, offering your expertise, organising the construction of a lab for us and generally being great problem solvers. Thank you also to Gill and the admin team for being vastly more organised than me, and managing to somehow herd a bunch of erratic, whimsical physicists into line. Finally in the department, thanks must go to Ken, Maurizio, Dan and Markus for keeping the department functioning, and to Will for keeping me on track with my project and offering external advice where it was required.

I have thanked many people above for helping me work, and I must now thank a couple of very special rabbles for helping me avoid working.

Firstly, Swansea University Sailing Club, you have been an excellent way to forget about physics and you have all become some of my best friends. The antics over the past 3 years have been exactly what I needed to keep me sane, you're all ridiculous people and I love you all for it, thank you.

Secondly, to my second Tring "family", we've grown up together and still managed not to grow up. Thanks for being supportive of me going off and doing this strange academia thing, and for smiling and nodding when I talk physics at you. The huge range of walks of life we are now all in help me see problems from many angles, a skill that has come in useful more than once over the course of this project, and doubtless in life in general.

Finally, to my now-colleagues at MBDA, without whom this thesis would have been finished 7 months sooner... Thanks for letting the problem-solving, learning, engineering and laser based work continue into the future. May there be many more years to come.

To everyone above, and everyone I haven't mentioned, thank you.

Contents

List of Figures

List of Tables

CHAPTER 1

Introduction

Levitated Optomechanics is a relatively new field of study that holds great promise as a platform for testing fundamental physics, as well as many possible sensing and metrology applications. This thesis will give details of an investigation into the thermodynamics of levitated optomechanical systems with a view to understanding them better and helping realise their potential.

§1.1. Thesis Structure Outline

The chapters of this thesis are laid out in such a way as to try and introduce the subject area and it's relevance, then explain the working principles upon which it relies, followed by the new work presented in this thesis and how said work was used.

1. **Introduction -** A primer on the field of levitated optomechanics, the history of it's inception as well as a brief overview of recent work by the leading research groups. The motivation behind why this research is worth performing is explored and related back to the applications of optomechanics in both real-world sensing and understanding fundamental physics.

2. **Background and Theory -** Any theoretical understanding required in subsequent chapters will be outlined and explored. This will include some basic optics, the trapping physics itself, as well as the thermodynamics in play.

3. **Fibre Interferometry -** The operating principles of the experimental system will be explained, building up an understanding from the motion of the particle in the trapping potential, incorporating a discussion on the interferometry involved and highlighting the different signal processing methods that can be used.

4. **Experimental Setup -** A description of the experimental system built. The different equipment will be described and the choice of hardware justified. Design decisions will be explained and linked back to how they help fullfil the aims presented in the introduction. and methods used during the course of this project.

5. **Trap Characterisation -** The specifications of the constructed optical trap will be given, and the behaviour of the particle dynamics will be shown over a wide parameter space of environmental conditions. This chapter can be used to compare the system produced in this project with those found in other experimental groups.

6. **Parameter Estimation -** The results of the project's main investigative arc will be presented, following a description of the problem to be solved. A detailed description of how these results were realised

will be given and the outcomes of investigations made using this new technique will be shown. These results will be placed in the context of the wider levitated optomechanics research community and how they verify or affect the results of other groups.

7. **Future Work -** A suggested plan for the continuation of this project is written up, and the steps justified in terms of the potential benefits and further insights they might provide.

8. **Conclusion and Outlook -** Progress towards the stated aims of the project will be evaluated and the main project results summarised.

§1.2. What is Levitated Optomechanics?

In order to place levitated optomechanics in context, we first introduce the wider topic of optomechanics in general.

§1.2.1. Optomechanics

Optomechanics is the study of systems in which an optical and mechanical element interact. A light field affects the motion of some oscillator, which in turn changes the properties of the light field. The most commonly used demonstrative example is of an optical cavity in which one of the cavity mirrors is attached to a spring (Fig 1.1). When the cavity is initially of a length resonant with the incoming laser light, the high finesse cavity accumulates photons and the radiation pressure on the moveable mirror increases. This force moves the mirror and changes the length of the cavity, meaning it is no longer resonant with the laser light. The cavity's decreased finesse, and therefore lower photon occupation, lowers the radiation pressure on the mirror and the restoring force of the spring takes over, returning the mirror to the resonant position, continuing the cycle. As the cavity mirrors are not perfectly reflective there is optical loss from the cavity, combined with the fact that there is energy dissipation into heat in the spring, the system will reach a state of dynamic equilibrium where the laser power entering the cavity is equal to the dissipated power [1]. This equilibrium situation means the mechanical mode of the mirror is in a thermal state.

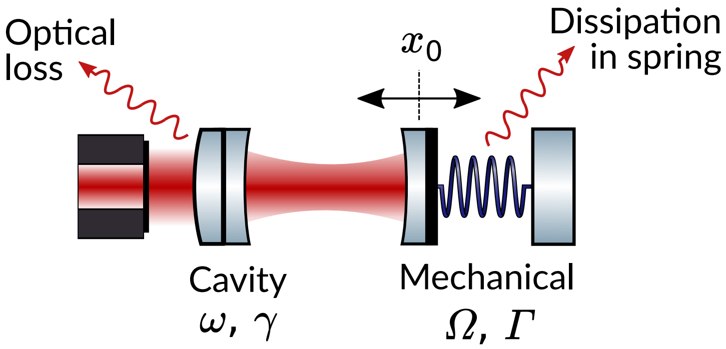

Fig. 1.1. *Moveable cavity mirror optomechanical system. Radiation pressure proportional to the cavity photon occupation number peturbs the mobile mirror, which is restored by a Hooke's law spring force inversely proportional to the mirror's displacement from equilibrium. Both the optical and mechanical modes have natural frequencies ω and Ω respectively, as well as loss or damping rates given by γ and Γ. For a formal description, see [1], equations 18 and 20.*

This example can be used as a starting point from which to understand other optomechanical paradigms.

The size and mass scales of these systems vary enormously, from single atoms [18] with a size (effective size in the case of individual atoms) of 10^{-10} m, to the 10^{0} m wide LIGO mirrors that are used to detect oscillation amplitudes of 10^{-19} m [19]. These different size scales give vastly different characteristic properties, and their research and development is undertaken with different goals in mind.

Figure 1.2 shows some examples of optomechanical systems. The devices pictured are all microfabricated devices produced to mechanically oscillate in some way, whilst minimising energy dissipation. One method of achieving this decoupling is to engineer the anchor points of the oscillator to have low cross sectional area, as is done in the systems depicted in figure 1.2, so that they transmit as few phonons as possible in the relevant frequency range, and result in lower energy dissipation rates. Another method is to use a particularly well isolated oscillator mode such as in [20], where a phononic band gap structure results in a low coupling rate between the phonons in the oscillator mode and thermal phonons in the bulk material.

The devices in figures 1.2a and 1.2b are cantilevers with mechanical nodes at the points they attach to the substrate and an antinode at their centre of mass. It is the position over time of the centre of mass that is measured. The microtoroid in figure 1.2c is made so that it can stretch with an oscillating diameter as well as flexing about the central pivot.

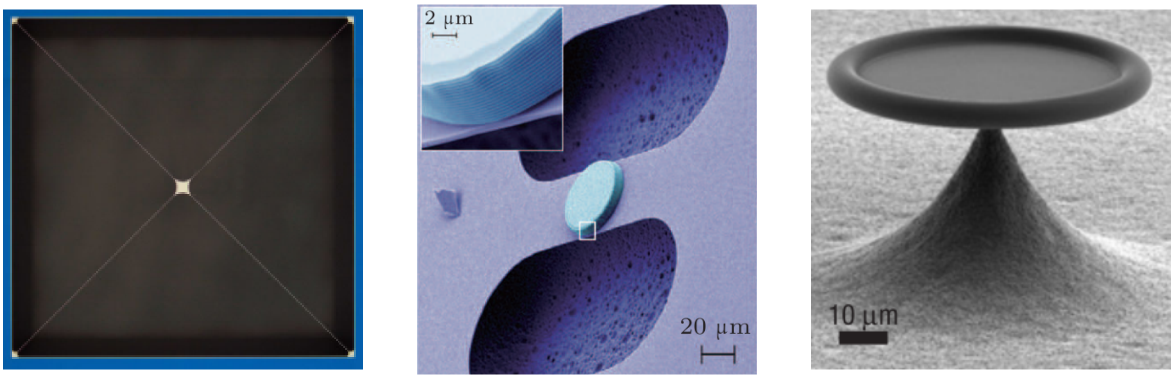

(a) *Trampoline* **(b)** *Micromirror* **(c)** *Microtoroid optical cavity*

Fig. 1.2. *Different types of optomechanical system. Fig 1.2a) is a silicon nitride trampoline with high aspect ratio tethers. The centre of mass of the trampoline oscillates in and out of the plane of the photograph [2]. Fig 1.2b) is a cantilever micromirror that oscillates with a wavelength twice the length of the 'bridge', with nodes where it connects to the substrate [3]. Fig 1.2c) and similar devices [4–6] consist of a circular optical cavity that couples to mechanical modes of the toroid, primarily a radial breathing mode.*

These systems are all, in some respect, damped harmonic oscillators (DHO). They have a natural frequency Ω and a damping rate Γ. The mechanism from which these arise varies between systems.

As experimental platforms, optomechanical systems are useful as they allow precise, fast control over the motion of the oscillator. Sufficiently accurate information about the phase and frequency of the oscillator make it possible to make predictions about the future position of the oscillator, as it can be assumed to follow a sinusoidal path that can be extrapolated using the information in question. This predicted future state can be used to calculate and then apply an appropriate force in order to steer the oscillator's position in phase space. Additionally, in some system architectures it is possible to resonantly enhance the emission of the system when it anti-Stokes scatters. This is when a photon happens to scatter off the system and leave with more energy than it entered with, taking the energy deficit from the oscillator itself by absorbing one or more phonons. Resonantly enhancing this process through sideband cooling does not require computation or tracking the state of the system and has resulted in some of the lowest temperature optomechanical systems seen to date [1,20]. Sideband cooling can be considered in the context of the case in figure 1.1, in which the optical cavity itself would be made of such a length that it was resonant with the blue-shifted, anti-Stokes scattered sideband shown below. In this way, the conversions of phonons in the oscillator into anti-Stokes photons is encouraged and the oscillator loses energy, resulting in cooling of it's centre of mass temperature.

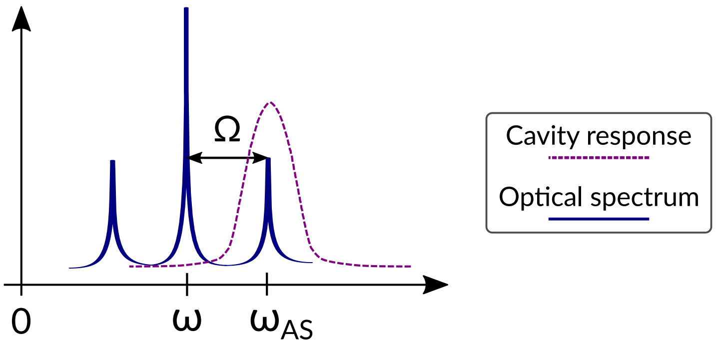

Fig. 1.3. *Sideband cooling - the spectra of the optical and mechanical modes of a moveable cavity mirror system. The cavity is tuned such that it is resonant with anti-Stokes scattered light, and much less favourable to Stokes scattered light, increasing the net cooling rate. See [1] §V.B*

These methods of control delivered through optical systems allow for the cooling of the oscillator, the advantages of which will be discussed later. This cooling is of the oscillator centre of mass temperature, which is related to the kinetic energy of the particle by equation 1.2. The total energy of the oscillator can be obtained using the equipartition theorem, which states that each quadratic degree of freedom of the system contributes $1/2 k_B T$ of energy. When thinking about a 3D harmonic oscillator, there are 3 kinetic and 3 potential degrees of freedom and so we write the total energy as in equation 1.1

$$E = E_U + E_K = 6 \times \frac{1}{2} k_B T_{\text{CoM}}. \tag{1.1}$$

If a single degree of freedom, $\left\langle \mathbf{z}^2 \right\rangle$, is measured and can be used to calculate the centre of mass temperature of the oscillator.

$$\frac{1}{2} k_B T_{\text{CoM}} = \frac{1}{2} k_z \left\langle \mathbf{z}^2 \right\rangle \tag{1.2}$$

$$T_{\text{CoM}} = \frac{k_z \left\langle \mathbf{z}^2 \right\rangle}{k_B} \tag{1.3}$$

where $\left\langle \mathbf{z}^2 \right\rangle$ is the variance of the oscillator position in the z direction, m is the oscillator mass and k_B is the Boltzmann constant. This is a temperature distinct from the more traditionally thought of internal temperature, T_{int}, this corresponding to the expectation value of the kinetic energy of a constituent particle, rather than of the object (nanoparticle) as a whole. A lower centre of mass temperature corresponds to a lower RMS position amplitude. This enables optomechanical systems to be ultra sensitive to forces of many kinds, such as gravity and electrostatics (discussed in more detail in §1.3.2), and opens up the possibilities of using them to look for new physics.

The optomechanical systems discussed above are all attached to a substrate in some way, so as to be mounted to the rest of the device. This is called clamping, and it allows heat to leak into the oscillator, raising the minimum temperature such systems can be made to reach. This can be thought of as the oscillators losing energy from the cooled mode through the clamp with each oscillation, lowering their mechanical 'quality-factor', 'Q factor', or Q, as defined in equation 1.4 [21]. These behaviors are linked through the fluctuation-dissipation theorem, which will be discussed more fully in §2.5.1 and §2.5.2.

$$Q \equiv \frac{\Omega}{\Delta\Omega} = 2\pi \times \frac{\text{energy stored}}{\text{energy dissipated per cycle}} \propto \frac{\Omega}{\Gamma} \tag{1.4}$$

where $\Delta\Omega$ is the full-width-half-maximum (FWHM) bandwidth of the oscillator. A lower Q can be thought of as a more heavily damped oscillator, with a higher damping rate, Γ. Higher damping rates are undesirable when trying to make precise measurements, as they broaden spectral features, leading to the loss of information. The removal of this clamping is therefore beneficial, as we shall see later.

§1.2.2. Levitated Optomechanics

Now that some of the general principles of optomechanics have been mentioned, we can explore the more specifically defined field of levitated optomechanics. This is the subset of optomechanics in which the oscillator is a particle held in space at the focus of a laser beam, and it seeks to take advantage of the benefits of removing the clamping mechanism and trading the noise and heating due to clamping for radiation pressure shot noise, which will be discussed later. Instead of an oscillator attached to, or manufactured from some substrate, particles that are smaller than the focus waist size (diameter) can be confined to a small region just downstream of the focus by the optical gradient force (fig 1.4), or by balancing the radiation pressure produced by a laser on a large particle with the force due to gravity [22]. The gradient force (§2.4.3) arises from the interaction energy of a polarisable particle in an external electric field, and the gradient in question is that of the laser intensity with respect to position.

It is the gradient of intensity that is important as for a generalised potential, the force is inversely proportional to the gradient of the potential, and in the case of optical trapping the potential is related to the trapping light intensity. For details, see §2.4.4.

$$F = -\nabla U \propto \nabla I \tag{1.5}$$

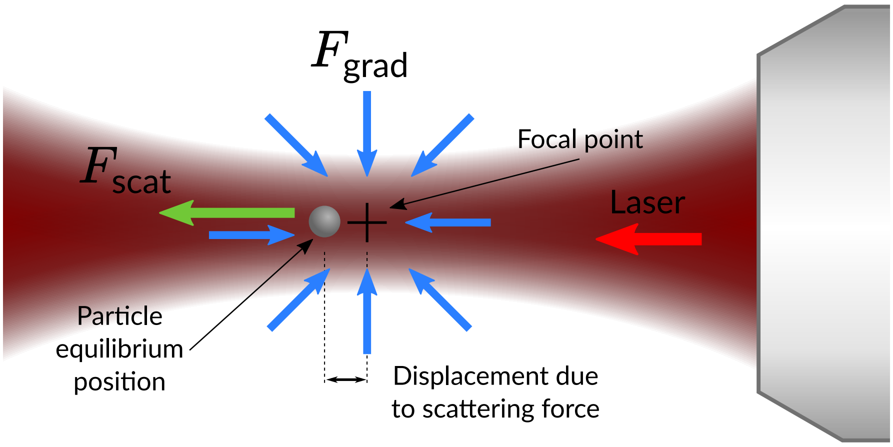

Fig. 1.4. *A typical levitated optomechical oscillator. A microscope objective focuses a laser beam to a tight focus. A particle (not to scale) is trapped and held in the focus.*

A highly convergent beam will create a narrow focus, the waist of which has a steep intensity gradient in the x, y and z directions. This intensity gradient produces a restoring force on the particle, pulling it towards the focal point. The physics of the particle motion and trapping mechanism will be covered fully in chapter 2, but for now it suffice to say that the particle oscillates around an equilibrium position like a mass on a spring, with characteristic frequencies in the x, y and z directions. The particle's time averaged position is shifted in the direction of the incoming beam wavevector $\hat{k}$ from the focal point, due to the radiation pressure from the laser. This is known as a scattering force. For particles significantly smaller than the trapping light wavelength, the scattering force is proportional to the particle volume squared ($\propto r^6$) and there is therefore a maximum radius of particle that can be stably trapped before the scattering force overcomes the gradient force. This maximum stable trap radius depends on the trap geometry but is usually approximately 1 μm, larger than this and the scattering force pushes the particle out of the trap unless it is balanced by either gravity or the scattering force from a second, counter-propagating laser.

The layout of the trapping mechanism means that the particle, usually a sphere or rod with diameter between 10 nm and 10 μm, is largely thermally and mechanically decoupled from it's environment. This decoupling means the particle's Q factor is determined only by the viscosity of the fluid through which it's moving (at least down to $\sim 10^{-8}$ mbar, after which see [23] and the RPSN discussion in §1.2.2.1). It's most often the case that levitated optomechanical systems start in air at atmospheric pressure and are then evacuated. This decreased gas pressure corresponds to an increase in Q. Increasing Q can be, and is usually, expressed as a decreasing damping rate Γ. Levitated optomechanics therefore provides a clean test mass that behaves as an underdamped harmonic oscillator.

§1.2.2.1. A brief history

Levitated Optomechanics uses the principles of optical tweezing to trap particles, the forces responsible for which were long thought to be so small they had no practical uses, and were declared by John Henry Poynting to have "extreme minuteness" [12]. Optical tweezing was first demonstrated in a seminal paper by Arthur Ashkin (winner of $1/2$ of the 2018 Nobel Prize in Physics) in 1970 [22, 24–26] when he used a focussed laser to trap micron sized latex particles suspended in water. Ashkin showed that the newly invented laser [27] made radiation pressure forces into a useful tool. Optical tweezers eventually became widely used and found uses in biomedical [28, 29], spectroscopic [30], fluid dynamic [31] and microfabrication [32] applications.

Initially, Ashkin used one laser beam per confinement direction, but continued the progression towards modern levitated optomechanics with the development of the single beam optical trap [33,34], that showed a tightly focussed beam could also confine a particle along the beam axis because of the axial intensity maximum. Ashkin and his colleague Dziedzic trapped particles from 25 nm to 10 μm with 514.5 nm wavelength light, showing it was possible to trap particles both much larger and much smaller than the wavelength of the trapping light. This method was the first use of a microscope objective to create a sufficiently convergent beam for the tight focussing required. Before moving on it is important to understand the properties of the microscope objectives, as well as other types of objectives used in optical trapping.

Interlude - objectives and NA

Microscope objectives are multi-element optical devices that use more than one lens to correct for aberrations caused by the preceeding focussing optics. They can be desgined in such a way that they are relatively tolerant to angular misalignment whilst maintaining a small focal spot.
A microscope objective uses refractive optics to focus a laser, but reflective optics can also be used. These mirror objectives have the advantages of being achromatic and geometries can be designed to create much more strongly converging light. Mirror objectives also have the advantage of the focus being some millimeters from the surface of the optic and therefore a trapped particle is significantly less influenced by surface effects from the device.

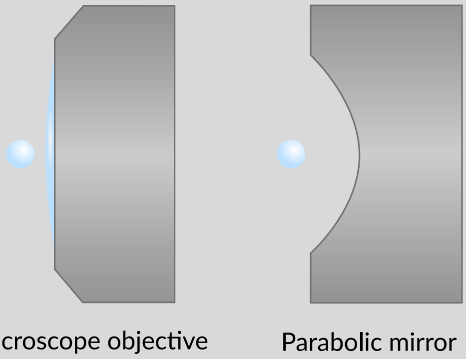

Fig. 1.5. *Surface distance comparison between a microscope ojective and a parabolic mirror trap*

As a tradeoff for these benefits, mirror objectives suffer from greater sensitivity to angular misalignment, with the intensity profile at the focus rapidly deviating from Gaussian as the incoming beam angle is altered. This means that the approximation that the intensity varies quadratically with position relaive to the optical axis becomes invalid if a mirror trap is misaligned. Numerical aperture (NA) is the most commonly used measure of how sharply light is focussed, and originates in microscopy [35]. Numerical aperture is related to the sine of the beam convergence half-angle θ (figure 2.1) and when modelling the light as a Gaussian beam, and thereby making the paraxial approximation (§2.2), can be related to the wavelength and focal waist diameter.

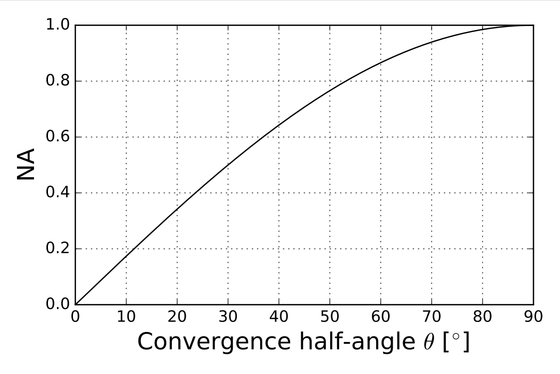

Fig. 1.6. *NA as a function of convergence angle*

$$\mathrm{NA} \equiv n \sin(\theta) \simeq \frac{\lambda}{\pi w_0} \tag{1.6}$$

Here n is the refractive index of the material through which the light is propagating, θ is the convergence half-angle, λ is the wavelength of light and w_0 is the radius at which the waist of the beam falls to e^{-2} of the on-axis intensity. Further information on beam geometry is given in §2.2.1.

The numerical aperture is not defined above $\theta = 90°$ because it originated in microscopy, in which this is the largest angle possible. The work contained in this thesis is all done in air or vacuum where $n = 1$, however many optical tweezers are used in oil or water with $n > 1$ in order to raise the NA.

The main immediate applications of Ashkin's work were in microbiology, where it was widely used to manipulate cells in quasi-2D chambers of liquid. On the contrary, progress in the development of optical tweezing for use in low pressure environments (both experimentally and theoretically) slowed after Ashkin's work until around the turn of the millenium when 3D trapping in air was demonstrated with a view to using this platform as a tool for investigating fundamental physics [36, 37].

In 2011, Li *et al.* continued Ashkin's work on trapping in vacuum and demonstrated the cooling of an optically trapped particle by the use of 3 cooling beams, in addition to the trapping beam [38–40]. The single beam trap was revisited from 2009 onwards by the work of a collaboration between the groups of Romain Quidant and Lukas Novotny at ICFO - Barcelona and ETH Zürich respectively. This resulted in the construction of a single beam optical trap (fig 1.7) that could cool particles to sub-kelvin centre of mass temperatures and the publishing of an influential paper [7, 41] that began a period of rapid progress, the results of which are seen in table 1.1.

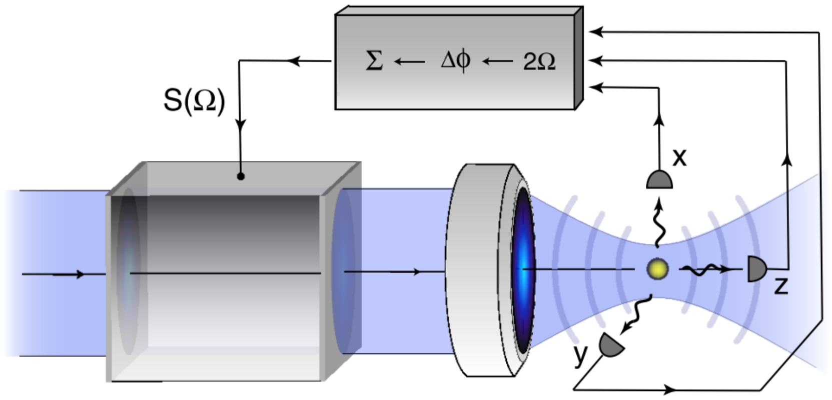

Fig. 1.7. *A schematic representation of the trapping and cooling setup used by Jan Gieseler et al. [7]. A microscope objective is used to create a laser focus, in which a nanoparticle is trapped. 3 photodetectors capture information about the oscillating position of the particle. These 3 signals are each frequency doubled, phase delayed by an appropriate degree and then summed together. The resulting signal is used to intensity modulate the trapping light, resulting in the cooling of the particle motion.*

Many research groups around the world are now interested in Levitated Optomechanics, some of the most relevant to this thesis are given below.

Institution	Group leader(s)	Major publications
University of Vienna	Markus Arndt	[42–44]
University of Vienna	Markus Aspelmeyer	[45–47]
University College London	Peter Barker	[48–56]
Northwestern, Chicago	Andrew Geraci	[57–64]
Purdue University	Toncang Li	[38–40, 60, 65, 66]
King's College London	James Millen	[42, 43, 67–70]
ETH Zürich / ICFO Barcelona	Lukas Novotny / Romain Quidant	[7, 8, 41, 71–78]
University of Southampton	Hendrik Ulbricht	[21, 79–87]

Table 1.1: Research groups overview **-** Ordered by surname and featuing some of their most relevant publications to this thesis.

There has been great progress in cooling particles held in single beam traps, with the state of the art being the work of Lukas Novotny, Romain Quidant, Jan Gieseler *et al.* [8], in which they show cooling of a nanoparticle (NP) down to temperatures best expressed as the expectation value of the phonon occupation number, $\langle n\rangle$, of a quantum harmonic oscillator (QHO):

$$\langle n\rangle = \frac{1}{\exp\left(\dfrac{\hbar\Omega}{k_B T_{\text{CoM}}}\right) - 1}. \tag{1.7}$$

When T_{CoM} is large, $\exp\left(\hbar\Omega/k_B T_{\text{CoM}}\right) \simeq 1 + \hbar\Omega/k_B T_{\text{CoM}}$, and equation 1.7 can therefore be reduced to equation 1.8,

$$\langle n\rangle = \frac{k_B T_{\text{CoM}}}{\hbar\Omega} - \frac{1}{2}, \tag{1.8}$$

which is valid to within 0.5% above approximately $\langle n\rangle = 5$.

Novotny *et al.* demonstrate a system cooling a particle to $n = 63$, corresponding to a temperature of $T_{\text{CoM}} = 450\,\mu\text{K}$. To reach the low damping rates required to reach temperatures of this order of magnitude, the gas pressure must be reduced such that it is no longer the dominant dissipation mechanism. The limiting factor on cooling then becomes (the as of 2011, unanticipated) radiation pressure shot noise (RPSN). This is a photon recoil heating effect in which the photons in the trapping beam impart momentum $\mathbf{p} = \hbar\mathbf{k}$ to the particle. Here the direction of $\mathbf{k}$ is random, weighted by the dipole emission pattern (§2.4.5), causing random momentum kicks that heat the particle's centre of mass motion. The ultimate temperature achievable through feedback cooling is linearly related to background gas pressure for $\Gamma \gg \Gamma_{\text{RPSN}}$. The lower viscosity of a rarefied gas causes less damping and so the particle oscillates coherently for a longer time. The position of the particle can be better predicted by the feedback system, leading to more effective cooling and a lower ultimate temperature as above. Fig 1.8 [8] shows the decreasing phonon occupation number with decreasing pressure.

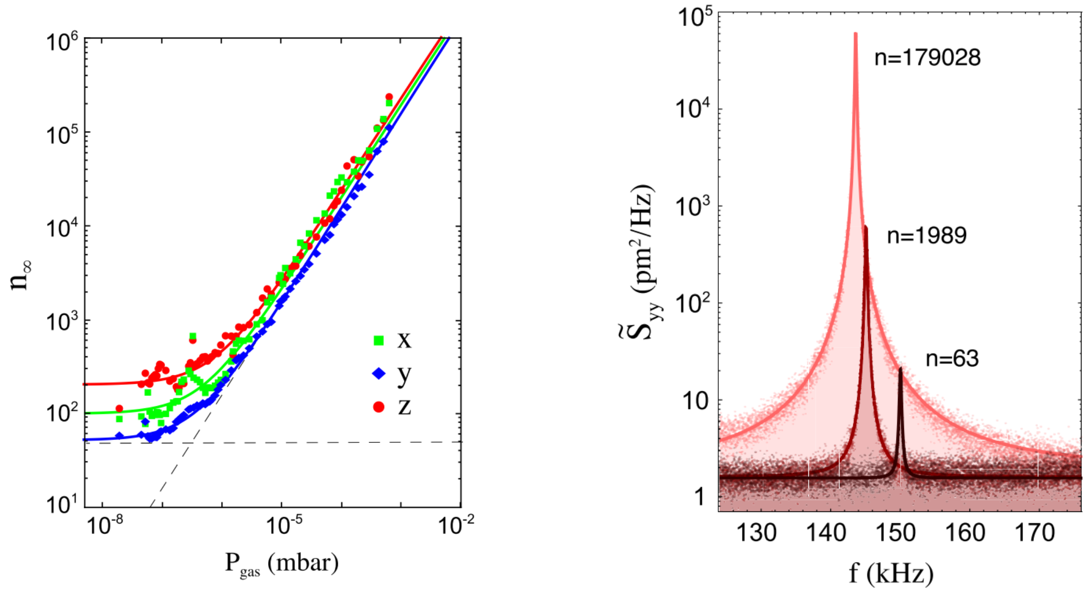

(a) *Steady state phonon occupation number as a function of background gas pressure. The RPSN limit is clearly visible.*

(b) *Power spectra for 3 decreasing gas pressures with decreasing integrated area corresponding to lower centre of mass temperatures.*

Fig. 1.8. *The relation between gas pressure and steady state cooled temperature from data collected and published by J. Gieseler* et al. *[8]*

Improved feedback cooling has opened up access to lower gas pressure regimes in which the damping rates are lower. Quality factors as high as 10^8 have been reported [7, 72, 88], surpassing those of cavity optomechanics [89]. Optomechanical cooling aims to reach the quantum ground state, where Q factors will be limited by RPSN and are predicted to have Q factors of 10^9 [72].

Feedback cooling the motion of levitated NPs creates low temperature states with a small volume in phase space, from which we can create something analagous to a squeezed state by modulating the trapping beam over time [73, 82]. Here when we talk about phase space, we mean the space of position and velocity in which the particle exists, represented by a Gaussian probability distribution due to our uncertain information about the particle motion at any particular time.

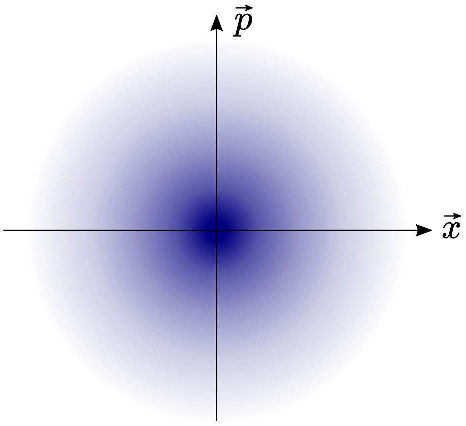

Fig. 1.9. *Phase space - when in a thermal state, a system such as a levitated nanoparticle is represented by a Gaussian with equal widths in the position (***x***) and momentum (***p***) directions, occupying a phase space volume proportional to it's entropy.*

It is possible to prepare non-thermal states and observe thermalisation over time. In this way, levitated optomechanics provides an excellent experimental platform for studying thermodynamics on the nanoscale.

§1.2.2.2. Trapped particles

The microscope objectives and parabolic mirrors mentioned in §1.2.2.1 are generally illuminated by laser beams with Gaussian intensity profiles. This maps to a Gaussian intensity profile at the trap site which is approximated to be quadratic close to the intensity maximum. This lets us treat oscillating NPs as DHOs, with a natural frequency Ω. This means the particle obeys Hooke's law and is subject to a linear restoring force. It has been shown, however, that in certain situations, the thermal effects of gas particles colliding with the oscillator are enough to drive the particle far enough away from equilibrium that the intensity profile is anharmonic [72], although active cooling can counter this.

Cooling the particle centre of mass motion allows for trapping at lower pressures, with lower damping rates. These lower damping rates allow for the detection of smaller forces perturbing the particle motion. Work has been completed on the theoretical framework required to use these systems in the low phonon occupation (low centre of mass temperature) limit [1, 67, 90–92] in anticipation of experimental systems reaching this limit in the not too distant future.

Using this method, a variety of forces are detectable, including the Coulomb force on a charged NP [79, 93], Van der Waals forces [94], and gravity [93]. Exquisite force sensitivities have been demonstrated, down to the zeptonewton level [58, 95]. Static forces move the average position of the particle, something which can be observed using the highly sensitive position detection systems used. A change in average position subjects the particle to different trap geometry dependent environmental conditions, for example moving the particle equilibrium position such that the intensity gradients it experiences are different and thereby changing the oscillation frequencies.

Time varying forces can often be seen in a fast Fourier transform (FFT) of the particle position as a function of time. A sinusoidally varying electric field will produce a time dependent force in phase with the electric field that will appear as a peak on an FFT.

All levitated optomechanical oscillators have damping rates sensitive to background gas pressure and so when well calibrated, can be used as small form factor pressure sensors. These applications all come with the advantage of being relatively compact systems with setups foreseeable that contain no electronics in the sensing head, rendering them much less vulnerable to electromagnetic noise. The use of these effects in sensing is discussed in §1.3.2.

§1.2.2.3. Rotational levitated optomechanics

Up to this point, discussion has been regarding the translational degrees of freedom of the particle centre of mass, and the particles in question have been isotropic. Rotational optomechanics looks at (sometimes only very slightly) anisotropic particles or rods that rotate about their centre of mass when trapped [43, 44, 96, 97]. These systems trap using the same physical mechanism discussed at the start of §1.2.2, and often cool the translational degrees of freedom in the same way as discussed earlier. When trapped with linearly polarised light, an anistropic particle's axis with highest polarisability will precess about the axis of the trapping laser's polarisation and, in the presence of dissipation, the two axes will gradually align to be parallel. This in itself affords some control of the rotational degrees of freedom, as rotating the laser polarisation will steer the orientation of the rod, where it will act as a torsion pendulum with alignment oscillating harmonically about the polarisation axis. The relevant geometry is shown in figure 1.10.

When circularly polarised light is used, and is partially absorbed by the particle, this polarisation axis is rotating too rapidly for the rod and polarisation to align, and the light transfers angular momentum to the rod [98]. A constant transfer of angular momentum causes the rod to rotate rapidly with angular frequency proportional to the driving laser power (sometimes one beam acts as trapping and driving laser) and inversely proportional to background gas pressure.

The discussion above concerns rod-like particles, the high aspect ratio of which gives them form birefringence. It is worth noting that spherical particles can also be driven in this way if they have material birefringence [96], an innate property of materials such as vanadate and lithium niobate ($LiNbO_3$). In these cases the particle polarisability is anisotropic.

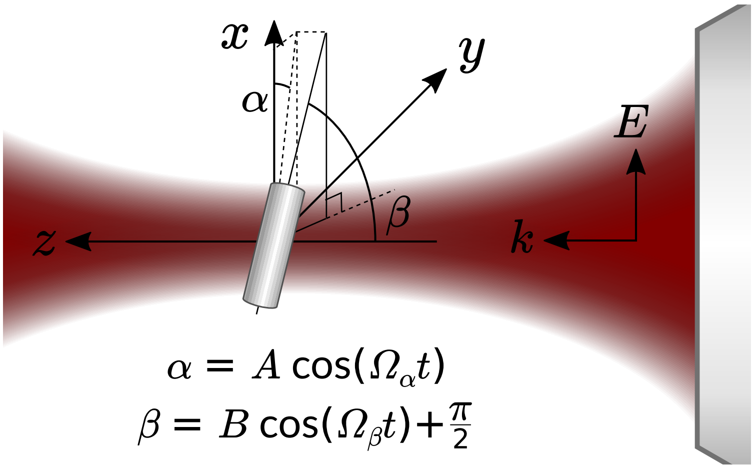

Fig. 1.10. *A nanorod in a single beam optical trap. There are 5 degrees of freedom: x, y, z and α, β. The nanorod axis will oscillate harmonically about the polarisation axis $\hat{E}$ in addition to the 3 translational oscillation frequencies.*

§1.2.2.4. NV centre nanodiamonds

The development of experimental systems to act as part of quantum information systems is becoming increasingly common. Levitated optomechanics offers potential as a testbed for enabling quantum information processing techniques. The isolated experimental platform afforded by a feedback cooled levitating particle is well suited to use as support for a qubit.

An example of a potential qubit that could make use of the isolation found in levitated optomechanics is the Nitrogen-vacancy (NV) centre. NV centres are photoluminescent lattice defects (fig 1.11a) in diamond consisting of the replacement of a carbon atom with a nitrogen, adjacent to a lattice vacancy. NV centres have a multi-level energy structure (fig 1.11b) that originates from electron spin resonance effects. This level system is optically addressable, allowing a state to be prepared using a laser, and then coherently manipulated using a series of radio frequency pulses to rotate the state on the Bloch sphere. This RF manipulation allows quantum information to be encoded in the NV centre state superposition between the excited and ground state levels. This ability to store information about a quantum state for appreciable times ($\sim 10^{-6}$ s [99–101]) before decoherence makes these systems candidates as qubits [102]. A nanodiamond with one or more NV centres can be optically trapped and feedback cooled [76], giving it good thermal and mechanical isolation from external sources of decoherence that would otherwise be undesirable. The NV centre can then be used as a coherent storage device for quantum information [103] with readout provided by the NV centre photoluminescence and coupling between NV centre state and the nanodiamond's mechanical motion. Unfortunately it is difficult to maintain a trapped nanodiamond at low background gas pressure, as they react with oxygen and burn when their temperature increases due to the lack of heat dissipation under these conditions [104].

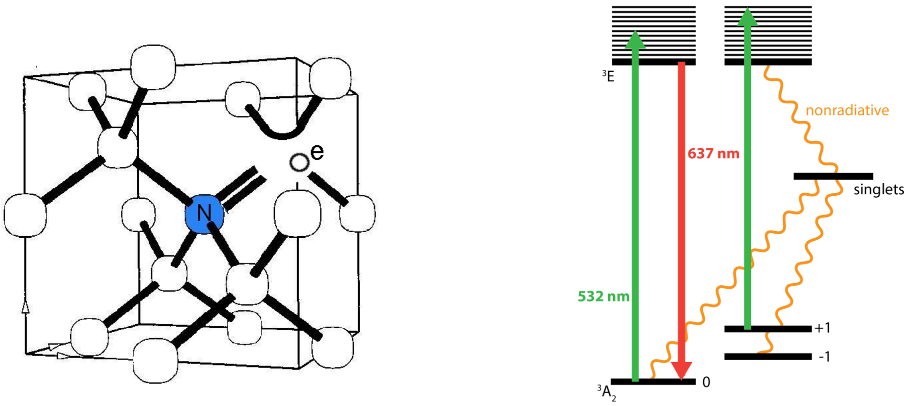

(a) *NV centre structure - The NV centre can be modelled as a quasi-molecule.* [105]

(b) *NV centre energy level diagram. Quasi- two level system consisting of a* $^3A_2$ *ground state and* ^3E *excited state.*

Fig. 1.11. *NV centres can act as qubits due to their energy level structure, and can be isolated from noise sources by optical tweezing.*

§1.3. Motivation

We have seen above that levitated optomechanics is a novel experimental platform upon which a variety of research can be based. On the one hand, levitated optomechanics allows for highly fundamental physics research, on the other hand we have proposals to use these optomechanical devices in useful engineering applications such as sensors, directly applying their capabilities and advantages in situations that play to their strengths. Here we will discuss both of these motivations.

The central theme of most levitated optomechanics experiments is precision measurement. Specifically the measurements of ultra small forces on well definied initial states. These capabilities mean that this area of physics shows promise in sensing modifications to gravity [106], collapse models [79, 84, 107–109], gravitational waves [59], quantum thermodynamics [110] and the investigation of the quantum-to-classical transition [84].

§1.3.1. Why do large objects not exhibit quantum behaviour?

Humans evolved with an intuitive understanding of how objects in the macroscopic word behave. Our common sense is relatively accurate when it comes to predicting where a thrown rock will land or how hard to push something. Physics in this macroscopic regime falls broadly under the term classical mechanics and has been studied and understood for hundreds of years. In the first half of the 20th century we learned of quantum mechanics and gradually became more comfortable with the idea that atoms, electrons and photons did not behave "sensibly". The Schrödinger's cat thought experiment serves as a reminder of how ridiculous it seems that objects as large and as complex as cats would exhibit quantum behaviour. We now

have the incredibly successful quantum electrodynamics (QED), a model of how matter behaves on the atomic scale and have yet to find any evidence that contradicts it. The question arises,
If the world is made of macroscopic objects, which themselves are made up of microscopic constituent parts, why does quantum mechanics explain the behaviour of the building blocks but not the object as a whole?

§1.3.1.1. The quantum to classical transition

The boundary between these two size scales is referred to as the quantum to classical transition, and objects that skirt this boundary are known as mesoscopic. The question of why quantum phenomena don't manifest in everyday objects has been studied theoretically, but experiments mainly fall neatly into one size category or the other. Atomic physics is a very mature field in which quantum theory and experiment agree beautifully, likewise in practice, fields like biology and ballistics seem to follow the laws of classical mechanics. The size scales of these two types of discipline do not meet, but levitated optomechanics may be the experimental test of the middle ground that can provide more information. Nanoparticles are mesoscopic, they have radii of around 50 nm, compared to a human red blood cell at 4000 nm [111] and a carbon atom at 0.07 nm [112].

To demonstrate that an object exhibits quantum behaviour, we need to see some kind of wavefunction-like behaviour. This is usually done by placing the object in a spatial superposition and, just as in Young's double slit experiment, allowing it to take multiple paths and interfere with itself. Doing this with photons and electrons is now so simple that it is a staple experiment in most undergraduate labs, but as the mass and size of the object being used increase, this process becomes more difficult. To date, some of the most massive superpositions are of spherical C_{60} molecules of Buckminsterfullerene, or "Buckyballs" (fig 1.12a). C_{60} molecules have been fired through a diffraction grating and shown to arrive distributed in a characteristic interference pattern (fig 1.12b) [113, 114].

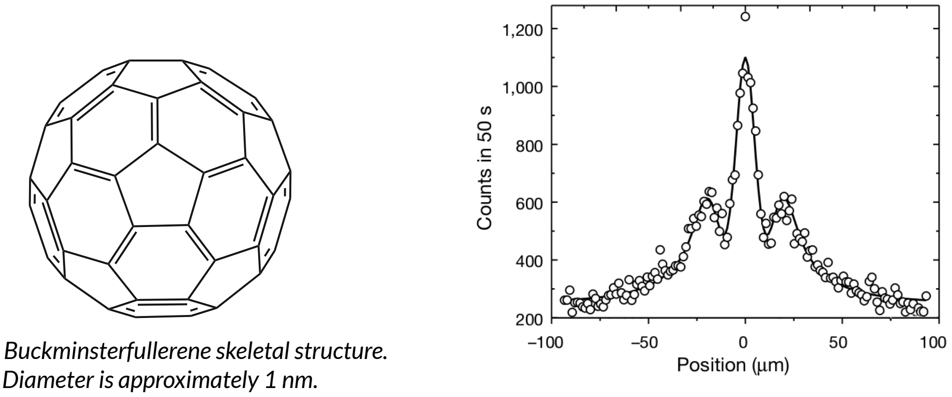

(a) *C_{60} Buckminsterfullerene skeletal structure. Diameter is approximately 1 nm.*

(b) *The interference fringes produced by diffracting molecules of C_{60}. Adapted from ref [113].*

Fig. 1.12. *The diffraction of Buckminsterfullerene*

Beyond the size scales of Buckyballs, complex biomolecules have been interfered, giving diffraction pattern results and showing that this is not a phenomenon that is limited to the size scale of a C_{60} molecule [115]. Increasing the size scale further, the levitated optomechanics community aims to interfere nanoparticles and improve the constraints placed on extensions to quantum mechanics provided by work with C_{60} [84, 116].

The process that inhibits quantum behaviour of these more massive objects is decoherence, the process by which the coherence of a quantum object gradually 'leaks' out into the surrounding environment, via the weak coupling it has to the thermal bath that is the rest of the world. A quantum object in a spatial superposition is represented by a wavefunction that spreads out and can interfere with itself. When the position of this object is measured, the wavefunction becomes strongly coupled to that of the measurement device, and a rapid version of decoherence occurs, known as measurement-induced collapse. As this process takes place, the particle is localised down to a small region corresponding to its measured position. Measurement in this context is any interaction between the object in question and another in the vicinity though electromagnetism, gravity, nuclear interaction etc. For tiny, isolated objects such as single electrons, these measurement events are rare and the coupling is weak, meaning the wavefunction can expand and travel through space relatively unimpinged. In contrast, a carbon atom making up part of a C_{60} molecule is coupled to, and constantly interacting with, the other atoms in the molecule, decohering everytime it is forced to give up information about it's position through measurement.

The precise method through which decoherence acts and wavefunctions are collapsed is one of the primary scientific goals of the levitated optomechanics community. The fundamental physics motivation behind levitated optomechanics can be summarised as "Is there a fixed limit where quantum mechanics must transition to classical mechanics, where is it, and what forces the transition?".

It's also possible that the laws of nature contain something akin to decoherence built in, rather than just as a result of coupling between quantum systems. A candidate theory for describing this kind of collapse behaviour is Continuous Spontaneous Localization (CSL) [108, 117–119], a two parameter collapse model described by a rate and a length scale that makes testable predictions about the rate at which an object decoheres. CSL is to be tested by future levitated optomechanics experiments such as MAQRO, detailed below. Importantly, collapse due to CSL would represent a decrease in the total coherence of a closed system, rather than the dispersion of some total amount of coherence into a thermal bath.

§1.3.1.2. MAQRO

The promise of levitated optomechanics is evidenced by the progress of the Macroscopic Quantum Resonators (MAQRO) mission proposal [116, 120]. MAQRO is a proposal for a European Space Agency (ESA) spacecraft with a scientific payload containing a cavity cooling levitated optomechanics experiment. The experiement will consist of optically trapping a nanoparticle, feedback and cavity cooling it's centre of mass motion, and then releasing it through a diffraction grating. If the particle can be cooled to (or near to) the quantum ground state then when released through a UV laser diffraction grating, the particle matterwave should diffract through the grating and exist in a spatial superposition and interfere. As in the Young's double slit experiment, repeating this freefall may or may not reveal an interference pattern, made up of repeated position measurements of where the nanoparticle was found to be when measured by UV laser and camera. The MAQRO mission aims to probe the quantum-to-classical transition and to see if relatively high mass objects such as nanoparticles can be made to behave in such a way that quantum mechanics is required to explain the observed results. The observations of quantum behaviour can then be used to constrain extensions to quantum mechanics that have been developed to help explain this transition from quantum to classical. Performing this test in space provides much longer freefall times for the evolution of an interference pattern, such that the properties of the particle matterwave are sufficient to constrain the proposed extensions to quantum mechanics. In addition, space acts as a low temperature heat bath, aiding in cooling and has low gas pressure to help with vacuum stability.

§1.3.2. Sensors

Alongside fundamental physics applications, levitated optomechanics show promise in sensing, some forms of which, such as short range gravity measurement [106, 121], are themselves methods for investigating fundamental physics. Here we will discuss some of the potentially useful ways these systems could be implemented.

Metrology is an enormously widespread field, with some type of sensor present in all kinds of consumer electronics, industrial plants, research labs, motor vehicles etc. Sensors are essential for safety, monitoring and optimisation; without information about the status of a system, it is difficult to apply appropriate correction in order to reach a desired state. Historically these sensors have been mechanical, usually transducing to some analogue voltage for readout. An anemometer (wind speed gauge) is an example of this type of sensor; airflow creates a force on the cups, turning the shaft and driving a dynamo that produces a voltage proportional to wind speed. More recently, sensors have been miniaturised to fit into smaller devices and where possible made using solid state or semiconductor technology. Advances in microfabrication techniques mean that sensors can be made cheaply down to scales around the micron level, rather than millimeters. These tiny systems are known as MicroElectroMechanicalSystems, or MEMS, and are present in smartphone and airbag accelerometers, the inertial measurement units in aircraft and motor vehicles, microphones and ultrasound scanners. Clearly, sensors are important to modern life and the economy as a whole. Levitated optomechanics holds promise for use in sensing applications, possibilities that are definitely worth investigating.

In principle, levitated optomechanics has the potential to sense any phenomena that peturbs the trapped particle in a reproducible way. This can be a quasi-static force that changes the equilibirum position of the particle, a sudden change in relative velocity between the lab and particle or a damping of the particle oscillation. It is worth noting however, that the highest force sensitivities are achieved when the perturbation of the particle is resonant with it's natural oscillation frequency, with minimum detectable force calculed by [58],

$$F_{\text{min}} = \sqrt{\frac{4k_B T b k}{\Omega Q}}, \tag{1.9}$$

where k_B is the Boltzmann constant, b is the measurement bandwidth, Ω is the natural oscillation frequency of the system, Q is the mechanical quality factor, k is the spring constant of the oscillator and T is the temperature of the bath with which the particle must be in thermal equilibrium.

These altered conditions all affect the particle position over time, something that can be read out and used to infer the value of the parameter being measured. These categories will each be discussed briefly.

§1.3.2.1. Gravity

In addition to the forces shown in figure 1.4, gravity is always acting on the particle, displacing it's equilibrium position slightly in the direction of the local apparent gravity. This is an example of a static force. The position of the particle can be measured and so as the orientation of the trap is changed with respect to gravity, in the frame of the trap the gravitational acceleration of the particle appears to rotate and can be measured . In principle it is possible to measure both the direction and magnitude of the force due to gravity using this method. The challenge here is cooling the centre of mass motion of the particle significantly that the small gravitational displacement is visible in amongst thermal fluctuations and background gas collisions. This has been achieved by Novotny *et al.* [93] and so it is conceivable to use a levitated optomechanical system to sense the magnitude of gravity at many positions and compute a density map of the material making up the surrounding environment. This will require close to ground state cooling, and the ability to measure the force on the particle with ultra-high precision. These capabilities could have applications including subsurface mapping, security screening, structural surveying, oil, gas and water prospecting, among many more. When developed further, this kind of device would be quite similar to existing cold atom gravimeters [122–127]. in that they use a sensitive physical system to test local gravity. Levitated optomechanics versions would not require quite the same level of isolation and shielding as a cold atoms system and it's feasible that they could be made to be more ruggedised.

§1.3.2.2. Electric fields

Nanoparticles can be given an electric charge either by electrons fired from a cathode ray tube or by positive ions. As a particle in an optical trap is electrically isolated, they can be highly charged by continual charge carrier deposition. This charge number represents the coupling strength between the particle motion and the local electric field, the latter of which creates a force on the particle proportional to the particle charge. This force changes the average position of the optically trapped nanoparticle. It has been shown experimentally that the charge can be well controlled and produces a force on the particle when placed in an electric field [9, 79]. Individual charges entering and leaving an optically trapped nanoparticle can be seen in figure 1.13. Electric field sensing in this way could be used to map the distribution of charge in a material, or to measure current without having to electrically connect to a circuit.

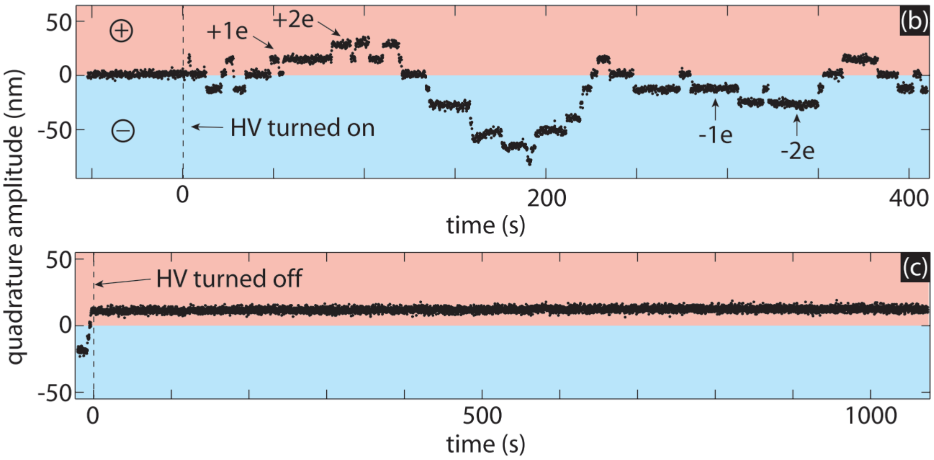

Fig. 1.13. *Individual charges entering and leaving an optically trapped nanoparticle. The net charge of the particle determines it's coupling to an external electric field and therefore the quadrature amplitude of it's oscillation [9]. Subfigure a) shows the position oscillation amplitude changing over time as the number of charges on the particle (and therefore it's coupling to the electric field) fluctuates. Subfigure c) shows the same but with the electric field deactivated, illustrating that these changes in amplitude are indeed due to an electrostatic force.*

§1.3.2.3. Acceleration

The previous sensing examples were of static forces, but levitated optomechanics expermients are also highly sensitive to the sudden acceleration of the particle with respect to the trapping apparatus. This situation occurs regularly in aircraft, satellites and seismometers. If the system experiences an acceleration, then the particle is dragged along behind it, apearing to have suddenly accelerated when viewed in the frame of the measurement equipment. The particle's excursion away from the normal equilibrium position can be detected and a value calculated for acceleration. These systems could be installed in aircraft and submarines and would be suitable as an inertial guidance system due to their high force sensitivity. These intertial guidance systems would take a known starting position measured by GPS, and calculate the current position from a history of measured acceleration. These devices would be desirable in GPS deprived environments, such as underground or underwater. The force sensitivity required to make sensors of this kind again requires ground state level cooling and precise information about the optomechanical system.

§1.3.2.4. Fluid dynamics

Gas flow and gas pressure can be measured using position data from a levitated nanoparticle too, but through quite different means. A net gas flow relative to the particle creates Stokes drag, another force that will pull the particle away from it's equilibirum position. In order to calculate a flow rate however, the pressure must be known. This is because Stokes drag is proportional to fluid viscosity and fluid flow rate (equation 1.10). If the drag force is measured, the viscosity must be calculated from the gas pressure, and then used to determine a flow velocity.

$$\mathbf{F}_{\text{Stokes}} = -6\pi\eta r\mathbf{v} \tag{1.10}$$

At the pressure and size scale regimes relevant in levitated optomechanics, this must be corrected slightly and is proportional to the damping rate (Γ), particle mass (m) and particle velocity ($\mathbf{v}$) as below [7, 39, 128].

$$\mathbf{F}_{\text{Stokes}} = \Gamma m\mathbf{v} = -6\pi\eta r\mathbf{v}\frac{0.619}{0.619 \cdot \mathrm{K_n}}(1 + c_K) \tag{1.11}$$

Here, η is the fluid viscosity, r is the radius of the spherical particle and $\mathbf{v}$ is the relative velocity between fluid and particle. Stokes drag and the quantities K_n and c_K will be explored further in §2.5.2.

Fortunately gas pressure measurements are entirely separable from flow measurements, as gas pressure manifests as a damping on the oscillation of the particle, appearing as a broadening of the spectral lineshape of particle position. The value for damping rate Γ can be used to infer the pressure; this will be covered later. Measuring gas pressure with this method is feasible from 100 mbar down to 10^{-6} mbar, limited only by issues in maintaining traps at this pressure without feedback cooling. These issues will also be discussed later. This is an excellent dynamic range compared to existing devices such as a Pirani gauge, which is useful between 100 and 10^{-4} mbar [129]. Pressure gauges are often bulky, and it is feasible that a sensor incorporating a levitated particle could be miniaturised below the volume of existing pressure measurement systems, for use in miniature vacuum systems. Pressure and gas flow measurement is vital to the vast majority of chemical and industrial processes, potential new sensing technologies like optomechanics are important to develop.

§1.3.2.5. Electrical isolation

Many modern sensors, with the exception of fibre optic sensors, use electrical components close to the sense head to either perform the actual measurement, digitising the recorded value, to power the device or to transmit the measured signal. In environments with high levels of electromagnetic (EM) noise such as engines, generators, motors, power supplies etc, this EM interference can degrade measurement and lead to a decreased signal to noise ratio (SNR). A levitated nanoparticle only requires a laser for trapping, which can be carried via fibre optic cable to the sense head, and is not susceptible to EM noise. The signal readout can be along this same fibre, connecting to an optoelectronics system that can be shielded, or far from the source of noise. These sensors are interferometric in nature and so have excellent sensitivity to changing particle position. Trapped nanoparticles can become charged and therefore become sensitive to EM noise, but it is posible to measure this effect and compensate by applying an opposing electric charge; although the accuracy to which this can be achieved then becomes the limiting factor.

The sensing applications discussed all share the need for low centre of mass temperature and precise, accurate information about the motion of the nanoparticle in the trapping potential. It is hoped that this thesis will contribute to the latter and thus help enable the use of these systems as sensors.

§1.3.3. Gravitational waves

The above sensing capabilities could be used for fundamental physics research with the goal of detecting gravitational waves. Proposed levitated optomechanical systems are 1 to 3 orders of magnitude more sensitive to gravitational waves in the 100 kHz frequency range than LIGO [59]. The specific frequency range is because this is the frequency range in which the particles naturally oscillate and therefore any gravitational wave distubances to the particle at these frequencies are resonantly enhanced.

These devices would consist of a nanoparticle trapped in a high finesse cavity and then cooled via feedback and cavity cooling. The position of the particle could be measured with such sensitivity that the effect of gravitational waves could be seen. This would extend the detectable frequency range of gravitational waves and compliment existing laser interferometer observatories whilst being a fraction of the size and cost. This extra information would greatly aid the understanding of phenomena predicted to emit gravitational waves in this frequency range.

§1.3.4. Short range forces and surface physics

In levitated optomechanics, the “probe” is held only with a beam of light, and as a result we can place it very close to a surface without mechanical constraints becoming a factor. From this position it’s possible to measure forces arising from it’s interaction with the surface, although care must be taken to account for the the effect of the surface on the trapping field itself and the subsequent alteration to the particle trap parameters. In other sensing geometries such as atom interferometry and non-levitated nanoresonators, the proximity to a surface can be an issue, either due to detrimental effects of the surface on the measurement characteristics or lack of physical access to the interesting region. In levitated optomechancs, a particle can be trapped less than a micron from a surface, which should allow exotic forces can be tested, including the Casimir-Polder force [94, 95], non-Newtonian gravity [106], van der Waals forces and patch charge effects [130]. These short-range forces alter the shape of the particle trapping potential, with either an attractive or repulsive force from the surface. This change in potential appears as a deviation from the linear restoring force expected of these systems and can be characterised at varying distance from the surface. The high mass of these levitated particles means they are testing a different parameter regime than that accessed by similar cold atom experiments, and so can be used in parallel to confine the parameters of proposed models for the forces above.

§1.3.5. Nanoscale thermodynamics

As technological progress continues, technology tends to reduce in size and mass, and in the near future devices will reach such a size that they are comparable with proteins and other complex molecules. These tiny molecular machines will have applications in medicine, construction, defence and beyond.

If we are to prepare for these types of nanotechnology we must understand how heat behaves on the nanoscale, and when dealing with a small number of particles rather than a macroscopic ensemble [67, 131, 132]. Levitated optomechanics provides an excellent test platform for the start of this research as it allows a single particle or rotor with known properties to be isolated and subjected to varying environmental conditions. The particle's thermodynamic properties can be measured and tracked as a function of heat transfer rates, damping, radius, mass, etc. Levitated optomechanics can be used to test different heat engine cycles [110] and to learn how to optimise the work that might be produced from future molecular machines. It is theorised that quantum heat engines might be able to surpass the classical Carno efficiency limit [133, 134], further motivating the development of the theory and experimental realisation of smaller molecular motors and engines [135, 136] .

These future nano-machines could be built in the millions through bottom-up chemical synthesis and effectively programmed by carefully controlling their structure such that motion is controlled by adjusting environmental conditions. They could be used to remove tumours, repair damaged tissue and break down waste on the molecular level, to aid with recycling [137–142]. In order to be useful, these machines will have to behave as thermodynamic engines, taking heat from an energy source such as the human body or sunlight and transferring it into useful work. The laws of thermodynamics have been well understood at macroscopic scales for hundreds of years, but because of their statistical nature they do not neccesarily apply in the molecular regime. The flow of heat in and out of just a few dozen atoms may well behave very differently to that of a mole of atoms.

Thermal fluctuations can have the energy of an appreciable percentage of the total energy of the system and so can cause large perturbations [143]. In addition to this, the inherently quantum nature of atoms and molecules means that their energy structures are not well approximated by the continuous distributions used in classical thermodynamics [144, 145]. For these reasons, it's important to use levitated optomechanics to further experimental research that can work with ongoing theoretical work into nanoscale and quantum thermodynamics.

§1.4. Project Aims

Better information is needed about the position and motion of nanoparticles held in optical traps. This improved information gathering will allow the motivating use cases described above to be developed further, and will hopefully be generalisable to other levitated optomechanical systems in order to benefit the wide variety of physics and engineering applications for which these devices show such promise. The overarching goal of the project was to gain a better understanding of what can be inferred from available measurements, achieved through the specific aims of this Ph.D. project outlined below. These goals are quite general and so have remained static throughout the course of the project, even if the methods by which they are achieved has changed multiple times; as is the nature of research.

- Create a levitated optomechanical trap capable of trapping at atmospheric pressure and then pumping down to high vacuum ($\sim 10^{-6}$ mbar).
- Build said system in such a way as to maximise long term stability and ease of use.
- Optimise the system to be maximally sensitive to the particle position in one axis, by collecting as much signal light as possible, making use of particle back-scatter for greater position sensitivity, and by using a fibre-coupled architecture to minimise information loss.
- Design an architecture for fast, reliable measurement and storage of spectrally clean particle position data.
- Use this data to develop methods for understanding how the thermodynamic properties of an optically trapped nanoparticle change with environmental conditions.
- Understand how the behaviour of these optomechanical systems can be tailored to enable better performance for future research.

CHAPTER 2

Background and Theory

In this chapter we will explore most of the background concepts important to levitated optomechanics, establishing a theoretical understanding that will support the new research in this project when it is covered in a later chapter. The theory discussion will include relevant topics from optics, elecromagnetism, thermodynamics, signal processing and a description of the optical trapping mechanism will be given.

§2.1. Definitions

Table 2.1 is given as a reference for the most important mathematical variables used in the following chapter. It is not exhaustive and is provided for convenience.

I	Intensity	c	Speed of light	ε_0	Permeability of free space
$\mathbf{E}$	Electric field	U	Potential	$\mathcal{P}$	Polarisation
χ	Susceptibility	K	Trap stiffness	$\mathbf{F}$	Force
$\mathbf{x}$	Position	q	Charge	$\mathbf{B}$	Magnetic field
$\mathbf{p}$	Dipole separation	α	Polarisability	Ω	Angular trap frequency
m	Particle mass	Γ	Damping rate	$\mathcal{F}_{\text{fluct}}$	Stochastic force
w_0	Beam waist at focus	λ	Trapping light wavelength	ρ	Density
ε_r	Relative permeability	P	Optical power	z_R	Rayleigh range of focus
NA	Numerical aperture	p	Pressure	Φ	Phase modulation depth
RIN	Relative intensity noise	κ	Phase evolution rate	z_R	Rayleigh range
Θ	Convergence angle	n	Refractive index	ψ	Gouy phase

Table 2.1: Variable definitions - Bold symbols represent vectors

§2.2. Gaussian Beams

The research caried out in this thesis, and (usually) in levitated optomechanics in general, uses lasers with Gaussian beam profiles. These are the most common, and often most readily created type of laser beam, and the Gaussian beam treatment is a paraxial solution to Maxwell's equations; it is useful, but not a complete electromagnetic description. The fundamental Gaussian mode is known as the TEM_{00} (transverse electro-magnetic) mode, where the "00" subscript denotes the number of radial and angular intensity nodes respectively, through the beam cross section. We use TEM_{00} beams in levitated optomechanics as they can be focussed to a smaller focal spot than higher mode-order beam profiles, leading to a higher optical trap stiffness; where trap stiffness is used as another term for the trap spring constant.

§2.2.1. Beam geometry

Gaussian beams are defined with respect to their focus waist, the point along the beam with minimum radius. A Gaussian beam has exactly one waist, with focal elements mapping one Gaussian beam into another. Positions along a beam are defined with cylindrical coordinates: a z coordinate along the optical axis, relative to the waist position and a radius, r, which is the perpendicular distance from the optical axis.

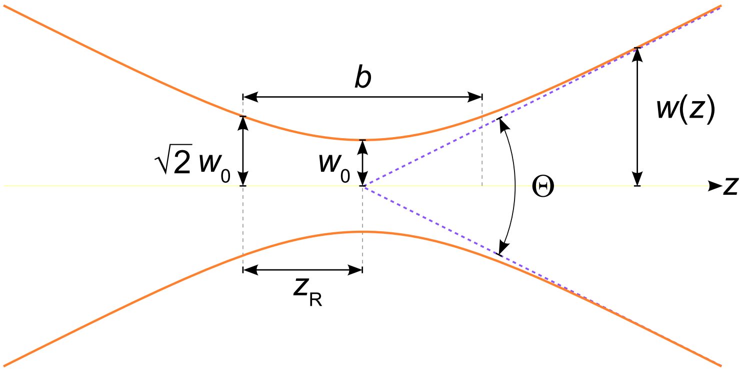

Fig. 2.1. *Gaussian beam waist geometry [10]*

Figure 2.1 shows the focal region of a Gaussian beam. w_0 is the focal waist radius, defined as the radial distance where the intensity falls off to e^{-2} of the maximum intensity at a certain z position. The waist radius varies as a function of z and is denoted by $w(z)$ rather than w_0 when $z \neq 0$. At distances greater than z_R, $w(z)$ can be well approximated varying linearly with z. z_R is the Rayleigh range, and is the distance at which the waist has grown to $\sqrt{2} \times w_0$. The more weakly convergent a Gaussian beam (smaller Θ) is when approaching the focus, the larger z_R and w_0 will be.

The Rayleigh range can be expressed in terms of the focal waist radius and the wavelength of the light, λ as

$$z_R = \frac{\pi w_0^2}{\lambda}. \tag{2.1}$$

The same is true for the divergence angle Θ, where

$$\Theta \simeq \frac{2\lambda}{\pi n w_0}. \tag{2.2}$$

Here n is the refractive index of the medium. Equation 2.2 is only valid at distances much larger than z_R from the focus. The waist diameter as a function of distance from the focus can be given as a function of the focal waist and wavelength by

$$w(z) = w_0 \sqrt{1 + \left(\frac{z}{z_R}\right)^2} = w_0 \sqrt{1 + \left(\frac{z\lambda}{\pi w_0^2}\right)^2}. \tag{2.3}$$

Wavefronts in a Gaussian beam are only flat at the focus and at $z = \pm\infty$. Everywhere else the wavefront radius of curvature, $R(z)$, is calculated as

$$R(z) = z\left[1 + \left(\frac{z_R}{z}\right)^2\right] = z\left[1 + \left(\frac{\pi w_0^2}{z\lambda}\right)^2\right]. \tag{2.4}$$

§2.2.2. Field distributions

The definitions in §2.2.1 can be used to understand the full electric field description of a Gaussian beam, described by equation 2.13 in a cylindrical coordinate system. To reach this, we start by considering a laser beam with the following electric field profile at the waist, following the derivation featured in [11],

$$\mathbf{E}\left(\mathbf{x},\mathbf{y},0\right)=\mathbf{E}_0\exp\left[-\frac{\mathbf{x}^2+\mathbf{y}^2}{w_0^2}\right]. \tag{2.5}$$

This has the spatial Fourier spectrum

$$\hat{\mathbf{E}}\left(\mathbf{k_x},\mathbf{k_y};0\right)=\frac{1}{4\pi^2}\int_{-\infty}^{\infty}\mathbf{E}_0\exp\left[-\frac{-\mathbf{x}^2+\mathbf{y}^2}{w_0^2}\right]\exp\left[-i\left(\mathbf{k_x x}+\mathbf{k_y y}\right)\right]\mathrm{d}\mathbf{x}\mathrm{d}\mathbf{y}, \tag{2.6}$$

$$\hat{\mathbf{E}}\left(\mathbf{k_x},\mathbf{k_y};0\right)=\mathbf{E}_0\frac{w_0^2}{4\pi}\exp\left[-\left({\mathbf{k_x}}^2+{\mathbf{k_y}}^2\right)\frac{w_0^2}{4}\right]. \tag{2.7}$$

The angular spectrum representation (ASR) has the form,

$$\mathbf{E}(\mathbf{x},\mathbf{y},\mathbf{z})=\mathbf{E}_0\frac{w_0^2}{4\pi}e^{i\mathbf{k_z}}\iint_{-\infty}^{\infty}\exp\left[-\left({\mathbf{k_x}}^2+{\mathbf{k_y}}^2\right)\left(\frac{w_0^2}{4}+\frac{i\mathbf{z}}{2\mathbf{k}}\right)\right]\exp\left[\mathrm{i}\left(\mathbf{k_x x}+\mathbf{k_y y}\right)\right]\mathrm{d}\mathbf{k_x}\mathrm{d}\mathbf{k_y}, \tag{2.8}$$

into which we can insert our spatial Fourier sprectrum from equation 2.7. We make the paraxial approximation to simplify the mathematics here, and to allow us to use the results from Gaussian beams mentioned above. This approximation is used to reach expressions that provide insight into the shape of the field distribution, but the high NA focussing used in levitated optomechanics means numerical results calculated using this approximation should be treated with caution. The paraxial approximation is made using the simplification,

$$\mathbf{k_z}=\mathbf{k}\sqrt{1-\left({\mathbf{k_x}}^2+{\mathbf{k_y}}^2\right)/\mathbf{k}^2}\approx\mathbf{k}-\frac{\left({\mathbf{k_x}}^2+{\mathbf{k_y}}^2\right)}{2\mathbf{k}}, \tag{2.9}$$

which can be expressed in cylindrical polar coordinates as,

$$\sin\left(\theta\right)\approx\theta,\quad\tan\left(\theta\right)\approx\theta,\quad\cos\left(\theta\right)\approx1-\frac{\theta^2}{2}. \tag{2.10}$$

Applying the approximation in equation 2.9 to equation 2.8 and inserting the Fourier spectrum gives

$$\mathbf{E}(\mathbf{x},\mathbf{y},\mathbf{z})=\mathbf{E}_0\frac{w_0^2}{4\pi}e^{i\mathbf{k_z}}\iint_{-\infty}^{\infty}\exp\left[-\left({\mathbf{k_x}}^2+{\mathbf{k_y}}^2\right)\right]\frac{w_0^2}{(4}+\frac{i\mathbf{z}}{2\mathbf{k}})\exp\left[\mathrm{i}\left(\mathbf{k_x x}+\mathbf{k_y y}\right)\right]\mathrm{d}\mathbf{k_x}\mathrm{d}\mathbf{k_y} \tag{2.11}$$

which integrates to

$$\mathbf{E}(\mathbf{x},\mathbf{y},\mathbf{z})=\frac{\mathbf{E}_0e^{\mathrm{i}\mathbf{k_z}}}{1+2\mathrm{i}\mathbf{z}/\mathbf{k}w_0^2}\exp\left[-\frac{\left(\mathbf{x}^2+\mathbf{y}^2\right)}{w_0^2}\frac{1}{\left(1+2\mathrm{i}\mathbf{z}/\mathbf{k}w_0^2\right)}\right]. \tag{2.12}$$

Converting to cylindrical polar coordinates ($\mathbf{r}^2=\mathbf{x}^2+\mathbf{y}^2$), but leaving the electric field polarised in the $\hat{x}$ direction, gives the expression for the electric field of a Gaussian beam,

$$\mathbf{E}\left(\mathbf{r},\mathbf{z}\right)=E_0\hat{x}\frac{w_0}{w\left(\mathbf{z}\right)}\exp\left[\frac{-\mathbf{r}^2}{w\left(\mathbf{z}\right)^2}\right]\exp\left[-i\left(k\mathbf{z}+k\frac{\mathbf{r}^2}{2R\left(\mathbf{z}\right)}-\psi\left(\mathbf{z}\right)\right)\right], \tag{2.13}$$

where we have defined

$$\begin{aligned} z_{\mathrm{R}} &= {}^{k w_0^2}/_2, \\ w(z) &= w_0 \sqrt{1 + {}^{z^2}/_{z_{\mathrm{R}}^2}}, \\ R(z) &= z\left(1 + {}^{z_{\mathrm{R}}^2}/_{z^2}\right), \\ \psi(z) &= \arctan\left({}^{z}/_{z_{\mathrm{R}}}\right). \end{aligned} \tag{2.14}$$

Equation 2.13 is valid for cases when the convergence angle of the light is small, due to the series of small angle approximations made in equation 2.10. In the derivation above, **r** and **z** are treated as position vectors and the incoming electric field is assumed to be polarised in the $\hat{x}$ direction, giving rise to the $\hat{x}$ unit vector.

It's worth noting that the ASR in equation 2.8 can be written more intuitively as the Debye equation,

$$\mathbf{E}\left(\mathbf{r}, \varphi, \mathbf{z}\right) = \frac{i\mathbf{k}_f e^{-i\mathbf{k}_\mathrm{f}}}{2\pi} \int_0^{\theta_{\max}} \int_0^{2\pi} \mathbf{E}_\infty\left(\theta_r, \phi_r\right) \exp\left[i\mathbf{k}z\cos(\theta_r)\right] \exp\left[\mathbf{k}r\sin(\theta_r)\cos(\phi_r - \varphi)\right] \sin(\theta_r) d\phi_r \theta_r. \tag{2.15}$$

in the case of a beam focussed from a reference sphere with geometry as below [11].

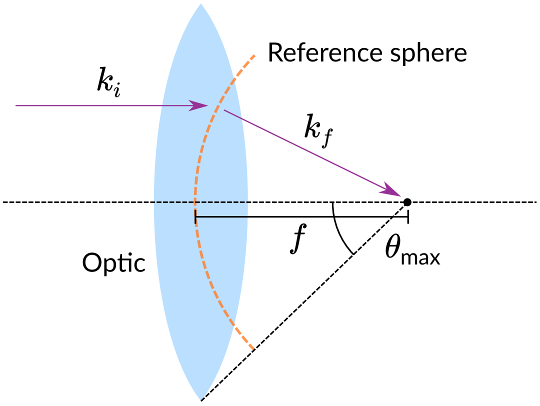

Fig. 2.2. *Angular spectrum representation cylindrical geometry. k_i and k_f are the initial and final wave vectors respectively.*

An interesting subtlety of a Gaussian beam focus is the Gouy phase, $\psi(z)$, defined in equation 2.16 [146]. This is a decrease of the rate at which a beam accrues phase as it propagates through the focus; it can be thought of as a region of increased effective wavelength around the focus.

$$\psi(z) = \arctan\left(\frac{z}{z_R}\right) \tag{2.16}$$

Over the course of travel across the entire focal region the beam will lose π radians of phase relative to a plane wave propagating the same distance. This effect becomes more important in highly divergent, and therefore tightly focussed, beams as the length over which this effect takes place is decreased, making it more apparent.

We can use the relation $I = c\epsilon_0 \langle \mathbf{E} \cdot \mathbf{E} \rangle$ to obtain the Intensity distribution as a function of **r** and **z**.

$$I\left(\mathbf{r}, \mathbf{z}\right) = I_0 \left[\frac{w_0}{w\left(\mathbf{z}\right)}\right]^2 \exp\left[\frac{-2\mathbf{r}^2}{w\left(\mathbf{z}\right)^2}\right] \tag{2.17}$$

Here I_0 is the peak intensity, found at $z = r = 0$.

Equation 2.17 can be used to compute a 2D intensity cross-section of a Gaussian beam with known waist size and wavelength.

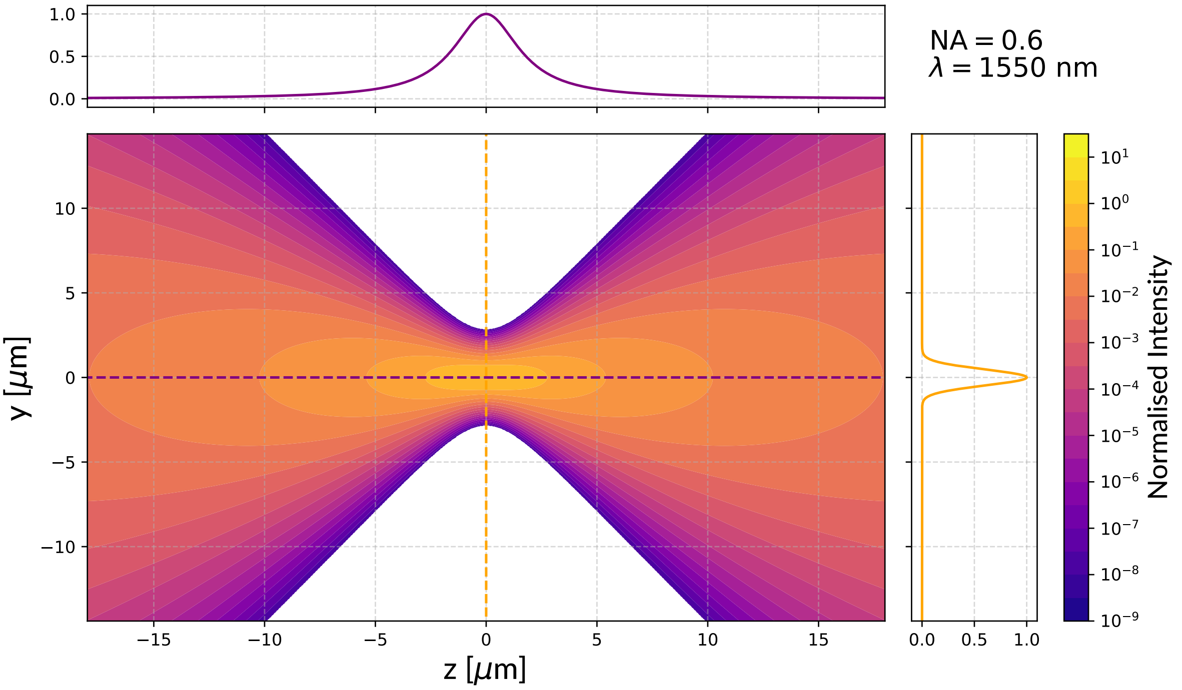

Fig. 2.3. *Intensity distribution of a Gaussian beam. 1550 nm light is focussed with an NA of 0.6. The 1D plots show intensity cross-sections through the focus along the optical axis and perpendicular to it. The Gaussian beam equations are used to calculate the intensity field distribution, but it should be noted that* NA $= 0.6$ *is highly non-paraxial and has been used to accentuate the focus shape for clarity.*

§2.2.3. Limitations of Gaussian beams

Gaussian beams are not strictly full solutions to Maxwell's equations, meaning the equations in 2.2.1 do not provide the full description of the electric and magnetic fields at every point in space. The description makes use of the paraxial approximation in order to simplify calculation and assumes that the beam is only gently diverging or converging with $\Theta \lesssim 50°$. This corresponds to an NA of about 0.4, the point at which the paraxial approximation deviates past a 10% cutoff. Consequently, when computing scenarios such as that above, which break the paraxial approximation, the calculated intensities will be inaccurate compared to the physical system. This error grows rapidly with increasing NA, and for NAs $\gtrsim 0.6$, Gaussian beam calculations yield results that do not reflect the behaviour of a real beam. The 3 small angle approximations made are given in equation 2.18, and result in the changing relative error shown in figure 2.4.

$$\sin(\theta) \approx \theta, \quad \tan(\theta) \approx \theta, \quad \cos(\theta) \approx 1 - \frac{\theta^2}{2} \tag{2.18}$$

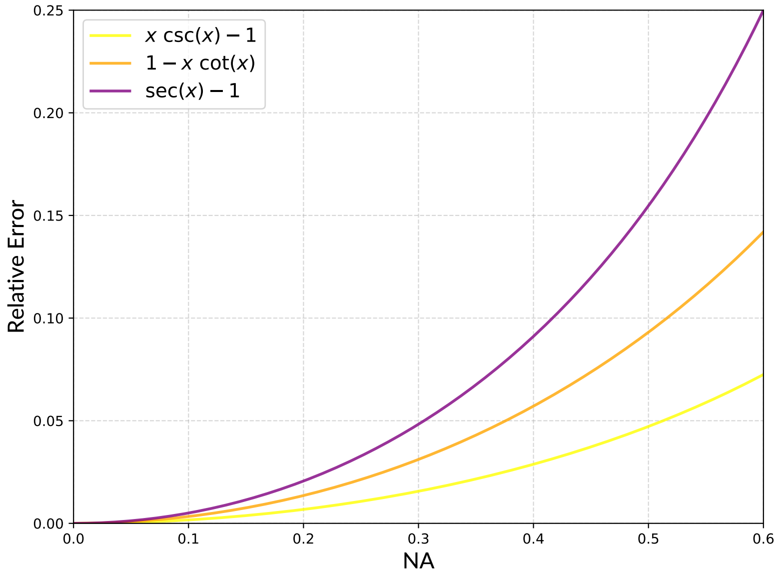

Fig. 2.4. *The relative error in the small angle approximations assosciated with the paraxial approximation.*

Because of these aproximations, and the fact that optical trapping neccesarily requires a high NA focus, Gaussian beams will not yield accurate numerical results, however this is still a useful simplified model that can aid with illustration and intuition. The alternatives to Gaussian beams are ray optics and a full electromagnetic simulation.

Ray optics is valid for high NA but is only useful for simulating the large scale behaviour of light, as it neglects wave-like behaviours such as diffraction. In ray optics, if an ideal lens focuses a collimated beam, the outgoing rays will converge to a point, completely neglecting the focal waist phenomena. In general, ray optics is too simplistic for the micron scale accuracy required when investigating behaviours of highly convergent light in a narrow focus.

Conversely, solving Maxwell's equations throughout the volume would provide an exact description of the behaviour of light in a relistic classical optics scenario, as it involves a full vector field treatment of the electromagnetic field in the region. Unfortunately this is enormously computationally intensive, as Maxwell's equations must be solved for each voxel in the volume of interest. These voxels have a maximum size of about $\lambda/10$ in order to maintain accuracy and therefore the number of voxels in the region of interest can be upwards of 10^{14} for a 1 cm^3 region. This can be reduced by varying the voxel size for regions of different electric field gradient, but a beam propagating through free space has a periodic electric field gradient that has a high magnitude across the entire region, meaning the benefits of variable voxel sizes are small. This kind of simulation requires very large amounts of computer memory, making finite-difference time-domain simulation impractical. Investigations into the behaviour of the electric field and Gouy phase around a high NA focus can be found in [16, 147], and will be used in §6.3.2 to make a correction to the Gouy phase.

Another approach is the surface-integral-equation / boundary-element method, in which we calculate the electric currents in the focussing objective using the Huygens-Fresnel (H-F) integral to calculate the field around the focus. This method does not require the field throughout the volume to be solved, but H-F is a scalar field theory that neglects polarisation and the vector field nature of light. For paraxial cases H-F can be sufficient, but in our high NA geometry, polarisation has a significant effect on the focus shape, meaning a vector field treatment is required. The Stratton-Chu (S-C) equations [148–150] are the vector field equivalent of H-F, where an arbitrary incident beam can be built by summation of a series of rectangular intensity distributions [151], and it may be possible to use an analytical approach to solve S-C for our case, but it was not undertaken as part of this project.

§2.2.4. The effects of truncation on the focal spot

This is the masking of a beam caused by the finite radius of the optical elements involved. For example a collimated Gaussian beam has an intensity distribution with wings that are theoretically non-zero out to $r = \infty$. When this beam is focussed by a lens, only the portion of the beam with radius less than or equal to the radius of the lens is captured. The total power of the beam is therefore decreased, and the focal waist is affected. It is common practice to expand collimated beams before passing them through an aperture or optic, as the filling factor of the incident beam can affect the characteristics of the outgoing beam.

The power transmitted through an aperture of radius r is given by equation 2.19 [146].

$$P(r,z) = P_0 \left[1 - \exp\left(-2r^2/w^2(z)\right)\right] \tag{2.19}$$

where P_0 is the total power of the beam. This means that 86% of the power is contained within the waist radius $w(z)$. If a beam has a waist radius equal to the radius of an optic, then it is said to have a filling factor, f_0 of 1, defined by equation 2.20.

$$f_0 = \frac{w(z)}{r_{\text{optic}}} \tag{2.20}$$

If our goal is to achieve maximum intensity at the focus, in order to maximise optical trap depth, then it logically follows that we ought to significantly underfill our focussing objective, in order to maximise the power collected by the lens. Unfortunately the situation is not as simple as this, as the filling factor affects the focal waist size, with a more overfilled lens giving narrower focal waist, up until the point that diffraction from truncation becomes the dominant effect. When calculating an optimal filling factor, these benefits of underfilling and overfilling must be balanced, as was done by Mahamdeh *et al.* [152], where they find the optimal filling factor for maximising optical trap stiffness (a figure of merit for an optical trap, see §2.4.6) to be around 0.95. The exact optimal filling factor depends subtely on the figure of merit used. In situations where excess optical power is available (such as this project), the sensible filling factor is shifted more towards underfilling as we can increase the total optical power to compensate for the truncation.

Figure 2.5 shows the effect of changing filling factor on a laser's focal intensity distribution. Overfilling the objective can be seen to produce a tighter focus, but decreases the total power. Polarisation induced asymmetry of the beam in the x and y directions can be seen in the smaller waist size cases (solid and dashed lines respectively).

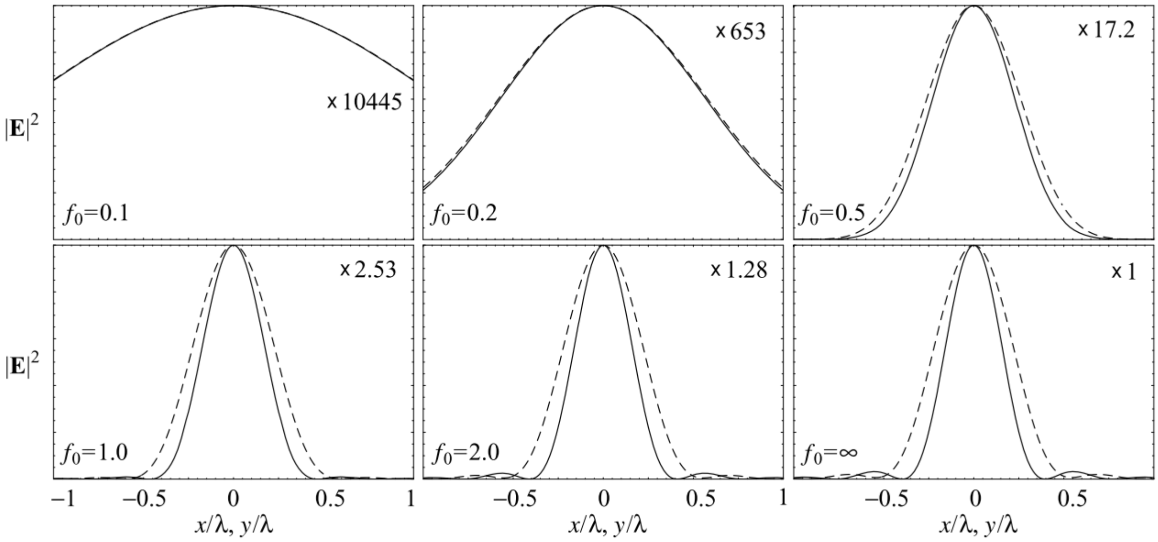

Fig. 2.5. *The influence of changing filling factor f_0 [11]. Filling factors are given, along with the normalisation multiplier in each case.*

§2.3. Ray Optics

In the kinds of geometries present in levitated optomechanics ray optics is not a good approximation of how light behaves; it is however useful for building an intuitive picture of a situation and so it is included here. We will discuss more appropriate, developed treatments later.

Now that §2.2 has laid out some of the framework for how light behaves in beams and when focussed, let us examine how light interacts with matter. In particular, we will look at the scattering that occurs in levitated optomechanics and how the light-matter interaction leads to the ability to trap nanoparticles in order to accomplish the goals of this thesis.

There are two main types of scattering that are important to understand in levitated optomechanics, and they occur at different size scales. The size parameter ($k_m a$) is a way of expressing the relative size scales of the object to be trapped and the wavelength of the trapping light.

$$k_m a = \frac{2\pi n_m}{\lambda_0} a \tag{2.21}$$

Here, k_m is the wavenumber of the trapping light in the medium, n_m is the refractive index of the medium, λ_0 is the wavelength of the trapping light in a vacuum and a is the size parameter of the object to be trapped [12]. For a nanosphere, a is simply the particle radius. If the size parameter is much larger than 1 ($k_m a \gg 1$) then the correct treatment of the scattering mechanism is to use a ray optics approach, conversely if $k_m a \ll 1$, then the mechanism is Rayleigh scattering. In this section, both will be explored in turn mainly following reference [12].

Mie thoery [11, 12] is the scattering theory of an electromagnetic plane wave scattering from a sphere, and Rayleigh scattering is a subset of this. Rayleigh scattering models the scatterer as a point dipole, with the whole volume of the particle subject to the same electric field at any one time. This is a valid simplification only when the wavelength of incident radiation (trapping light) is much larger than the particle, ie the electric field does not vary significantly across the particle. The ray optics picture, valid for large particles, will be investigated first.

§2.3.1. Fresnel coefficients

In this size regime rays can be treated individually, the force exerted on the particle by each ray calculated and then summed to find the net force on the particle. We will use this approach to determine the force on a glass microparticle. When a ray of trapping light is incident on the microparticle surface, it is partially reflected and partially refracts into the glass according to Snell's law (equation 2.22).

$$\frac{n_1}{n_2} = \frac{\sin(\theta_t)}{\sin(\theta_i)} \tag{2.22}$$

Where θ_i and θ_t are the angles of incidence and transmission respectively, with respect to the surface normal. The intensity reflection and transmission coefficients of an interface between two media of refractive indicies n_1 and n_2 are given by the Fresnel equations and are shown in equations 2.23 - 2.24.

$$R_s = \left|\frac{n_i \cos\theta_i - n_t \cos\theta_t}{n_i \cos\theta_i + n_t \cos\theta_t}\right|^2 \qquad R_p = \left|\frac{n_i \cos\theta_t - n_t \cos\theta_i}{n_i \cos\theta_t + n_t \cos\theta_i}\right|^2 \tag{2.23}$$

$$T_s = \frac{4 n_i n_t \cos\theta_i \cos\theta_t}{|n_i \cos\theta_i + n_t \cos\theta_t|^2} \qquad T_p = \frac{4 n_i n_t \cos\theta_i \cos\theta_t}{|n_i \cos\theta_t + n_t \cos\theta_i|^2} \tag{2.24}$$

In the above, $R_{s,p}$ and $T_{s,p}$ are the reflection and transmission coefficients for s and p polarised light respectively. S and p polarised light are the polarisation components of the ray with polarisations normal to, and parallel to, the surface of the glass, at the location where the ray crosses the interface. Due to the conservation of energy, at each interaction of the light ray with the interface, the total power must be conserved and so $P_i = P_r + P_t$. Here $P_{i,r,t}$ are the incident, reflected and transmitted powers respectively. The power balance between the reflected and transmitted part of the ray are shown in figure 2.6, calculated using equations 2.23 - 2.24.

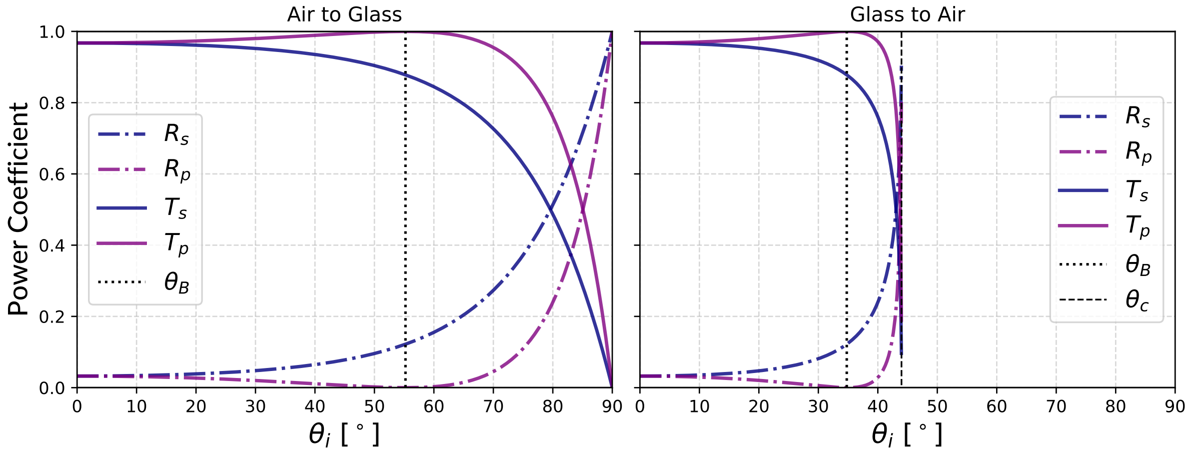

Fig. 2.6. *The behaviour of the Fresnel power reflection and transmission coefficients with changing angle of incidence from a glass-air boundary. The glass has refractive index* $n = 1.44$ *and the air has* $n = 1$*. Brewster's angle and the critical angle are labelled* θ_B *and* θ_c *respectively.*

Figure 2.6 shows the Brewster's angle θ_B, at which the p-polarised light is completely transmitted, as well as the critical angle θ_c above which light is totally internally reflected. These angles are calculated using equations 2.25 and 2.26, but are not of major importance in the context of this thesis.

$$\theta_B = \arctan\left(\frac{n_t}{n_i}\right) \tag{2.25}$$

$$\theta_c = \arcsin\left(\frac{n_t}{n_i}\right) \tag{2.26}$$

§2.3.2. Forces from ray optics

We have seen that the total energy of the light is conserved each time a ray meets an interface and reflects or refracts, the same is not true of the light's momentum. When considering the conservation of momentum we must consider also the momentum of the object it reflects from; in our case the glass sphere. Upon reflection/refraction the light ray imparts momentum to the glass sphere, which is equivalent to saying it produces a force on the particle. In order to calculate the force, we first need to know the momentum change. A light ray containing optical power P carries $N = {}^{P}/_{u}$ photons, where u is the photon energy given by equation 2.27.

$$u = \frac{hc}{\lambda_0}, \tag{2.27}$$

and h and λ_0 are the Planck constant and vacuum wavelength of the photon. Using the Minkowski definition of the momentum of a photon [153] (equation 2.28, with $\hat{r_\gamma}$ as the photon direction), we can then find the total momentum of the ray (equation 2.29). It's worth noting that the Abraham-Minkowski controversy surrounding the definition of photon momentum has essentially been resolved [154, 155]. The photon momentum is

$$\mathbf{p}_\gamma = n\frac{h}{\lambda_0}\hat{r_\gamma}, \tag{2.28}$$

meaning the momentum of a ray scattering from the sphere is

$$\mathbf{p}_{\text{ray}} = n_i N\frac{h}{\lambda_0}\hat{r_i} = n_i\frac{P_i}{u}\frac{h}{\lambda_0}\hat{r_i} = n_i\frac{P_i\lambda_0}{hc}\frac{h}{\lambda_0}\hat{r_i} = \frac{n_i P_i}{c}\hat{r_i}. \tag{2.29}$$

The change in this quantity over the course of the scattering event is equal to the force on the glass sphere, according to Newton's second law, and so we can say that the force produced by a single reflection/refraction is given by equation 2.30.

$$\mathbf{F} = \frac{n_i P_i}{c}\mathbf{r_i} - \left[\frac{n_i P_r}{c}\mathbf{r_r} + \frac{n_t P_t}{c}\mathbf{r_t}\right] \tag{2.30}$$

After the ray has entered the glass sphere, it continues to undergo a series of internal reflections and refractions through the volume, as in figure 2.7.

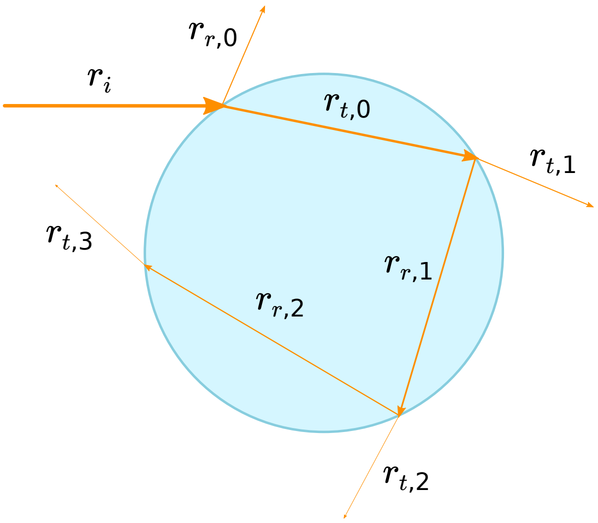

Fig. 2.7. *The path of a light ray entering a glass microsphere. The ray will go through multiple subsequent internal reflections before the majority of the original optical power leaves the sphere.*

If we ignore the absorption of light in the glass by stating that the transmitted and refracted fraction of the optical power at each interaction sum to 1, eventually all of the optical power associated with the original incident light ray refracts out of the glass sphere and leaves the system, we can calculate the net force on the particle produced by this ray using equation 2.31.

$$\mathbf{F}_{\text{ray}} = \frac{n_i P_i}{c}\mathbf{r_i} - \frac{n_i P_r}{c}\mathbf{r_r} - \sum_{m=1}^{+\infty} \frac{n_t P_{t,m}}{c}\mathbf{r_{t,m}} \tag{2.31}$$

When multiple rays are incident on the sphere, each of these rays produces a net force on the particle, equal to the sum of the force produced each time it scatters from the glass-air interface. The net forces produced by the rays can be summed in order to find the total force on the particle (equation 2.32).

$$\mathbf{F}_{\text{tot}} = \sum_j \mathbf{F}^{(\mathbf{j})}_{\text{ray}} = \sum_j \left[\frac{n_i P_i^{(j)}}{c}\mathbf{r}_{\mathbf{i}}^{(\mathbf{j})} - \frac{n_i P_r^{(j)}}{c}\mathbf{r}_{\mathbf{r}}^{(\mathbf{j})} - \sum_{m=1}^{+\infty} \frac{n_t P_{t,m}^{(j)}}{c}\mathbf{r}_{\mathbf{t,m}}^{(\mathbf{j})} \right] \tag{2.32}$$

The force on the particle from a ray can be treated as the combination of an optical scattering force and an optical gradient force, as discussed in §1.2.2. The scattering force always acts in the direction of the incident ray, and the gradient force acts perpendicular to it.

$$\mathbf{F}_{\text{ray}} = \mathbf{F_s} + \mathbf{F_g} = F_s \hat{r_i} + F_g \hat{r_\perp} \tag{2.33}$$

When many rays are made incident on the glass sphere with directions $\mathbf{r}_{\mathbf{i}}^{(\mathbf{j})}$ being strongly converging towards a focus, the total gradient force $\mathbf{F_g}$ generated by these rays is that of a restoring force, with direction towards the focus and magnitude proportional to the particle displacement from equilibirum. This proportionality can be expressed as a spring constant K. Equation 2.34 expresses the optical gradient force as a restoring force according to Hooke's law, with $l = x, y, z$.

$$\mathbf{F_{g,l}} \approx -K_l \left(\mathbf{l} - \mathbf{l_{eq}}\right) \tag{2.34}$$

§2.4. Rayleigh Scattering

As mentioned at the start of §2.3, Rayleigh scattering is a subset of Mie theory in which the particle is small compared to the trapping light wavelength. This allows us to treat the particle as a point dipole in the presence of a spatially uniform but time varying electric field. The Rayleigh approximation is incredibly useful as it reduces the summation of an theoretically infinite series of terms in equation 2.32 to a simple expression for the scattered intensity, given below.

$$I(R,\theta) = I_0 \frac{\chi^2}{\lambda^4 R^2} \cos(\theta)^2 = I_0 \left(3V\frac{\varepsilon_r - 1}{\varepsilon_r + 2}\right)^2 \frac{1}{\lambda^4 R^2} \cos(\theta)^2 \tag{2.35}$$

R is the distance between the particle and intensity detector, θ is the scattering angle and d is the diameter of the particle. χ is the material susceptibility and is obtained from the Clausius-Mosotti relation that will be covered in §2.4.1. When equation 2.35 is integrated over all angles, the Rayleigh scattering cross-section can be obtained.

$$\sigma_s = \frac{\chi^2 \pi}{\lambda^4} \tag{2.36}$$

In order to understand the origin of equation 2.35 and the behaviour of light when it Rayleigh scatters from a nanoparticle, let us examine the idea of a dipole and how it behaves in an electric field.

§2.4.1. Dipoles

An electric dipole consists of a pair of charges, with charges + and - q. In order to act as a dipole, these charges must be separated by some distance l, creating a dipole moment

$$\mathbf{p_d} = q l \hat{u}, \tag{2.37}$$

where $\hat{u}$ is the unit vector joining the two charges in space. When placed in an electric field, an electric dipole experiences a torque $\mathbf{T_d} = \mathbf{p_d} \times \mathbf{E}$, aligning it with the field. This torque causes the dipole to precess around the electric field direction and through dissipation, settle into the alignment of lowest potential, according to equation 2.38,

$$U_d = -\mathbf{p_d} \cdot \mathbf{E} = -p_d |\mathbf{E}| \cos\theta, \tag{2.38}$$

where θ is the angle between the dipole alignment $\hat{u}$ and the electric field $\mathbf{E}$.

Atoms, molecules and nanoparticles are all made of spatially bound, positively charged nuclei each surrounded by negatively charged electron cloud. This electron cloud feels a Coulomb attraction towards the nucleus and so in the absence of an external electric field, the centre of mass of the negative charge distribution will move to the point of lowest potential energy, centred on the nuclei centre of mass. In this configuration there is no charge separation between the nucleus and electron cloud, however when an electric field is applied, the two charge distributions feel forces in opposite directions and they separate, forming a dipole. This is atomic polarisation. Atomic polarisation can occur in any number of atoms in a molecule or nanoparticle and the collective charge separation causes the object to be polarised. This form of polarisation is known as induced polarisation or an induced dipole and can itself cause further polarisation of the atoms around it, due to the electric field created by the existence of the dipole. Atomic polarisation is quantified by equation 2.39:

$$\mathbf{p_a} = \alpha \mathbf{E} \tag{2.39}$$

where α is the polarisability of the atom. If each atom in a material has atomic polarisation $\mathbf{p}$, then the material (or nanoparticle) has polarisation $\mathcal{P}$,

$$\mathcal{P} = \varepsilon_0 \chi \mathbf{E}. \tag{2.40}$$

We define the susceptibility, χ, of a material in equation 2.41, as a bulk analogy to the atomic polarisability α.

$$\chi = \frac{\alpha}{\varepsilon_0} \tag{2.41}$$

In reality when discussing the electric field inside a medium, in our case a nanoparticle, we use the displacement field, $\mathbf{D}$, rather than $\mathbf{E}$. The displacement is a function of the relative dielectric permittivity of the particle ε_r and is defined in equation 2.42,

$$\mathbf{D} = \varepsilon_0 \varepsilon_r \mathbf{E}. \tag{2.42}$$

ε_r can be found from the polarisability of the particle using the Clausius-Mossotti relation, which we will briefly derive [12]. We first assume an isotropic, homogeneous, non-magnetic spherical particle, small compared to any spatial variations of the electric field. We place the particle at the origin of a spherical coordinate system and apply an electric field such that

$$\mathbf{E_p} = E_p \hat{s} = E_p \cos(\theta) \hat{r} - E_p \sin(\theta) \hat{\theta}, \tag{2.43}$$

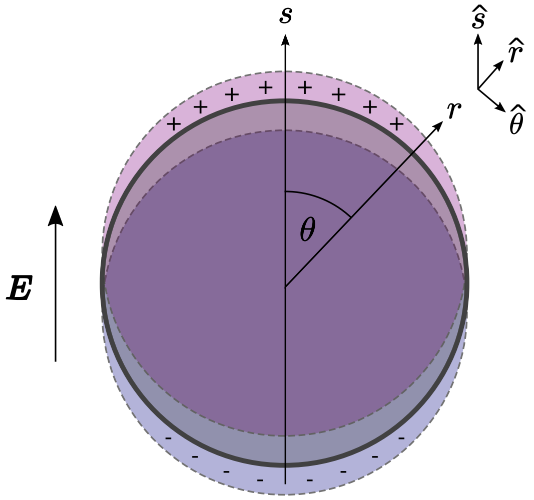

Fig. 2.8. *Radial and tangential components of the electric field at the boundary of a medium. Adapted from [12].*

where E_p is the electric field inside the particle and $\hat{s}$ is the unit vector along the s-axis. This polarisation can also be thought of as a bulk charge separation, and therefore the whole particle acts as a dipole with dipole moment $\mathbf{p_{sp}}$ aligned along the $\hat{s}$ axis.

The electric displacement field can now be used to find the radial (equation 2.44) and tangential (equation 2.45) electric field by applying the boundary condition, that there is no charge current across the boundary in media ([12] p49), that must exist at the interface $r = a$, where a is the particle radius. Here, the subscripts “ff”, “i” and “d” denote far-field (at a distance much larger than the particle radius), internal and dipole.

$$\mathbf{D}_{\mathbf{pol,r}}(a) = \mathbf{D}_{\mathbf{i,r}}(a) + \mathbf{D}_{\mathbf{d,ff,r}}(a) \Rightarrow \varepsilon_r \mathbf{E}_{\mathbf{p,r}}(a) = \mathbf{E}_{\mathbf{i,r}}(a) + \mathbf{E}_{\mathbf{d,ff,r}}(a) \tag{2.44}$$

$$\mathbf{E}_{\mathbf{pol},\theta}(a) = \mathbf{E}_{\mathrm{i},\theta}(a) + \mathbf{E}_{\mathrm{d,ff},\theta}(a) \tag{2.45}$$

Setting $E = |\mathbf{E}|$, we find that

$$\varepsilon_r E_p \cos(\theta) = E\cos(\theta) + \frac{2p_{\mathrm{sp}}\cos(\theta)}{4\pi\varepsilon_0 a^3} \tag{2.46}$$

and

$$-E_p \sin(\theta) = -E\sin(\theta) + \frac{p_{\mathrm{sp}}\sin(\theta)}{4\pi\varepsilon_0 a^3}. \tag{2.47}$$

Using the magnitude of the dipole moment $p_{\mathrm{sp}} = |\mathbf{p}_{\mathrm{sp}}|$, we find that the magnitude of the field inside the sphere is $E_p = \frac{3}{\varepsilon_r+2}E$. Substituting this into equations 2.46 and 2.47, we find the dipole moment:

$$p_{\mathrm{sp}} = 4\pi\varepsilon_0 a^3 \frac{\varepsilon_r - 1}{\varepsilon_r + 2} E, \tag{2.48}$$

and from this, using $\chi = \varepsilon_0 {}^{p_{sp}}/_{E}$, we find the susceptibility as expressed by the Clausius-Mossotti relation:

$$\chi_{\mathrm{CM}} = 3V\frac{\varepsilon_r - 1}{\varepsilon_r + 2}. \tag{2.49}$$

§2.4.2. Optical forces from Rayleigh scattering

Returning to the idea of the simple point dipole in an electric field, this time allowing the field to change in time, the optical forces acting on a dipole will be found, following the derivation found on page 59 in [12].

Neglecting gravity for the time being, the motion of each element of the dipole is governed by the Lorentz force it experiences according to equation 2.50,

$$\mathbf{F}_{\mathrm{L}} = q\mathbf{E} + q\mathbf{v} \times \mathbf{B}, \tag{2.50}$$

where q and $\mathbf{v}$ are the charge and velocity of the dipole element respectively, and $\mathbf{B}$ is the magnetic field. Each element of the dipole also experiences a force due to the mutual Coulomb attraction between them that creates the internal electrostatic potential U_{int}. This force is inversely proportional to the gradient of the potential and is given by equation 2.51,

$$\mathbf{F}_{\mathrm{int}} = -\nabla U_{\mathrm{int}}. \tag{2.51}$$

From these forces we can write the equations of motion of the individual dipole elements with charges $\pm q$ as a function of time t, where we define their position vectors to be $\mathbf{r}_{\pm}$ and their separation to be $\Delta\mathbf{r} =$

$\mathbf{r}_+ - \mathbf{r}_-$.

$$m\frac{d^2\mathbf{r}_\pm}{dt^2} = \begin{cases} +q\left[\mathbf{E}\left(\mathbf{r}_+, t\right) + \frac{dr_+}{dt} \times \mathbf{B}\left(\mathbf{r}_+, t\right)\right] - \nabla U_{\text{int}}(\Delta\mathbf{r}, t) \\ \\ -q\left[\mathbf{E}\left(\mathbf{r}_-, t\right) + \frac{dr_-}{dt} \times \mathbf{B}\left(\mathbf{r}_-, t\right)\right] + \nabla U_{\text{int}}(\Delta\mathbf{r}, t) \end{cases} \tag{2.52}$$

Performing a Taylor expansion on the electric and magnetic fields in equation 2.52 about the average position of the dipole elements ($\mathbf{r_d} = \frac{\mathbf{r}_+ + \mathbf{r}_-}{2}$) gives the following:

$$\mathbf{E}\left(\mathbf{r}_\pm, t\right) \approx \mathbf{E}\left(\mathbf{r_d}, t\right) + ((\mathbf{r}_\pm - \mathbf{r_d}) \cdot \nabla)\mathbf{E}\left(\mathbf{r_d}, t\right) \tag{2.53}$$

$$\mathbf{B}\left(\mathbf{r}_\pm, t\right) \approx \mathbf{B}\left(\mathbf{r_d}, t\right) + ((\mathbf{r}_\pm - \mathbf{r_d}) \cdot \nabla)\mathbf{B}\left(\mathbf{r_d}, t\right) \tag{2.54}$$

Equations 2.53 and 2.54 can be substituted into equation 2.52, which can then be summed in order to find the total force acting on the dipole:

$$\mathbf{F_d}(\mathbf{r_d}, t) = \left[\mathbf{p_d} \cdot \nabla\right]\mathbf{E}(\mathbf{r_d}, t) + \frac{d\mathbf{p_d}}{dt} \times \mathbf{B}(\mathbf{r_d}, t) + \frac{d\mathbf{r_d}}{dt} \times \left[\mathbf{p_d} \cdot \nabla\right]\mathbf{B}(\mathbf{r_d}, t). \tag{2.55}$$

The magnetic field is a function of position and time, i.e. $\mathbf{B}(\mathbf{r_d}, t)$, but the dipole position is also a function of time, $\mathbf{r_d} = \mathbf{r_d}(t)$, and therefore $\mathbf{B}(t, \mathbf{r_d}(t))$. The full differential of magnetic field with respect to time is therefore

$$\frac{d\mathbf{B}}{dt} = \frac{\partial\mathbf{B}}{\partial t} + \frac{\partial\mathbf{x}}{\partial t} \cdot \nabla\mathbf{B}. \tag{2.56}$$

The particle will always be moving slowly compared to the change in the electric field (non-relativistic), and therefore we neglect the second term in equation 2.56, using the approximation

$$\frac{\partial\mathbf{B}}{\partial t} \approx \frac{d\mathbf{B}}{dt} \tag{2.57}$$

and use Maxwell's equation

$$\nabla \times \mathbf{E}(\mathbf{r}, t) = -\frac{\partial\mathbf{B}(\mathbf{r}, t)}{\partial t} \tag{2.58}$$

to rewrite the second term of equation 2.55,

$$\frac{d\mathbf{p_d}}{dt} \times \mathbf{B} = \frac{d}{dt}\left(\mathbf{p_d} \times \mathbf{B}\right) - \mathbf{p_d} \times \frac{d\mathbf{B}}{dt} = \frac{d}{dt}\left(\mathbf{p_d} \times \mathbf{B}\right) + \mathbf{p_d} \times \left(\nabla \times \mathbf{E}\right). \tag{2.59}$$

We can also neglect the third term in equation 2.55 for the same reason. This leaves us with the time dependent force on the dipole:

$$\mathbf{F_d}(\mathbf{r_d}, t) = \left[\mathbf{p_d} \cdot \nabla\right]\mathbf{E}(\mathbf{r_d}, t) + \mathbf{p_d} \times \left[\nabla \times \mathbf{E}\left(\mathbf{r_d}, t\right)\right] + \frac{d}{dt}\left[\mathbf{p_d} \times \mathbf{B}\left(\mathbf{r_d}, t\right)\right]. \tag{2.60}$$

Taking the time average over many oscillations of the optical frequency reduces the last term of equation 2.60 to zero,

$$\mathbf{F_d} = \langle\mathbf{F_d}\rangle = \langle\left[\mathbf{p_d} \cdot \nabla\right]\mathbf{E}(\mathbf{r_d}, t)\rangle + \langle\mathbf{p_d} \times \left[\nabla \times \mathbf{E}\left(\mathbf{r_d}, t\right)\right]\rangle, \tag{2.61}$$

$$\mathbf{F_d}(\mathbf{r_d}) = \sum_{j=x,y,z} \langle p_{d,j} \nabla E_j(\mathbf{r_d}, t) \rangle \,, \tag{2.62}$$

where $\langle \cdots \rangle$ denotes the time average.

If we treat **E** as a complex phasor, rather than just the physical (real) field, the induced dipole moment can be expressed in terms of $\mathbf{r_d}$:

$$\mathbf{p_d}(\mathbf{r_d}) = \alpha_d \mathbf{E}(\mathbf{r_d}), \tag{2.63}$$

and equation 2.60 can be rewritten as

$$\mathbf{F_d} = \frac{1}{2}\,\mathrm{Re}(\alpha)\,\mathrm{Re}\left[(\mathbf{E}\cdot\nabla)\,\mathbf{E}^* + \mathbf{E}\times(\nabla\times\mathbf{E}^*)\right] - \frac{1}{2}\,\mathrm{Im}(\alpha)\,\mathrm{Im}\left[(\mathbf{E}\cdot\nabla)\,\mathbf{E}^* + \mathbf{E}\times(\nabla\times\mathbf{E}^*)\right] \tag{2.64}$$

where $\mathrm{Re}(\alpha)$ and $\mathrm{Im}(\alpha)$ represent the real and imaginary parts of α_d respectively.

We can use the vector identities in equations 2.65 and 2.66,

$$\nabla\left(\mathbf{E}\cdot\mathbf{E}^*\right) = (\mathbf{E}\cdot\nabla)\,\mathbf{E}^* + \mathbf{E}\times(\nabla\times\mathbf{E}^*) + (\mathbf{E}^*\cdot\nabla)\,\mathbf{E} + \mathbf{E}^*\times(\nabla\times\mathbf{E})\,, \tag{2.65}$$

$$\nabla\times(\mathbf{E}\times\mathbf{E}^*) = \mathbf{E}\,(\nabla\cdot\mathbf{E}^*) - \mathbf{E}^*\,(\nabla\cdot\mathbf{E}) + (\mathbf{E}^*\cdot\nabla)\,\mathbf{E} - (\mathbf{E}\cdot\nabla)\,\mathbf{E}^*, \tag{2.66}$$

and $\nabla\cdot\mathbf{E} = \nabla\cdot\mathbf{E}^* = 0$, to make the substitutions in equations 2.67 and 2.68,

$$\mathrm{Re}\left[(\mathbf{E}\cdot\nabla)\,\mathbf{E}^* + \mathbf{E}\times(\nabla\times\mathbf{E}^*)\right] = \frac{1}{2}\nabla\left(\mathbf{E}\cdot\mathbf{E}^*\right) = \frac{1}{2}\nabla\left(|\mathbf{E}|^2\right), \tag{2.67}$$

$$\mathrm{Im}\left[(\mathbf{E}\cdot\nabla)\,\mathbf{E}^*\right] = \frac{1}{2}\nabla\times(\mathbf{E}\times\mathbf{E}^*)\,, \tag{2.68}$$

in order to rewrite equation 2.64 as equation 2.69,

$$\mathbf{F_d} = \frac{1}{4}\,\mathrm{Re}(\alpha)\nabla\left(|\mathbf{E}|^2\right) - \frac{1}{2}\,\mathrm{Im}(\alpha)\,\mathrm{Im}\left[\mathbf{E}\times(\nabla\times\mathbf{E}^*)\right] - \frac{i}{4}\,\mathrm{Im}(\alpha)\nabla\times(\mathbf{E}\times\mathbf{E}^*)\,. \tag{2.69}$$

Finally, using Maxwell's equation for the curl of the electric field $\nabla\times\mathbf{E}(\mathbf{r}) = i\omega_o\mathbf{B}(\mathbf{r})$, where ω_o is the optical angular frequency, and defining the extinction cross-section,

$$\sigma_{\mathrm{ext,d}} = \frac{k_0\,\mathrm{Im}(\alpha)}{\varepsilon_0}, \tag{2.70}$$

where k_0 is the vacuum wavenumber of the light, we find the total force on a particle under the dipole approximation (equation 2.71) expressed in terms of the electric field and other physically intuitable parameters.

$$\mathbf{F} = \frac{1}{4}\,\mathrm{Re}(\alpha)\nabla|E|^2 + \frac{\sigma_{\mathrm{ext,d}}}{c}\mathbf{S} - \frac{1}{2}\sigma_{\mathrm{ext,d}}c\nabla\times\mathbf{s_d} \tag{2.71}$$

In equation 2.71, **S** is the Poynting vector and $\mathbf{s_d}$ is the spin density of the incident electric field defined by equations 2.72 and 2.73 respectively.

$$\mathbf{S} = \frac{1}{2}\,\mathrm{Re}\left[\mathbf{E}\times\mathbf{H}^*\right] \tag{2.72}$$

$$\mathbf{s_d} = i\frac{\varepsilon_0}{2\omega_o}\mathbf{E} \times \mathbf{E}^* \tag{2.73}$$

Each term in equation 2.71 can be investigated separately and are recognisable as the gradient, scattering and optical torque forces respectively. In the context of this thesis, $\mathbf{s_d}$ can be regarded as zero as linearly polarised light and spherical, non-birefringent particles are used and hence there is negligible optical torque exerted on the trapped particles. The sphericity of the particles used in this project is discussed in §5.4 and this approximation is found to be valid.

§2.4.3. The gradient force

It is useful to express the gradient force in terms of intensity rather than electric field, as this is the measurable quantity associated with a trapping laser. The intensity is defined as

$$I = |\langle \mathbf{S} \rangle| = \frac{1}{2}c\varepsilon_0|\mathbf{E}|^2 \tag{2.74}$$

and so the first term of equation 2.71 can be written as

$$\mathbf{F}_{\text{grad}}(\mathbf{r_d}) = \frac{1}{2}\frac{\text{Re}(\alpha)}{c\epsilon_0}\nabla I(\mathbf{r_d}). \tag{2.75}$$

From equation 2.75 it is clear why the gradient force is named as such. Any dielectric material with a refractice index higher than the surrounding medium that is placed in a non-uniform intensity distribution will experience a force in the direction of the intensity gradient. In the context of levitated optomechanics this means that a glass nanoparticle placed in a Gaussian beam experiences a force towards the centre of the beam. If the intensity gradient is sufficiently steep, the particle will be confined in two dimensions but free to move along the beam axis. If this Gaussian beam is made strongly convergent then an intensity gradient is also established along the optical axis and the particle will be attracted to the point of highest intensity, i.e. the focus.

The gradient force exists because the position of lowest potential energy for an electric dipole is to be polarised in alignment to an applied electric field. When the oscillating electric field of the trapping laser propagates through the particle, the electron clouds in the material are in a lower energy state when they follow the rapidly changing electric field exactly, and the larger the electric field, the lower the potential energy of the state representing the electron cloud following the field in this way. For this reason, the more intense the light field is in the region of the particle, the less potential energy the system has, so the particle will feel a force compelling it to migrate to a region of higher intensity and therefore lower potential. We will look at the optical potential a little more in the next subsection, approaching the derivation of the gradient force from a different angle.

§2.4.4. Optical potential

The equation for the gradient force can be reached using classical electromagnetics as above, but can also be found from the form of the potential. This is perhaps a more intuitive picture of the origin of this force, as the potential can be formulated in terms of the intensity, a scalar field with a value at every point in the region of the trap. Using a little of what we have learned about dipoles we calculate **F** below and confirm it is the same as the gradient force found in §2.4.2. This process will then be repeated but in a slightly different way so as to obtain the optical potential, and therefore the gradient force, in terms of quantities that are more easily measured in regards to a real experimental system.

§2.4.4.1. Gradient force from the interaction energy potential

Starting with the definition of intensity in terms of the Poynting vector, using $\langle \cdots \rangle$ to mean the time average,

$$I = |\langle \mathbf{S} \rangle| = \left| \frac{1}{\mu_0} \langle \mathbf{B} \times \mathbf{E} \rangle \right| \tag{2.76}$$

and using the definitions

$$|\mathbf{B}| = \frac{|\mathbf{E}|}{c}, \tag{2.77}$$

$$c^2 = \frac{1}{\mu_0 \varepsilon_0}, \tag{2.78}$$

we can then rewrite the definition of intensity as:

$$\begin{aligned} I &= c\varepsilon_0 \langle |\mathbf{E}|^2 \rangle \\ &= \frac{1}{2} c\varepsilon_0 E_0^2 \end{aligned} \tag{2.79}$$

where $\mathbf{E} = \mathbf{E}_0 e^{i\omega t}$ and $E_0 = |\mathbf{E}_0|$.

Using the potential, U, of a dipole in an electric field (equation 2.38), and including a factor of $\frac{1}{2}$ due to the fact that this is an induced dipole [156],

$$U = -\frac{1}{2} \langle \mathcal{P} \cdot \mathbf{E} \rangle, \tag{2.80}$$

and equations 2.40 and 2.41 for the polarisation and susceptibility respectively, we get:

$$\mathcal{P} = \varepsilon_0 \chi \mathbf{E}. \tag{2.81}$$

We substitute the definition of $\mathcal{P}$ into equation 2.80,

$$U = -\frac{1}{2} \varepsilon_0 \chi \langle \mathbf{E} \cdot \mathbf{E} \rangle = -\frac{1}{2} \varepsilon_0 \chi \langle |\mathbf{E}|^2 \rangle \tag{2.82}$$

and we recall that

$$\begin{aligned} I = c\varepsilon_0 \langle |\mathbf{E}|^2 \rangle &= \frac{1}{2} c\varepsilon_0 E_0^2 \\ \langle |\mathbf{E}|^2 \rangle &= \frac{1}{2} E_0^2 \end{aligned}, \tag{2.83}$$

and substitute this into equation 2.82

$$U = -\frac{1}{2} \varepsilon_0 \chi \left(\frac{1}{2} E_0^2 \right) \tag{2.84}$$

Rearranging the first line of equation 2.83 gives

$$2\frac{I}{c\varepsilon_0} = E_0^2, \tag{2.85}$$

which we substitute into equation 2.84 to give

$$U = -\frac{1}{2}\varepsilon_0\chi\left(\frac{1}{2}\left(2\frac{I}{c\varepsilon_0}\right)\right) \tag{2.86}$$

Simplifying this gives

$$U = -\frac{1}{2}\frac{\chi I}{c} \tag{2.87}$$

We use the general case for the force from a potential:

$$\mathbf{F} = -\nabla U, \tag{2.88}$$

which in our specific case, using equation 2.87, becomes:

$$\mathbf{F} = \frac{1}{2}\frac{\chi}{c}\nabla I \tag{2.89}$$

agreeing with equation 2.75 from the electromagnetics approach.

§2.4.4.2. Gradient force from trap characteristics

Now that we have used the concept of the potential and know the force due to a potential has a standard form $\mathbf{F} = -\nabla U$, this force can be recalculated in terms of experimentally obtainable parameters. This equation for the gradient force can then be used to calculate the force vector field at any point in space.

Starting again with the potential energy of a dipole, and substituting in for **p** from equation 2.38, we get

$$U = -\mathbf{p}\cdot\mathbf{E} = -\alpha|\mathbf{E}|^2. \tag{2.90}$$

The refractive index, n, of a material can be defined in terms of its relative permittivity ε_r and relative permeability μ_r using $n = \sqrt{\varepsilon_r\mu_r}$. We can assume our trapped nanoparticle is non-magnetic, and therefore $\mu_r = 1$, meaning $\varepsilon_r = n^2$. This can be subsituted into the Clausius-Mossotti relation from equation 2.49, giving

$$\alpha = 3V\varepsilon_0\frac{n^2-1}{n^2+2} \tag{2.91}$$

The Clausius-Mossotti definition of polarisability can then be substituted into equation 2.90 to give

$$U = -3V\varepsilon_0\frac{n^2-1}{n^2+2}|\mathbf{E}|^2 \tag{2.92}$$

Intensity can be expressed as the optical power per unit area and as a function of the electric field:

$$I = \frac{P}{\pi w\left(z\right)^2} = \frac{1}{2}c\varepsilon_0|\mathbf{E}|^2 \tag{2.93}$$

from which we can make the substitution

$$|\mathbf{E}|^2 = \frac{2P}{\pi \varepsilon_0 c w\left(z\right)^2} \tag{2.94}$$

in equation 2.92 and obtain

$$U = -3V\varepsilon_0 \frac{n^2-1}{n^2+2}\frac{2P}{\pi \varepsilon_0 c w\left(z\right)^2}. \tag{2.95}$$

We expand out for the volume of the spherical particle, with particle radius a, and simplify to get the minimum potential energy of a nanoparticle in an optical trap as a function of the physical parameters of the system [157].

$$U = -\frac{8P}{w\left(z\right)^2 c} a^3 \frac{n^2-1}{n^2+2} \tag{2.96}$$

With good focussing optics, the focal waist can be estimated to be close to the theoretical best that can be expected and we set it equal to the wavelength, and so we can calculate with $w\left(z\right) = \lambda$, $P = 0.5$ W, $n = 1.44$ and $a = 50$ nm to get a value for potential energy where we set the potential to zero when the particle is far from the trap. The potential energy of the particle in this system is:

$$U = -1.83 \times 10^{-19}\ \mathrm{J} = -1.14\ \mathrm{eV} \tag{2.97}$$

The thermal energy of the nanoparticle is calculated below with six degrees of freedom.

$$E_{\text{thermal}} = \frac{6}{2} k_B T \tag{2.98}$$

This can be compared with the potential depth and we find that the parameters above give a typical trap depth of around 14 $\mathrm{k_B T}$ or around 4,400 K. This large trap depth means the trap should be stable and long lived. The distribution of energy kicks the particle receives from the thermal bath of gas follow a Boltzmann distribution which is theoretically non-zero up to $E = \infty$ meaning there is still some tiny, yet non-zero chance of escape due to many molecules happening to give similar momentum kicks within a short time of each other.

The shape of the potential can now be calculated by reworking equation 2.96 so that is a function of position relative to the focus. We can recall the intensity distribution of a Gaussian beam with waist radius w_0, from equation 2.17, repeated below for convenience:

$$I(\mathbf{r},\mathbf{z}) = I_0 \left[\frac{w_0}{w(\mathbf{z})}\right]^2 \exp\left[\frac{-2\mathbf{r}^2}{w(\mathbf{z})^2}\right]$$

We can use the general form of a conservative force from a potential along with equation 2.17, and then simplify to get,

$$\mathbf{F}\left(\mathbf{r},\mathbf{z}\right) = -\nabla U\left(\mathbf{r},\mathbf{z}\right) \tag{2.99}$$

$$\mathbf{F}\left(\mathbf{r},\mathbf{z}\right) = \frac{8P}{c} a^3 \frac{n^2-1}{n^2+2} \nabla \left(w\left(\mathbf{z}\right)^{-2} \exp\left[\frac{-2r^2}{w\left(\mathbf{z}\right)^2}\right]\right) \tag{2.100}$$

$$\mathbf{F}\left(\mathbf{r},\mathbf{z}\right)=\frac{16P}{c}a^3\frac{n^2-1}{n^2+2}\exp\left[\frac{-2r^2}{w\left(\mathbf{z}\right)^2}\right]\left[\hat{r}\frac{2r}{w(z)^4}+\hat{z}\left(\frac{w_0^2}{w(z)^4}-\frac{2r^2w_0^2}{w(z)^6}\right)\right] \tag{2.101}$$

This form is a little unweildy and so not commonly used, however it now takes arguments P, a, n and w_0, all of which are measurable quantities asosciated with a particular experimental system. Equation 2.101 can be used to predict the gradient force field on a nanoparticle, if the other design parameters are known.

The gradient force has now been investigated and calculated; we can now look at the scattering force, how it behaves and the effects it has on an experimental optical trap.

§2.4.5. Scattering force

The scattering force results from the change in photon momentum when photons Rayleigh scattering from the particle in an optical trap. Rayleigh scattering is symmetric in the $\pm z$ scattering direction, as can be seen from figure 2.9.

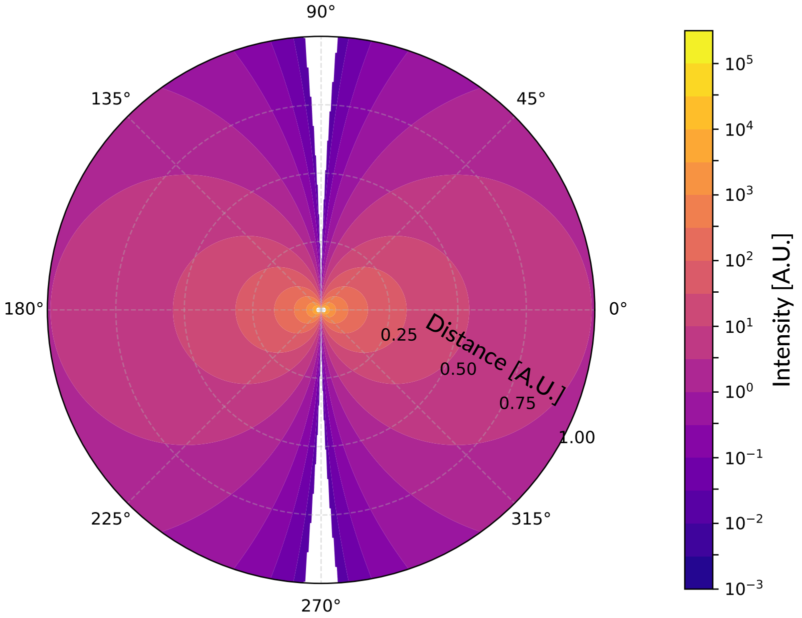

Fig. 2.9. *Rayleigh scattering intensity profile as a function of scattering angle. A wavelength of 1550 nm is used, scattering from a 100 nm diameter particle with a refractive index of 1.44. The intensity of the incident light at the particle is* 1×10^{19} *Wm*$^{-2}$.

The intensity of Rayleigh scattered light in a spherical polar co-ordinate system is given by equation 2.35, where the $\cos^2(\theta)$ term causes the $\pm z$ symmetry. This symmetry means the resulting average photon momentum after scattering is zero, however the trapping beam is aligned with the $+z$ axis, and so has non-zero momentum before scattering occurs. The total momentum of the system must be conserved through the process and so we can deduce that momentum equal to that of the scattered fraction of the incoming trapping beam has been imparted to the particle. This change in momentum is felt as a force on the particle in the direction of the Poynting vector of the trapping beam and can be calculated as below,

$$\mathbf{F}_{\text{scat}} = \frac{n\sigma_s}{c}\langle \mathbf{S} \rangle. \tag{2.102}$$

σ_s is the scattering cross-section from equation 2.36, and $\langle \mathbf{S} \rangle$ is the time average Poynting vector, and can be expressed in terms of the electric field, and therefore intensity, using only the direction of the Poynting vector, $\hat{S}$. We can make these substitutions and obtain an expression for the scattering force:

$$\mathbf{F}_{\text{scat}} = \chi^2 \frac{8\pi^3}{3c}\frac{1}{\lambda^4} I\hat{S} \tag{2.103}$$

The scattering force always acts in the direction of the Poynting vector of the trapping laser, displacing an optical trap. The magnitude of this force determines the equilibrium position of the particle along the optical axis, found when the gradient force is equal and opposite to the scattering force. The magnitude of the scattering force also determines whether such a stable position even exists at all; if the scattering force is too large then it will overcome the confining gradient force and a stable trap will be impossible. The magnitude of the scattering force can be seen to scale rapidly with particle radius, meaning that larger particles feel a disproportionately higher scattering force and cannot be trapped. This effect is exacerbated by the fact that the gradient force only scales with r^3 as opposed to r^6 for the scattering force, meaning an increase in r negatively affects the scattering force much faster than it positively impacts the gradient force. The condition for stable trapping based on this relative scaling is given in equation 2.104 and evaluates to about 500 nm for sensible trap parameters.

$$r < \sqrt[3]{\frac{3\lambda^4}{16\pi^4}\frac{\nabla I}{I}\left(\frac{n^2+2}{n^2-1}\right)} \tag{2.104}$$

The behaviour of the optical forces on the particle along the optical axis can be plotted, and we can see the equilibrium position of the particle emerge. This is where the total force on the particle has a zero crossing and it can be seen to vary linearly in this region, as we would expect for a harmonic oscillator. The gradient of this linear response is known as the trap stiffness, discussed in the the next subsection. The optical forces are plotted in figure 2.10.

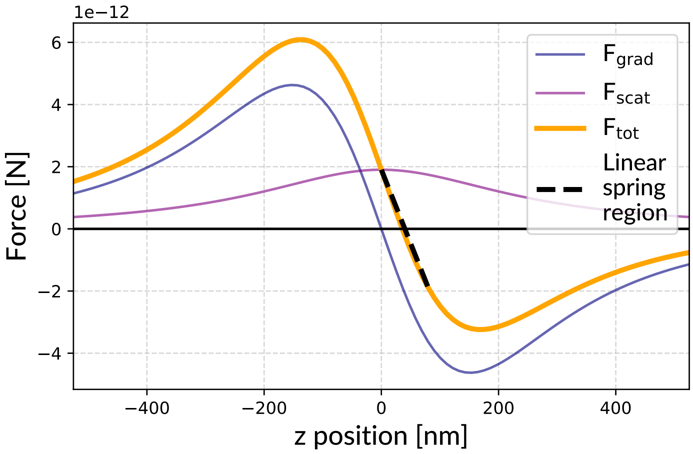

Fig. 2.10. *The optical forces acting on a trapped particle with* $n = 1.44$ *and* $r = 50$ nm. *The dashed line shows the linear spring regime. Under typical conditions, the particle does not leave this region.*

The scattering force always acts in the direction of the trapping beam, and is added to the gradient force to calculate the total force. The gradient force changes sign as we move through the focus, meaning it always acts to restore the particle to it's equilibrium position, slightly displaced from the intensity maximum.

§2.4.6. Trap stiffness

In §2.4.4 we found the form of the optical potential, and in §1.2.2 it was mentioned that we can approximate this true Gaussian form as quadratic close to the intensity maximum. This is done because a quadratic potential is the leading nonlinear term in a Taylor expansion of the potential around the focus. Conveniently, the physics of quadratic potentials are well understood, and an object in such a potential behaves as a harmonic oscillator. These systems feel a linearly increasing restoring force with increasing displacement from the equilibrium position, as described by Hooke's law (equation 2.105).

$$\mathbf{F} = -K\mathbf{x}, \tag{2.105}$$

where position $x = 0$ represents the equilibrium position. In general K is the spring constant of the system, and in levitated optomechanics is called the trap stiffness. The restoring force in question here is the gradient force, we can therefore decompose the force into it's x, y and z components.

$$\mathbf{F}^{(i)}_{\text{grad}} = \begin{cases} -K_x\mathbf{x} \\ -K_y\mathbf{y} \\ -K_z\mathbf{z} \end{cases} . \tag{2.106}$$

We can solve for the trap stiffnesses, $K_i = -\frac{\partial \mathbf{F}^{(i)}_{\text{grad}}}{\partial \mathbf{x}}$ using the force from the intensity of a Gaussian beam, expressed in terms of the laser power. This can in turn be expressed in terms of the wavelength and NA, $w_0 = \frac{\lambda}{\pi \text{NA}}$, although it should be kept in mind that these definitions rely on the paraxial approximation and so are not reliable when numerical accuracy is required rather than a qualitative guide. Making the substitutions gives: [7, 158]

$$K_i = \begin{cases} \frac{4\alpha \text{NA}^4 \pi^3}{c\epsilon_0 \lambda^4} P \\ \frac{4\alpha \text{NA}^4 \pi^3}{c\epsilon_0 \lambda^4} P \\ \frac{2\alpha \text{NA}^6 \pi^3}{c\epsilon_0 \lambda^4} P \end{cases} , \tag{2.107}$$

all of which are highly dependent on the trapping light NA and linearly dependent on laser power. Just as with a more common mechanical example of a harmonic oscillator such as a mass on a spring, the natural angular frequency, Ω, of the system can be found using the spring constant and mass:

$$\Omega = 2\pi f = \sqrt{\frac{K_{\text{x,y,z}}}{m}} \tag{2.108}$$

§2.4.6.1. Potential energy in the "spring" degrees of freedom

Now that we have an expression for the trap frequencies, we can use this information to calculate the potential energy per quadratic degree of freedom using equation 2.109,

$$U_i = \frac{1}{2} m \Omega_i^2 |\mathbf{r}_i|^2, \tag{2.109}$$

where **r** is the appropriate position vector, relative to the particle's equilibrium position. Equation 2.96 can be Taylor expanded and the second-order components equated with equation 2.109 to give equation 2.110 [159].

$$\Omega_i^2 = \begin{cases} \frac{4\alpha}{m\pi w_0^4 c\varepsilon_0} P \\ \frac{4\alpha}{m\pi w_0^4 c\varepsilon_0} P \\ \frac{2\alpha\lambda^2}{m\pi^3 w_0^6 c\varepsilon_0} P \end{cases} . \tag{2.110}$$

These frequencies can be measured and the ratio used to estimate the focal waist using equation 2.111.

$$\frac{\Omega_{x,y}}{\Omega_z} = \frac{\pi w_0}{\lambda} \sqrt{2} \tag{2.111}$$

This method only uses the approximation that the intensity is quadratic very close to the focus, and therefore does not rely on the sweeping assumptions used in Gaussian beams.

§2.4.7. Absorption - silica and 1550 nm wavelength light

The scattering force results from the transfer of photon momentum to the particle, and we have seen how this can happen through Rayleigh scattering; another way this can happen is from absorption of photons by the particle. This absorption adds to the scattering force and can be included in the expression for the scattering force through the use of the extinction cross-section σ_{ext}, a combination of the scattering and absorption cross sections σ_{sca} and σ_{abs}.

$$\sigma_{\text{ext}} = \sigma_{\text{sca}} + \sigma_{\text{abs}} \tag{2.112}$$

This definition allows us to redefine the scatter force in terms of extinction cross-section.

$$\mathbf{F}_{\text{sca}} = \frac{\sigma_{\text{ext}}}{c} I \hat{S} \tag{2.113}$$

In this thesis, silica nanoparticles are trapped by a 1550 nm laser, a wavelength and material combination designed to produce minimum extinction, quantified as around 0.2 dB/km [160], most of which is due to Brillouin scattering due to density fluctuations, meaning attenuation in a nanoparticle is negligible. This wavelength and material choice is partially to minimise the undesirable scattering force, but mainly to avoid the adverse thermal effects absoption can have on an optical trap. Absorbed photons are converted into heat inside the nanoparticle, raising it's internal temperature, which couples to it's centre of mass temperature, increasing the probability that the particle will escape from the trap. The particle will also lose heat to the heat bath of background gas it is immersed in, settling at an equilibrium temperature when the heat flux into the particle is balanced by the heat flux out. The rate of heat flow from the particle to the gas is determined by their difference in temperature and by the gas pressure. A lower gas pressure means less gas collisions with the particle per unit time and therefore fewer opportunities for the particle to transfer it's heat, resulting in a higher internal temperature. As a vital part of levitated optomechanics experiments is minimising the background gas pressure in order to minimise the damping rate, absorption can cause significant problems as it raises the internal temperatue of the silica particle to such a point where the particle melts or breaks apart, releasing it from the trap. This is the primary reason to design an optical trap using a wavelength and material combination at which there is very low material absorption, especially as the particle is trapped in a region of incredibly high intensity. Most levitated optomechanics experiments use silica particles and either 1550 nm or 1064 nm lasers.

The absorption curve for silica can be seen in figure 2.11 [13].

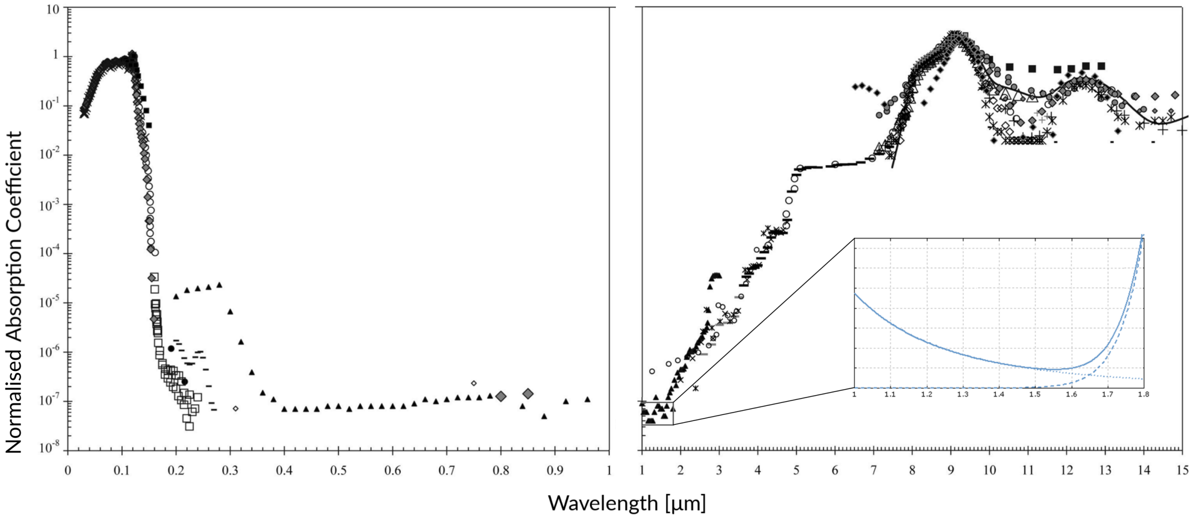

Fig. 2.11. *Absorption spectra of silica. Adapted from [13] and [14] (inset). The spectra has been normalised to have a coefficient of 1 at its maximum. The inset plot shows the behaviour around the absorption minimum and is calculated from the total extinction caused by Rayleigh scattering and material absorption.*

The heated particle can also lose heat through blackbody radiation at a rate given by the Stefan-Boltzmann law:

$$P = A_\lambda \epsilon \sigma T^4. \tag{2.114}$$

where A_λ is the object effective area, given by $\frac{2\pi}{\lambda}\,\mathrm{Im}\left[\chi\right]$ [84]. λ is the blackbody wavelength at which the power is radiated, σ is the Stefan-Bolzmann constant and T is the object's internal temperature. A blackbody at temperature T has emission spectrum given by the Rayleigh-Jeans law (equation 2.115), and the peak emission wavelength given by Wien's displacement law (equation 2.116),

$$B_\lambda(T) = \frac{2ck_BT}{\lambda^4} \tag{2.115}$$

$$\lambda_{\mathrm{max}} = \frac{b}{T} \tag{2.116}$$

where b is Wien's displacement constant. In order to allow the particle to thermalise to as low a temperature as possible, a material with high blackbody emissivity at the wavelengths corresponding to the expected temperature is desirable. The wavelength of maximum emission can be found from equation 2.116, using $T \approx 400$ K. For a 100 °C particle (chosen because the particle will be heated by the trapping laser), the peak emission wavelength is around 8 μm. The more a material absorbs light at a specific wavelength, the higher it's emmisivity is at that wavelength, and figure 2.11 shows silica has a much higher absorption, and therefore emissivity, at 8 μm than at 1.55 μm. This means a silica particle in a 1550 nm trapping beam will have very low absorption and high thermal emission, lowering it's equilibrium temperature, furthering the case for this wavelength and material choice.

§2.5. Motional Dynamics

In the previous section, the various optically induced forces on an optically trapped nanoparticle were discussed. We examined the physical mechanisms that give rise to the gradient and scattering forces, in the case of both small and large particles compared to the wavelength of light. In this section we will investigate the motion produced by these forces and how this translates into a power spectrum. The origin and behaviour of the damping force behind this damped harmonic oscillator will also be explained.

We have seen that the potential felt by an optically trapped nanoparticle can be well approximated as quadratic near the focus. This means we can treat the forces involved as those of a damped harmonic oscillator subject to a linear restoring force. The trapping potential has mirror symmetry about all three planes in the coordinate system we are using, where the z and x axes are aligned with the incoming wavevector and polarisation vector respectively, the full tensor expression for the relation between trap frequencies and trap stiffnesses can be reduced down to three separable definitions as in equation 2.117, where $i = x, y, z$.

$$\Omega_i = \sqrt{\frac{K_i}{m}} \tag{2.117}$$

§2.5.1. Equation of motion

In the following discussion, $\mathbf{x}$ will be used to denote the position of the particle, however the equations given are equally valid for the y and z directions. $\dot{\mathbf{x}}$ and $\ddot{\mathbf{x}}$ are used to mean the first and second differentials of $\mathbf{x}$ with respect to time.

We start with Newton's second law for the net force on the particle, neglecting the scattering force as this is static and only shifts the minimum of the effective potential. In addition to the harmonic restoring force we include a Stoke's drag term that produces a resistive force in opposition to the velocity of the particle. The Stoke's drag and damping rate Γ will be discussed in §2.5.2. We also include a stochastic force due to random momentum kicks from impinging gas molecules imparting momentum to the particle via collisions.

$$\mathbf{F} = m\ddot{\mathbf{x}}(t) = \mathcal{F}_{\text{th}} - m\Gamma\dot{\mathbf{x}}(t) - m\Omega^2\mathbf{x}(t) \tag{2.118}$$

$$m\ddot{\mathbf{x}}(t) + m\Gamma\dot{\mathbf{x}}(t) + K\mathbf{x}(t) = \mathcal{F}_{\text{th}}(t) \tag{2.119}$$

Substituting in for K using equation 2.117, we get

$$\ddot{\mathbf{x}}(t) + \Gamma\dot{\mathbf{x}}(t) + \Omega^2\mathbf{x}(t) = \frac{\mathcal{F}_{\text{th}}(t)}{m}, \tag{2.120}$$

where $\mathcal{F}_{\text{th}}(t)$ is a Langevin force satisfying

$$\langle \mathcal{F}_{\text{th}}(t)\mathcal{F}_{\text{th}}(t')\rangle = 2m\Gamma k_B T\delta(t-t'). \tag{2.121}$$

This force behaves according to the fluctuation-dissipation theorem [41, 68, 161]. We will show the origin of this expression shortly. Setting the right hand side of equation 2.120 equal to 0 gives the solution

$$x(t) = x_0 \sin(\Omega t + \phi) \tag{2.122}$$

where $\mathbf{x}_0$ is the amplitude of the position oscillation of the particle and ϕ is an arbitrary phase. This solution confirms the harmonic nature of the particle motion in the trap.

The particle position over time can be recorded and seen to oscillate about an equilibrium position, however it's more useful to examine this motion as a function of frequency rather than time. This is done using a power spectral density (PSD) function that illustrates how much each frequency component contributes to the total position variance of the particle. We calculate an expression for the PSD by first Fourier transforming the equation of motion (equation 2.120) to obtain equation 2.124. The general form of the Fourier transform is given be equation 2.123.

$$\hat{f}(\omega) = \int_{-\infty}^{\infty} f(x)e^{-2\pi i x\omega}dx \tag{2.123}$$

where $\hat{f}(\omega)$ is the function in terms of frequency rather than time. Fourier transforming the equation of motion [7, 88] gives

$$-\omega^2 x(\omega) - i\omega\Gamma x(\omega) + \Omega^2 x(\omega) = \frac{\mathcal{F}_{\text{th}}(\omega)}{m} \tag{2.124}$$

This allows us to find the PSD of position, $S_{xx} = \left\langle |x(\omega)|^2 \right\rangle$,

$$S_{xx}(\omega) = \frac{1}{m^2}\frac{\left\langle |\mathcal{F}_{\text{th}}(\omega)|^2 \right\rangle}{\left(\Omega^2-\omega^2\right)^2+\Gamma^2\omega^2}. \tag{2.125}$$

As the PSD is a description of the spectral variance contribution, we can find the total variance, or expectation value, of x^2, denoted $\langle x^2 \rangle$ by integrating S_{xx} over all frequencies.

$$\begin{aligned}
\left\langle x^2 \right\rangle &= \int_0^{\infty} S_{xx}d\omega \\
\left\langle x^2 \right\rangle &= \frac{1}{2}\int_{-\infty}^{\infty} S_{xx}d\omega \\
\left\langle x^2 \right\rangle &= \frac{\left\langle |\mathcal{F}_{\text{th}}(\omega)|^2 \right\rangle}{2m^2}\int_{-\infty}^{\infty}\frac{d\omega}{\left(\Omega^2-\omega^2\right)^2+\Gamma^2\omega^2} \\
\left\langle x^2 \right\rangle &= \frac{\left\langle |\mathcal{F}_{\text{th}}(\omega)|^2 \right\rangle}{2m^2}\frac{\pi}{\Omega^2\Gamma}
\end{aligned} \tag{2.126}$$

From equipartition (see §2.5.3), we know that each quadratic degree of freedom contributes $1/2 k_B T$ of energy, meaning

$$E = \frac{1}{2}k_B T = \frac{1}{2}m\Omega^2\langle x^2 \rangle, \tag{2.127}$$

$$\langle x^2 \rangle = \frac{k_B T}{m\Omega^2}. \tag{2.128}$$

We can substitute in the variance definition found in equation 2.126,

$$\frac{k_B T}{m\Omega^2} = \frac{\left\langle |\mathcal{F}_{th}(\omega)|^2 \right\rangle}{2m^2} \frac{\pi}{\Omega^2 \Gamma}, \tag{2.129}$$

$$\left\langle |\mathcal{F}_{th}(\omega)|^2 \right\rangle = \frac{2mk_B T\Gamma}{\pi}. \tag{2.130}$$

Bringing together equations 2.125 and 2.129 gives the commonly used form of the PSD of the particle position, shown in equation 2.131 [7, 157, 159]. The form of $S_{xx}(\omega)$ is shown in figure 2.12 below.

$$S_{xx}(\omega) = \frac{k_B T}{\pi m} \frac{\Gamma}{\left(\Omega^2 - \omega^2\right)^2 + \Gamma^2\omega^2} \tag{2.131}$$

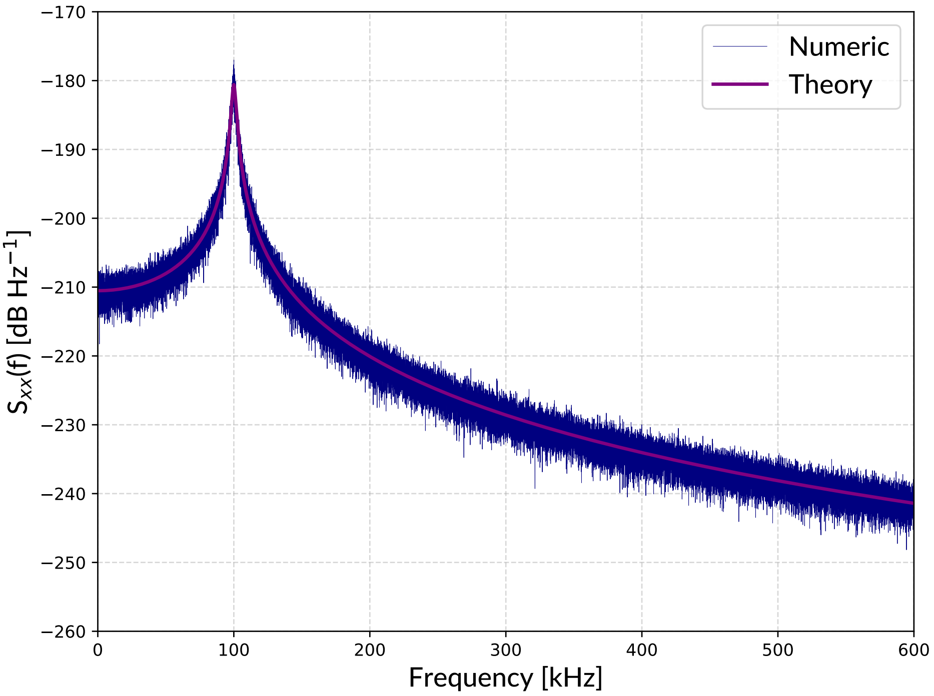

Fig. 2.12. *The power spectral density of particle position when oscillating at 100 kHz, with a damping rate of 500 s^{-1}. The "numeric" plot is produced by taking the PSD of the position of a simulated stochastic harmonic oscillator. Particle position over time is simulated using an Ito process in Mathematica [15] and used to create a position time series, which is then used to calculate the PSD.*

Equation 2.131 gives an analytical form for the power spectrum of an oscillating optically trapped particle as a function of frequency, however often the experimentally accesible information is the particle position as a function of time. In the idealised case, when the position of the particle can be known for an infinitely long time, the Wiener-Khinchin theorem states that the power spectrum is given by equation 2.132,

$$S(f) = \int_{-\infty}^{\infty} R_{xx}(\tau) e^{-2\pi i f \tau} d\tau, \tag{2.132}$$

where $R_{xx}(\tau)$ is the autocorrelation function of the particle position, given by

$$R_{xx}(\tau) = \lim_{T\to\infty} \left[\frac{1}{T} \int_0^T x(t+\tau)x(t)dt \right] . \tag{2.133}$$

In reality, position data can only be recorded for finite time durations, and therefore the above integral to $t = \infty$ isn't feasible. In these situations the PSD is estimated using Welch's method [162]. Welch's method consists of dividing up the time series data into M segments and applying a windowing function. These segments can be overlapping by a chosen amount and the windowing function works to reduce unwanted noise due to the finite length of the segment. After windowing, a periodogram is computed from each segment and then these modified periodograms are averaged. The periodogram is calculated using the discrete time Fourier transform (DTFT) [163] and produces a adjustable number of frequency bins and the corresponding variance contribution. The average of these periodograms is the end result of Welch's method and is usually what is meant when talking about the calculated PSD of a digital signal, and in the case of this thesis, the PSD of the particle position.

§2.5.2. Stokes damping

A trapped particle experiences a damping force that acts against it's motion with respect to the equilibrium position, resisting high velocities. This damping thermalises the kinetic energy of the particle through many collisions with background gas particles, transfering momentum to and from the particle. This thermalisation is quantified by the damping rate, Γ, and is proportional to background gas pressure. The reciprocal of the damping rate is the damping time, after which, when prepared in an arbitrary initial state in phase space, the particle will have relaxed back to a thermal state. The damping force follows the fluctuation-dissipation theorem, relating the magnitude of the dissipation mechanism to the physical properties of fluctuations in the system [161]. In the case of an optically trapped particle, the fluctuations in question are those of the momentum kicks from impinging gas molecules. The damping rate is given by equation 2.134 [7, 39, 128].

$$\Gamma = \frac{6\pi\eta r}{m} \frac{0.619}{0.619 + K_n} \left(1 + \frac{0.31K_n}{0.785 + 1.152K_n + K_n^2} \right) , \tag{2.134}$$

where $K_n = \bar{l}/r$ [129]. K_n is the Knudsen number that quantifies how well described a situation is by continuum fluid mechanics, rather than statistical mechanics. The coefficients used in equation 2.134 have been determined empirically from analysis of the dynamics of spheres moving in a rarefied fluid, hence their seemingly unusual values; for more information, see [128]. For $K_n > 1$, the length scales involved in a physical system are comparable with the mean free path, $\bar{l}$, of a molecule in the gas and therefore statistical mechanics must be used. The mean free path is calculated using equation 2.135, where a_m is the diameter of the gas molecules and p is the background gas pressure.

$$\bar{l} = \frac{k_B T_{\text{gas}}}{\sqrt{2}\pi a_m^2 p} \tag{2.135}$$

In equation 2.134, η is the viscosity of the gas and r is the particle radius. This calculation for the damping rate assumes a spherical object moving through a gas with mean free path much longer than the diameter of the particle.

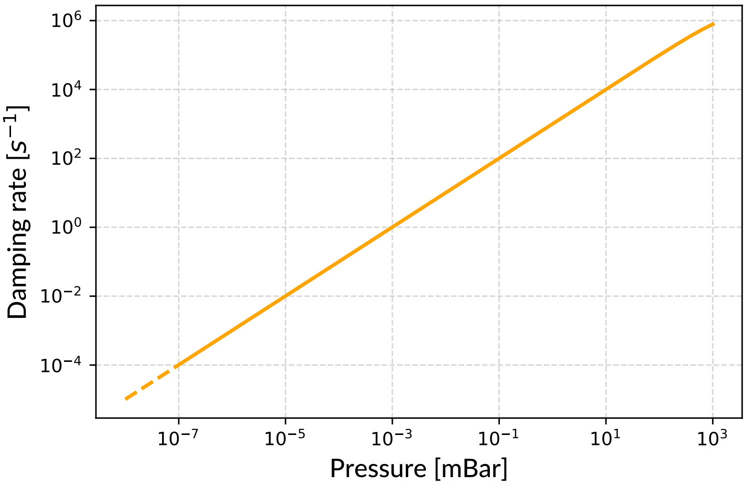

Fig. 2.13. *Damping rate as a function of background gas pressure. Calculated using a particle temperature 400 K, a diameter of 100 nm and a mass density of 2295 kgm^{-1}. The molecular diameter of the gas is 355×10^{-12} m.*

At higher gas pressure, an optically trapped particle will thermalise more quickly with it's environment and will oscillate coherently for a shorter time. The longer duration of coherent oscillation associated with a lower damping rate means that a better estimate of the particle's future state can be made. If the particle's position in phase space is known at time t then it's state can be well estimated at time $t + \tau$ where $\tau < {}^1\!/\Gamma$. A higher value for Γ means that spectral features are broadened and when close to atmospheric pressure, these features are obfuscated completely making it difficult to use a PSD to obtain information about the dynamics of the particle. Figure 2.14 shows the PSD of an optically trapped nanoparticle at different gas pressures, and therefore different damping rates. The peak due to the natural trap frequency of the particle can be seen to be broadened by corresponding degrees.

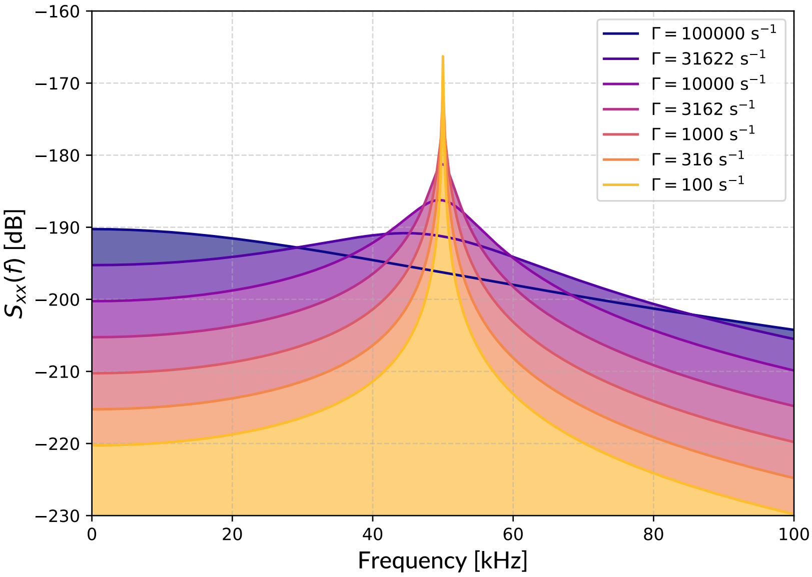

Fig. 2.14. *The power spectral densities of particles oscillating with different damping rates. The spectral broadening due to higher damping rates can be seen.*

§2.5.3. Equipartition

The equipartition theorem is the idea that in a physical system that's well represented by continuum mechanics, the total energy of the system is shared equally between degrees of freedom. Degrees of freedom can include many types of mechanical motion including translational, rotational, vibrational, potential etc. This means that the translational kinetic energy $E_k = {}^1\!/_2 m|\mathbf{v}|^2$ asosciated with one component of the motion of a diatomic molecule in a gas is equal to it's rotational energy $E_{k,\mathrm{rot}} = {}^1\!/_2 I\omega_m^2$.

The equipartition theorem predicts that because the kinetic energy of an object is quadratic with it's velocity, each translational degree of freedom will contain ${}^1\!/_2 k_B T$ Joules of energy. When considering the translational motion of an object in three dimensions, the total kinetic energy then becomes:

$$E_k = \frac{3}{2} k_B T. \tag{2.136}$$

If present, other types of degrees of freedom can add to the total energy of the system and will each an additional ${}^1\!/_2 k_B T$ of energy. The active degrees of freedom of a specific system depend on it's makeup, for example in the case of a monatomic gas there are no vibrational or rotational degrees of freedom and so the expression in equation 2.136 gives the whole picture. In an optically trapped nanoparticle the internal degrees of freedom are neglected as they are well decoupled from the centre of mass motion of the particle.

The well known expression for kinetic energy given above is one example of a quadratic degree of freedom, but the energy contained in the harmonic oscillation of a trapped nanoparticle in the x direction can be given by

$$E = \frac{1}{2} m\Omega_x^2 \langle x^2 \rangle. \tag{2.137}$$

This is a quadratic degree of freedom and so also contributes $E = {}^1\!/_2 k_B T$. This is useful expression in levitated optomechanics as the trap frequency Ω is easily measured, and therefore a temperature can be calculated.

The idea of equipartition stems from classical thermodynamics and is not valid for quantum systems. This means that equipartition breaks down when the temperature of the object in question is close to or below the the temperature represented by the enegy of a state transition in the quantum system. In this situation the energy contained in each degree of freedom will be less than is predected by equipartition.

§2.6. Fibre Optics

Much of the optical system presented in chapter 4 is based on fibre optics rather than the more conventional free space optics. This approach comes with increased robustness and allows for the use of high quality, low cost fibre telecoms components. In preparation for a discussion on the optical system, the theory behind how fibre optics function will be discussed briefly.

An optical fibre in its simplest form is a quasi one dimensional waveguide; light enters one end of the fibre and is efficiently guided to the output. Picturing a simple glass rod, there is a cone of angles (the acceptance cone) through which light rays can enter the fibre, refract into the glass and then be travelling along the fibre at an angle less than the critical angle of the material (equation 2.26). As these rays are travelling at an angle shallower than the critical angle with respect to the glass-air boundary, they are totally internally reflected and continue propagating down the waveguide until they reach the end, refract out and can be collected. The angle subtended by the acceptance cone of a fibre is used in the same way as in equation 1.6 to calculate the NA of the fibre.

In reality, optical fibres are not simply glass rods but are made of multiple layers of material with slightly different refractive indices and thicknesses that fulfil different design criteria. Almost all optical fibre consists of a core surrounded by a lower refractive index cladding, the index contrast between which ensures that light remains confined to the core and determines the NA of the fibre. The radii of these layers and the shape of the index transition between the two varies depending on use case, and often the cladding itself is protected by a much thicker protective polymer coating. Figure 2.15 shows different varieties of optical fibre cross-section.

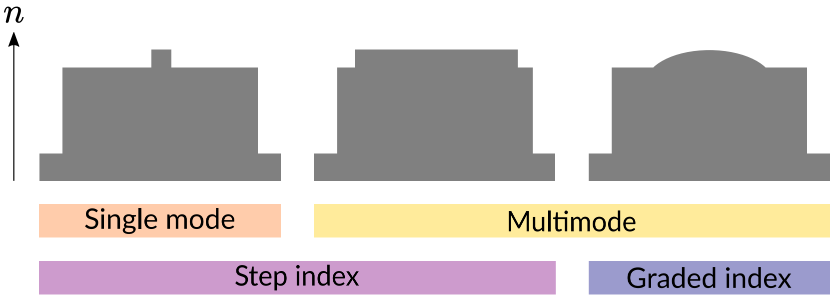

Fig. 2.15. *Optical fibre refractive index cross-sections*

The multimode and single mode labels in figure 2.15 arise from the different ratios of the core and cladding radii. A multimode fibre is one that has a core wide enough that a ray optics description of light shows rays reflecting many times from the core-cladding boundary. Rays that enter the fibre at a steep angle will reflect many more times than a ray that enters normal to the face of the fibre. These high order rays travel a longer distance in order to traverse the fibre than the axial ray and therefore take longer to do so; causing dispersion effects that are discussed below. In order to make the field transmitted by the fibre as coherent, and therefore as useful as possible, single mode fibres are used. These have a much smaller core radius and so only allow the propagation of the axial rays.

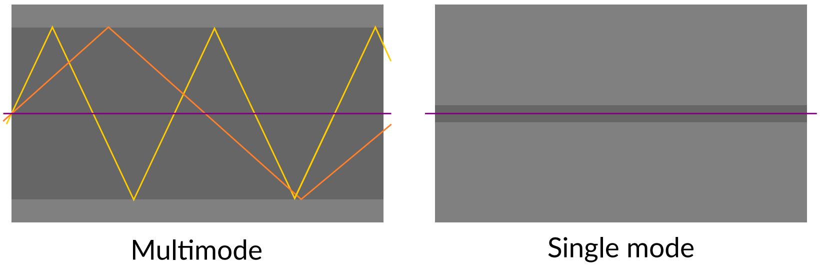

Fig. 2.16. *Ray optics view of mode coupling in an optical fibre*

The ray optics description of this behaviour is limited and in order to better understand the difference between single and multimode fibre we refer to the electromagnetic modes that the fibre can support. A singlemode fibre only allows the propagation of the fundamental transverse electromagnetic (TEM) mode, known as TEM_{00}, whereas multimode fibres can support much more complex mode structures. The subscripts on a TEM mode are p and l and denote the radial and angular mode order respectively. A TEM_{pl}

mode has intensity given by equation 2.138 below.

$$I_{pl}(r,\varphi) = I_0 r^l \left[L_p^l(r)\right]^2 \cos^2(l\varphi) e^{-r}, \tag{2.138}$$

where L_p^l is the Laguerre polynomial of order p and index l. This equation is for a cylindrical coordinate system with radius r and angle φ. The first few orders of the TEM modes are shown below in figure 2.17.

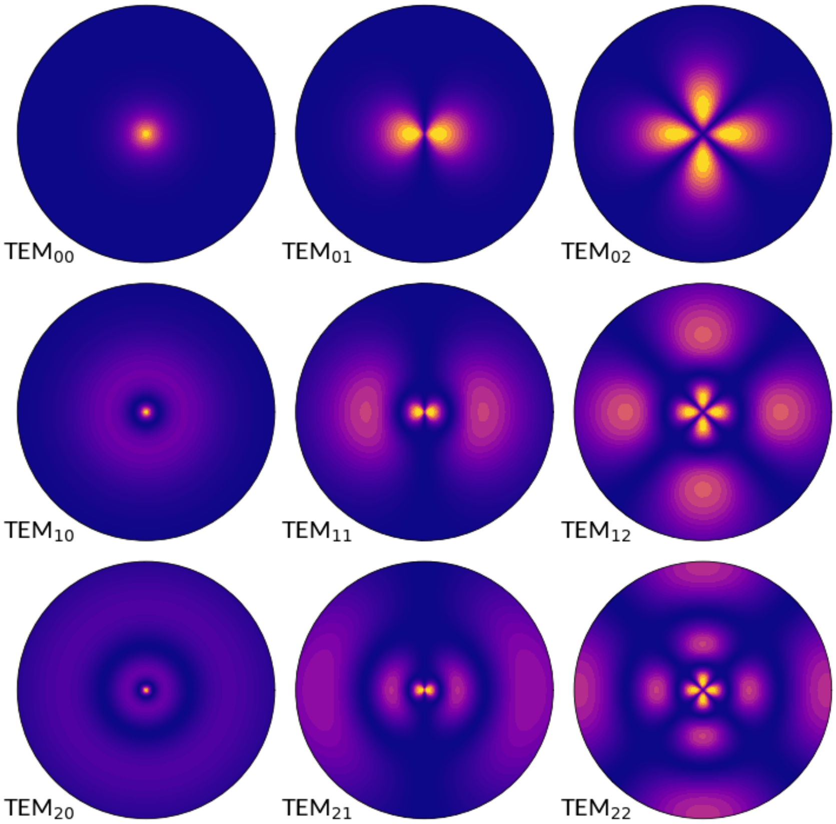

Fig. 2.17. TEM$_{pl}$ *modes up to* $p = l = 2$. *Intensities are normalised to the peak intensity of each mode and colour is logarithmically scaled.*

The number of modes supported by a particular optical fibre is a function of the fibre's V number, or normalised frequency, calculated using equation 2.139,

$$V = \frac{2\pi}{\lambda} a \sqrt{n_{\text{core}}^2 - n_{\text{clad}}^2}, \tag{2.139}$$

where a is the radius of the fibre core and n denotes refractive index. It can be seen that this is determined by the refractive index contrast of the fibre, as well as the size ratio of the fibre core to the wavelength of light to be guided. As the V number decreases different modes become unsupported, down to $V = 2.405$ (the first root of the zeroth order Bessel function) where the fibre becomes single mode. Multimode fibres support some number of modes, the intensity distributions of which sum together to create a complex intensity pattern. This pattern evolves as light propagates down the fibre and means that light leaving a multimode fibre can have many intensity maxima, making it unsuitable for use as the trapping beam in a levitated optomechanics application.

The fibre optic hardware used in the project presented in this thesis is all singlemode, step index fibre. This is a result of the fact that most fibre optic telecoms technology has been developed to follow this standard meaning the best suited products operate in this way. In addition to this, the nature of the project requires the pure Gaussian intensity profile of the TEM_{00} mode. Using fibre that cannot possibly support the propagation of higher order modes is an excellent way to ensure mode purity.

In the next subsection the theory of how fibre optic telecoms technology functions is discussed, again saving the specific technical discussion of the hardware used in this project for chapter 4.

§2.6.1. Fibre telecoms

In the last 60 years, optical fibre has become the primary method humans use to move data around the planet. Expensive, heavy copper cables have been replaced with glass fibre that can carry orders of magnitude more information per second (bandwidth). This infrastructure crosses every ocean and continent and is an enormously economically valuable tool.

The basic building blocks of the fibre optic telecoms system are actually quite simple; fibres carry pulses of laser light in such a way that the pulses hold their shape and power over many hundreds of kilometers so that they can be decoded after a travel time on the order of nanoseconds. Optical fibre has much lower losses ($0.18\ \text{dB km}^{-1}$ [164]) than an electrical transmission cable and so repeaters that boost the power are needed less frequently. Optical frequencies are also much higher than those of the radio waves used for data transmission, meaning their bandwidths are inherrently much higher to match.

In order to maximise the bandwith of a single optical fibre, the pulses of light (bits) are made as short as possible in time with as great a signal to noise ratio as possible. This ensures both maximum throughput as well as minimum chance of decoding error. Unfortunately there are various effects that work against these goals such as dispersion, absorption, scattering etc. The light representing the binary bits of data is sent in square pulses which need to remain relatively intact in order to be decoded without errors. The intensity recieved by the photodetector at the output of a fibre needs to be sharply changing in time, and pulses well separated. Transmission rates can be lowered in order to decrease the likelihood that a bit will be misread, but this decreases bandwidth, and ultimately an optimal trade off must be found.

If many paths are available for light to take along the fibre then the different paths will have diffferent lengths and so the photons traversing said paths will arrive at the detector at different times, smearing out the pulses and making bits harder to decode. Single mode fibre is used to avoid this effect, known as waveguide dispersion. A narrow linewidth light source is also required so that the light in the fibre is as monochromatic as possible in order to avoid the dispersion of a pulse created by the slightly different, wavelength dependent, group velocities in the medium. The different velocities experienced by different frequencies are because the refractive index of a material is wavelength dependent; a property called material dispersion. The total dispersion can be minimised by using a light source with a wavelength very close to the material's zero dispersion wavelength (ZDW). This is where the waveguide and material dispersions cancel each other out and the total dispersion coefficient of the material has a zero crossing. This is where the overall dispersion of the wavelength distribution produced by the laser is at it's lowest. In order to choose the light source to be at the ZDW, the material choice must first be made. The telecoms industry standard is ultra pure silica glass as it has incredibly low material absorption at wavelengths close to its ZDW. The 1550 nm absorption minimum in silica decreases the need for additional repeaters along a fibre and combined with the ZDW at 1300 nm, made 1550 nm the industry standard that is used in infrastructure today. The absorption spectrum for silica can be seen in figure 2.11, where the same low absorption properties that make it suited as a fibre optic make it suitable for optical trapping.

As previously mentioned, the experimental system built in this project uses hardware developed for use in a fibre telecoms scenario; it is worth briefly exploring the working principles behind them in order to make their operation clearer when discussing the setup later. The main relevant components are the fibre laser, the erbium doped fibre amplifier (EDFA) and the acousto-optic modulator (AOM). Here we discuss them each in turn.

§2.6.1.1. Fibre laser

In general, lasers consist of an active gain medium inside some form of cavity that allows light to pass through the gain medium many times, create stimulated emission and then eventually leave as part of the output beam. In a fibre laser this cavity consists of an active fibre, doped with a rare earth element, with fibre Bragg gratings (FBGs) at either end. The doped fibre contains atoms of an element with a convenient energy levels structure in order to produce emission at the desired laser wavelength. In the case of the components in this project the dopant is erbium as it has a 3 level energy structure with an absorption at 980 nm that produces an emission at 1550 nm. When this erbium doped glass is pumped with 980 nm light, the erbium atoms absorb a pump photon, an electron is excited to an upper state and then quickly decays down to an intermediate meta-stable state. After 10 ms [165] the electron relaxes back to its ground state, emitting a 1550 nm photon in the process. This 1550 nm photon is emitted into the active fibre and travels through the medium until it meets another excited erbium atom and causes the stimulated emission of another coherent photon. As long as sufficient pump light is provided to the gain fibre, this is a continous process and the fibre starts lasing. The cavity of a more standard laser is often a pair of highly reflective, and very accurately aligned cavity mirrors; however in the case of a fibre laser, FBGs are used to the same effect. FBGs are periodic modulations of the refractive index of the fibre core and are tuned to the desired laser wavelength. The gratings are highly effective mirrors and ensure that the vast majority of 1550 nm photons are reflected back down the fibre in order to stimulate further emission.

One of the major reasons erbium is used is the convenient emission at close to the optimum wavelength for silica as discussed in above, another is that the pump wavelength is one at which it is easy to make pump laser diodes. These diodes are included in most fibre laser packages and produce a low quality 980 nm beam that is coupled into the cladding of the active fibre. The pump light propagates through the cladding and refracts into the active core where it is absorbed. This extra step is required as the poor beam profile makes the pump light difficult to couple directly into the fibre.

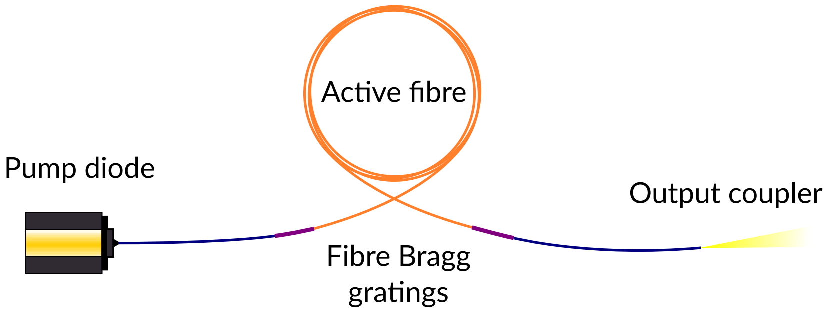

Fig. 2.18. *The main components of a fibre laser*

Fibre lasers are highly efficient and robust making them well suited to deployment in communications infrastructure such as undersea cables and internet exchanges. They require very little skilled maintenance and can produce higher optical power for their volume when compared to diode lasers or gas lasers as the gain medium can be coiled up and kilometers long. Erbium based fibre lasers are widespread because of their 1550 nm wavelength that works very well with the telecoms industry standards.

§2.6.1.2. Erbium-doped Fibre Amplifier

The Erbium-doped fibre amplifier (EDFA) is very similar to an erbium based fibre laser, except it does not contain the FBG cavity that allows a fibre laser to actually lase. An EDFA consists of an input fibre that accepts 1550 nm signal light, an internal 980 nm pump laser diode(s), a length of active fibre and an output coupler. EDFAs are designed to be positioned periodically along an optical telecoms line and to boost the power of the signal without significant distortion. The pump diodes excite the active fibre just as in a fibre laser, and the signal light causes stimulated emission, increasing the number of 1550 nm photons leaving the device. As the photons produced are done so via stimulated emission, they are spatially and temporally coherent with the signal light; this is coherent amplification. EDFAs are the primary component used as repeaters in submarine and long distance fibre optic cables and are available in high output power, ruggedised packages. The gain or output optical power of an EDFA can be tuned and are often internally PID controlled using a monitor photodiode.

§2.6.1.3. Acousto-optic modulator

The last optical component for discussion is the Acousto-optic modulator (AOM); these are diffractive devices used for fast intensity modulation and frequency shifting. An AOM consists of a block of glass attached to a piezo-electric transducer, with the light to be modulated passing through the glass perpendicular to the direction of transducer operation. The piezo element is driven to expand and contract rapidly by applying an RF voltage, causing an acoustic wave to travel through the glass. This acoustic wave modulates the density of the glass block and with that, its refractive index. When the input light passes through the diffraction grating formed by the acoustic wave, it Brillouin scatters and is diffracted by an angle θ. Due to the regular structure in the glass, fringes are formed at integer multiples of the diffraction angle, giving bright spots at $m\theta$ where $m = ... - 2, -1, 0, 1, 2....$ The diffraction angle is a function of the ratio of the optical and acoustic wavelengths and is given by equation 2.140,

$$2\Lambda \sin(\theta) = m\frac{\lambda_0}{n}, \tag{2.140}$$

where Λ is the acoustic wavelength and n is the refractive index of the glass. Adjusting the RF power to the piezo transducer alters the proportion of power diffracted into the first order fringe, and thus if the first order fringe is collected, an AOM can be used to convert an electrical RF signal into an amplitude modulation of light. A diagram of a typical AOM is given in figure 2.19.

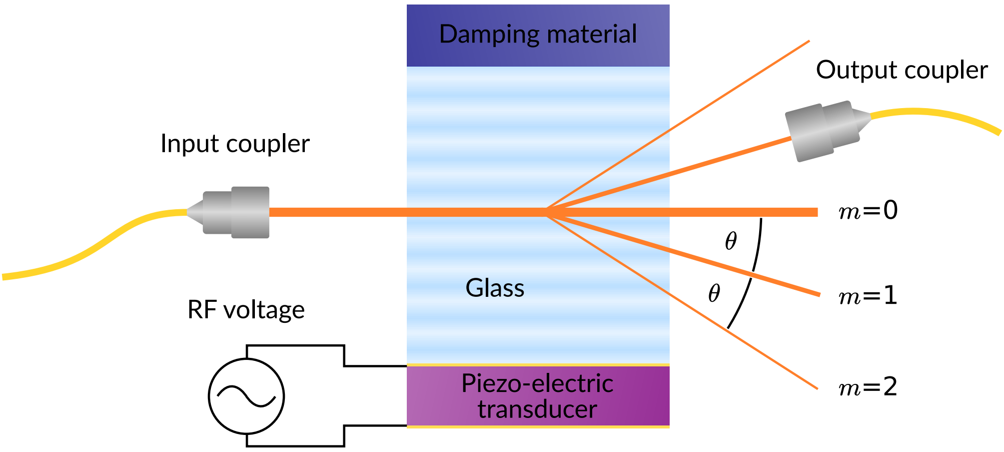

Fig. 2.19. *A typical AOM*

Often an acoustic absorber is positioned directly opposite the transducer so that the acoustic wave is not reflected back across the glass at the interface. Having a single travelling wave in the glass means that the signal light is diffracted from a moving surface and so is doppler shifted by the driving frequency of the AOM. Light diffracted into the m^{th} order fringe is frequency shifted to $\omega + m\omega_{\text{AOM}}$. This is how a frequency shifted reference field is created for use in the heterodyne measurement technique used in this thesis.

CHAPTER 3

Fibre Interferometry

In this chapter we will walk through the theory behind the operation of the experimental system presented in chapter 4. The discussion here will be not be specific to the system constructed but instead will explain the basic principles behind each part so that a full technical description can be given later. We will follow the information flow in the experimental system, starting with the optically trapped particle, moving on to the fibre interferometer and finishing with the signal processing and detection.

§3.1. Phase modulating light with a trapped nanoparticle

Information about the position of the trapped particle must be collected and transmitted to a detector in order to be processed. It has been discussed previously that the particle is trapped with a single focussed laser beam and the trap site is a region of very high intensity. The particle scatters light which can be used to infer the particle's position in the trap; this light is collected either by a refractive or reflecting optic, and in the case of the system used in this thesis, the scattered light is collected by the same parabolic mirror used to focus the trapping light (figure 4.16). From the collection optic the scattered signal light is transmitted to the signal processing system. As the signal light is almost completely monochromatic, as it travels from the collection/focussing optic to the particle and back again it accrues a certain phase, φ.

In §2.2.2, equation 2.16, we mentioned the Gouy phase that a beam lags by when propagating through a focus, and as the trapping beam is just such a focussed beam this effect must be taken into account. The focussed trapping light experiences this effect as it behaves as a Gaussian beam, however the scattered light does not, as Rayleigh scattered light is emitted spherically. The wavefronts of the scattered light do not go through a curvature reversal, as occurs in a Gaussian beam focus, and so do not accrue the extra phase. The total extra phase over the round trip is therefore given by

$$\varphi = (k + k') \times (x + L), \tag{3.1}$$

where k is the wavenumber of the trapping light, k' is the effective wavenumber of the Gouy shifted light, x is the particle position relative to its equilibrium position and L is the distance from the particle equilibrium position to the collection optic. φ is the phase modulation that is imparted to the signal light by the motion of the particle in the trap, and it means that as the position of the particle changes, the phase of the signal light at the collection optic changes. As discussed earlier, the particle is in a quadratic potential and so its position as a function of time, $\mathbf{x}(t)$, is harmonic, and we remind ourselves of the solution to the particle equation of motion from equation 2.122,

$$\mathbf{x}(t) = \mathbf{x}_0 \sin(\Omega t + \phi) . \tag{3.2}$$

Subsituting this into 3.1 gives the phase modulation as a function of time,

$$\varphi = (k + k') \times (\mathbf{x}_0 \sin(\Omega t + \phi) + L) \,. \tag{3.3}$$

This equation can be simplified as the absolute phase is not of any particular interest, it is how it changes over time relative to other oscillators that will be of interest shortly. For this reason we make the choice that $\phi = 0$ and we neglect L as it is static in this experimental geometry. The electric field of the signal light is given by

$$\mathbf{E}_{\mathrm{sig}}(t) = \mathbf{E}_{\mathrm{sig},0} \sin(\omega t + \varphi), \tag{3.4}$$

where ω is the angular frequency of the trapping light. The sine term in equation 3.4 can be rewritten as a complex phasor to give

$$\mathbf{E}_{\mathrm{sig}}(t) = \mathbf{E}_{\mathrm{sig},0} \exp\left[i(\omega t + \varphi)\right] . \tag{3.5}$$

§3.2. Homodyne

The signal light is modulated by the particle motion, however this is not yet experimentally useful as we can only measure intensity, a quantity not dependent on the phase of the electric field. In order to produce an intensity that depends on the particle position, we must use an interferometer. Specifically, in this thesis we use a Mach-Zehnder interferometer, a system that takes a single oscillating field (the trapping laser) splits it into two paths, one of which travels an extra (time dependent) distance to the trapped particle, causing a phase modulation. This field is scattered by the particle and then is recombined with the original field. When the two fields (E_{sig} and E_{ref}) recombine they no longer have equal phase as their optical path length is different. Treating the optical path length of E_{ref} as static, the relative phase between the two fields changes as a function of the particle position because the signal field has had to travel some extra fixed distance plus the distance from the particle to its equilibrium position. Figure 3.1 shows a schematic view of a Mach-Zehnder interferometer and the origin of the non-zero relative phase between the reference and signal fields.

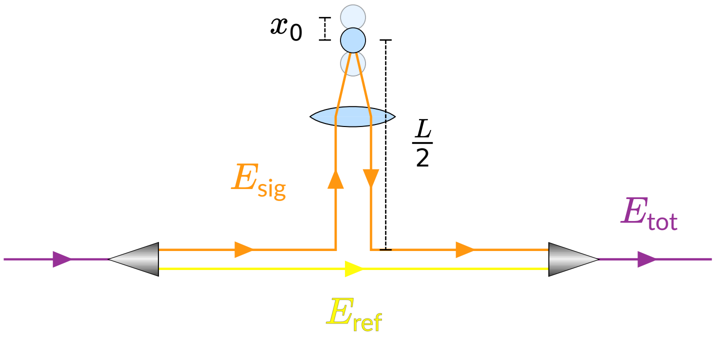

Fig. 3.1. *Mach-Zehnder interferometer in which light is phase modulated by the motion of a mobile scatterer.*

The paths taken by the optical fields in an interferometer such as this can be either as collimated beams through free space or confined by some form of waveguide. In this thesis, a fibre interferometer was used in which the fields were separated and recombined in an optical circulator (see chapter 4 for details). In a fibre interferometer used for levitated optomechanics the trapping light ($\mathbf{E}_{\mathrm{sig}}$) must leave the fibre and by focussed in order to trap the particle. The trapping light is scattered by the particle and this scattered field then becomes $\mathbf{E}_{\text{sig}}$. $\mathbf{E}_{\text{ref}}$ is guided by fibre for the entire process and recombines with $\mathbf{E}_{\text{sig}}$ in the circulator (§4.2.5).

When the fields recombine we take their sum (remembering they are complex) to produce $\mathbf{E}_{\text{tot}}$, and depending on the relative phase between $\mathbf{E}_{\text{sig}}$ and $\mathbf{E}_{\text{ref}}$ they will interfere constructively or destructively, producing a field with a magnitude that varies between $|\mathbf{E}_{\text{ref}} - \mathbf{E}_{\text{sig}}|$ and $|\mathbf{E}_{\text{ref}} + \mathbf{E}_{\text{sig}}|$. This resultant field can be made incident on a detector and its intensity measured, and found to produce a signal, V, that varies between $|\mathbf{E}_{\text{ref}} - \mathbf{E}_{\text{sig}}|^2$ and $|\mathbf{E}_{\text{ref}} + \mathbf{E}_{\text{sig}}|^2$. This method for detecting a phase modulation is known as Homodyne detection where the prefix “homo” denotes that the two fields being mixed are of the same frequency as they originate from the same laser. The signal at a detector is the sum of the fields,

$$V = |\mathbf{E}_{\text{tot}}|^2 = |\mathbf{E}_{\text{ref}} + \mathbf{E}_{\text{sig}}|^2, \tag{3.6}$$

with $\mathbf{E}_{\text{ref}}$ defined below,

$$\mathbf{E}_{\text{ref}}(t) = \mathbf{E}_{\text{ref},0} e^{i\omega t}. \tag{3.7}$$

Using equation 3.5, we can substitute these in to get equation 3.8.

$$V = \left|\mathbf{E}_{\text{ref},0} e^{i\omega t} + \mathbf{E}_{\text{sig},0} e^{i\omega t} e^{i\varphi}\right|^2, \tag{3.8}$$

setting $\mathbf{A} = \mathbf{E}_{\text{ref},0} e^{i\omega t}$ and $\mathbf{B} = \mathbf{E}_{\text{sig},0} e^{i\omega t}$ for convenience, we continue to expand and obtain,

$$V = |\mathbf{A}|^2 + |\mathbf{B}|^2 + \mathbf{A}\mathbf{B}^* e^{-i\varphi} + \mathbf{A}^*\mathbf{B} e^{i\varphi}, \tag{3.9}$$

$$V = A^2 + B^2 + 2AB\cos(\varphi), \tag{3.10}$$

implying the amplitude of signal V is

$$V_{\text{max}} - V_{\text{min}} = 4AB. \tag{3.11}$$

§3.3. Phasor diagram

In the previous subsection we saw how the signal from an interferometer can be be constructed from a phase modulated signal field and a reference field. Equation 3.8 gives the expression for the detector signal, but can be somewhat opaque when attempting to understand the origin of features in an experimentally recorded signal. A more useful method is to plot the phasors involved as vectors in the complex plane, where the real component represents the physical field. Using this method $\mathbf{E}_{\text{tot}}$ is just the vector sum of $\mathbf{E}_{\text{sig}}$ and $\mathbf{E}_{\text{ref}}$ and V is the square of the length of vector $\mathbf{E}_{\text{tot}}$. To make this illustration more intuitive, we can put ourselves in the rotating frame of the laser frequency ω, meaning that $\mathbf{E}_{\text{ref}}$ is a stationary vector with an arbitrary initial phase (direction) that we can set to be along the real axis. We can also normalise the magnitudes of the fields involved to the magnitude of $\mathbf{E}_{\text{ref}}$, meaning it becomes of length 1. From this point, the relative length of $\mathbf{E}_{\text{sig}}$ and $\mathbf{E}_{\text{ref}}$ is arbitrary and according to the design of the physical system, however its sensible to use fields of comparable magnitude in order to increase the signal to noise ratio of V. Figure 3.2 shows an example phasor diagram with the relevant quantities labelled.

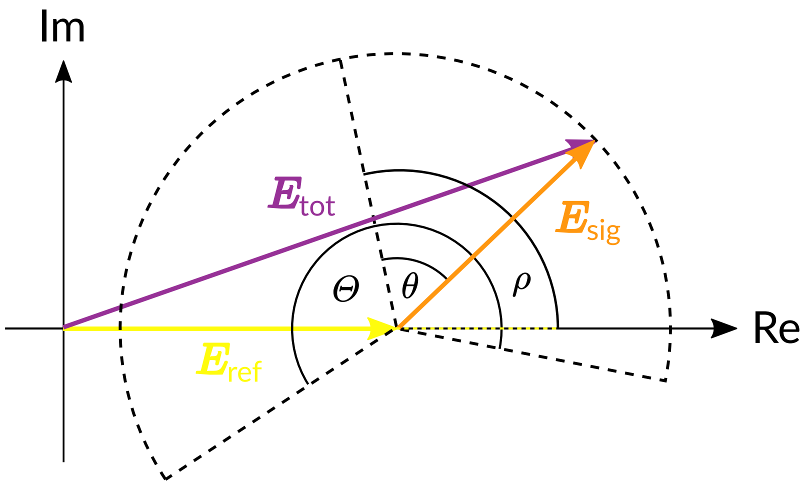

Fig. 3.2. *Phasor diagram showing how* $\mathbf{E}_{\mathrm{tot}}$ *is the vector sum of* $\mathbf{E}_{\mathrm{ref}}$ *and* $\mathbf{E}_{\mathrm{sig}}$*. The phase of the particle motion and the relative phases of* $\mathbf{E}_{\mathrm{ref}}$ *and* $\mathbf{E}_{\mathrm{sig}}$ *are represented graphically by* θ *and* ρ *respectively.*

The phase modulation of the signal field corresponds to an angle change when viewed on the complex plane; and therefore a sinusoidal phase modulation, as is the case for the oscillating nanoparticle, creates a sinusoidally oscillating vector. $\mathbf{E}_{\mathrm{sig}}$ oscillates through some angle Θ, sweeping out a circular sector. At time t, $\mathbf{E}_{\mathrm{sig}}$ is at an angle θ to the centre of the sector swept out and due to the harmonic nature of the particle motion, $\theta = \Theta \sin(\Omega t)$. There will also be a non-zero phase offset between $\mathbf{E}_{\mathrm{sig}}$ and $\mathbf{E}_{\mathrm{ref}}$ due to the extra fixed optical path length L travelled by the reference field. This phase offset results in an angle offset ρ, proportional to the path length difference. If L is not static in time, either due to thermal or mechanical optical path length drift, then ρ will drift stochastically.

As $\mathbf{E}_{\mathrm{sig}}$ oscillates back and forth, the length of $\mathbf{E}_{\mathrm{tot}}$ changes and therefore so does V. This can result in a signal that shows unexpected features, especially if the vector $\mathbf{E}_{\mathrm{sig}}$ sweeps through being parallel or anti-parallel to $\mathbf{E}_{\mathrm{ref}}$. It is important to note that the signal V is never exactly sinusoidal and depending on ρ and Θ, may contain large higher frequency components. Figure 3.3 shows a vector diagram, the time series data for $x(t)$ and $V(t)$, as well as their respective power spectra.

Part A of figure 3.3 shows that as the sector is swept out by $\mathbf{E}_{\mathrm{sig}}$, there is a maximum and minimum value for the magnitude of $\mathbf{E}_{\mathrm{tot}}$, these are the radii of circles centred at the origin and are shown as dashed lines. The same dash lines in part B show the corresponding maximum and minimum values for V. If the sector crosses the real axis then $\mathbf{E}_{\mathrm{tot}}$ passes through a minimum or maximum depending on the direction of alignment. This is what causes the 2Ω frequency components, and when the sector is symmetric about the real axis the second harmonic can be more prevalent than the fundamental frequency. As ρ drifts, the power balance between odd and even order harmonics drifts and can be seen in the changing PSD over time.

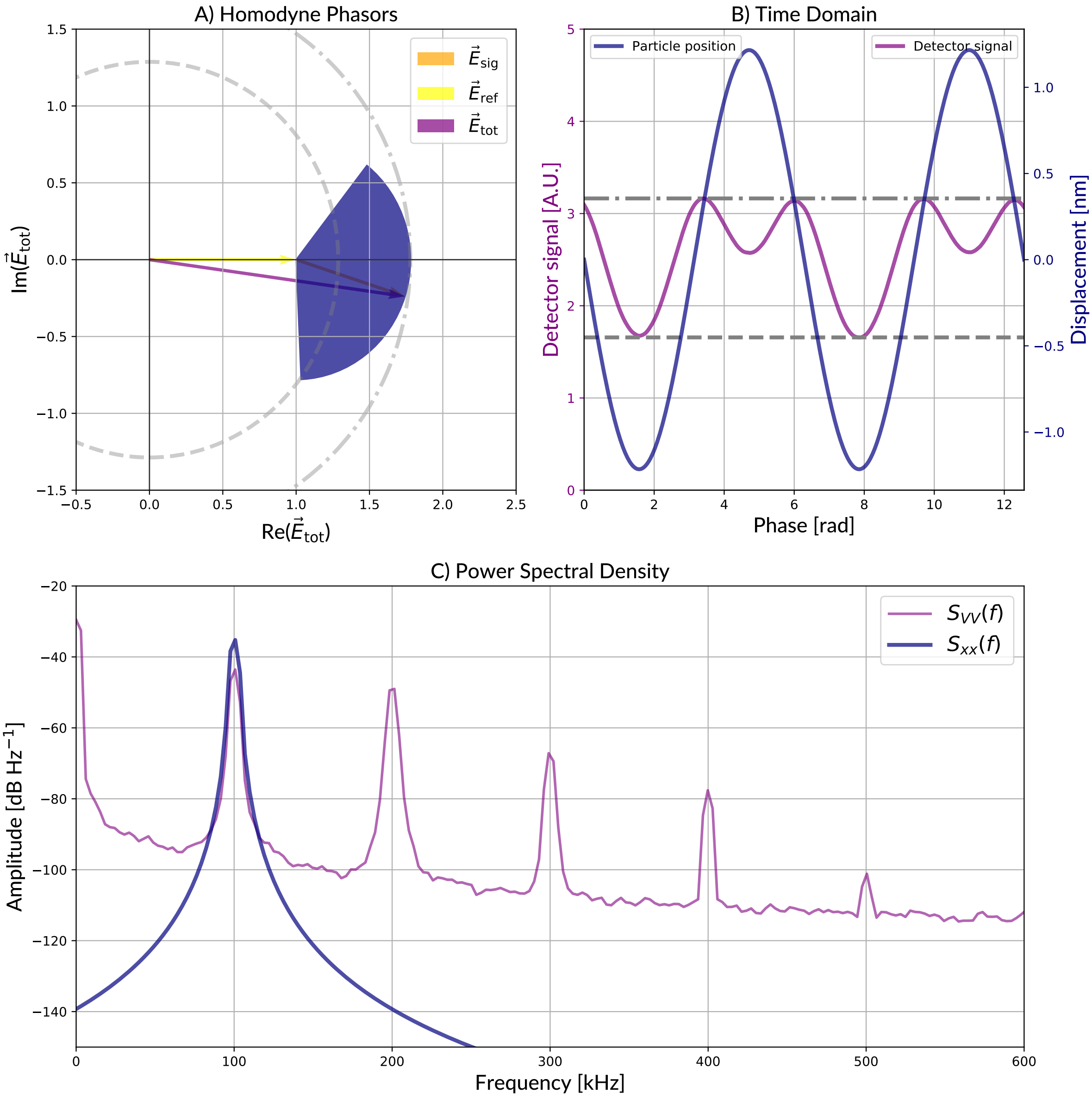

Fig. 3.3. *Homodyne phasor signals. A) The complex plane phasor representation of the Mach-Zehnder interferometer. B) Time domain signals for both the particle position and the detector signal. C) PSD of the particle position and detector signal over time.*

Its possible to simulate the behaviour of the vectors involved in this description (equation 3.8) and incorporate elements of stochastic drift and random starting conditions. The simulated detector signal can be plotted as a function of time and compared to experimentally recorded detector signals. Figures 3.4 and 3.5 each show 3 examples of $V(t)$ time traces, simulated and experimental respectively.

The details of the experimental setup used to produce the experimental data are given in chapter 4, the traces are included here to validate the phasor description of the phase modulation by comparison with the simulated traces.

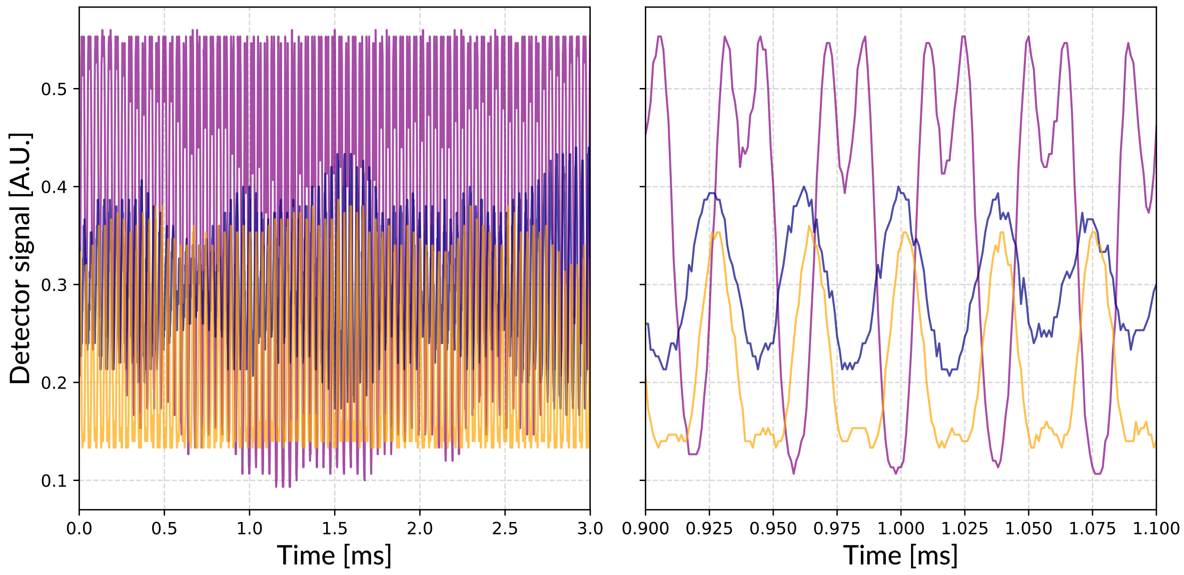

Fig. 3.4. *Experimental interferrogram - The two subplots show the same data on different timescales. Large second harmonic components can be seen as well as the non-sinusoidal nature of the signal.*

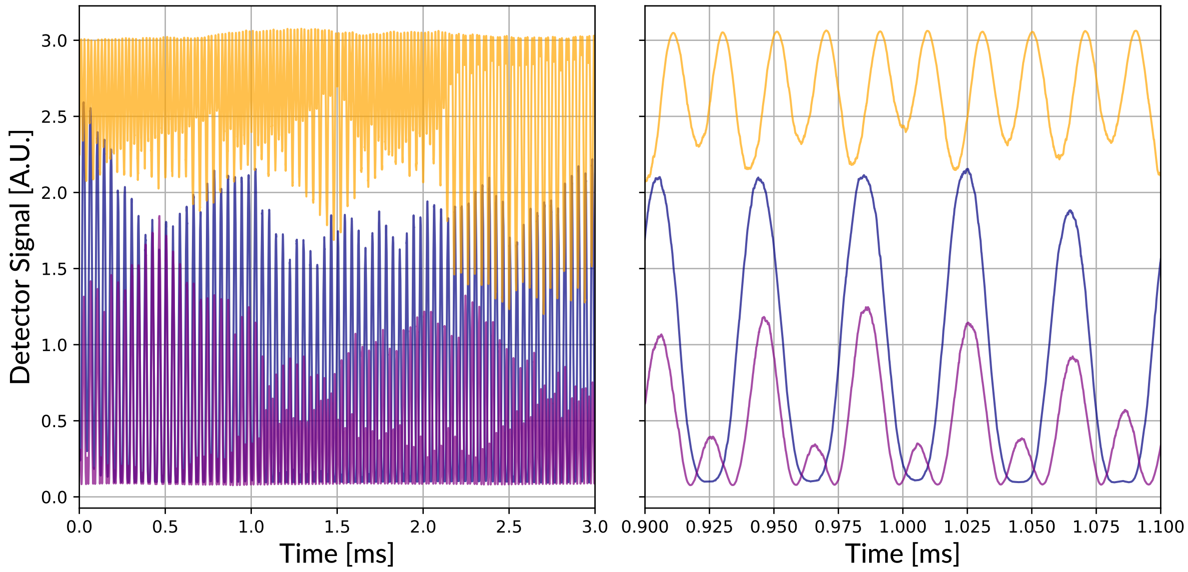

Fig. 3.5. *Simulated interferrogram - Simulation using comparable physical parameters gives qualitatively very similar behaviour. Traces above of the same colour do not share any characteristics specifically, colours are only to distinguish between individual curves on each plot.*

Thinking about the particle using this graphical based logic can allow certain conclusions to be drawn relatively easily. For example in figure 3.4, one can deduce that when the purple trace was taken, the particle was oscillating with a larger amplitude than for the navy trace. The purple trace can only have been created from the oscillation of E_{sig} through a circular sector subtended by a larger angle than for the navy trace, corresponding to a larger phase modulation of the light and therefore a larger amplitude of oscillation. At times when the detector signal is seen to "fold back" at both its maximum and minimum extents, it must be the case that Θ is larger than π radians, and therefore the amplitude of the particle's motion must be larger than $\lambda/2$. When no double fold back is seen, this can be used as an upper bound on the oscillation amplitude.

Up until this point in this section, the discussion has been of a homodyne system, i.e. mixing two fields of equal frequency but differing phase in order to measure the particle position. In the next section an improvement to the simpler homodyne case will be introduced.

§3.4. Heterodyne

As mentioned in §3.2, homodyne measurements produce a double-sided power spectrum centred at 0 Hz, where the negative frequencies reflect about the origin and interfere with the positive frequencies, with a fluctuating relative phase.

In levitated optomechanics experiments that use a forward-scatter geometry, such as those that using microscope objectives or aspheric lenses to focus the trapping light, the signal and reference fields used to perform interferometry travel the same path, with the phase modulation to the signal field caused only by the Gouy shift experienced by light travelling through the focus. In contrast, in a back-scatter geometry, such as with the parabolic mirror used in this project, there is a macroscopic path length difference between the signal and reference fields that are combined to produce an interferometric measurement. This path length difference represents a constant phase offset between these two fields. In this project, this constant offset is the length of the fibre arm between the circulator and particle trap site (see chapter 4). In any real-world situation, there are thermal fluctuations that cause this extra optical path length to drift in magnitude as the fibre contracts and expands slightly. This causes the "constant" phase offset between the signal and reference fields to drift over 10 second timescales, creating the fluctuating relative phases of the positive and negative homodyne sidebands.

The relative phase between positive and negative frequencies means they interfere either constructively or destructively, leading to a changing amplitude of odd and even order peaks in the power spectrum over time. Altering the shape and amplitude of spectral features in this way loses information about the particle motion. In order to avoid this kind of information loss we can mix fields in such a way as to shift the power spectrum so that it is centred on a frequency greater than 0. This is achieved by instead of mixing two fields with the same frequency, mixing two with different frequencies. Practically, we acomplish this by frequency shifting the reference field and then recombining it with the signal field as in the homodyne case. This is then called a heterodyne measurement.

Heterodyne measurement makes use of the trigonometric identity,

$$\sin(\theta_1)\sin(\theta_2) = \frac{1}{2}\cos\left(\theta_1 - \theta_2\right) - \frac{1}{2}\cos\left(\theta_1 + \theta_2\right), \tag{3.12}$$

where we substitute in $\theta = 2\pi f t$, in order to express the problem in terms of the frequencies of two fields, f_1 and f_2. This gives

$$\sin\left(2\pi \mathrm{f}_1 \mathrm{t}\right)\sin\left(2\pi \mathrm{f}_2 \mathrm{t}\right) = \frac{1}{2}\cos\left[2\pi\left(\mathrm{f}_1 - \mathrm{f}_2\right)\mathrm{t}\right] - \frac{1}{2}\cos\left[2\pi\left(\mathrm{f}_1 + \mathrm{f}_2\right)\mathrm{t}\right], \tag{3.13}$$

where the terms on the right hand side represent two distinct, seperable signals at the difference and sum frequencies of f_1 and f_2 respectively.

In this project, f_1 and f_2 are the signal light from the particle and a reference frequency, shifted by Δ, such that the signal and reference field frequencies are ω and $\omega - \Delta$, the power spectrum is generated at the sum and difference frequencies of the two, the difference frequency being simply Δ. Typically this frequency shift is achieved using an acousto-optic modulator (AOM, covered in §2.6.1.3) at a frequency of around 80 MHz, shifting the Heterodyne spectrum to 80 MHz. This frequency is higher than is desirable, as it requires high bandwidth electronics for data capture and a greater number of samples per second, meaning a shorter time series will use up the total available memory. Time series over a larger number of particle oscillations will produce a more accurate PSD and so for this reason, this 80 MHz signal is downshifted. The signal is downshifted to δ by mixing it with a local oscillator (LO) at $\Delta - \delta$, giving a spectrum at the difference frequency ($\Delta - [\Delta - \delta] = \delta$). This means δ can be chosen in order to position the heterodyne spectrum at will, away from other interfering signals and at a frequency well suited to the signal processing equipment to be used, typically a few MHz. This process means the negative frequency reflection no longer occurs and so negative and positive frequencies do not interfere, maximum information about the particle motion is retained and the spectrum is more stable in time. As a disadvantage to this process, the information about the particle position is now encoded in two separate spectral features that must be treated in the analysis process rather than a single peak, however this is a relatively minor inconvenience.

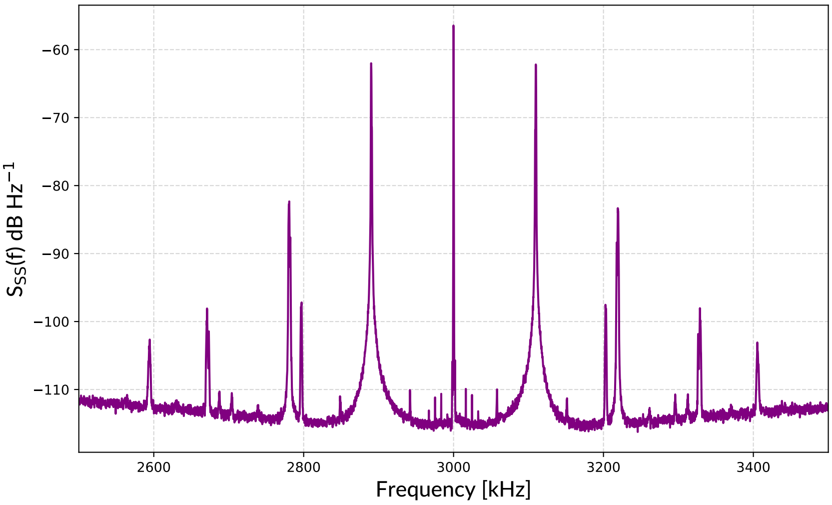

Fig. 3.6. *Heterodyne PSD - The first to fourth harmonics of the particle motion in the z direction are visible as well as lower amplitude peaks corresponding to the motion in the x and y direction. The smallest peaks are linear combinations of the 3 natural frequencies in x, y and z.*

The process above gives a Heterodyne spectrum similar to the homodyne case but double sided, as can be seen in figure 3.6. The large central peak is a result of the downshifting process and does not contain information about the particle motion. The largest sidebands are the fundamental frequency of particle motion in the z direction, and subsequent further sidebands can be seen at integer multiples of this spacing, moving away from the central peak in both the positive and negative directions. There are also some much smaller peaks at frequencies other than the multiples of the z direction frequency, these represent the particle motion in the x and y directions, and their relatively small amplitude is due to the experimental system's deliberate insensitivity to this motion. The fundamental x and y frequencies are approximately double the fundamental z frequency, due to the much smaller trap potential radius in these directions, causing a much higher trap stiffness.

One of the main aims of this thesis is to build and optimise a levitated optomechanics system for maximum information collection. For this reason heterodyne was used over homodyne for the vast majority of the work presented from here onwards. The more practical elements of the use and implementation of heterodyne measurement will be covered in chapter 4. In figures 3.7 and 3.8 below, homodyne and heterodyne spectrograms are compared, highlighting the differences between the two approaches. In figure 3.7, fluctuations can be seen in the amplitudes of the peaks over 4 second time scales. This is the undesireable fluctuation that can be avoided by using heterodyne measurement, which can be seen in figure 3.8, and does not show this same slow drift. Faster fluctuations of the amplitude of the peaks in both the homodyne and heterodyne cases are not affected and are accentuated here by the spectrogram process which breaks the time series data into small divisions before calculating a PSD. When viewing this data as a power spectrum rather than specrogram, these small fluctuations are averaged out and we have a spectrum as seen in figure 3.6.

The datasets used to create these homodyne and heterodyne spectrograms happen to be from experimental situations where the particle trap frequency, and hence the peak spacing in the PSD are significantly different. In figure 3.7 the fundamental frequency of the motion of the particle in the z direction is approximately 25 kHz, an uncharacteristically low value for this setup. The low trap frequency is due to the usage of low trapping laser power ($\sim$200 mW). In the homodyne spectrogram in figure 3.8, the trap frequency is around 80 kHz, leading to the much larger separation of the peaks on the plot y axis. The difference in these trap frequencies does not affect the stability of the odd and even sidebands when comparing homodyne to the more stable heterodyne case, the behaviour that these plots are intended to illustrate.

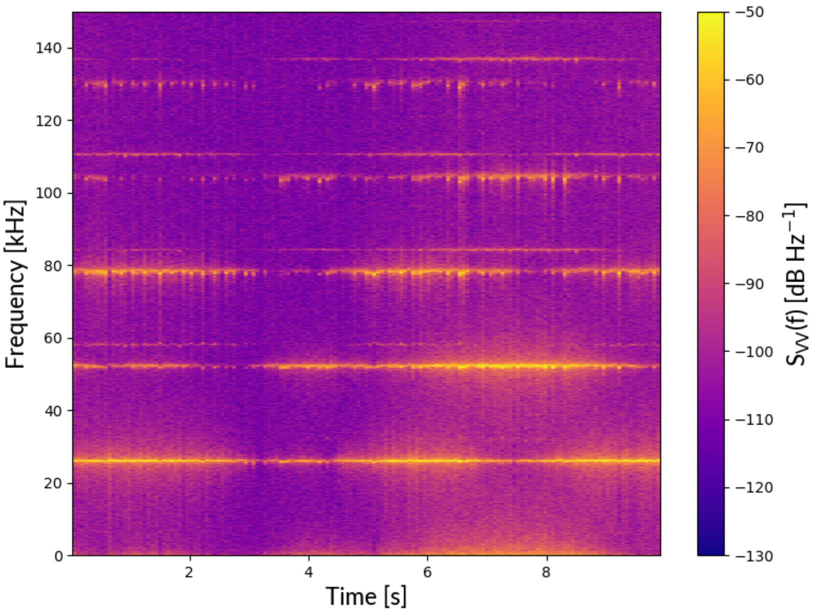

Fig. 3.7. *Homodyne spectrogram - This can be seen to fluctuate with time. The anti-correlated behaviour of odd and even order peaks is visible.*

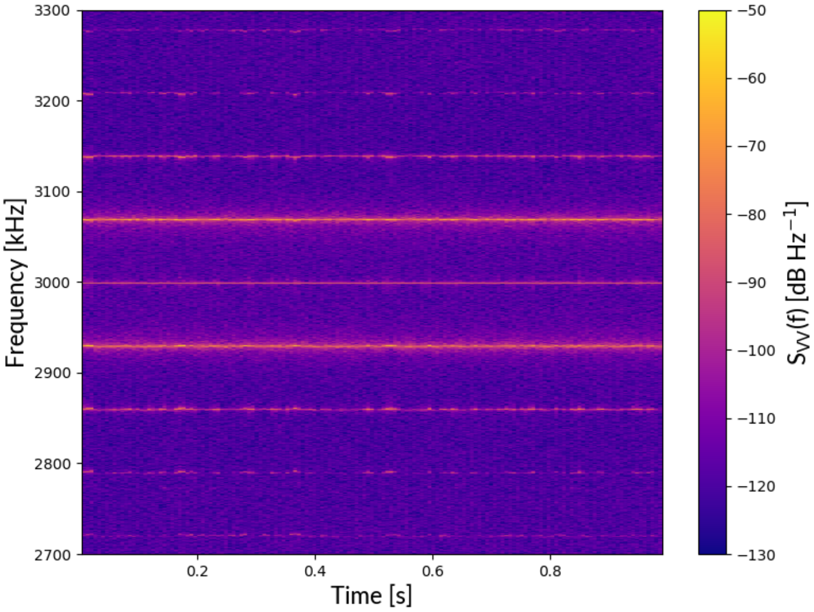

Fig. 3.8. *Heterodyne spectrogram - A double-sided spectrum where peaks no longer fluctuate in amplitude over time. This technique gives greater stability and avoids the loss of information resulting from interfering positive and negative sidebands. Although created from a shorter duration sampling, the above is representative of behaviour on the same timescale shown in figure 3.7.*

This concludes the background and theory chapters; in the next chapter the more technical details of the experimental system built during this project will be given.

CHAPTER 4

Experimental Setup

This chapter will detail the experimental system constructed as part of this project. This discussion will include design considerations, hardware specifications and pictures/diagrams of the different subsystems. The setup description will link back to the aims of the thesis given in §1.4 and how each choice helps to enable their fulfillment, as well as the inevitable tradeoffs that had to be made.

§4.1. System Overview

The experimental system can be divided into three main subsystems, each containing multiple components. These are the optics, vacuum system and signal processing. These three subsystems will be explored in turn, evaluating the hardware in each. In order to understand how the system works, its useful to look at an overview of the system and how the subsystems tie together. Figure 4.1 shows how the information/influence flows from one system to another in the setup, and is useful as a reference when discussing where a specific component fits into the system later.

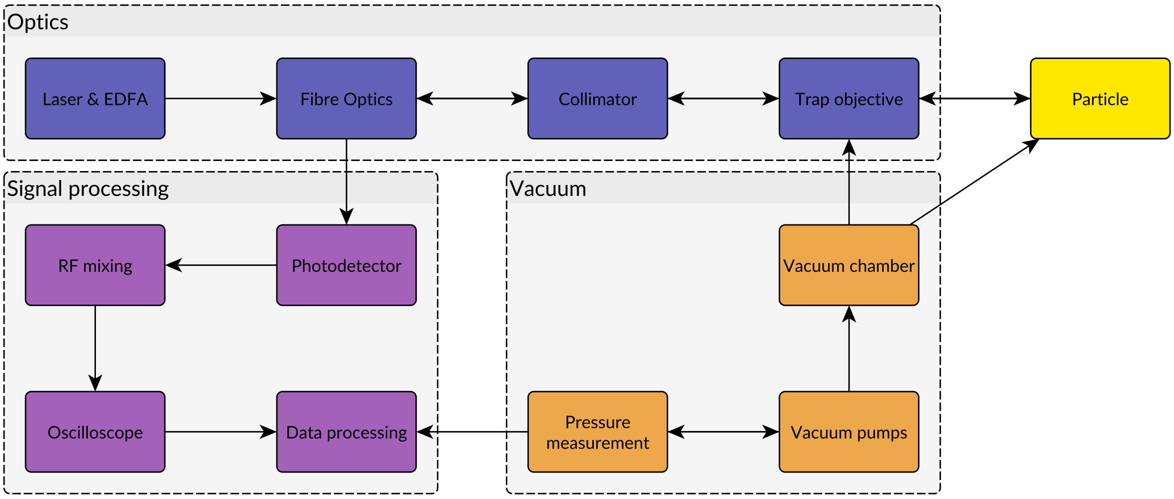

Fig. 4.1. *Schematic view of setup subsystems. Components are grouped according to subsystem and arrows show the flow of information.*

§4.2. Optics

The optics subsystem has two objectives:

1. Produce a stable 1550 nm TEM_{00} laser beam of an appropriate power for trapping a silica nanoparticle and form it into a very high NA waist where the particle can be trapped.

2. Capture the Rayleigh scattered light from the trapped particle and interfere it with another field for either homodyne or heterodyne measurement, then measure the intensity of the resultant field.

Figure 4.2 shows a diagram of the optical components and the fibre network that connects them; in this section we will walk through these components one by one, beginning with the optical fibre itself.

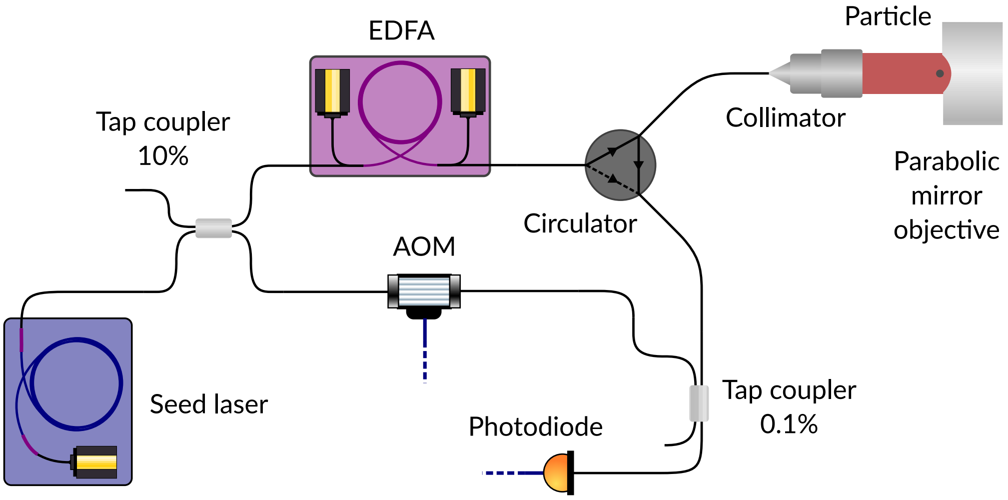

Fig. 4.2. *The optics subsystem setup for heterodyne measurement*

§4.2.1. Fibre

The optics in this project are almost entirely fibre coupled and so physical arrangement and alignment is less of an issue than might be the case with a free-space optics system. The decision to use a fibre optics system was possible as this setup was built from scratch during the course of this project, and so there was no need to be compatible with a pre-existing system, as is often the case.

The choice to use fibre optics comes with a number of advantages, the foremost of which is one of practicality for the experimenter; as when two components are connected together they remain aligned, negating the need to spend time realigning the system, an activity that can take an appreciable time for a free space experiment. Another practical advanage is the removal of the risk of accidental beam interruption that would cause the particle to be released from the trap. The optical system can be worked on freely and even rearranged without needing to be careful not to block the beam and release a particle which would create more work for the experimenter and cause great frustration!

Using a fibre trapping system also enables the more efficient transfer of signal light from the trap objective to the active area of a photodetector, a step that allows us to retain the valuable information about the particle position. This is an important difference if, as a research community, we intend to reach the standard quantum limit of particle position detection. This advantage is shared by the parabolic mirror trap, which collects a full π steradians of Rayleigh scatter in our case, rather than the smaller angular subtense of a microscope objective. This could be further improved by using a deeper parabola, such as in [166, 167].

Fibre trapping does come with its disadvantages however, mainly the increased optical path length drift relative to free space systems. This occurs as there are multiple metres of solid medium in which the light in the interferometer is travelling, all of which can be at a fluctuating temperature. This increases the distance travelled by the light and therefore the phase of the electric field when the two arms of the interferometer are recombined. In a free space system this distance is dictated by the spacing between mirrors, which can change with environmental temperature, but to a much lesser degree. The flucutuating density of the air in which the free space beam travels also has an effect, but realistically the laboratory air temperature is likely to be very homogeneous.

The science goals of this project require a low-noise, stable setup to enable high precision measurement, meaning the appropriate wavelength is 1550 nm, as used in fibre telecoms systems. It follows that the appropriate fibre to use for building such a system is telecoms fibre. The most commonly used telecoms fibre is “SMF28” [164], produced by Corning Inc. A variant of this, SMF28e+, was used to link optical components and to carry both the trapping and signal light in the experiment. SMF28e+ does not differ from SMF28 in any way that is significant for this experiment; it is slightly lower loss, features a polymer coating and was used as it is the most readily available variant of this class of fibre. The SMF28 family of fibres are single mode silica fibres, designed to carry 1550 nm light pulses with minimal loss. Figure 4.3a shows an optical setup made using SMF28 fibre, and figure 4.3b shows the cross section of standard SMF28 fibre.

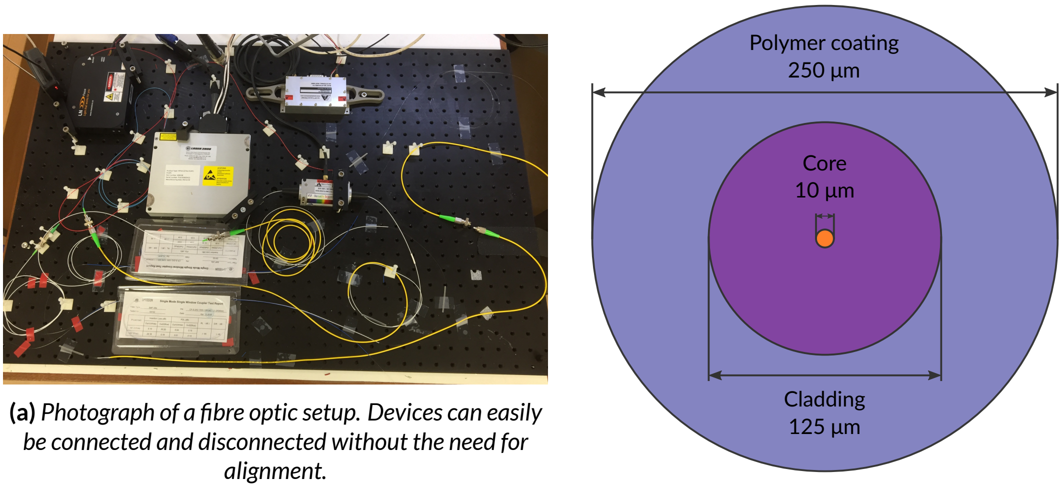

(a) *Photograph of a fibre optic setup. Devices can easily be connected and disconnected without the need for alignment.*

(b) *Cross-section of SMF28 fibre*

Fig. 4.3. *Setup illustration and cross-sectional diagram of the fibre optics used in this project.*

§4.2.1.1. Advantages

SMF28 is an appropriate choice as it is the fibre upon which comercially available fibre optic hardware is designed and manufactured, meaning the links between devices can be made with no mismatch in the fibre shapes when spliced, using a fibre that is cheap to purchase. While dispersion is not an issue on the fibre length scales used in this experiment, the very low optical losses present in SMF28 mean that a negligible amount of laser power is lost to heat. This allows the full power range of the EDFA to be used without significant heating of fibre coupled components. In optical trapping it can be useful to have the option of using high optical powers, either to compensate for percentage losses in optical components or to maximise trap stiffness.

Stimulated Brillouin scattering (SBS) occurs when a medium has a slightly varying refractive index in the direction of light propagation. If the refractive index variations are to some degree periodic, light will partially reflect from the boundary and over many periods of the refractive index fluctuation the back reflected light field can accumulate considerable amplitude. SBS requires some initial refractive index fluctuation but can become self sustaining as phonons are created in the material when light scatters inelastically from a fluctuation. The phonons then add to the material lattice wave and the amplitude of refractive index modulation increases, leading to a feedback process. High optical powers and materials with pre-existing refractive index fluctuations over long optical path lengths can both cause SBS, which can lead to appreciable laser power being back reflected into the laser cavity, possibly causing damage. SMF28 fibre can carry over 5 W of optical power continously, and does not exhibit SBS due to the very low variation in refractive index along the fibre. In our experiment only of order 10 m of fibre is in use, an insufficient distance for SBS to become a problem.

Due to the ubiquity of SMF28, tools designed to increase its ease of use are readily available, and have been ruggedised for use in field applications. This includes fibre splicers and cleavers, used to join two fibres into a single continuous piece of glass. In this setup fibre splicing was used extensively to connect components without light needing to leave the fibre. This decreases losses enormously when compared to a simple "butt coupler" and avoids the heating associated with such losses. Splicing also completely removes the need for alignment, saving time and making the system more reliable. Fibre cleaving is the process of cleanly cutting a fibre either so it can then be spliced or so that light leaves the fibre tip without distortion.

In summary, SMF28 is the current standard in telecoms wavelength optical fibre, it is compatible with most off the shelf devices that one might want to use and its cost makes it essentially disposible. Years of research and development for use in the telecoms industry mean that the technical specifications of SMF28 far exceed the needs of this project, making it the natural choice. It does however come with a few drawbacks, as we shall see below.

§4.2.1.2. Disadvantages

There are a number of tradeoffs when choosing to use SMF28 fibre, the first being that nominally it is not polarisation maintaining (PM). This means that even if the polarisation of light leaving the fibre laser is static, it can vary over time when measured at the output of the fibre optic system. This effect, like most of the disadvantages of fibre is made worse the longer the length of fibre in use. In this particular levitated optomechanics experiment this wasn't an issue as the polarisation of the trapping laser only affects the x and y motion of the particle; breaking the x-y symmetry of the trap site. As this system is optimised for examining the motion of the particle in the z direction, non-PM fibre is of little consequence. The effects of non-PM fibre can be seen in some of the later particle spectrograms, where the small x and y peaks can be seen to drift in frequency over time as the shape of the trap site changes due to polarisation drift.

Another disadvantage that becomes increasingly severe with increasing path length is the thermal length drift that occurs in a solid medium such as glass. Due to subtle temperature fluctuations in the glass making up the fibre, the density of different regions of the fibre will fluctuate over time. This changes the overall length of the fibre, and when the length change is comparable with $^{\lambda}/_{10}$, there is an appreciable phase modulation of the light traversing the fibre. In the context of this experiment this must be taken into account when considering the recombination of fields in the interferometer; fibre lengths of 10 m can easily experience length changes of a micron or more. This slow, stochastic phase modulation is taken into account when simulating the phasor behaviour in figure 3.5, as it is clearly present in the experimental version. This effect is more noticeable as the light used in this project almost entirely propagates in a solid medium that is more susceptible to this kind of length change, although its worth noting that the effect does also present in free-space optics travelling through air. Practically, the length change in the setup was minimised by securing fibres to a large thermal mass, the optical table, in order to decrease the length drift due to thermal effects as well as mechanical bending losses.

Bend losses are another downside to SMF28 as it is designed to be used with multiple layers of protective coating, ranging from a thin polymer coating through to metal and glass fibre armour plating. This means that SMF28 is not engineered to be tolerant to bend radii of less than approximately 10 cm [164]. When wound tighter than this, large (>0.5 dB) macrobend losses are incurred with a risk of breaking the brittle core and cladding material. The risk of breaking is increased if the region contains a stress concentration such as an imperfection in the glass or a splice point.

§4.2.1.3. Splicing

Fibre splicing is a useful technique for joining two fibres without an interface between them that might cause loss. In fibre splicing the two fibres to be joined are stripped of their protective layers so that only the glass cladding and core are left exposed. The fibres are cleaned and cleaved such that the faces to be spliced together are flat, parallel to one another and normal to the axis of the fibre. The fibres are positioned colinear under a microscope and an electrical discharge is used to heat and melt the glass, just as the fibres are moved together. This naturally forms a single continous fibre with very little deviation from the normal fibre cross-section, resulting in a very low loss join (typically between 0.05 and 0.1 dB [168]). Splicing is used in fibre telecoms to join fibres at junctions or to repair damaged sections. In this project, a fusion splicer was used to assemble the optical system depicted in figure 4.2, and we ignore losses resulting from splices as they are small compared with those due to loss in other components such as the circulator and AOM. Images of the splicer and cleaver are given in figure 4.4, both of which are relatively inexpensive, comercially available components. Figure 4.5 shows before and after images of the splicing process.

(a) *Fibre cleaver - used for preparing the end facet for splicing, we used a Fujikura* `CT-30`

(b) *Fibre splicer - used for joining fibres, our device is a Fujikura* `FSM-18S`

Fig. 4.4. *Fibre handling hardware*

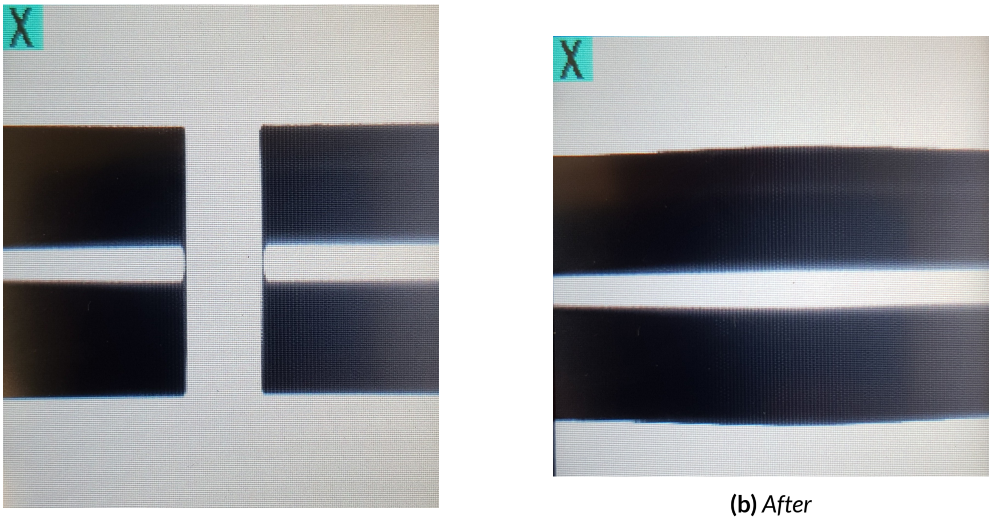

(a) *Before*

(b) *After*

Fig. 4.5. *Fibre fusion splicing - fibre is joined under a microscope so that it forms a continuous piece of glass. The splice point is visible only as a small region of slightly increased radius and losses were not measurable with the available photodetectors.*

Having covered the fibre itself, we now examine the various hardware used in the optics subsystem; starting with the fibre seed laser.

§4.2.2. Seed laser

The seed laser's purpose is to produce a low power, low noise light field that can be amplified later. The seed laser is a 1550 nm fibre laser with low phase and relative intensity noise (RIN), designed for use in telecoms. The seed laser is produced by LN Solutions, model `LN-Focus-32`, and has a stated linewidth of less than 500 Hz. The RIN is stated to be less than -150 dB between 500 kHz and 1 MHz; its important that this high frequency noise is low as the EDFA used to amplify the seed laser acts as a high pass filter with a cut off frequency of approximately 100 kHz. Any RIN in the trapping laser beam results in a changing local intensity at the particle trap site and therefore a frequency shift of the particle motion. When particle position data is recorded over a time period this frequency shift broadens spectral features and leads to loss of information about the particle motion. The seed laser does not have an adjustable power output and was measured to be approximately 60 mW, varying by 1% over timescales of around a minute. This power level is ideal for our application as a 10% tap coupler can be used in order to reduce the optical power to just under 6 mW, which is then connected to the input coupler of the EDFA. The other 90% of the optical power produced by the seed laser can either be dumped or connected to an AOM for frequency shifting when using heterodyne measurement.

The seed laser package itself was developed for field applications in fibre telecoms and as such is completely modular and ruggedised. It was chosed for its low RIN, narrow linewidth and relatively low cost ($\sim$£6000). The chosen model of seed laser performed as expected and there have been no real disadvantages to this choice of hardware.

The seed laser RIN is below the white measurement noise floor apart from some narrow spectral features that are likely caused by electrical noise. The shot noise level is at -160 dB for this power and wavelength combination. At the trap frequency the RIN is below the noise floor, which is white at the same level shown in figure 4.6b.

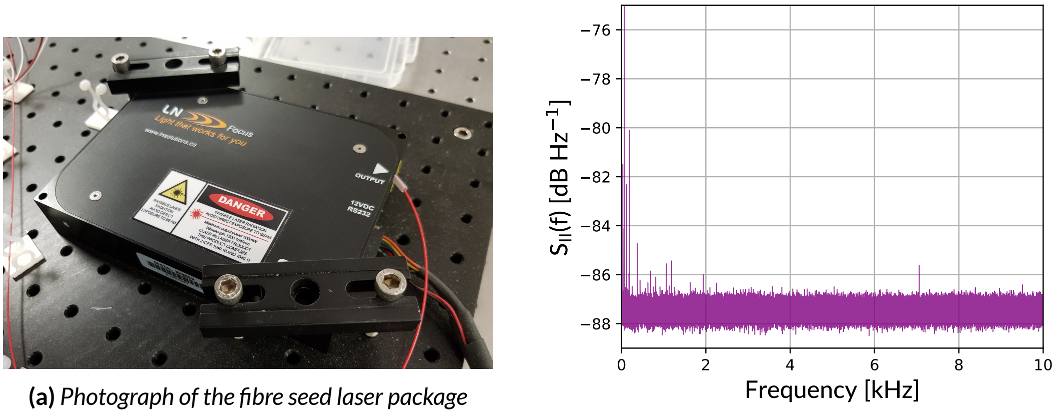

(a) *Photograph of the fibre seed laser package*

(b) *Seed laser RIN spectrum*

Fig. 4.6. *Seed Laser photo and RIN specification*

§4.2.3. EDFA

The EDFA takes the low power seed laser field and optically amplifies it up to a maximum power of 5 W. Due to the coherent nature of the amplification in an EDFA, the output beam retains the desirable characteristics of the high quality seed laser, and amplifies the field to a power that can be used to optically trap a nanoparticle. The product used in this project was the BKTEL `HPOA-S`, with a maximum optical power of 5 W. This device is stated to introduce 5.5 dB of noise during amplification, 3 dB of which is physically unavoidable due to the mechanism through which optical amplification is achieved [169, 170]. This product is also designed for field deployment and so is housed in a robust and miniaturised package that is highly convenient for laboratory use. The amplifier has a gain bandwidth of 30 nm, centred on 1550 nm, the wavelength at which it was used.

The EDFA has several modes, all of which are different methods for selecting the desired output power. The EDFA has internal monitor photodiodes that measure the input and output power, and are used to feedback to the pump diode current to maintain the desired output power level. For the work presented in this thesis the amplifier was almost always in a “constant power” mode in which the current to the diode is automatically adjusted to keep the output optical power constant. The power drift was meaured to be 0.5% in the relevant operating range, with power fluctuations occurring on time scales around 5 minutes, likely due to thermal effects inside the device. The desired output power is selected over a serial data connection that can also be used to interrogate the devices status, monitor photodiode readings, internal temperature etc. In our laboratory this was permanently connected to a Raspbery Pi that regularly requested all the EDFA internal state information and logged it to a file on the network. This means that any unusual behaviour can be investigated retroactively.

This particular product was chosen as it has the correct output power range ($\sim$200 mW - 5 W), low noise, convenient interfacing options and was offered at a reasonable price ($\sim$£5000). Multiple technical difficulties were experienced as a result of manufacturer error when comissioning the device, that resulted in 4 months of experimental down-time. As a high power optical device, the gain fibre is supposed to be relatively long in order to spread the thermal load from optical pumping/gain over a larger volume; this longer fibre option was not used upon commisioning and so the heat produced caused one of the EDFA's internal pump diodes to malfunction multiple times. Eventually this error was noticed by the manufacturer and corrected, after which the amplifier functioned as intended. When performing as intended the product fulfilled all expectations and the serial interface made it especially easy to fully integrate into the lab infrastructure. Figure 4.7 shows the EDFA package.

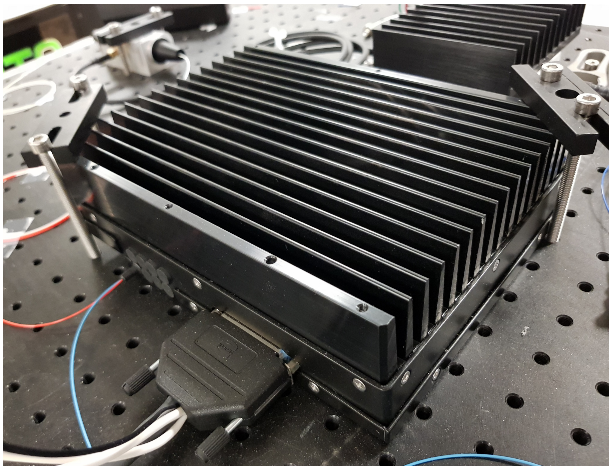

Fig. 4.7. *EDFA package*

The EDFA output power was characterised by measuring the optical power of the trapping beam as it enters the vacuum chamber. It was found to be linear with EDFA power setpoint; the results are shown in figure 4.8.

This calibration allows us to be more certain that the optical power at the trap site is as expected and that therefore subsequent investigations that depend on optical power are more reliable and represent a real relationship to the trapping light intensity.

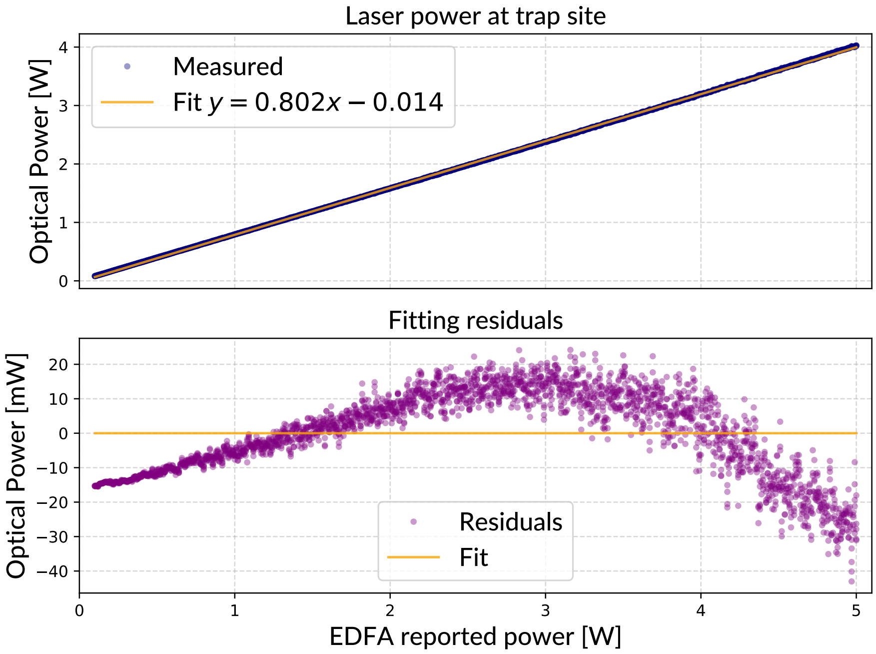

Fig. 4.8. *EDFA power calibration - Optical power at the trap site is shown to be very close to linear with the power reported by the monitor photodiode at the EDFA.*

§4.2.4. Tap couplers

Tap couplers are the fibre optic analogy of a free-space beamsplitter, they have 2 inputs and 2 outputs and a given cross-coupling percentage. For a 10% tap coupler, of any light field entering the device through input port 1, 10% of it will leave output port 2 with the remaining power continuing unaffected.

Tap couplers work by exploiting the fact that bringing the cores of two optical fibres close to one another causes the evanescent wave travelling in the cladding to 'leak' power into the core of the opposing fibre. The rate at which this occurs is related to the separation distance, and so the length that two fibres should be brought into proximity in order to obtain a specific cross-coupling is calcuable. These devices are simply two fibre cores brought together at the correct distance and for the correct length in order to obtain the desired cross talk percentage. They are not polarisation dependent and so the coupling ratio remains constant even if the polarisation of the input light drifts. The polarisation of the light may be altered when cross coupling through a tap coupler, but the entire fibre system in this experiment is non polarisation maintaining and the particle dynamics are unaffected by polarisation and so this change is not an issue.

These devices are both input-output symmetric and bilaterally symmetric, meaning the behaviour above is the case for any given fibre pigtail. Fibre tap couplers are available in a wide range of coupling ratios, in this project 10%, 1%, 0.1% and 50% were used although no coupler gives exactly the specified cross-coupling percentage and they must be individually characterised before use. The cross-coupling percentage varies with temperature and mechanical stress so these devices should be thermally equilibrated with a large thermal mass and well mounted. Tap couplers can be used in series to cut power to any given proportion of the original and maximise the SNR of a particular measurement. For example, when monitoring the laser power at the trap site, a 0.1% tap coupler was used to direct a small amount of optical power to a photodiode from the main beamline. 50% tap couplers can be used to make a fibre based Mach-Zehnder interferometer where optical power is divided evenly and then recombined later.

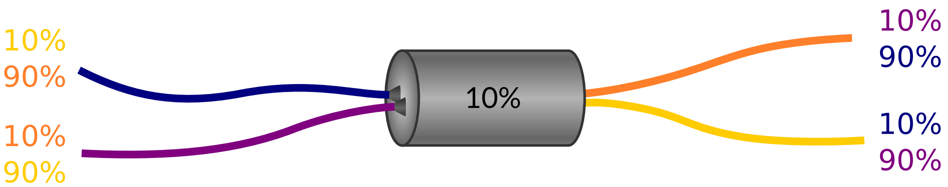

Fig. 4.9. *Tap coupler optical power cross-coupling - 90% of the light entering through the blue fibre leaves through the orange fibre, the remaining 10% through the yellow.*

Tap couplers are how different light fields in this experiment were mixed together in order to make homodyne or heterodyne measurement. When mixing the scattered signal light from the particle with a frequency shifted reference field, a 0.1% tap coupler was used in order to retain as much of the valuable signal light as possible. The intensity of the signal field coming into the tap coupler was adjusted to be 1000 times that of the signal light such that 0.1% of the reference gives a 1:1 intensity ratio between signal and reference fields, producing a high contrast interferogram.

§4.2.5. Circulator

An optical circulator is a non-reciprocal fibre optic device used to separate counter-propagating fields. In this project a fibre circulator was used to separate the trapping light from the weak signal field scattered by the particle. This requires a large degree of isolation as the trapping light is many orders of magnitude more intense than the signal field.

The product used to achieve this was an Optosun 3 port circulator for 1550 nm light. This gives >40 dB of isolation between ports, >50 dB return loss and <0.8 dB insertion loss. It is also rated for 5 W CW optical power and so is well suited to our use case, giving a good SNR at port C while costing under £500. Conveniently, it was found that the intensity of light 'leaking' from port A to port C was comparable to that of the collected signal light and so the cross-talk could be used as a homodyne reference signal, negating the need for separate reference beamline.

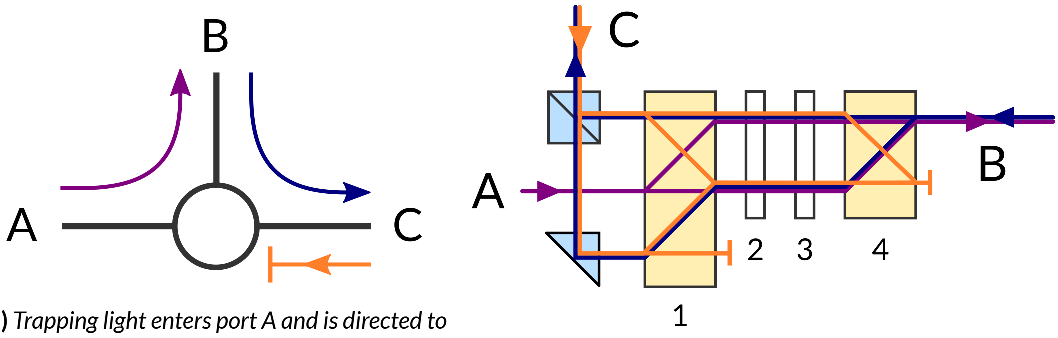

(a) *Trapping light enters port A and is directed to the trap site from port B, scattered signal light enters through port B and is directed to a photodiode at port C.*

(b) *Optical element diagram of a fibre circulator - A Faraday rotator (2) and half wave plate (3) are used to break the symmetry of the device. 1 and 4 are birefringent crystals.*

Fig. 4.10. *Fibre optic circulator*

Optical circulators use a Faraday rotator to affect the polarisations of counter-propagating beams in opposite ways, counter rotating their polarisations so that after passing through a half wave plate, they travel along different paths through a birefringent crystal. The mechanism for separating the two fields can be seen to rely on the non-reciprocity of the Faraday effect.

The multi-element arrangement shown in figure 4.10b is subject to very tight alignment tolerances, and in a device such as the one used in this project, these elements are miniaturised into a package that is approximately 6 x 6 x 40 mm, meaning thermal expansion can have noticeable effects. The chosen product performed within the parameters given, however when using 5 W of optical power there were some losses in the circulator, causing it to heat up and the power couplings to decrease by as much as 20% after switching on, over timescales of approximately an hour, as a result of changing alignment. This meant that the laser should be switched on and the circulator left to come to thermal equilibrium before attempting any precise measurements.

§4.2.6. AOM

As discussed in §2.6.1.3, the acousto-optic modulator (AOM) in this setup is primarily used to frequency shift a reference field for use in heterodyne measurement. As such, any product bought for this purpose must collect and output couple the first diffracted order, as this is the light that experiences a frequency shift. There are limits on the transmission of such AOMs as after saturation the proportion of the incident power diffracted into the first order fringe increases less than linearly as RF power is increased. This means the first diffracted order is limited to 80% of the optical power entering the device, and without very high RF power the reality is often closer to 50%. The diffraction efficiency of a given order is given by $\eta = {}^{I_1}/_{I_{\text{tot}}} = \sin^2\left({}^{\pi}/_{2}\sqrt{{}^{P_{\text{in}}}/_{P_{\text{sat}}}}\right)$, where P_{in} and P_{sat} represent the input and saturation RF powers respectively. This relationship is backed up by experimental measurement, as is the regime in which our device was operated. The device used was an AA-optoelectronic `MT80-IIR30-FIO-SM5-J1-A-VSF`, meaning it is designed to be driven at 80 MHz, has a 30 ns rise time and a maximum optical power of 5 W CW. This product is stated as having a nominal 2 dB (63%) transmission, with the absolute maximum loss stated as 3 dB (50%). Our device had a transmission efficiency of 51% when driving with the recommended RF power, which is understandable as this was measured when using 5 W of optical power, at the limits of the device's design parameters. The AOM was driven with a `BKPrecision 4064` signal generator producing an 80 MHz sine wave connected to a fixed-gain RF amplifier. The signal generator has a 14-bit DAC and runs at 500 MSa/s. The RF amplifier was a `Minicircuits ZHL-1-2WX-S+`, with a 500 MHz bandwidth 29 dB gain. The signal generator could be amplitude modulated (AM) in order to adjust the power transmitted by the AOM.

This particular model of AOM was chosen as it achieved sufficient diffracted power for our application; as well as because it could be driven by an RF system other than the included driver in order to get better control of the output coupled light field. Generally AOMs are supplied with a voltage controlled oscillator (VCO) driver that produces an RF voltage output of the correct frequency to drive the AOM. These drivers often have an AM input as well as a frequency modulation (FM) input that take between 0 and around 10 V. The device outputs a sine wave with amplitude proportional to the AM voltage and frequency that is some base frequency plus a difference proportional to the FM input. This allows for amplitude control of the light being transmitted by the AOM, as well as some control over the frequency shift of the light caused by the diffraction process. We replaced this VCO driver with the signal generator and amplifier as mentioned above to provide more precise, direct control over the signal. A voltage amplitude could be directly input into the signal generator, rather than having to calculate the require AM voltage that produces a given RF amplitude.

Ideally the insertion loss of the AOM would have been lower, however a pragmatic choice had to be made and the device fulfilled its purpose well.

Fig. 4.11. *The AOM package - This is a single mode fibre coupled device that transmits the first diffracted order with a power related to the RF driving power. This device acted as an intensity modulator and frequency shifter for use when performing heterodyne measurement.*

§4.2.7. Focussing objectives

The focussing objective is perhaps the most important optical element in a levitated optomechanics setup, as it determines the shape and quality of the focus and so determines the characteristics of the particle motion in the trap. A number of approaches to the design of this part of the experiment are possible, those that were investigated are detailed below. The common technique of using a microscope objective was not used as there were no commercially available devices designed for the wavelength in use. Microscope objectives are designed for a specific wavelength and so the use of an optic optimised for a wavelength far from 1550 nm would have resulted in a highly aberrated beam and and a poor trap.

The purpose of an objective in this project is to take the high power trapping beam from fibre and create a stable, high NA focus without introducing aberrations or distortions, as is needed for high quality optical trapping. Three systems were used during the project, however most of the results presented later in this thesis were made using the parabolic mirror in §4.2.7.3. The different objective systems will be discussed in chronological order of their development.

§4.2.7.1. Ellipsoidal mirror

The first system was a combination of cleaved fibre and an ellipsoidal mirror to make use of the geometric properties of an ellipse to remove the need for a collimator. The bare fibre produces a cone of light which can be thought of as originating from a point (in order to simplify the geometry), which becomes one focus of an ellipsoid, where the particle is to be trapped at the other. The properties of an ellipse mean that if the fibre is positioned correctly, an ellipsoidal mirror will map the light from the fibre to a point at the other focus. In reality the light does not originate from a point but from a slightly extended source of radius $\sim 3\lambda$ for a 10 µm core diameter in an SMF28 fibre. The focus is therefore close to a diffraction limited spot. This tight waist becomes the particle trap site, and when a particle in this position Rayleigh scatters light into the mirror, the same geometric relation causes the scattered signal light to be mapped back to the fibre tip.

Using this arrangement a bare fibre can produce a high NA focus and recieve the phase modulated signal light scattered by the particle, all with only a single optical element.

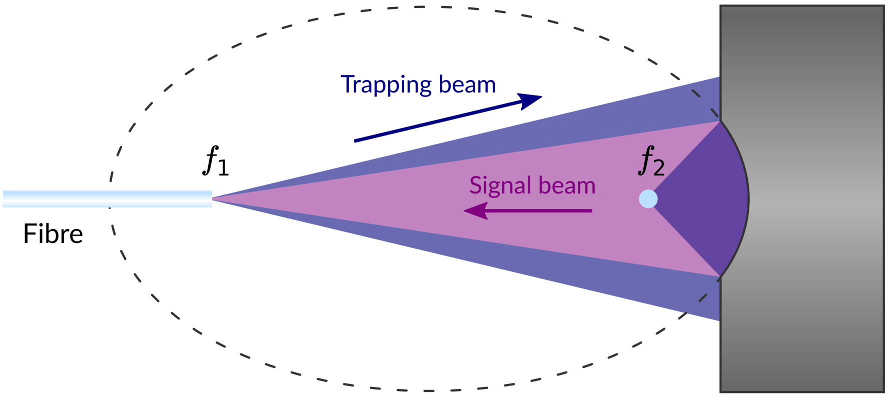

Fig. 4.12. *Ellipsoidal mirror geometry*

Implementing this design required a very high reflectivity mirror with a precise geometry, dictated by the desired size of the ellipse, mirror radius, NA etc. A geometry was devised with an NA of 1, using the known NA of the fibre and an interfocus distance of 15 mm such that the final assembly would be a suitable size. This mirror was manufactured by Symons Mirror Technology Ltd. using a diamond turning process with aluminium. A custom adjustable mounting solution for the fibre was designed and constructed in order to interface with the vacuum system. The mirror and mirror assembly can be seen in figures 4.13a and 4.13b respectively.

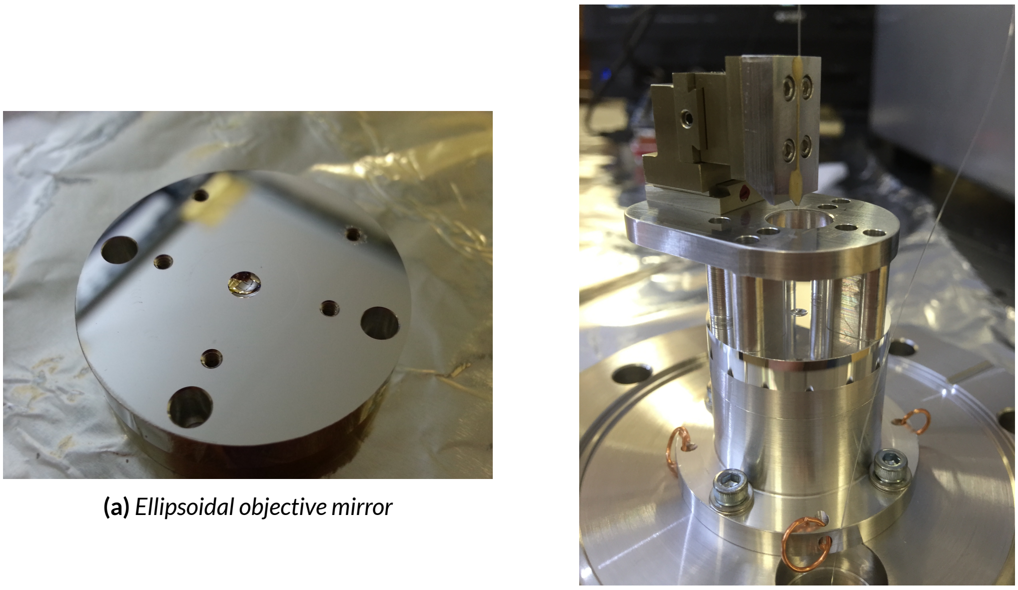

(a) *Ellipsoidal objective mirror*

(b) *Ellipsoidal mirror assembly*

Fig. 4.13. *Ellipsoidal mirror*

There were a number of problems with this first objective design, the first being the reflections from the plane cleaved fibre. When a fibre is plane cleaved, its end face is perpendicular to its axis and there is significant reflection (-15 dB [171]) from the glass air interface in both directions. In this case the major issue was the reflection of the high power trapping laser when leaving the fibre through this interface. The intensity of which was enough to swamp any signal light collected and coupled back into the fibre. It proved very difficult to resolve this problem as the geometry relies on a plane cleave and any attempted reduction in the reflected trapping light also reduced the measured signal light, thus the SNR remained unchanged.

The second issue with this design was the adjustability of the position of the fibre tip. Whilst the miniature 3 axis translation stage used provided the required stability and resolution, the read-out method used for optimising the trap alignment is the particle oscillation frequency; the higher the frequency the tighter the focus and thus the better aligned the fibre must be. Unfortunately, at atmospheric pressure the spectral features from which we can deduce the trapfrequency are broadened such that it is very difficult to obtain a value, and so in order to determine the trap frequency the system must be evacuated below approximately 1 mbar. When at this pressure in a vacuum chamber the translation stage can then no longer be adjusted, making this process prohibitively slow and relying on good initial alignent to even be viable at all.

It was suggested that the translation stage could be electrically driven from outside the chamber in order to align the fibre whilst at low pressure but any commercially available products with the required position resolution and physical size were far beyond the available budget. A design was made for a custom solution driven by stepper motors controlled from outside the chamber; a sensible option because the required minimum pressure tolerance was much higher than those offered by commercial solutions. In actuality however, the manufacture of the intricate parts required was deemed to be too time consuming and costly, and so was not undertaken. The proposed design is shown in figure 4.14.

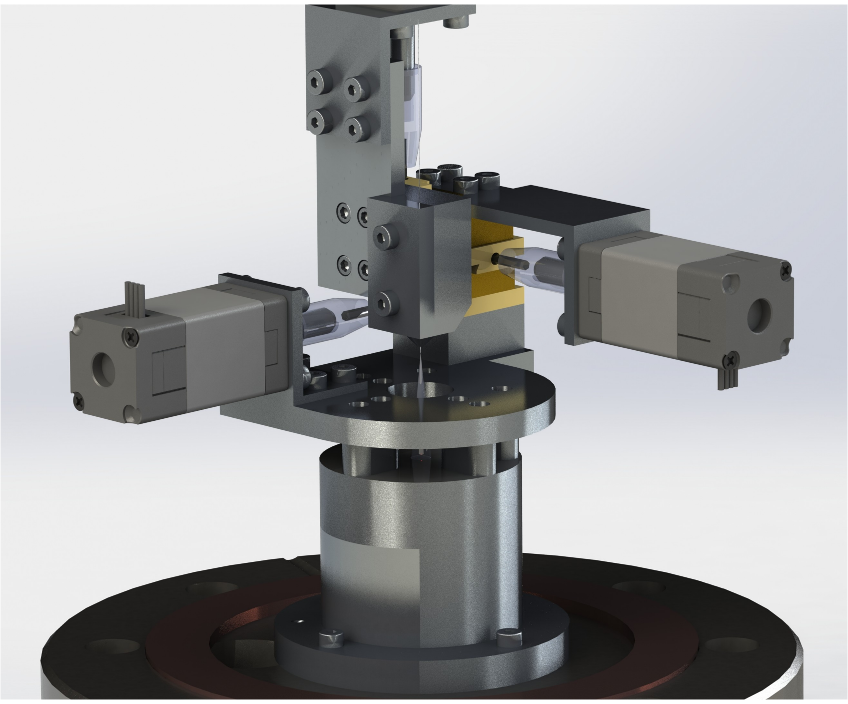

Fig. 4.14. *Externally driveable fibre alignment assembly*

The final, less severe problem with the design in figure 4.13b was the fragility of the trailing fibre where it entered the chamber; sealed with a compressed graphite ferrule. The fibre coils round the assembly and is bonded to the translation stage. This fibre was prone to breaking and the exact angular alignment of the fibre in the "v-groove" of the translation stage was not repeatable, due to the tendency of the glue to displace the fibre due to capillary action, decreasing the effectiveness of the entire assembly.

Overall, a plane cleaved fibre does not act as a good launch platform for trapping light, and better results can be achieved with a collimated beam.

§4.2.7.2. Aspheric lens

Light leaving a fibre can easily be collimated using a comercially available fibre collimator connected via an angle plane cleave (APC) connector so as to avoid the reflections mentioned above. Many of these products are available, but in this project a Thorlabs `TC18APC-1550` was used. This is a triplet collimator that is specified to produce a 3.33 mm diameter waist 12.91 mm from the device. These values are ideal as the beam diameter is closely matched to an available focussing optic such as the Thorlabs `C660TME-C`, and the focal distance is comparable with the length scales of an assembly that could be designed to fit in the existing vacuum chamber. The `C660TME-C` is an aspheric lens with an effective focal length of 2.97 mm and an NA of 0.6. This is very high for a singlet optical element and this lens is designed for use at 1550 nm, making it an ideal choice for a refracive objective. The NA of the aspheric is slightly lower than the ellipsoidal mirror and so the trap stiffnesses can be expected to be lower, but the simplicity of the setup and the removal of the plane cleaved fibre more than make up for this minor disadvantage.

The collimator and aspheric were placed in kinematic mounting hardware and attached to an optical rail as can be seen in figure 4.15. This assembly was placed inside the chamber with a fibre passing into the chamber as above and connected to the collimator APC socket. This arrangement was much easier to initially align; particles could be trapped robustly and then the entire piece placed into the vacuum chamber and pumped down to low pressure.

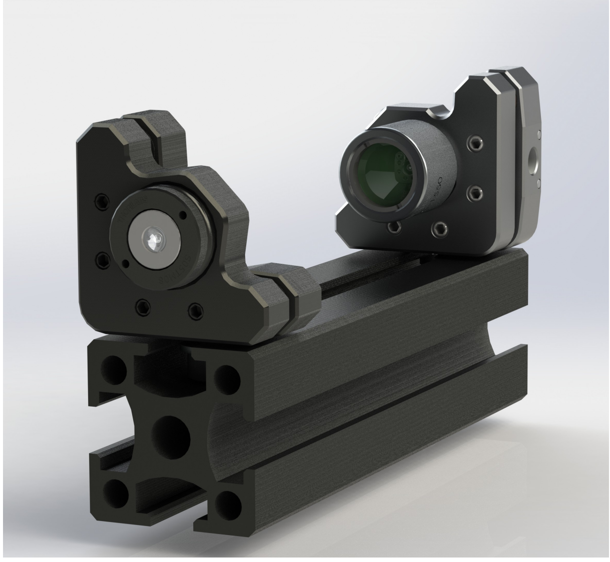

Fig. 4.15. *Aspheric lens and collimator - 3D CAD rendering with the aspheric in the foreground*

Unfortunately this initial arrangement of collimator and aspheric suffered from the same alignment issues as the ellipsoidal mirror in that it could not be precisely aligned when inside the chamber. To achieve this, the setup was changed so that the aspheric was suspended inside the chamber and the collimator was placed outside, the beam passing through an anti-reflection coated window in the chamber, to the lens inside. This allows the collimator in its kinematic mount to also be attached to a 2 axis translation stage, such that its position and angle can be fully adjusted whilst a particle is trapped at low pressure inside the chamber. From here, the alignment of the trap is a hill climb problem with 4 degrees of freedom as inputs and the measured particle trap frequency as the parameter to optimise. Eventually a maximum frequency is found and the trap can be said to be aligned.

The points for improvement from this design to the next mainly revolved around the mounting mechanism for the focussing objective. The aspheric was mounted in a cage plate bolted to a flange of the vacuum chamber and whilst secure, it was not completely rigid, with mechanical resonances around the 50 Hz frequency range that could be excited by impacts to the chamber or optical table, or simply by the vacuum pumps attached to the chamber.

The NA of an aspheric lens is not as high as can be achieved with a reflective objective and so it is desirable to move to a paraboloidal mirror. A single fixture was designed and machined to be compatible with both the aspheric lens and parabolic mirror. This fixture held the lens more rigidly, and was then swapped out for a mirror.

§4.2.7.3. Parabolic mirror

The external collimator proved to be highly beneficial and enabled stable trapping for many hours when used in conjunction with the aspheric lens mounted in the custom fixture, however the lower NA and forward scatter geometry could be improved upon by using a parabolic mirror. A parabolic mirror perfoms the same mapping as an ideal lens but is achromatic and collects the back-scattered light rather than the forward scatter; an approach that is more sensitive to changes in position [41, 88]. A parabolic mirror is a special case of an ellipsoidal mirror in which one of the two foci is at infinity, i.e. mapping a collimated beam to a tight focus. The optical layout of this objective is shown in figure 4.16.

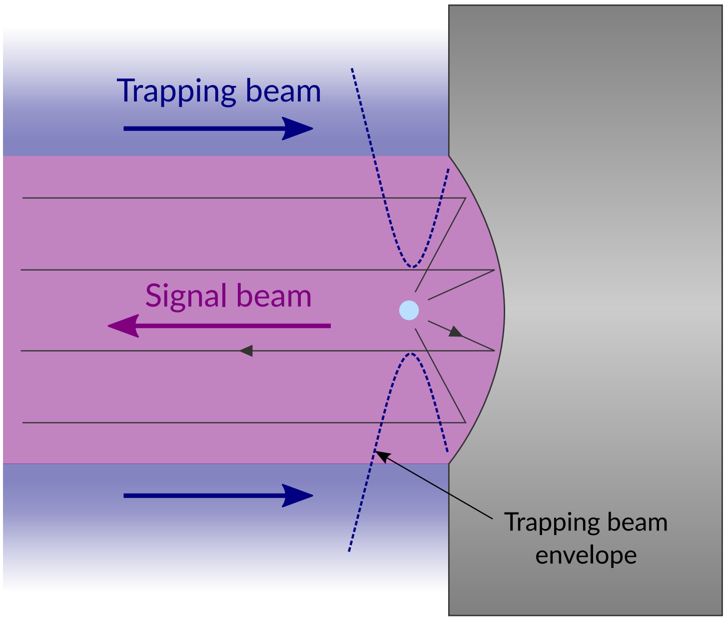

Fig. 4.16. *Parabolic mirror focussing*

A parabolic mirror was designed and manufactured in the same way as with the ellipsoidal mirror, however with a parabolic geometry the number of defining parameters is significantly reduced. The parabolic mirror was designed to have an NA of 0.98, meaning the particle trap site is slightly offset from the face of the mirror and has a curved section with radius corresponding to the optimum filling factor of the incident beam. In this case the radius is determined by the radius of the output beam from the collimator. The defining measurements of the parabolic mirror are shown in the figure below.

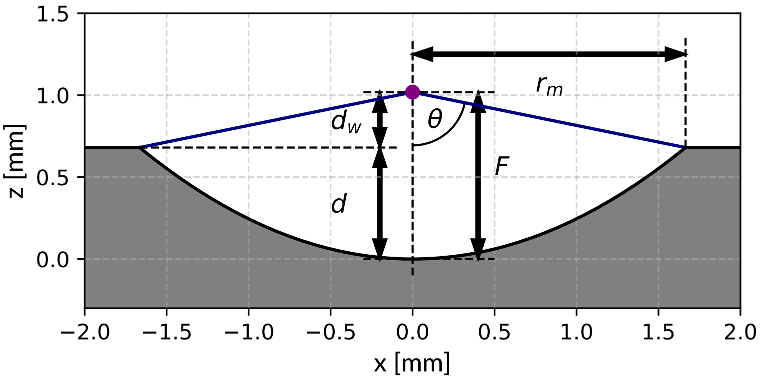

Fig. 4.17. *Specification of the parabolic mirror - The parabolic mirror is defined by the mirror section radius r_m, focal length F, depth d, working distance d_w and NA which is related to angle θ.*

For a given desired NA and r_m, the other parameters can be calculated. The z coordinate of all points on the diameter cross-section of the mirror satisfy the equation $z = \frac{x^2}{4F}$. The working distance is simply the focal length subtract the parabola depth, $d_w = F - d$ where $d = \max(z)$. The maximum value for z occurs when $x = r_m$, which we can substitute in to get $d_w = F - \frac{r_m^2}{4F}$. From the diagram of the geometry we can see that $\mathrm{NA} = \sin\left[\mathrm{atan}\left(\frac{r_m}{d_w}\right)\right]$; subsituting d_w into this gives,

$$\mathrm{NA} = \sin\left[\mathrm{atan}\left(\frac{r_m}{F - \frac{r_m^2}{4F}}\right)\right]. \tag{4.1}$$

When creating a focussing object for levitated optomechanics, its desirable to maximise NA and therefore minimise the focal waist, to create a deeper trap. Initially an NA of 1 was to be used, however this places the focus exactly in plane with the front face of the mirror, possibly producing a time varying scatter signal as the particle moved through the plane of the front face; for this reason an NA of 0.98 was chosen.

Inputting our desired value for NA and r_m and solving for F provides a value for focal length, and from this the other parameters can be found easily. An NA of 0.98 gives a focal distance of 1.02 mm. The relations between the different parameters, as well as the chosen values are shown below.

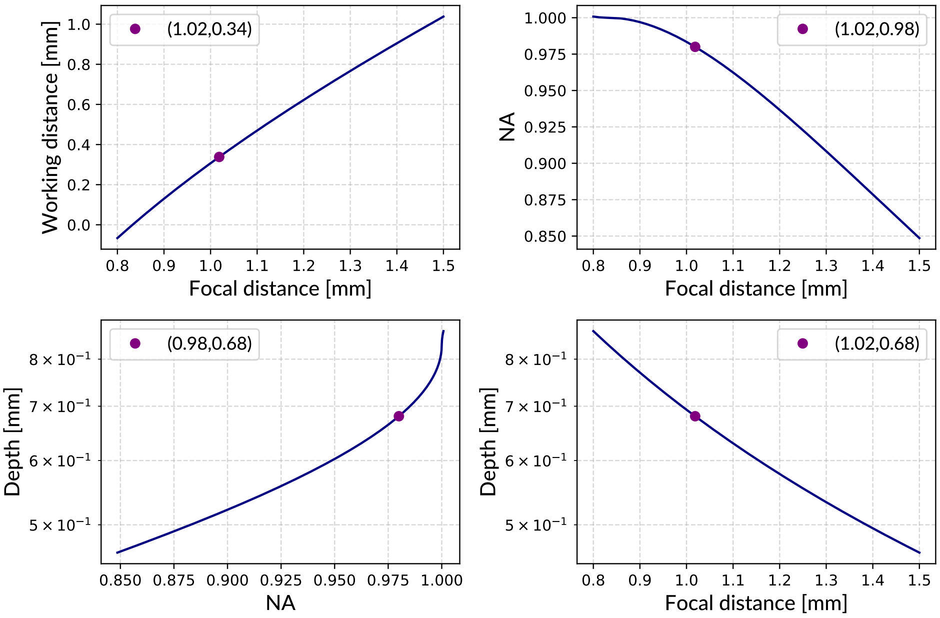

Fig. 4.18. *The relation between the defining parameters of the parabolic mirror. Markers indicate the chosen values used in the mirror manufacture, with the coordinates given in the legend. These plots were generated by calculating the various parameters of the paraboloid as a function of a sensible range of input values of the other parameters, with a fixed mirror radius determined by the trapping beam diameter.*

The mirror surface is specified to have an RMS surface roughness of 4 nm, and is machined by separately sweeping out the paths required to create the curved parabolic surface and the flat front face. This is done as opposed to creating the cross-sectional profile in a a single operation by blending the geometry to ensure that the edges of the mirror are as sharp as possible. This is to reduce and aberation of the focus caused by the ring of non-parabolic mirror surface that would be present. It was not possible to quantify the corner radius of the flat to parabolic transition edge, but no negative effects that could be linked to this kind of imperfection were noticed during the project. The mirror geometry was submitted to the manufacturer with tolerances of ±5 μm, however it was not possible to verify this with the tools available.

The front face of the mirror was also machined to be optically flat so that it could be used to align the collimated beam normal to the surface. This greatly reduces the time taken to align, but a significant proportion of the optical power hits this flat surface and is reflected back towards the collimator, generating a Poisson's spot that swamps the signal light. To avoid this, the mirror fixture was designed with a slot to accept an aperture that occludes the flat section when it is no longer required. In this way the SNR is maximised and a stable trap is formed. Figures 4.19a and 4.19b show the parabolic mirror and the aperture respectively.

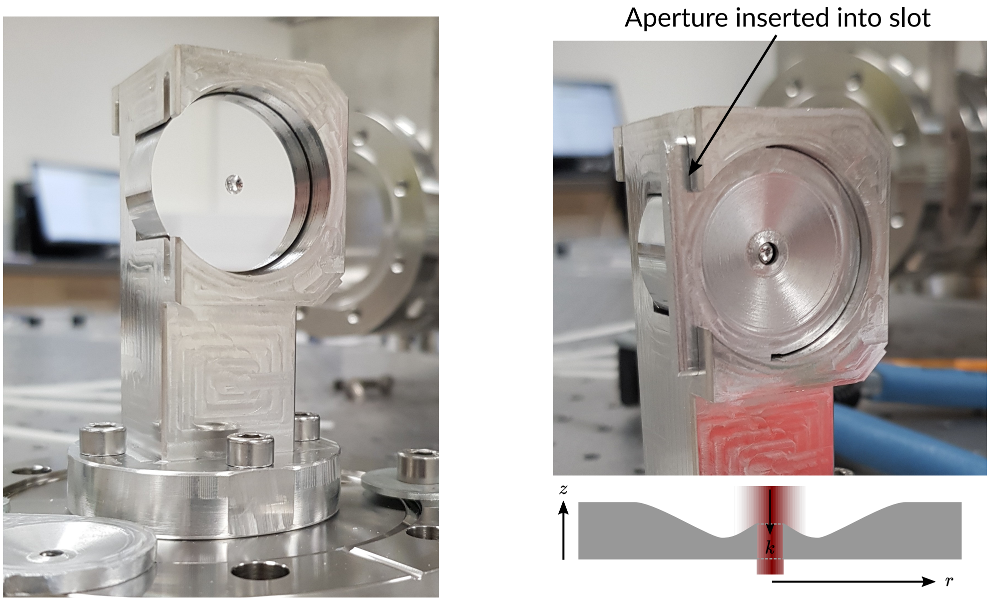

(a) *Parabolic mirror mounted in the custom fixture*

(b) *Aperture overlayed on mirror to remove poisson spot, and cross-section of aperture profile.*

Fig. 4.19. *Parabolic mirror objective - The optic is shown in its custom mount with and without the custom aperture used to block the Poisson's spot.*

This arrangement is the experimental setup in which the data presented in this thesis was taken and represents the final form of the objective. Figure 4.20a shows the poisson spot created by illuminating the flat face of the mirror.

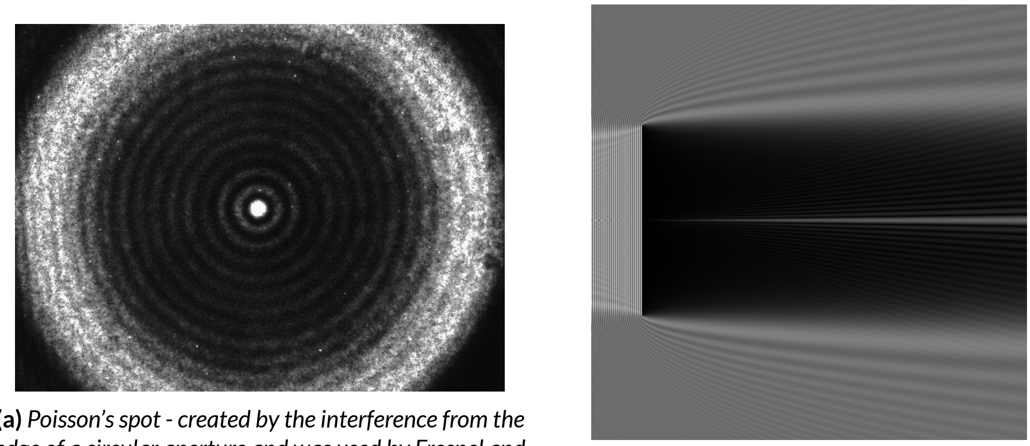

(a) *Poisson's spot - created by the interference from the edge of a circular aperture and was used by Fresnel and Arago around 1818 as one of the earliest examples of proof of the wave-like behaviour of light. [172]*

(b) *A profile view of the formation of a Poisson's spot. The central bright spot can be seen to form and spread as distance from the aperture/disc increases. [173]*

Fig. 4.20. *Poisson's / Arago's / Fresnel's spot - An optical artifact created by the diffraction of the laser at the edge of the parabolic mirror section. An unexpected central bright spot is produced.*

Light collected by the objective is directed back into the collimator where, due to the geometry of a parabola, it will re-enter the fibre and be guided to the circulator. At the circulator the signal light is separated from the more intense counter-propagating trap light and will mix with the reference field 'bleed-through' from the circulator. This combined field is E_{tot} from §3.3 and can be sent to a photodetector in order to perform homodyne measurement. In the case of heterodyne measurement this homodyne field is mixed with a frequency shifted reference field by combining them in a fibre tap coupler (§4.2.4), before being sent to the photodetector.

§4.2.8. Photodetector

The photodetector/photodiode is used to measure the intensity of the resultant electric field from the signal and reference beams. The chosen hardware needs to be fast when compared with the difference frequency between the two optical fields (80 MHz in our case) and needs a measurement range on the order of the total optical power of the signal and reference fields. The photodetector should also be designed to be sensitive at the correct wavelength and ideally would produce an output voltage than can be connected directly to the scope via a $50\,\Omega$ impedance BNC connector. A completely analogue device would be preferable as any analogue to digital converter (ADC) based hardware would introduce noise at the sampling frequency and would sacrifice position resolution. Digitisation will be required eventually, but at this stage it is sensible to aim for high quality analogue measurement and then digitise later with an oscilloscope.

The device chosen to fulfil these requirements was the Femto `HCA-S-200M-IN`, a 200 MHz photodiode with inbuilt transimpedance amplifier. This device saturates at 60 µW of optical power and has a very low noise equivalent power (NEP) of 5.2 pW Hz$^{-1/2}$. Detectors for 1550 nm light are more expensive and less available as the photon energies involved are less than the bandgap energy of silicon, meaning silicon based semiconductors cannot be used. The replacement semiconductor of choice is indium gallium arsenide (InGaAs) which is more expensive as the manufacturing industry surrounding this material is slightly less developed due to the inherent added complexity of manufacturing III-V semiconductors compared to silicon. A maximum power of 60 µW is perhaps slightly lower than ideal as the expected optical power of the signal beam is comparable to this, and therefore when combined with a heterodyne signal the total field can exceed the saturation threshold of the detector. Fortunately, the heterodyne field can be cut down with a tap coupler meaning the full dynamic range of the detector is being used. The chosen hardware is available with an APC connector so it can be easily connected to the fibre optic system.

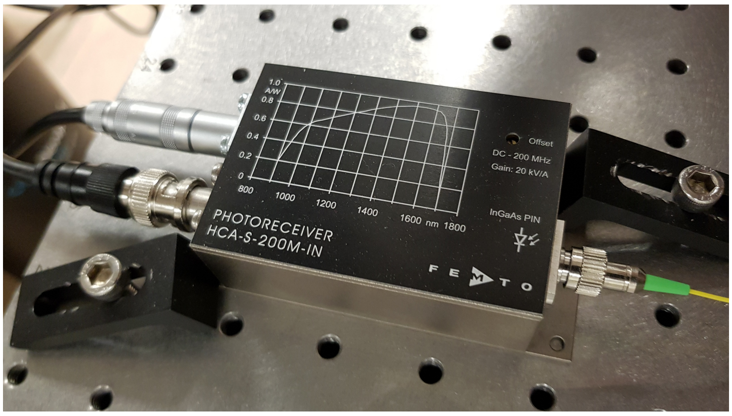

Fig. 4.21. *Fast photodiode*

The Femto device proved well suited to the task, notably it has very low noise characteristics however the low saturation power meant that extra care had to be taken when changing the optical setup so as not to risk damaging the device. This was possible through the use of a power meter with a maximum power of 20 W that could be used to check the damage threshold was not exceeded before connecting to the fast photodetector. When used in tandem, these devices fulfilled the requirements of this part of the optics subsystem well.

This completes the review of the optics subsystem. Much of the optics is designed to create the high NA focus for use in trapping, which has to be done inside a vacuum chamber so that background gas can be removed in order to decrease damping rates.

§4.3. Vacuum

The vacuum system is centred around the parabolic mirror trap and must be able to reduce the pressure around the particle to below 10^{-6} mbar, ideally 10^{-9} mbar in order to allow ultra-high vacuum (UHV) testing. These kinds of UHV chamber are generally constructed from steel parts with “DNXX-CF” connection between them, where XX is the diamater of the part in question. This is a system of flanges that bolt together and use deformable copper gaskets to create a seal. Multiple sizes are available and all would be suitable for our needs.

The volume needed to house the mirror objective is around 500 cm^3, and the assembly has a diameter of approximately 5 cm. As a result of the required space and the available diameter standards, a vacuum system based around the “DN63-CF” system was chosen. The trap is housed in a cubic chamber, with various sections connecting the different pumps, as well as a pressure gauge and a gate valve to allow physical access to the chamber for introducing nanoparticles.

The configuration of the vacuum chamber is shown in figure 4.22a and the viewport is shown in figure 4.22b.

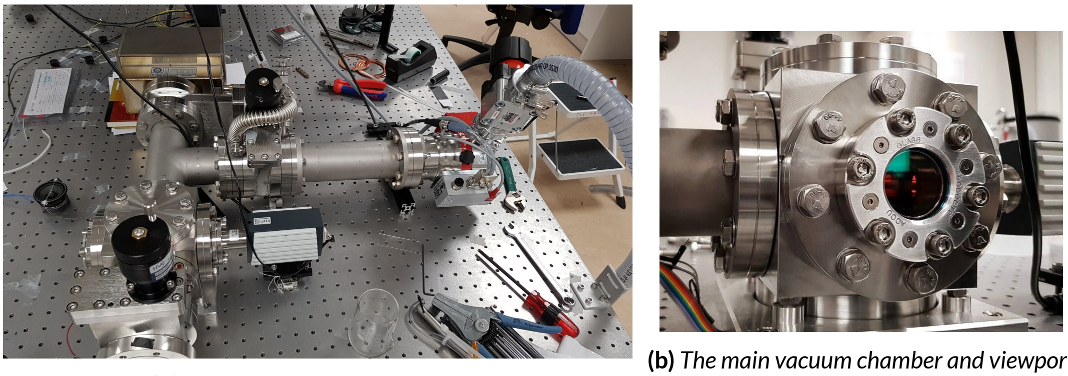

(a) *Vacuum chamber arrangement*

(b) *The main vacuum chamber and viewport*

Fig. 4.22. *Vacuum chamber - The ion, turbo and scroll pumps are visible, along with the bleed down system and viewport.*

The chamber features a scroll pump for decreasing the pressure from atmospheric pressure to 10^{-3} mbar, a turbopump for reaching 10^{-7} mbar, and an ion pump that allows the chamber to reach 10^{-9} mbar, whilst allowing the turbo pump and scroll pump to be deactivated. This is important as the latter pumps have moving parts, the motion of which introduces vibrations that added artefacts to the particle spectrum.

A viewport is used on the main chamber in order to use an external collimator to couple light into the chamber, as discussed in §4.2.7. This is an anti-reflection coated window designed for the laser wavelength in use, that is vacuum sealed (with a metal to glass bonded seal) and gives minimal distortion to the trapping beam. This is installed in front of the mirror trap, so light enters normal to the window and so distortions are minimal. Another noteworthy feature of the chamber is the pressure "bleed-down" system consisting of a needle valve and gate valve that allows pressure in the chamber to be reduced at a very finely tunable rate so as to not perturb the particle with turbulent gas flow. This system also has a gate valve that can open fully in order to take full advantage of the turbo pump when in the ballistic gas regime.

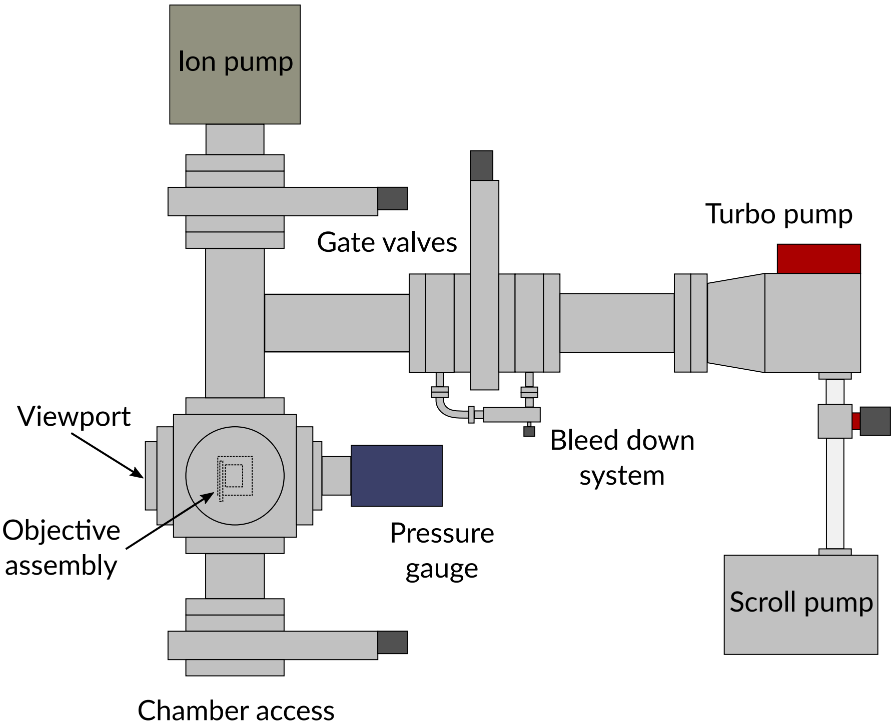

Fig. 4.23. *Chamber schematic - The layout of the chamber is shown, with the position of the major components indicated.*

§4.3.1. Pumps

The process of evacuuating the chamber requires three pumps, each of which operate at a different pressure range. The scroll pump is used initially to bring the chamber from atmospheric pressure (1000 mbar) to approximately 10^{-2} mbar, bringing the particle from the continuous flow regime to the Knudsen regime in which molecular flow starts to become ballistic, i.e. a given gas molecule is likely to encounter the walls of the chamber before it encounters another gas molecule. At this pressure the turbo pump can be engaged to bring the system into the molecular flow regime in which gas molecules are ballistic; the turbo pump can reach an ultimate pressure of about 10^{-7} mbar. The ion pump can then be turned on to provide slow pumping down to UHV at 10^{-9} mbar, although at these pressures it is very difficult to maintain a trapped particle; an effect that is theorised to be due to internal heating.

The chosen scroll pump is an Edwards `nXDS6i`, rated to have a pumping rate of 1.7×10^{-3} m^{3}s^{-1}, and an ultimate pressure of 2×10^{-2} mbar. The turbo pump is a Pfeiffer `HiPace 80` with a peak pumping rate of 6.7×10^{-2} m^{3}s^{-1} and an ultimate pressure of 10^{-11} mbar. The ion pump is from Gamma Vacuum, model number `TiTan 45S`. The ion pump has an ultimate pressure of 10^{-11} mbar and and a pumping rate of 4×10^{-3} m^{3}s^{-1}.

The pumps performed within their respective specifications and caused no major issues although the mechanical vibrations mentioned above from the scroll and turbo pumps were more detrimental to the particle dynamics than expected, neccesitating the addition of the ion pump. The turbo pump takes a very long time to reach base pressure, as around 10^{-6} mbar water begins to desorb from the chamber walls meaning baking is required. This was not a major issue though as most of the work done in this thesis was performed at medium pressures (10^{-6} mbar).

§4.3.2. Pressure measurement

The pressure is measured by a gauge that must be able to give reliable readings across the entire available pressure range. A single gauge is unlikely to be capable of this as different varieties of gauges rely on different working principles that do not function across the whole range. The best single component solution is a hybrid gauge that operates as a Pirani gauge at high pressure and then switches mode to cathode gauge below the cuttoff at 10^{-4} mbar. In this project a Leybold `ITR 90` was used, this is a hybrid Pirani - hot cathode gauge that is sensitive down to 10^{-8} mbar and with a mode switch pressure of 2×10^{-2} mbar. This device can easily be mounted to a DN63-CF system through the use of an adaptor and pressure data is output to an RS232 serial port that was logged every 5 seconds by a computer. Regular information on the chamber pressure is important in debugging performance as, if a particle is lost, its useful to keep track of the pressure at which this occurs in order to track the improvement of the trap at low pressure through development. Accurate pressure information is also needed when investigating the behaviour of damping rates as a function of pressure; without good pressure information an incorrect value for particle radius etc. will be found. It is also important to position the pressure gauge close to the particle trap site, as a spatial pressure gradient across the chamber can result in a reading that does not reflect the environmental conditions close to the particle.

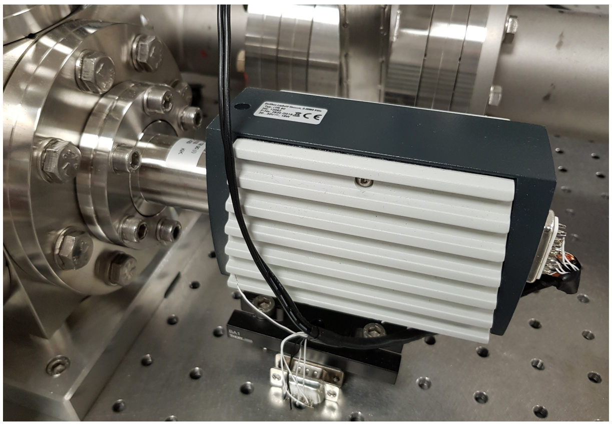

Fig. 4.24. *Pressure gauge*

The chosen gauge performed well below approximately 100 mbar, but above this pressure the readings were much noisier (with a standard deviation $\sigma_P = 300$ mbar) than we would have liked, making initial debugging hard. In this pressure regime it is important to use a low pumping rate so as not to disturb the particle with turbulent gas flow, but uncertain pressure readings make it difficult to tell whether valves are open to the correct degree to achieve this. This often means that pumping rates are increased rapidly and the particle is pushed out of the trap by bulk gas flow, resulting in wasted time. In the end an etalon pattern produced by the viewport was used to tell when pumping was working, as the reduction in pressure moves the glass window slightly and creates a changing interference pattern. The etalon pattern is created when trapping light that has undergone a number of internal reflections inside the glass viewport interferes with light that was transmitted straight through. The result is a pattern cast onto the mirror that was viewed through a camera. The etalon pattern is created by interference between two coherent fields and is therefore interferometrically sensitive to changes in the viewport position along the optical axis, a quantity that changes when the pressure in the chamber is reduced. This means the etalon pattern can be used as a highly sensitive readout of the change in pressure inside the chamber and the bleed down valves could be adjusted to produce a slow pump down with minimal turbulence.

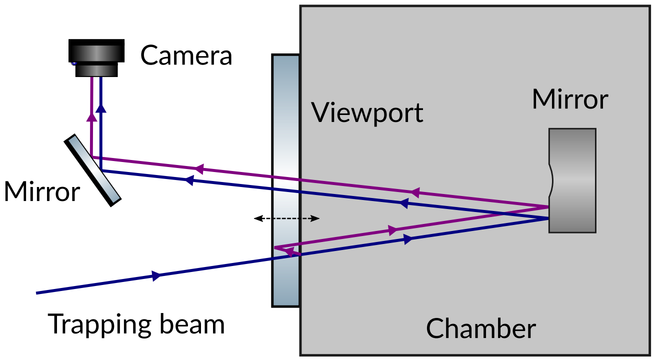

Fig. 4.25. *Generation of the etalon pattern used for detecting changes in pressure at close to atmospheric pressure. Light reflected inside the viewport glass interferes with that which passes straight through to give an interference pattern that depends on the position of the glass-air interface. Angles have been exaggerated for clarity.*

§4.3.3. Chamber access

Unlike most vacuum systems, this project requires frequent physical access to the chamber in order to load nanoparticles into the trap. This involves spraying a few microlitres of an aqueous aerosolised nanoparticle solution into the trapping chamber and waiting for a droplet to diffuse via Browninan motion close enough to the trapping beam to become confined. In order to inject the nanoparticle solution with the best chance of trapping quickly, the nebuliser must be close to the mirror and therefore open access to the chamber is needed.

The first solution to this need was a blank flange that was unbolted and reattached every time the chamber was opened and closed. This proved timeconsuming and so a quick access door was swapped in. The quick access door used a viton gasket, hinged door and single screw thread to seal, but proved to leak too much and made high vacuum impossible. The correct solution was a gate valve, of which compatible DN63-CF versions are available. A gate valve can hold a seal down to approximately 10^{-7} mbar and retracts to leave the entire inside diameter of the chamber clear. These valves are also quick to actuate making loading less time consuming.

The optics system creates a viable trap and is responsible for capturing the particle position signal, and the vacuum system enables a trap with low damping rate in order to see coherent oscillation over as long a time scale as possible. The position information encoded in the phase modulated light must then be recorded and processed in order to draw any conclusions and measure the behaviour of the particle dynamics. We will go through this signal processing chain in the next section.

§4.4. Signal Processing

While the photodetector has been included in the review of the optics system, it is also the first component of the signal processing system. The Femto photodetector outputs a signal between 0 and 3.4 V, representing the full 0 - 60 μW power range. This voltage is output to a BNC coaxial connection where it is passed to the mixing and filtering circuits.

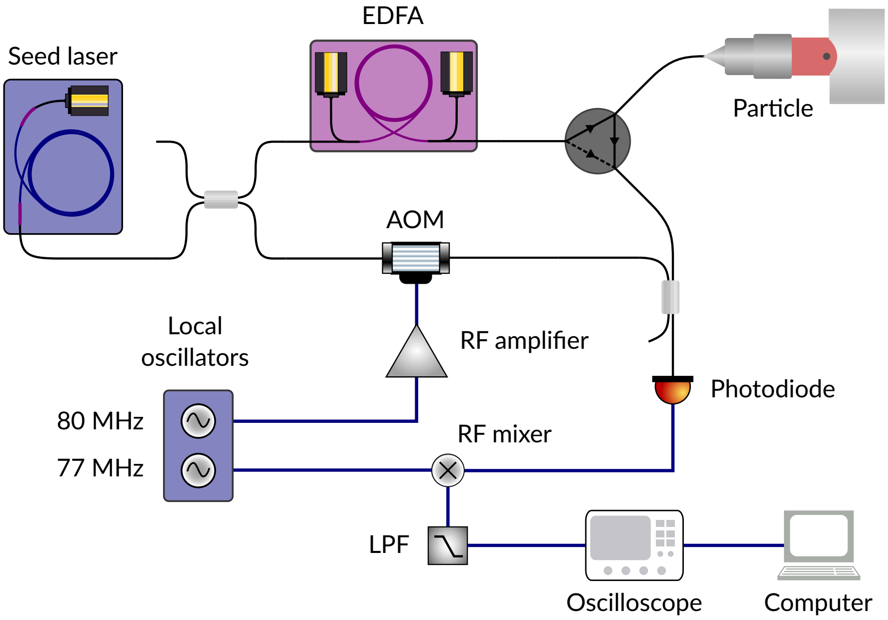

Fig. 4.26. *RF signal processing network - RF components take the signal measured at the photodiode, process it using analogue electronics, digitise and then store it.*

§4.4.1. Filters

As mentioned above, the mixing process creates both sum and difference frequency spectra, of which only the difference frequency is required. In addition to this, there are many other sources of undesirable high frequency noise that degrade the SNR. To attenuate these we use a low pass filter (LPF) with a cutoff frequency of 5 MHz. This allows the full bandwidth of the heterodyne spectra through but removes the approximately 160 MHz sum frequency. If evidence of these higher frequencies is still present, multiple filters can be placed in series. In the case where the homodyne signal being present on top of the heterodyne is undesirable, a high pass filter can be used with a cutoff between the two spectra. In the case of this project that was not needed as the chosen 3 MHz difference frequency proved suitable.

§4.4.2. Data collection and storage

When the analogue voltage signal has propagated through the RF circuitry it must then be recorded so it can be analysed later. It is at this point that its unavoidable that we lose some amount of information due to the ADC process. Although some information is lost, the design considerations of the preceeding components are intended to maximise the SNR of what is recorded.

In general the ADC and recording are done by an oscilloscope ('scope') of some description with the required bit depth, sampling rate and maximum number of data points to allow for useful analysis later. In our case the LeCroy `Wavesurfer 3024` was used as it can store 10 million datapoints, has a maximum sampling rate of 2 GSs^{-1} and a 12 bit ADC. This scope has the benefit of a large touchscreen with an intuitive interface for ease of use. This scope was also chosen as it can be networked and controlled over a USB serial connection to allow data to be recorded and saved automatically. Virtually any setting can be set remotely meaning that complex experimental procedures can be programmed in advance and carried out repeatably and rigorously. It was the intention of this project to make full use of automation of the data/network infrastructure in the lab and this choice of scope makes the signal processing system into a powerful tool for collecting large datasets with ease. The scope met the requirements so well that a second was purchased for general use.

Data recorded by the scope is of the photodetector voltage and is proportional to the signal V produced by the interferometer. This data is sent over the network to a fileserver on which different datasets can be organised and then accessed by any other network connected machine. In this way when many files need processing or fitting, a task which is rather computationally intensive, many computers can be used to gradually process a dataset sequentially. This distributed processing can cut computation time by an order of magnitude.

§4.4.3. Mixers / LOs

When using homodyne measurement, the signal from the photodetector is not mixed further before recording as it is already centred around 0 Hz as it should be when the PSD is created later. In this case no mixers are used and the signal is passed straight to the filter.

In the case of heterodyne measurement the photodiode signal shows a spectrum centred on the difference frequency between the two optical fields. This is equivalent to the AOM driving frequency and in our case is 80 MHz. It is desirable to down-mix this 80 MHz signal to allow slower sampling rates to be used and therefore the signal to be recorded for a longer duration before memory is exhausted. This down-mixing shifts the spectrum to both the sum and difference frequency of the two frequencies involved. In our case these are the 80 MHz AOM frequency and a 77 MHz sinusoidal signal produced by a signal generator or local oscillator (LO). 77 MHz is chosen as this shifts the spectrum to a difference frequency of 3 MHz, outside the frequency range of the homodyne signal but low enough that a full second of data can be recorded before memory is used up. This is an optimum between placing the spectrum at as low a frequency as possible and keeping the homodyne and heterodyne spectra well separated in frequency space.

The source of the LO signal was a BK Precision `4064`, 120 MHz signal generator. This is a 14 bit device that can also interface with a computer over a serial connection making automated scans very easy. This device has low noise characteristics (2 ns timing jitter, $\pm$0.3 dBm amplitude accuracy, $\pm$2 ppm frequency accuracy) and was well suited for use in as all the LOs throughout the system.

The 80 and 77 MHz signals were mixed using a Minicircuits `ZAD-6+` to give a 3 MHz heterodyne spectrum and then filtered.

§4.4.4. Logging

Alongside the lab fileserver was a centralised log of the status of much of the lab at any particular time. Lab equipment was connected either to Raspberry Pis or to a standard desktop computer which would periodically poll the equipment for its status. The attached computer would be networked and then report the status of the hardware in question to a central lab internet relay chat (IRC) channel which was recorded to the fileserver. The synchronised log contained information on the chamber pressure, pump status, lab environmental conditions, laser status and power etc, and proved helpful when trying to understand the recorded particle data in a wider context. Software was written that made it quick and easy to request a plot of the pressure or laser power on a given day as these systems were continuously running.

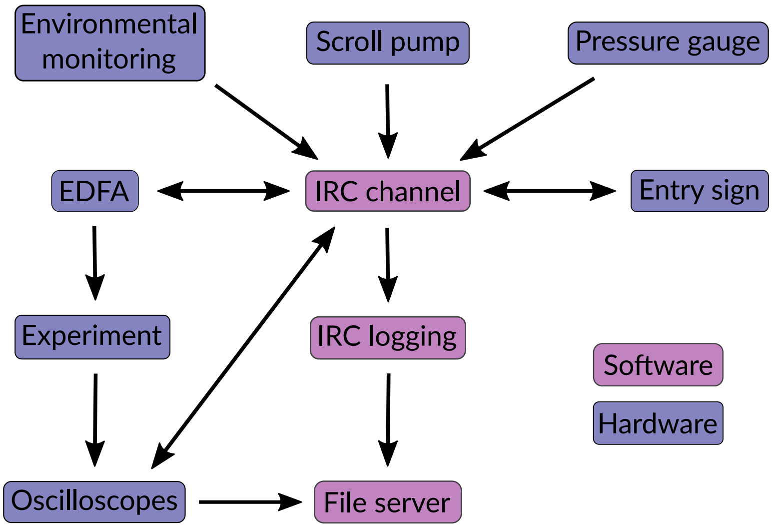

Fig. 4.27. *Systems level overview of the lab - Information flow and centralised logging architecture for the various hardware in the lab*

This IRC chat could also be used to allow lab equipment to communicate with one another when information was required. An example of this is the automatic laser safety notice outside the lab that could request the status of the different lasers and display health and safety access advice accordingly.

CHAPTER 5

Trap Characterisation

In this section the experimental setup constructed in this project will be characterised in order to provide a reference relative to similar systems used by other research groups. Parameters of the trapped particle system featured in plots in this chapter are extracted from experimental data fitted to as described in chapter 6.

§5.1. Trap frequency

The particle oscillation frequency is a function of the intensity gradient around the focus, which can be increased in a couple of ways. The first is better alignment, resulting in a narrower focus and therefore a steeper intensity gradient. The second method is to increase the overall optical power entering the focussing objective. Throughout the project alignment techniques improved resulting in a gradually improving alignment of the incident trapping beam to the objective in use at that time. Trap frequencies in the z direction reached as high as 170 kHz by the end of the project, compared to 40 kHz at the beginning, using a typical optical power of 2 W. The improvement over time was due to improved trap alignment and higher NA focussing provided by the parabolic mirror. Operating at pressures around 0.02 mbar, this proved to be a good optimum between tight confinement and minimising the risk of heating the particles to the point where they melt or disintegrate. The optical power can be reduced in order to reduce heating effects, lowering the trap frequency accordingly.

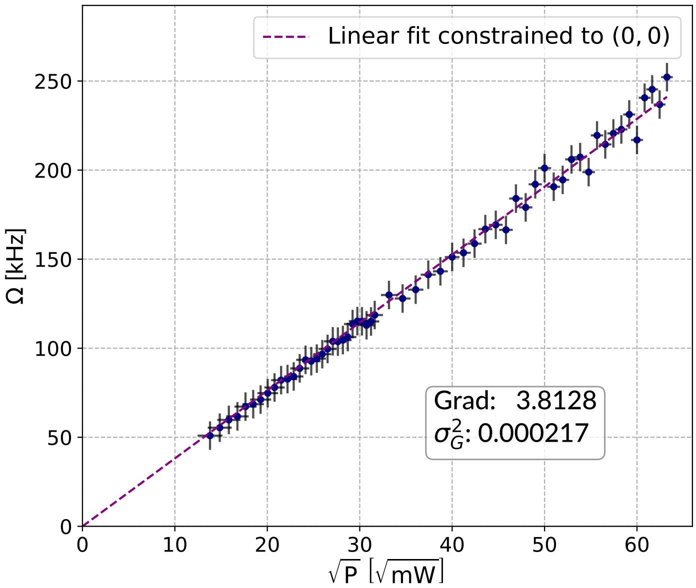

Fig. 5.1. *Trap frequency as a function of trapping laser power, with* $^{\Omega}/_{2\pi \mathrm{kHz}} = m\sqrt{^{P}/_{mW}}$. Ω *is found by fitting to the fundamental frequency peak in the recorded PSD.*

Figure 5.1 shows the square root relation between optical power and trap frequency. Laser power was measured using an integrating sphere optical power meter and the trap frequency was found by fitting a Lorentzian lineshape peak to a narrow region on the power spectrum, in a simplified version of the method explained in §6.4.2.

§5.2. Focal intensity

It is useful to assign values to the intensity at the trap site, doing so can show just how extreme the conditions around the particle are. We begin with the output power of the collimator and, lacking a computationally simple alternative, use the equations for Gaussian beam geometry defined in §2.2, bearing in mind that the paraxial approximations upon which they rely are strongly broken here. The numerical results found are likely to be accurate to an order of magnitude at best and should be treated with caution. For ease of calculation, we set the initial optical power to be 1 W. The collimator creates a focus with a waist diamter of 3.33 mm at a distance of 12.91 mm. The parabolic mirror is at a position $z = 0$ relative to this focus, meaning the collimated beam has a waist radius of $w_c(z) = {}^{3.33}/_{2} = 1.665$ mm at the mirror. The optical power contained within this radius is captured by the parabolic mirror and focussed, given by equation 5.1,

$$P_{\text{foc}} = P_0 \left[1 - \exp\left(\frac{-2r_{\text{mirror}}^2}{w_c^2(z)} \right) \right]. \tag{5.1}$$

The parabola focusses light down to a focal spot radius of w_0, meaning the focal spot area is

$$A_{\text{foc}} = \pi w_0^2. \tag{5.2}$$

The reflectivity of aluminium in the near infrared is approximately 95% [174], we call this R_{Al}. The power contained inside radius r of the focussed beam is

$$P_{\text{trap}} = R_{\text{Al}} P_{\text{foc}} \left[1 - \exp\left(\frac{-2r^2}{w^2(z)} \right) \right]. \tag{5.3}$$

To find the power inside the wasit radius at the focus, we write

$$P_{\text{trap}} = R_{\text{Al}} P_{\text{foc}} \left[1 - \exp\left(\frac{-2w_0^2}{w_0^2} \right) \right]. \tag{5.4}$$

Dividing this by the area of the focus, A_{foc}, gives the average intensity inside the focal waist,

$$\mathcal{I}_{\text{trap}} = \frac{P_{\text{trap}}}{A_{\text{foc}}}, \tag{5.5}$$

$$\mathcal{I}_{\text{trap}} = \frac{R_{\text{Al}} P_{\text{foc}} \left[1 - \exp\left(\frac{-2w_0^2}{w_0^2} \right) \right]}{\pi w_0^2}, \tag{5.6}$$

$$\mathcal{I}_{\text{trap}} = 94.1\,\text{GWm}^{-2}. \tag{5.7}$$

The peak intensity at the trap site can be calculated by taking the limit of equation 5.5 as $r \to 0$,

$$I(0,z) = \lim_{r\to 0} \frac{P_{\text{trap}}(r)}{A_{\text{foc}}(r)}, \tag{5.8}$$

$$I(0,z) = \lim_{r\to 0} \frac{R_{\text{Al}} P_{\text{foc}} \left[1 - \exp\left(\frac{-2r^2}{w^2(z)}\right)\right]}{\pi r^2}. \tag{5.9}$$

This can be simplified using L'Hôpital's rule, and the relevant values input to give,

$$I(0,z) = \frac{R_{\text{Al}} P_{\text{foc}}}{\pi} \lim_{r\to 0} \frac{4r \cdot \exp\left(\frac{-2r^2}{w^2(z)}\right)}{2r \cdot w^2(z)}, \tag{5.10}$$

$$I(0,z) = \frac{2R_{\text{Al}} P_{\text{foc}}}{\pi w^2(z)} = \frac{2R_{\text{Al}} P_0 \left[1 - \exp\left(\frac{-2r^2}{w^2(z)}\right)\right]}{\pi w^2(z)}, \tag{5.11}$$

$$I(0,z) = 229.1 \pm 30\,\text{GWm}^{-2} = 22.91 \pm 3\,\text{MWcm}^{-2}. \tag{5.12}$$

This very high intensity is the reason it is so important to use nanoparticles with very low absorption at the laser wavelength, and high emissivity at the peak blackbody emission wavelength (§2.4.7). The large uncertainty is due to the uncertainty in $w(z)$, a value which is difficult to measure experimentally. Absorption in an intensity such as that above creates a large heating effect and if not balanced by dissipation to the surrounding gas molecules, can cause the internal temperature of the particle to exceed its melting point at which point it is lost from the trap.

The intensity calculated in equation 5.12 implies a large electric field, which it can be useful to calculate when thinking about the forces involved in levitated optomechancics in comparison to other areas of experimental physics. The electric field is calculated using equation 2.79, and we calculate the peak electric field from the peak intensity,

$$E_0 = \sqrt{\frac{2I}{c\varepsilon_0}} = \sqrt{\frac{2 \times 229.1 \times 10^9}{c\varepsilon_0}} = 1.314 \times 10^7\,\text{Vm}^{-1}. \tag{5.13}$$

§5.3. Trap Site Geometry

Multiple focussing objectives were used during this project but the majority of the data presented later was taken using a single parabolic mirror with radius 1.665 mm and an NA of 0.98, corresponding to a half-angle $\theta = 78.5°$. This places the intensity maximum 0.33 mm in front of the flat mirror surface. Neglecting the small shift in equilibirum position due to the scattering force, the particle is trapped 1.02 mm from the nearest surface. The relations between these values can be found in §4.2.7.3.

We can use the equations for a Gaussian beam, bearing in mind that this situation is far outside what is reasonable to call paraxial, to get a very rough estimate of the focal waist diameter. As the particle trap frequencies are related to the width of the intensity maximum in each direction, we can use the ratio of frequencies to infer the shape of the trap site, where w_0 acts as a measure of the curvature of the trap site.

By the end of the project the fundamental radial and axial trap frequencies were measured to have a ratio of 2.12:1. By using equation 2.87 and substituting in the definition for intensity in terms of power and area we get,

$$U = -\frac{\alpha}{\pi w_0^2 c\varepsilon_0} P_0, \tag{5.14}$$

which can be Taylor expanded to second order in r and z about $r = 0$ and $z = 0$, ($U_r|_{z=0}$ and $U_z|_{r=0}$) respectively [159],

$$U_r|_{z=0} = -\frac{\alpha}{\pi w_0^2 c\varepsilon_0} P_0 + \frac{2\alpha}{\pi w_0^4 c\varepsilon_0} P_0 r^2 + \mathcal{O}(r)^3, \tag{5.15}$$

$$U_z|_{r=0} = \frac{\alpha}{\pi w_0^2 c\varepsilon_0} P_0 + \frac{\alpha\lambda^2}{\pi^3 w_0^6 c\varepsilon_0} P_0 z^2 + \mathcal{O}(z)^3. \tag{5.16}$$

The second order terms above can be substituted into equation 2.137 and thus the radial and axial frequencies can be found.

$$\omega_r^2 = \frac{2\alpha}{m\pi w_0^4 c\varepsilon_0} P_0 \tag{5.17}$$

$$\omega_z^2 = \frac{\alpha\lambda^2}{m\pi^3 w_0^6 c\varepsilon_0} P_0 \tag{5.18}$$

Taking the ratio of these frequencies we obtain a compact expression that depends on w_0,

$$\frac{\omega_r}{\omega_z} = \frac{\pi w_0}{\lambda}\sqrt{2}. \tag{5.19}$$

Using the measured ratio of trap frequencies, equation 5.19 gives $w_0 = 740$ nm $= 0.48\lambda$.

This value can be compared with that calculated using a non-paraxial method for finding the electromagnetic field distribution at a focus, as found in [16, 175, 176]. The beam waist diameter in the non-paraxial case is modelled as being the paraxial solution, modified by a function of the numerical aperture of the focus,

$$w\left(\mathrm{NA}\right) = f\left(\mathrm{NA}\right)\frac{\lambda}{\pi \mathrm{NA}}, \tag{5.20}$$

where $f\left(\mathrm{NA}\right)$ is the modification function. In the Gaussian beam case, $f\left(\mathrm{NA}\right) = 1$, and in all other cases $f\left(\mathrm{NA}\right)$ can be found by solving the integrals found in the references above in order to calculate the electric field around the focus for a given NA. The focal region is parameterised by $u = kz\sin^2(\theta)$ and $v = k\left(x^2+y^2\right)^{\frac{1}{2}}\sin(\theta)$, where θ is the convergence angle of the light and k is the trapping light wavenumber. The result of this calculation is shown in figure 5.2.

The field distribution can be used to calculate the $1/e^2$ radius of the focal spot and then find the modification factor ($f\left(\mathrm{NA}\right)$) required to yield this value when compared to the Gaussian beam case. The modification factor as a function of NA is plotted in figure 5.3.

In this project, the NA of the focussing objective used was 0.98, and we find that $f\left(0.98\right) = 1.493$, and therefore the predicted waist size from this method is $1.493 \times \frac{\lambda}{0.98\pi} = 752$ nm, in good agreement with the value found using the ratio of the trap frequencies above.

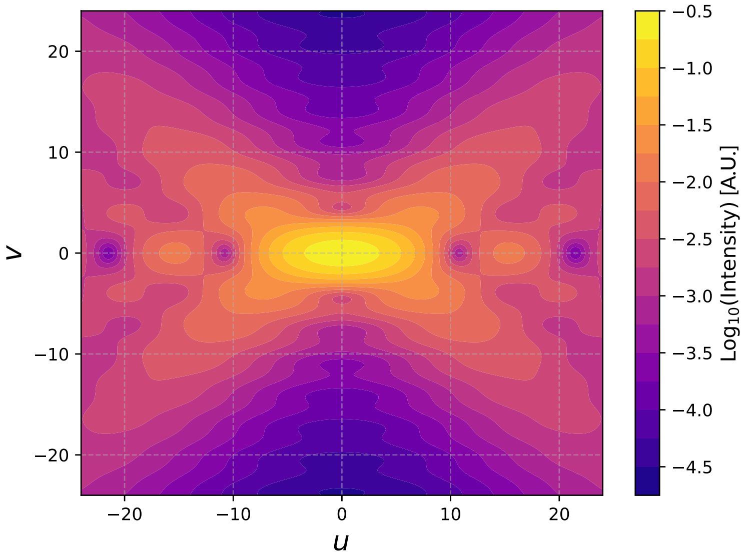

Fig. 5.2. *Near field intensity distribution calculated using the work of Pang* et al. *The adjusted waist size is extracted from this map and used to produce a function* $f(\mathrm{NA})$ *with which to modify the waist diameter calculated using the Gaussian beam equations.*

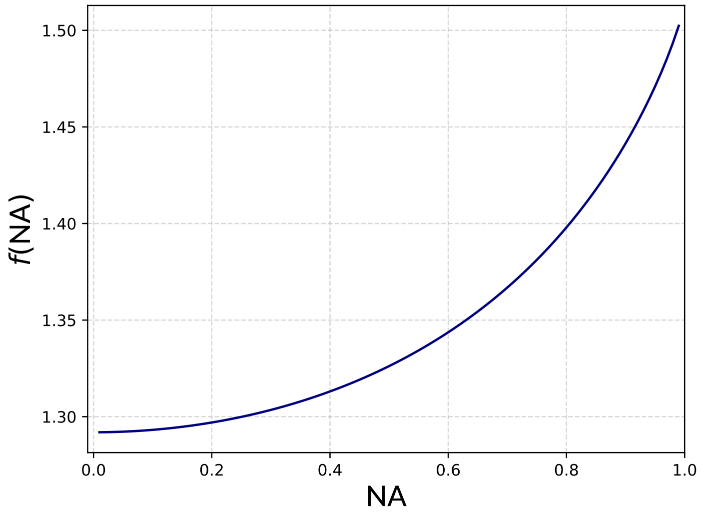

Fig. 5.3. *Modification factor that must be applied to the focal waist diameter as found from Gaussian beams, in order to match the computed non-paraxial field distributions [16].*

§5.4. Nanoparticles and Stokes damping

The nanoparticles used in this project were nominally 100 nm diameter silica, purchased from NanoComposix, and manufactured via a bottom-up approach known as the Stöber process [177] in which a molecular precursor is prepared in solution and silica molecules are allowed to aggregated around them. The process is highly controllable and allows manufacturers to produce nanoparticles with vary narrow size distributions ($\sigma_r = 4$ nm). These particles from NanoComposix are an appropriate radius for optical trapping and have low 1550 nm material absorption. These nanoparticles were imaged with a scanning electron microscope (SEM) in order to confirm their size statistics and shape. They were found to match the specifications given by the manufacturer, with an average diameter of 101.6 nm and a standard deviation of 3.7 nm when sampling over 320 nanoparticles. These measurements were performed using a centroid finding algorithm that locates nanoparticles and records intensity cross-sections of the local region of the SEM image in order to deduce a diameter. The surface of the nanoparticles appears smooth in SEM imagery, however it was difficult to determine this in detail with the equipment available. An SEM image of the particles deposited on a silicon substrate is shown in figure 5.4.

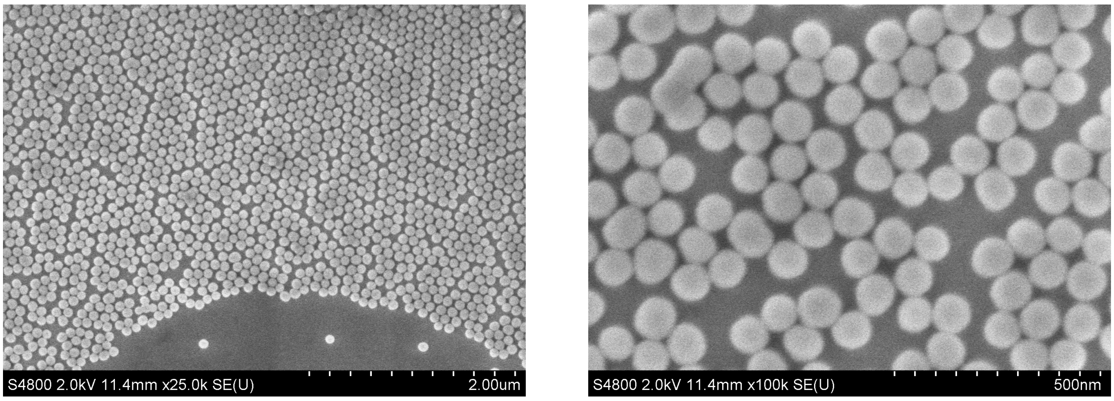

(a) *A wide shot shows close packing due to the Van der Waals forces that minimise surface energy.*

(b) *Greater zoom levels show the particles to be consistently quite circular and very close to the stated diameter.*

Fig. 5.4. *SEM images of the 100 nm silica nanoparticles used in this project, taken in the Centre for Nano-health at Swansea University.*

When more scattered light was needed due to a misaligned trapping beam 200 nm particles were used, but these were found to be less stable due to their higher cross-sectional area meaning they experience a greater scattering force, and were only used temporarily. An additional supplier of 100 nm particles was used later in the project to test whether less material absorption occurred and therefore these particles could be trapped at lower pressures, however they yeilded the same results as the NanoComposix product.

It is interesting to note that there has been a recent increase in the scientific consensus that these silica particles trapped by various research groups around the world are quite porous and therefore have a lower mass density than might be expected given their material makeup. Investigations into similar, although substantially larger, particles have calculated the density of silica particles to be 1.55 gcm^{-3} rather than the value for bulk silica of 2.22 gcm^{-3} [178]. This structural difference will have implications in chapter 6.

Stokes damping arises from the drag that a spherical particle experiences when moving through a fluid. The drag increases with gas pressure and with particle radius, the expression for which is covered in §2.5.2. A value for the damping rate, Γ, can be obtained by fitting to the PSD calculated from measured particle position data. This can be recorded as the gas pressure around the particle is decreased and a graph of Γ as a function of pressure can be plotted, as in figure 5.5. Multiple runs in which a particle is trapped at atmospheric pressure and then the chamber is evacuated are plotted together. The exact path each particle takes through this space can be seen to be different, likely as a result of slightly different particle radii. It is also possible that as the pressure is decreased and particles lose their ability to dissipate heat to their environment, their rising internal temperature causes the structure of the silica making up the particle to rearrange in a process similar to tempering. The changing structure could change the effective radius of the particle and in turn change the damping rate.

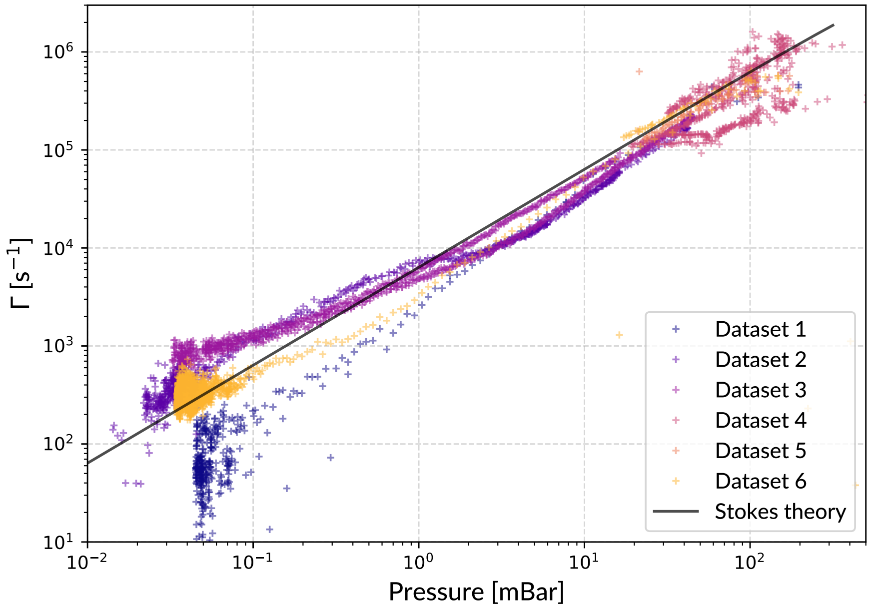

Fig. 5.5. *Comparison of measured and calculated Stokes damping for multiple particles as a function of pressure*

As the damping rate decreases, eventually the peaks in the PSD representing the harmonic motion of the particle are narrow enough that broadening due to local relative intensity noise (RIN) is visible below 10^{-1} mbar. This effect broadens intensity dependent spectral features by the intensity-time distribution that occurs during the capture of data. When RIN broadening is larger than broadening due to Stokes damping it becomes harder to measure Γ and therefore plots of Γ against pressure become far noisier below the threshold. This can be seen by plotting a single particle trajectory in the same parameter space as in figure 5.5. Figure 5.6 shows a single data set and the transition from Stokes dominant to RIN dominant can be seen just below 10^{-1} mbar.

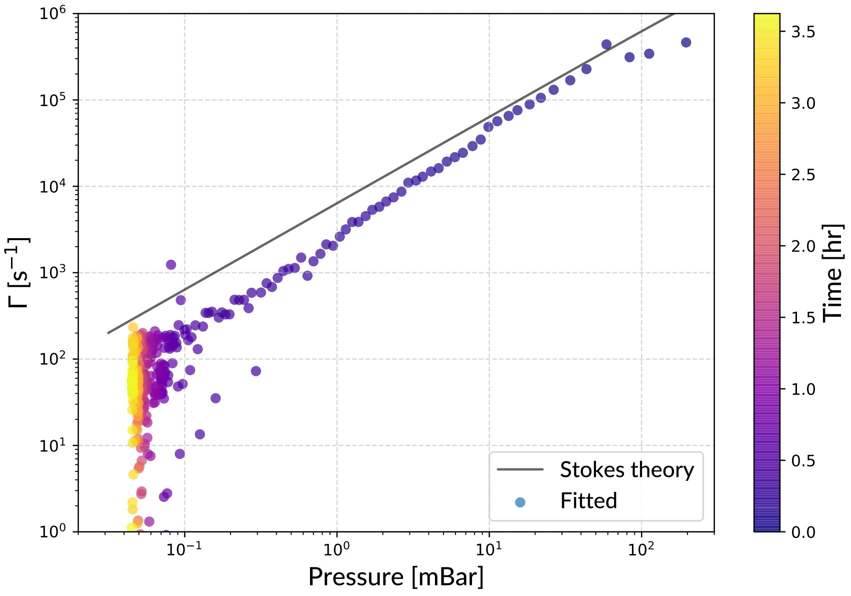

Fig. 5.6. *Isolating a single dataset clearly shows the increased uncertainty in Γ below the dominant broadening threshold.*

The threshold between Stokes damping dominant and RIN broadening dominant defines two distinct regions in which the lineshapes of the peaks on a particle PSD are described by two different functions. The importance in relation to fitting a theoretical spectrum to a measured PSD will be dicsussed further in §6.4.3. Two PSDs are shown below, focussing on a single peak corresponding to fundamental frequency of the particle oscillation. Figure 5.7 shows both the lineshape of a peak produced when a particle is above the threshold, with the shape dominated by Stokes broadening, and an analagous peak, but at a pressure where RIN broadening is dominant; the qualitative difference in shape can be seen.

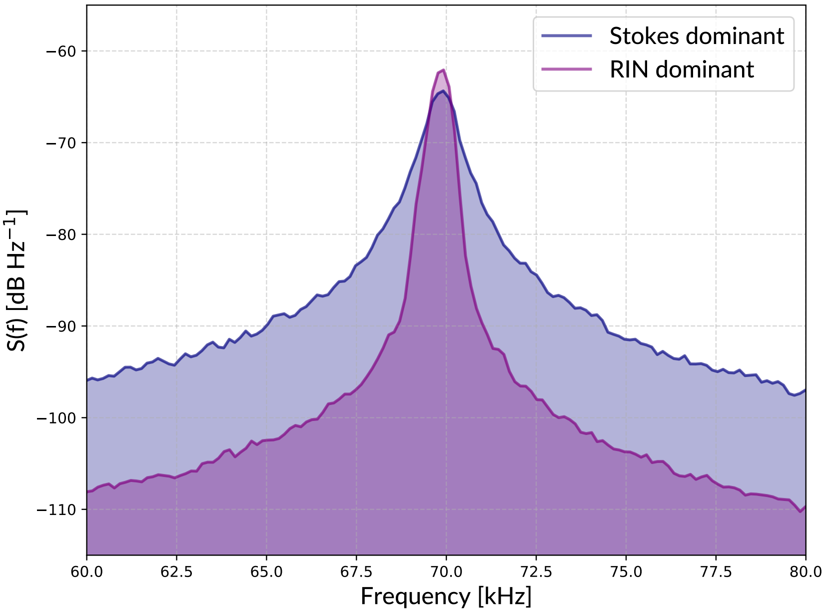

Fig. 5.7. *Comparison of Stokes dominant and RIN dominant spectral peaks - The Stokes dominant peak has a Lorentzian line shape, but the RIN dominant shape has a rounded, broadened region around the peak caused by the true, much narrower Lorentzian lineshape drifting in the x direction over time and being integrated to give the measured spectrum as is seen here. The very different overall widths are due to the different pressures the two sets of data were captured at, leading to the very different damping rates required to make the comparison between Stokes and RIN broadening.*

This concludes the description of the setup constructed during the project, as well as the characterisation of the trap. The hardware used has been detailed, with some justification given for the design decisions made. The most important parameters of the trap itself have been given, along with a description of the techniques used to process and analyse the data produced.

Now that the experimental setup has been discussed we will move onto the new research performed once the system was up and running. This research enabled the data plotted in this chapter to be recorded, and eventually went on to involve the development of a method for calculating uncertainties on the plots seen above.

CHAPTER 6

Parameter Estimation

The research completed in this thesis was towards the more effective estimation of state parameters, and their associated uncertainties, of an oscillating levitated nanoparticle. Previous techniques have been used in which spectra are estimated from time series, truncated to narrow "well behaved" regions and then fitted with a variety of (often undisclosed) cost functions. These methods can be improved upon with a more thorough treatment.

Much of the work in this chapter forms the main body of a paper published by the author during the course of the project, which can be found on the ArXiv [179] and the Journal of the Optical Society of America B [17]. There is a large degree of overlap between this thesis and the paper, as the same research led to the writing of both in parallel; as a result, this chapter in its entirety can be regarded as citing the paper above.

The newly developed technique involves the application of a technique from RF engineering [180–182] as a method for generating the power spectrum of a sinusoidal signal that is phase modulated by a Gaussian random process with known power spectrum. To our knowledge, this is a new application of an existing technique that should allow for more rigorous advances in this area of levitated optomechanics.

We calculate the autocorrelation function, R_{VV}, of the signal, V, where $V(t)$ is a sinusoidal function phase modulated by a function $\phi(t)$.

$$V(t) \propto \sin(\omega t + \phi(t)) \tag{6.1}$$

As in the common existing derivation, the Jacobi-Anger identity is used to obtain the correlation function R_{VV} as a summation of modified Bessel functions of the first kind, rather than unmodified [71,159], altering the resulting estimated physical parameters.

In our case, we were concerned with the generation of the power spectrum of intensity at the photodetector, a signal that is sinusoidally dependent on particle position, which we model as a stochastic harmonic oscillator. In our experiment we have designed the system such that the spectrum is stable in time and largely clear of polluting spectral features.

This method gives an exact power spectrum that depends on the state of the oscillator. This spectrum can be fit to, in order to estimate the parameters of an experimental system from recorded intensity data. The power spectrum is generated using the Middleton expansion of the harmonic oscillator for a signal that is sinusoidally related to a spectrum with some arbitrary given form, in our case the harmonic motion of the particle.

Using the expression for the PSD of detector signal, we show excellent agreement with experimental data, and use a least squares fitting algorithm to extract physically interesting parameters such as phase modulation depth (Φ), frequency, damping rate etc. We notice that below a transition frequency broadening due to Stokes drag no longer dominates over relative intensity noise (RIN) at the particle and broadening occurs that is not accounted for in the above model. We show that this broadening can be reasonably well modelled by applying a Gaussian intensity distribution that creates a summation of weighted PSDs for a range of trap frequencies and from this reproduces the measured lineshape. This method can be used to extract a value for the RIN at the particle by fitting the width of Gaussian needed to match the experimental spectra.

§6.1. Problem Statement

The current most common method for obtaining experimental parameters of levitated optomechanics systems is to fit to a homodyne PSD or simply integrate the PSD under the peaks to obtain a variance contribution. These PSDs are created from an interferometric signal produced on a photodiode between a phase modulated signal field and a reference field. PSDs such as these are well understood and take the form of a double sided spectrum of peaks separated by the particle oscillation frequency, centred on 0 Hz. In order to be useful, these spectra are either fitted as individual Lorentzian lineshape peaks or fitted to a summation of Bessel functions to give an approximation of the whole spectrum. From fittings such as these, parameters like damping rate and frequency can be obtained.

The method above presents a number of issues that can be improved upon using the technique described in this chapter. We see the issues as follows:

Spectral overlap - In many cases, spectral features are close together and can be broad enough that they run into one another. In cases such as these, the integrated area from individual features can be innacurate as they include contributions from other harmonics. This can lead to incorrect calculations for temperature and other thermodynamic quantities.

Sideband interference - The homodyne spectrum is centred around 0 Hz and so positive and negative sidebands are reflected about the origin and interfere either constructively or destructively depending on their relative phase. This changes the relative amplitudes of the odd and even order harmonics in the homodyne spectrum and means information about the particle motion encoded in the relative amplitudes of the orders is lost. As one of the main current goals of levitated optomechanics is to reach the standard quantum limit (SQL) of position measurement, we must attempt to preserve information about the particle. Where possible, the wastage of information like this should be avoided. It is noted that this is a problem specific to experimental geometries making use of back scattered light, and forward scatter systems are not affected.

Non-linear measurement dependence - There is an important distinction to be made between measuring the signal at the detector and measuring the position of the particle. As we saw in §3.3, the detector signal is only approximately linear with particle position over a small distance and in reality is only close to sinusoidal with position. This distinction has implications about the correct representation of the power spectrum of V, and will be discussed.

Anharmonic motion - In order to measure the power spectrum of a damped harmonic oscillator, we have to record the oscillator position for a time longer than the characteristic damping time, $1/\Gamma$. This time is such that by definition, after the time has elapsed the oscillator is no longer in phase with a pure sinusoid of the same frequency. It is then not representative of the physics involved, to model the motion of the oscillator (particle) as purely harmonic during the measurement period.

§6.2. Previous State of the Art

We can treat the traditional detection mechanism as taking the sum of two fields, a reference and a signal field, with phases θ and ϕ, and then taking the modulus squared to obtain a value for intensity. This signal is composed of a modulation due to the phase difference between the two fields ($\theta - \phi$) superimposed on a constant intensity offset.

$$V = |\mathbf{E}_{\text{tot}}|^2 = |\mathbf{E}_{\text{ref}} + \mathbf{E}_{\text{sig}}|^2 \tag{6.2}$$

$$\mathbf{E}_{\text{ref}} = E_{\text{ref},0} e^{i\omega t} \tag{6.3}$$

$$V = \left| E_{\text{ref},0} e^{i\omega t} + E_{\text{sig},0} e^{i\omega t} e^{i\kappa x(t)} \right|^2 \tag{6.4}$$

$$V = E_{\text{ref},0}^2 + E_{\text{sig},0}^2 + 2E_{\text{ref},0} E_{\text{sig},0} \cos\left(\omega t + \kappa x(t)\right) \tag{6.5}$$

The ideal case is where the phase of the reference field is fixed, the particle motion is purely harmonic and the phase shift is linear with particle position. In this case we have constant θ, and position and phase as a function of time are given by equations 6.6 and 6.7 respectively,

$$x(t) = x_0 \sin(\Omega t), \tag{6.6}$$

$$\phi(t) = \phi_0 \sin(\Omega t), \tag{6.7}$$

with $\phi_0 = \kappa x_0$.

We use the trigonometric identity in equation 6.8, to rewrite the sinusoidal dependence of detector signal on particle position,

$$\cos(\alpha - \beta) \equiv \cos(\alpha)\cos(\beta) + \sin(\alpha)\sin(\beta). \tag{6.8}$$

The rewrite gives us the following,

$$\cos(\phi_0 \sin(\Omega t - \theta)) \equiv \cos(\phi_0 \sin(\Omega t))\cos(\theta) + \sin(\phi_0 \sin(\Omega t))\sin(\theta). \tag{6.9}$$

We can substitute for the two terms in equation 6.9 using the real-valued expressions of the Jacobi-Anger identity (equations 6.10 and 6.11),

$$\cos(z \sin(\varphi)) \equiv J_0(z) + 2\sum_{n=1}^{\infty} J_{2n}(z)\cos(2n\varphi), \tag{6.10}$$

$$\sin(z \sin(\varphi)) \equiv 2\sum_{n=1}^{\infty} J_{2n-1}(z)\sin\left[(2n-1)\varphi\right], \tag{6.11}$$

where J_n is the n$^{\text{th}}$ order Bessel function. We obtain an expression for detector signal that is a sum of Bessel functions,

$$\cos(\phi_0 \sin(\Omega t - \theta)) = \cos(\theta)\left[J_0(z) + 2\sum_{n=1}^{\infty} J_{2n}(z)\cos(2n\varphi)\right] + \sin(\theta)\left[2\sum_{n=1}^{\infty} J_{2n-1}(z)\sin\left[(2n-1)\varphi\right]\right]. \tag{6.12}$$

This can be expanded, and we notice that $\sum_{n=1}^{\infty} J_{2n} \equiv \sum_{n\geq 2}^{\text{even}} J_n$ and $\sum_{n=1}^{\infty} J_{2n-1} \equiv \sum_{n\geq 1}^{\text{odd}} J_n$, so we write

$$\cos\left[\phi_0 \sin(\Omega t) - \theta\right] = \cos(\theta) J_0(\phi_0) + 2\cos(\theta)\sum_{n\geq 2}^{\text{even}} J_n(\phi_0)\cos(n\Omega t) + 2\sin(\theta)\sum_{n\geq 1}^{\text{odd}} J_n(\phi_0)\sin(n\Omega t), \tag{6.13}$$

and use this as our expression for signal. When using this (or similar) expressions in calculations, it is common to sum to approximately $n = 10$, as this sum determines how many sideband orders are used and often fewer than 6 are visible. The choice of n ensures that all peaks above the noise floor are treated without extending the computation time needlessly.

The variable κ is the rate of change of phase with respect to particle position, and its value depends on the wavelength of light involved as well as the focussing geometry. There are two subtly different experimental geometries for capturing the fields involved in this homodyne scheme: forwards scatter and backwards scatter. The practical difference between the two is whether the collection optics are up or downstream of the particle in the beamline. In the forwards scatter case (usually performed using a focussing lens or microscope objective) the phase shift imparted onto the signal light is simply given by the Gouy shift (equation 2.16) accumulated through the focus, and is $\kappa = {}^{1}\!/_{z_R}$. In the backwards scatter case the phase is more sensitive to position and is twice the wavenumber, subtract the Gouy shift: $\kappa = 2k - {}^{1}\!/_{z_R}$, where k is the trapping light wavenumber and z_R is the Rayleigh range of the focussed light.

In equation 6.13 we can see the emergence of the behaviours of the odd and even sidebands that reflect about the origin and interfere with each other. This occurs because the two fields being mixed are at the same frequency and therefore have a difference frequency of 0 Hz, meaning the spectrum is centred on 0 Hz. In equation 6.13 this is represented by the fact that the time averages of both θ and ϕ do not depend on t.

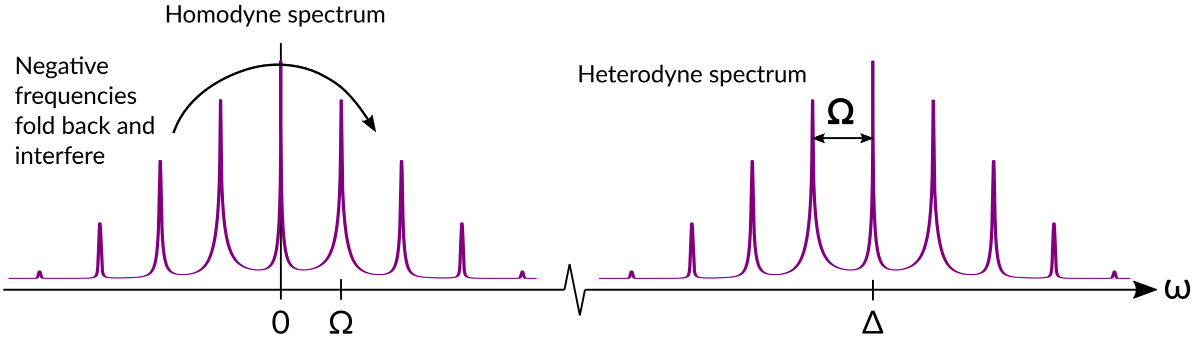

Fig. 6.1. *Homodyne and heterodyne spectra - Spectra are positioned at the difference frequency of the two fields from which they are formed.*

Instead of holding θ constant, we can make the subtitution $\theta = \Delta t + \theta_0$, where $\Delta \gg \Omega$, using a Heterodyne measurement (§3.4) to shift the spectrum to be centred on frequency Δ, removing the interference of negative and positive sidebands.

We saw in §2.5.1 that the PSD of damped harmonic oscillator is given by

$$S_{zz}(\omega) = \frac{2k_BT}{m}\frac{\Gamma}{\left(\omega^2-\Omega^2\right)^2+\Gamma^2\omega^2}, \tag{6.14}$$

which has previously been combined with equation 6.13 by setting $\theta = \pi/2$ and assuming that the amplitude of the phase modulation is small. This allows us to approximate the signal as linear with particle position over the range in question and simplify equation 6.13 significantly to obtain equation 6.16,

$$\cos\left[\phi_0\sin(\Omega t)-\theta\right] = \cos\left(\frac{\pi}{2}\right)J_0(\phi_0) + 2\cos\left(\frac{\pi}{2}\right)\sum_{n\geq 2}^{\text{even}} J_n(\phi_0)\cos(n\Omega t) + 2\sin\left(\frac{\pi}{2}\right)\sum_{n\geq 1}^{\text{odd}} J_n(\phi_0)\sin(n\Omega t), \tag{6.15}$$

$$\cos\left[\phi_0\sin(\Omega t)-\theta\right] = 2\sum_{n\geq 1}^{\text{odd}} J_n(\phi_0)\sin(n\Omega t). \tag{6.16}$$

This is valid for forward scatter experiments where the spatial exploration amplitude of the particle is much smaller than the wavelength of the trapping light, but isn't representative otherwise. Equations 6.14 and 6.16 represent two fundamentally different physical systems. Equation 6.14 gives the power spectrum of a DHO which can only be estimated by recording motion for longer than $1/\Gamma$, meaning that by definition the motion of the oscillator cannot by purely harmonic as is assumed when deriving equation 6.16. In the literature these are combined *ad-hoc* by scaling a delta function at each frequency according to the form of equation 6.14. Figure 6.2 shows the power spectra of the two different approaches, which are not equivalent even in the limit of low Γ.

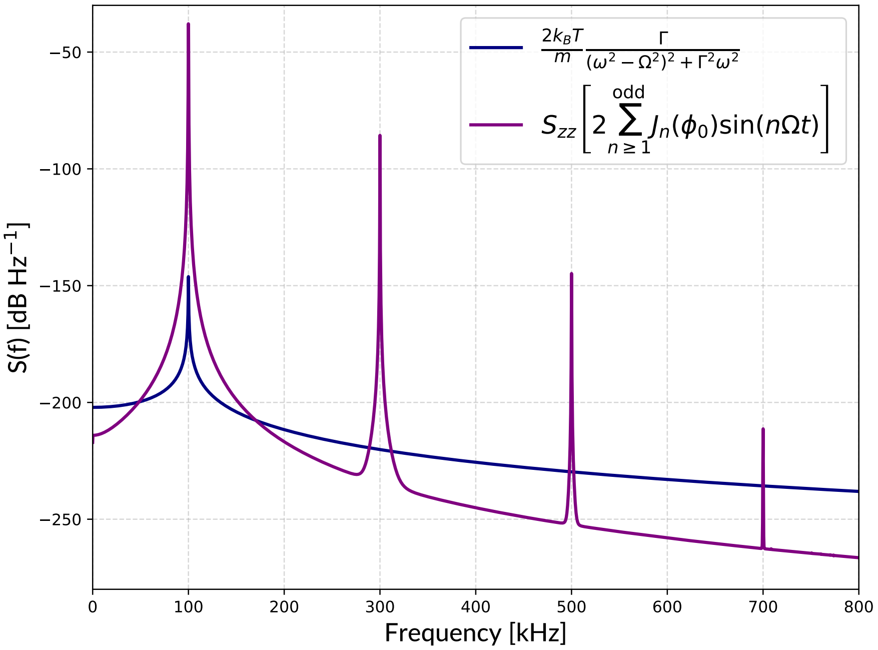

Fig. 6.2. *The PSD of the particle motion according to the PSD of the DHO and the summation of Bessel functions method. These are not equivalent and require incompatible assumptions. The legend shows the analytical form of the DHO PSD, however the time domain form of the Bessel function method is shown, which is then used to calculate the PSD shown in the figure via a Fourier transform of equation 6.16.*

In the next section we propose a more exact method that can be used as a replacement.

§6.3. Applying the Middleton Spectrum

The damping rate Γ can be used to give a duration $^{1}/_{\Gamma}$, for which the particle oscillation can be said to be harmonic. In order to obtain a power spectrum, we must record the signal for a time longer than $^{1}/_{\Gamma}$ and it is therefore inaccurate to assume the particle position is sinusoidal with time over the whole period. Instead we treat the particle as a stochastic harmonic oscillator, phase modulated by a Gaussian random process $\phi(t)$. The signal becomes

$$V(t) = V_0 \sin\left(\omega t + \phi(t)\right) \tag{6.17}$$

where $V_0 = 2E_{\mathrm{ref},0}E_{\mathrm{sig},0}$. The correlation function of $V(t)$ is

$$R_{VV}(\tau) = \langle V(t)V(t-\tau)\rangle_t \tag{6.18}$$

where τ is the time delay between correlated samples. This has the form, [183]

$$R_{VV}(\tau) = V_0^2 \exp\left[R_{\phi\phi}(\tau) - \left\langle \phi^2(t)\right\rangle\right]. \tag{6.19}$$

This has the frequency-domain form, [180, 182]

$$\sigma_{VV}(t) = \frac{1}{2}e^{-\langle\phi^2\rangle}\sum_{n=0}^{\infty}\frac{\left\langle\phi^2\right\rangle^n}{n!}\sigma_{xx}(f)\overset{n}{\circledast}\sigma_{xx}(f), \tag{6.20}$$

which we call the Middleton spectrum. For practicality in calculation we will be using a maximum n of 10, after which there is negligible alteration to the spectrum. The phase variance is given by $\left\langle\phi^2\right\rangle = \kappa^2\left\langle x^2\right\rangle$ and $\sigma_{xx}(f) = {}^{S_{xx}(2\pi f)}/_{\left\langle x^2\right\rangle}$ is the normalized power spectrum of position, such that $\int_{-\infty}^{+\infty}\sigma_{xx}(f)df = 1$.

Equation 6.20 uses the n$^{\text{th}}$ order convolution infix operator, $\overset{n}{\circledast}$, which is defined recursively as

$$a\overset{n}{\circledast}a = a\circledast a\overset{n-1}{\circledast}a \tag{6.21}$$

with $a\overset{2}{\circledast}a = a\circledast a$ being the standard convolution operation, $a\overset{1}{\circledast}a = a$, and $a\overset{0}{\circledast}a = \delta$ being the Dirac delta function.

Equation 6.20 produces a spectrum similar to equation 6.16, with peaks spaced by the oscillator frequency Ω (figure 6.3). The recursive convolution means that the fundamental frequency peak and the other low order peaks recieve amplitude contributions from higher-order convolutions, increasing their integrated area above that of the high-order peaks. This represents the fact that there is physically only the fundamental mode of particle oscillation, and higher orders are created by the mixing process.

The centre frequency f_0 mixes with the particle oscillation frequency f to make the first order peak; these first order peak signals at $f_0 + f$ then mix with particle frequency again at f to create a peak at $f_0 + 2f$. This process is not 100% efficient however and so the second order peak is smaller in amplitude than the first. The process then continues creating smaller peaks until they are below the noise floor, with high-order peaks contributing significantly less to the overall signal variance. The integrated area under a peak is proportional to the energy contained in the corresponding signal mode and is calculated by a series summation from the recursive convolution process.

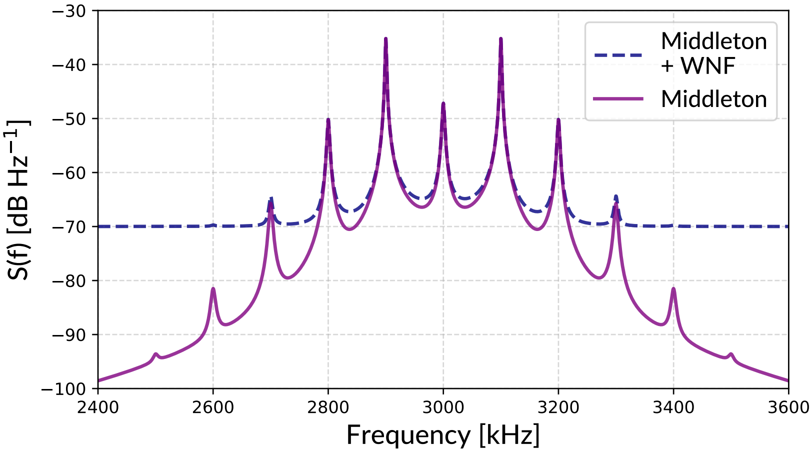

Fig. 6.3. *Theoretical Middleton spectrum calculated for $\phi = 0.5$, $\Omega = 2\pi \times 100$ kHz and $\Gamma = 1000$. The shape of the spectrum is shown with and without an artificial white noise floor (WNF) as it will be compared to experimentally measured results which feature such a noise floor that masks the lower amplitude peaks.*

§6.3.1. Narrow band processes

When Γ is small, $\phi(t)$ can be classed as a narrow-band process and we treat it as having a sinusoidal correlation function (equation 6.22), rather than relying on it having a sinusoidal position function, as is used to produce equation 6.16. We do this to allow us to make a subsitution into equation 6.19, in which we replace $R_{\phi\phi}$ with

$$R_{\phi\phi} = \left\langle \phi^2 \right\rangle \cos(\Omega t). \tag{6.22}$$

To find the correlation function of V from this, we first rearrange equation 6.19 slightly, and then substitute in $R_{\phi\phi}$ to get equation 6.24,

$$R_{VV}(t) = V_0^2 e^{-\left\langle \phi^2 \right\rangle} e^{R_{\phi\phi}} \tag{6.23}$$

$$R_{VV}(t) = V_0^2 e^{-\left\langle \phi^2 \right\rangle} e^{\left\langle \phi^2 \right\rangle \cos(\Omega t)}. \tag{6.24}$$

We can represent the term $e^{\left\langle \phi^2 \right\rangle \cos(\Omega t)}$ in equation 6.24 as $\exp\left(R_{\phi\phi}\right) = e^{\left\langle \phi^2 \right\rangle \cos(\Omega t)} = e^{iz\cos(\vartheta)}$, where $z = -i\left\langle \phi^2 \right\rangle$ and $\vartheta = \Omega t$. We do this so that is is recognisable as a form that we can replace using the Jacobi-Anger (J-A) identity; although we will first manipulate the form of this replacement, starting with the commonly used expression for J-A,

$$e^{iz\cos(\vartheta)} = \sum_{n=-\infty}^{\infty} i^n J_n(z) e^{in\vartheta}. \tag{6.25}$$

This sum from $-\infty$ to $+\infty$ can be split into an $n = 0$ term and a sum over the positive and negative contributions for $n \geq 1$,

$$e^{iz\cos(\vartheta)} = J_0(z) + \sum_{n=1}^{\infty} \left[i^n J_n(z) e^{in\vartheta} + i^{-n} J_{-n}(z) e^{-in\vartheta} \right]. \tag{6.26}$$

We can use the fact that $J_{-n}(x) = (-1)^n J_n(x)$ to rewrite the second term in the sum in equation 6.26, and obtain equation 6.27,

$$e^{iz\cos(\vartheta)} = J_0(z) + \sum_{n=1}^{\infty} \left[i^n J_n(z) e^{in\vartheta} + i^{-n}(-1)^n J_n(z) e^{-in\vartheta} \right]. \tag{6.27}$$

After making the small simplification $i^{-n}(-1)^n = i^n$, we write

$$e^{iz\cos(\vartheta)} = J_0(z) + \sum_{n=1}^{\infty} \left[i^n J_n(z) e^{in\vartheta} + i^n J_n(z) e^{-in\vartheta} \right], \tag{6.28}$$

which we simplify again using $e^{i\theta} + e^{-i\theta} = 2\cos(\theta)$ to get,

$$e^{iz\cos(\vartheta)} = J_0(z) + 2\sum_{n=1}^{\infty} i^n J_n(z) \cos(n\vartheta). \tag{6.29}$$

This is the form that we use to replace $e^{\langle\phi^2\rangle\cos(\Omega t)}$ in equation 6.24, with $z = -i\langle\phi^2\rangle$ and $\vartheta = \Omega t$. This replacement is made explicit in equation 6.30,

$$e^{\langle\phi^2\rangle\cos(\Omega t)} = e^{iz\cos(\vartheta)} = J_0\left(-i\left\langle\phi^2\right\rangle\right) + 2\sum_{n=1}^{\infty} i^n J_n\left(-i\left\langle\phi^2\right\rangle\right)\cos(n\Omega t). \tag{6.30}$$

From here we use the relation between the unmodified and modified Bessel functions, $J_n(ix) = i^n \mathcal{I}_n(x)$, to express equation 6.30 in terms of modified Bessel functions,

$$e^{\langle\phi^2\rangle\cos(\Omega t)} = \mathcal{I}_0\left(\left\langle\phi^2\right\rangle\right) + 2\sum_{n=1}^{\infty} i^n i^n \mathcal{I}_n\left(\left\langle\phi^2\right\rangle\right)\cos(n\Omega t), \tag{6.31}$$

which can be simplified using $\mathcal{I}_n(-x) = (-1)^n \mathcal{I}_n(x)$ to obtain our final expression that will be substitued in for $e^{R_{\phi\phi}}$,

$$e^{\langle\phi^2\rangle\cos(\Omega t)} = \mathcal{I}_0\left(\left\langle\phi^2\right\rangle\right) + 2\sum_{n=1}^{\infty} \mathcal{I}_n\left(\left\langle\phi^2\right\rangle\right)\cos(n\Omega t). \tag{6.32}$$

This substitution is made in equation 6.24, and we get our final form of the autocorrelation function of V,

$$R_{VV}^{(\text{narrow})}(t) = V_0^2 e^{-\langle\phi^2\rangle}\left[\mathcal{I}_0\left(i\left\langle\phi^2\right\rangle\right) + 2\sum_{n=1}^{\infty} \mathcal{I}_n\left(i\left\langle\phi^2\right\rangle\right)\cos(n\Omega t)\right]. \tag{6.33}$$

Making the substitution $\Phi = \sqrt{\langle\phi^2\rangle}$, as will be discussed in a moment, we can more concisely write

$$R_{VV}^{(\text{narrow})}(t) = V_0^2 e^{-\Phi^2}\left[\mathcal{I}_0 + 2\sum_{n=1}^{\infty} \mathcal{I}_n \cos\left(n\Omega t\right)\right] \tag{6.34}$$

This form differs from the previously used non-modified Bessels [77, 159], which we suggest are valid only for small values of Φ. The relative ratios of the fractions of a signal contained in the nth order peak of a particle spectrum is given in the figure below, in which we can see the divergence of the non-modified and modified Bessel functions J_n and $\mathcal{I}_n$ respectively.

Importantly, the non-modified Bessel functions have a zero crossing at around 3.8, which has a confusing physical meaning in the previously used case. This new approach does not present such a problem as the modified Bessel functions do not have a zero crossing.

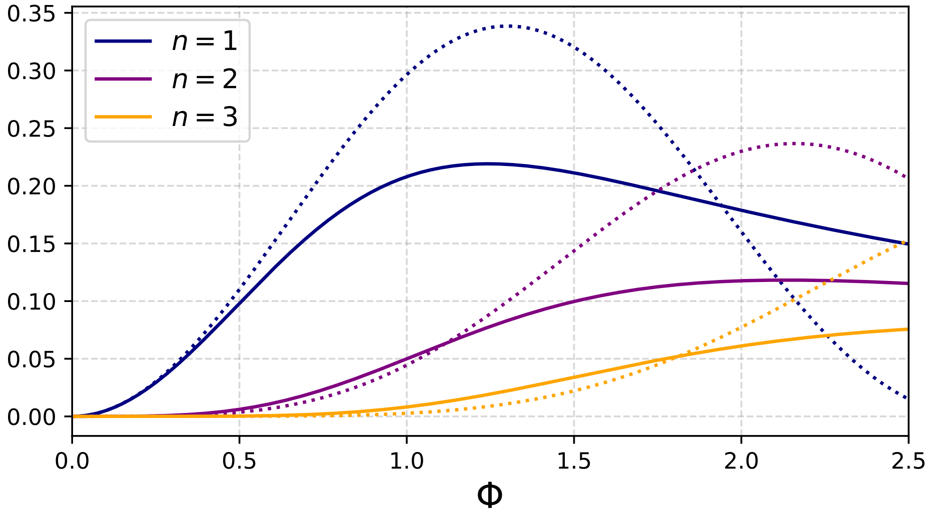

Fig. 6.4. *Ratios of the modified and non-modified Bessel functions [17]. The importance of this new method at large values of* Φ *can be seen in the divergence of the two functions. The variance of* $\phi = \phi_0 \cos(\Omega t)$ *is* $\phi_0^2/2$*, so we plot* $J_n(\sqrt{2}\Phi)^2$ *and* $e^{-\Phi^2} I_n(\Phi^2)$*, in order to draw the most sensible comparison.*

§6.3.2. Phase modulation depth: Φ

When fitting equation 6.20 to an experimentally recorded power spectrum, one of the fitting parameters is the phase modulation depth, Φ. This describes the root-mean-squared (RMS) phase modulation amplitude as a proportion of an entire trapping light wavelength. If the effective wavenumber is known to high accuracy, Φ can be used to calculate the root-mean-squared spatial exploration amplitude of the particle. Φ is defined in equation 6.35 [180].

$$\Phi = \sqrt{\langle \phi^2 \rangle} = \kappa x_{\mathrm{RMS}}, \tag{6.35}$$

$$\Phi = (k + k')x_{\mathbf{RMS}}, \tag{6.36}$$

where k' is the local wavenumber at the trap site, incorporating the effect of the Gouy shift. Using the Gouy shift from the paraxial Gaussian beam model, we obtain

$$k' = k - \frac{1}{z_R} = \frac{2\pi}{\lambda} - \frac{\lambda}{\pi w_0^2}, \tag{6.37}$$

however as our geometry is highly non-paraxial (NA=0.98) we can use the work of Wolf, Pang *et al.* [16,176] to make a correction to the Gouy shift. The method in the references assume a rectangular intensity distribution, and from this allow us to calculate the phase profile. In Gaussian beams this would be parameterised as $1/z_R$, where z_R is the Rayleigh range, calculated using the NA of the focussed light. Using the method in [16], we calculate $\partial_x \phi$ for the appropriate convergence angle and compare it with the simpler case from Gaussian beams. The ratio of the rates of change is found to be 1.41, and so we use this to calculate the corrected value for κ.

From this corrected Gouy shift we can calculate the RMS oscillation amplitude,

$$x_{\mathrm{RMS}} = \frac{\Phi}{\kappa} = \frac{\Phi}{\frac{4\pi}{\lambda} - \frac{1.41\lambda}{\pi w_0^2}} \tag{6.38}$$

It is revealing to actually calculate the values of k and k', to show the effect of the Gouy shift. In §5.3 the ratio of trap frequencies was used to calculate the focal waist radius, and was found to be 0.48λ. This technique approximates the cross section of the intensity distribution to be Gaussian, an assumption that is accurate close to the maximum, even in this strongly non-paraxial case.

The wavenumber of the scattered light does not experience a Gouy shift as it propagates spherically, whereas the incoming trapping beam is focussed and so requires a wavenumber correction. k is found in equation 6.39,

$$k = \frac{2\pi}{\lambda} = 4.05 \times 10^6\ \mathrm{m}^{-1}. \tag{6.39}$$

The Gouy shift corrected wavenumber of the trapping light is found in equation 6.40,

$$k' = \frac{2\pi}{\lambda} - \frac{1.41\lambda}{\pi w_0^2} = 2.80 \times 10^6\ \mathrm{m}^{-1}. \tag{6.40}$$

There is a very appreciable difference between these wavenumbers, due to the tight focussing. The ratio of the two works out to be $k'/k = 0.69$, and $\kappa = k + k' = 6.85 \times 10^6\ \mathrm{m}^{-1}$.

§6.3.3. Temperature to mass ratio

In §2.5.3 we explored the idea of equipartition and how each quadratic degree of freedom of a physical system contains a given amount of energy, related to the relevant thermodynamic temperature of the system. One such quadratic degree of freedom is the potential energy stored in the "spring" that is the optical gradient force. The time averaged energy contained in a single dimension of spring potential is given by equation 6.41,

$$\frac{1}{2} m\Omega^2 x_{\mathrm{RMS}}^2 = \frac{1}{2} k_B T_{\mathrm{CoM}}. \tag{6.41}$$

We can substitue in x_{RMS} from §6.3.2 to get the temperature to mass ratio as a function of measurable parameters,

$$m\Omega^2 \left[\frac{\Phi}{\kappa}\right]^2 = k_B T_{\mathrm{CoM}}, \tag{6.42}$$

$$\frac{T_{\mathrm{CoM}}}{m} = \frac{\Omega^2}{k_B}\left[\frac{\Phi}{\kappa}\right]^2. \tag{6.43}$$

§6.4. Results from Middleton

We now look at how one can use the method described in the previous section and show the results of doing so. It will be shown that the new method closely fits measured power spectra and some of the quantitative results generated using the method will be discussed.

§6.4.1. Spectral density estimation

When calculating the power spectrum of any recorded quantity made up of discrete data points we are performing a spectral density estimation, which is an inexact process. Usually, and as is the case in this project, we use Welch's method (see §2.5.1) of dividing the time series data into sections and Fourier transforming to obtain periodograms that can be averaged. Welch's method provides a good approximation of the true power spectrum, especially when a large number of chunks are used, but its important to remember that the dataset produced has been subject to a windowing function and can contain artefacts that are a result of the finite-time nature of the sample.

The optimum size of the window used for a particular set of data depends on the desired spectral resolution of the PSD. The minimum size of spectral features visible in the PSD will be equal to the bandwidth of the windowing function used to create the PSD, given by Nyquist's theorem. Windows wide enough to resolve this minimum feature size should therefore be used, maximising the number of segments (remembering that windows will overlap by a certain percentage of their width) that will be used to calculate the periodogram.

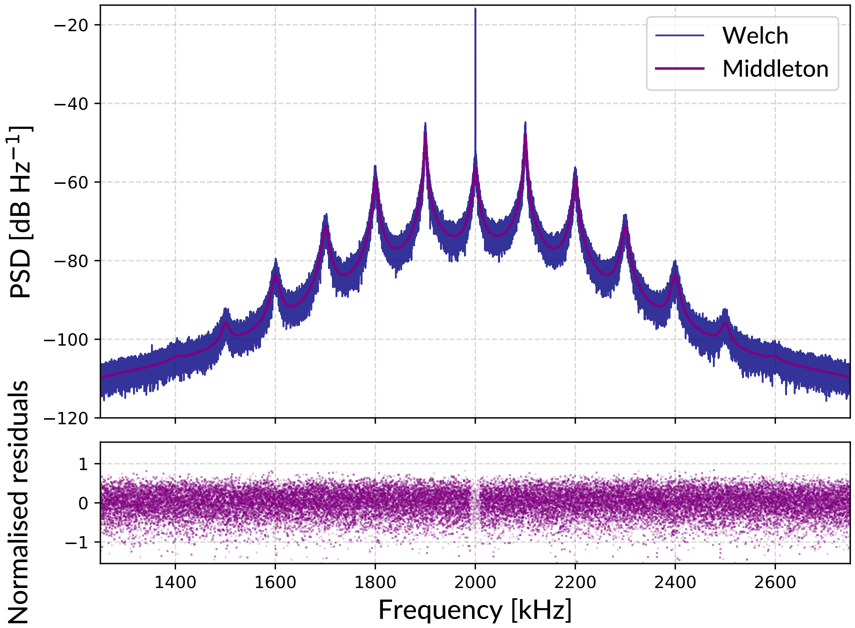

Fig. 6.5. *Power spectral density of a simulated oscillator and corresponding Middleton spectrum. These show excellent agreement and the normalised residuals can be seen to be featureless and* χ_k^2 *distributed.*

Welch's method produces a slightly biased spectral density estimate, meaning that the mean of the estimate is correct but data points are not normally distributed around the true power spectrum. In fact the normalised residuals of the measured PSD and Middleton spectrum are χ_k^2 distributed, where the number of degrees of freedom of the distribution is equal to twice the number of non-overlapping time series segments that were used in the spectral density estimate [184]. In the limit of a large number of degrees of freedom, the χ^2 distribution tends to the normal distribution and so it is beneficial to use many such time series segments and an appropriate windowing function (such as the Tukey–Hanning window [185]) so that we can use a standard least squares minimisation algorithm in order to fit a theoretical curve to the power spectrum estimate. Figure 6.5 shows the power spectrum of a simulated particle position signal overlaid with a Middleton spectrum. Normalised residuals are χ_k^2 distributed around zero. Figure 6.6 shows a histogram of the normalised residuals and a fitted χ_k^2 probability distribution function that matches very closely.

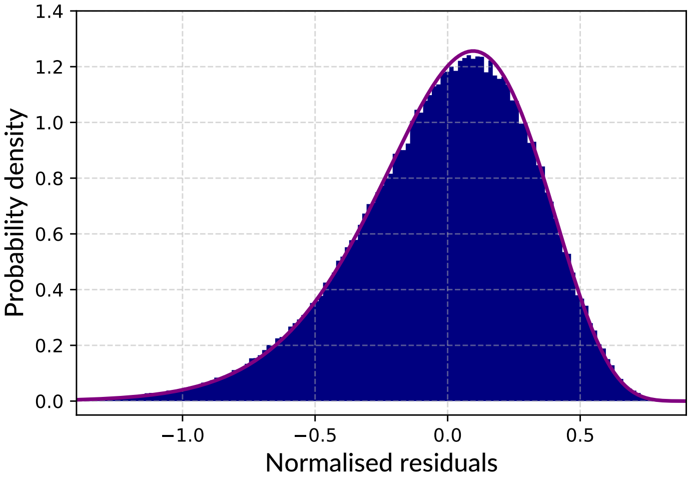

Fig. 6.6. *A histogram of the residuals from figure 6.5 and a fitted χ_k^2 probability distribution function. In this example a low number of time series chunks was used in order to make the difference from Gaussian more discernable by eye. Here the number of degrees of freedom $k = 18$.*

It is worth noting that in the case where a measured signal is linear with oscillator position, it is possible to estimate the physically interesting parameters of the oscillator dynamics directly from time series data [186], these methods replace the need to perform spectral density estimates and then least squares fitting with a likelihood calculation for the physical parameters themselves [187]. Unfortunately, real experimental time series are noisy and contain contributions due to aspects of the experiment not captured in the model. These unwanted features are difficult to remove in the time domain but can be filtered out with ease in the frequency domain and so we perform our analysis by this non-parametric approach. Additionally, time domain methods such as autoregressive maximum likelihood used for likelihood estimation rely on linearity of measurement, a property not possessed by our system. These factors combine to mean that it is easier to process the data produced by such a system in the frequency domain as described below.

§6.4.2. Least-squares fitting to a PSD

In general, fitting algorithms take a dataset and a function with one or more arguments and attempt to find the argument(s) to the function that most closely reproduce the example dataset. Fitting algorithms are used in virtually all branches of science to fit models to real-world or simulated data in order to test hypotheses. One of the most common fitting algorithms is least-squares fitting or least-squares regression. In this case, the minimisation process attempts to minimise the error between function output and data by taking the square of the difference between the two. Using a dataset, D, containing M points along an x axis, and a function f that can be evaluated along this same axis using two model parameters a and b, the error, $\mathcal{E}$, is given by

$$\mathcal{E} = \sum_{i=0}^{M} \left(f(x, a, b) - D_i \right)^2 . \tag{6.44}$$

In general we can say that if a model function takes N fit parameters (2 in the example above) then the fitting algorithm is exploring a scalar, N-dimensional parameter space where the value at any point is the error from equation 6.44. Ideally, a fitting algoritm will locate the global minimum in the space at which the fit parameters and model most closely represent the data. In the N=2 case, its relatively easy to visualise this on a plane and for higher values of N the analogy of exploring a volume can be useful. If the dataset is unbiased and therefore points are normally distributed in each axis then the parameter space of error can be thought of as an N-dimensional multi-variate Gaussian, with a (not neccessarily equal) width in each of the N directions.

In some models, the fit parameters are not independent and perturbing the value of one requires changing another in order to minimise the error. This is called covariance and can be graphically represented by the ellipsoid-like shape of the error space being aligned along an axis other than those of the unit vectors of the space. For this reason, one must be careful when looking at cross-sections of the N-dimensional space, as there may be unanticipated behaviours present off-axis. Figure 6.7 shows a sampling of a 3D Gaussian in which covariance between the parameters a, b and c can be see. To get a full description of the shape, we need a covariance matrix, the diagonal elements of which give the width in the unit vector directions, and the off diagonals give the covariances.

The covariance matrix describing the shape in figure 6.7 would have the form,

$$M_{\text{cov}} = \begin{bmatrix} \sigma^2_{aa} & \sigma^2_{ab} & \sigma^2_{ac} \\ \sigma^2_{ba} & \sigma^2_{bb} & \sigma^2_{bc} \\ \sigma^2_{ca} & \sigma^2_{cb} & \sigma^2_{cc} \end{bmatrix} \tag{6.45}$$

and therefore the uncertainty in the parameters a, b and c is given by $\sigma_{a,b,c} = \sqrt{\text{diag}(M_{\text{cov}})} = [\sigma_a, \sigma_b, \sigma_c]$.

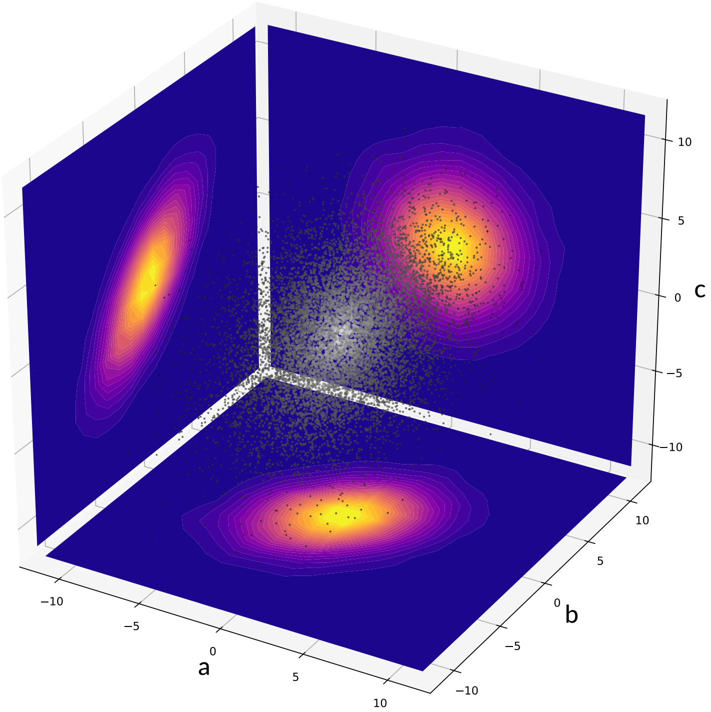

Fig. 6.7. *Sampling of a 3D covariant multivariate Gaussian. Density plots are given for the data in each of the 3 unit vector projections. The density plots utilise all the data in a particular projection to illustrate correlations and contain information that could be missed using a cross-section.*

In this project a least-squares regression fitting algorithm was used; these take a starting point in the space and move around based on the gradient of the scalar field at that location. Steps are taken in the direction of $\nabla\mathcal{E}$ with a step size proportional to the magnitude of the gradient. This is an iterative process that tends to the local minimum in the parameter space. This method is used with the function for generating the Middleton spectrum from equation 6.20, taking a number of fitting parameters as inputs. Due to the complex shape of the PSD of a damped harmonic oscillator, 5 fit parameters are needed to reproduce a measured PSD. They are listed in table 6.1 below. It's important to note that even with a reasonably large number of fitting parameters such as this, there is not arbitrary freeedom to fit to any spectrum shape. Each parameter given below has a very specific effect on the shape of the spectrum and a physical explanation behind it. These parameters, and the Middleton spectrum itself cannot be used to fit a spectrum generated by a system with physics that are not explained by the Middleton spectrum, i.e. a phase modulation by a Gaussian random process.

Parameter	Physical explanation	Value range
Φ	**Phase modulation depth -** Affects the amplitude of the peaks as well as the amplitude fall off rate. Subtle effect on the relative amplitudes of odd and even order peaks.	0.1 - 0.7
Sc	**Scale -** Scales the signal by a linear factor and alters the position of the spectra in the y direction of the PSD.	10^{-14} - 10^{-11}
Ω	**Particle angular trap frequency -** Changes the peak spacing.	$2\pi \times 50$ - 100 kHz
Γ	**Damping rate -** Determines the width of the peaks and therefore the degree of spectral overlap.	10^{5} - 10^{-4} s^{-1}
RIN	**Relative intensity noise -** The width of the intensity distribution producing the required broadening of each peak.	0.5 - 2%

Table 6.1: Fit parameters

We also fit separately to the noise floor in order to be able to include this in the final model. The noise floor is modelled as having a central fixed level and logarithmically increasing as we move away from the central peak. This symmetric increase is likely due to the signal filtration that is used to attenuate the Heterodyne sum frequency being upshifted to the heterodyne difference frequency, and it does not represent any behaviour of the particle. There is also a tail off to the noise floor with increased frequency, likely due to a decreased response of the electronics at high frequencies. This behaviour is paramaterised with the three noise floor variables in table 6.2.

Parameter	Physical explanation	Value range
NF	**Noise floor level -** Base level of the noise floor at the centre of the heterodyne spectrum.	10^{-13} - 10^{-11} dB Hz^{-1}
NFm	**Noise floor gradient -** Noise floor slope away from f_0	10^{-20} - 10^{-17} dB Hz^{-2}
Slant	**Linear attenuation -** Scales the noise floor with frequency.	-1 - 1 dB Hz^{-2}

Table 6.2: Noise floor fit parameters

The parameters in tables 6.1 and 6.2 are those required to reproduce the measured PSD, and optimum values are obtained for each in order to minimise the mismatch between calculated spectrum and experimentally measured PSD. In addition to the position of the minimum in this N-dimensional parameter space, we need to know the uncertainty in each parameter. To find this, we test each dimension in turn, gradually moving away from the optimum value for a single parameter and refitting the remaining parameters on an $N-1$ dimensional cross-section of the parameter space. From this we obtain a new sub-optimal minimum of the error, $\mathcal{E}$, that is larger than the global minimum by some factor. As we move futher from the optimal value of the parameter being tested, the in-plane optimum becomes gradually worse until eventually it is greater than the global minimum by a factor of 2, at which point we define the distance between the global minimum and the current value of the tested parameter as the uncertainty in that parameter. The factor of 2 is a result of the exponential dependence of probability that parameter a is correct and the total error, $\mathcal{E}$, i.e.

$$P(a) \propto e^{-\mathcal{E}} \tag{6.46}$$

and therefore if $\mathcal{E} \rightarrow 2\mathcal{E}$, this implies that $P(a) \rightarrow {}^{P(a)}/_{e}$.

This process is repeated N times to obtain an uncertainty for each of the N parameters. This method is fairly computationally intensive, but is rigorous in the sense that off-axis covariances are accounted for and captured in the uncertainties produced. The more naïve method that can miss this kind of contribution is to take a 1D cross-section along the axis of each of the N directions and see how far from the optimum the error rises by a factor of 2.

Figure 6.8 shows a series of power spectra recorded at different pressures and then fitted with a Middleton spectrum as described above. The varying pressure results in a changing value for Γ (according to the relation given in §2.5.2 and figure 5.5) and the spectrum produced using this new method reproduces this. Below we show a number of measured PSDs for a particle with different damping rates, achieved by varying the background gas pressure. These rates are estimated from the width of the peaks by fitting the Middleton spectrum to the measured PSD. The fitting process works best in the intermediate pressure regime and it can be seen that the spectrum with highest damping rate deviates from the measured power spectrum as the error does not vary greatly with varying state parameters due to the poorly defined spectral features.

At low pressure the broadening due to Stokes damping is surpassed by broadening from intensity drift. This means that an unbroadened theoretical sprectrum will no longer fit the measured data well, as this kind of RIN broadening is not included in the calculation of the Middleton spectrum.

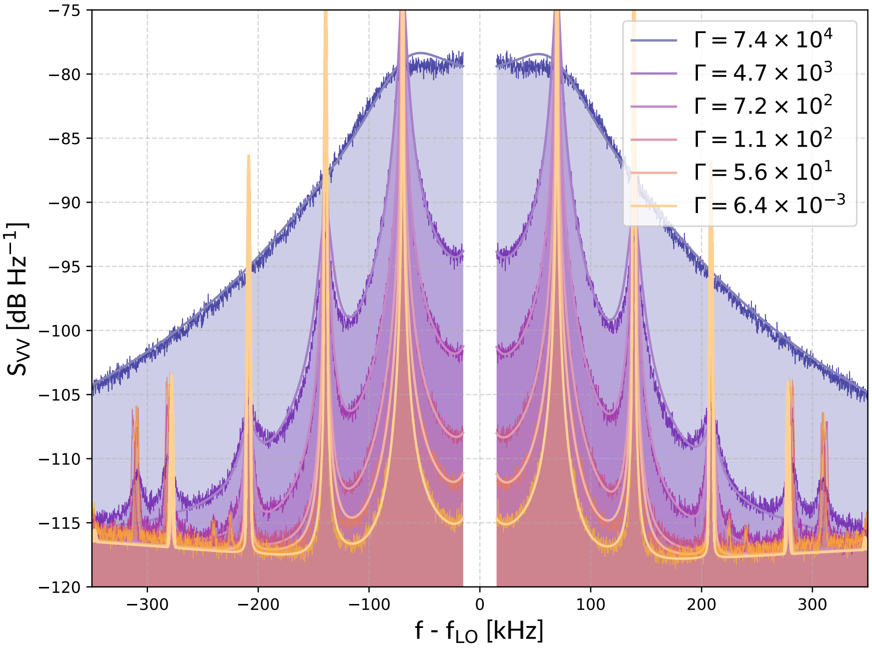

Fig. 6.8. *Experimentally measured heterodyne power spectra fitted with a Middleton spectrum generated by equation 6.20. Damping rates are given in* s^{-1} *for pressures between 100 mbar and* 10^{-5} *mbar.*

§6.4.3. Broadening from local intensity drift

The model was expanded to include a broadening parameter that describes the width of a Gaussian intensity distribution with which the spectral features are broadened from the phase modulation spectrum. This is done as a reasonable approximation of the behaviour of the local intensity gradient at the particle during the integration time of the measurement. A varying intensity gradient changes the trap frequency of the particle and so spreads the peaks in the PSD. We average a set of spectra with adjusted values of the trap frequency and amplitudes weighted according to the Gaussian distribution, effectively convolving the spectrum with a Gaussian to form a Voight-like lineshape at integer multiples of the trap frequency. This is a single operation performed on the entire spectrum at once during its calculation, and affects the peaks to different extents, reproducing the change in peak shapes seen in the experimental system. The difference in shape can be seen in figure 6.9, and the form of the spectrum is given in equation 6.47 [17].

$$S'(\Phi, \Omega, \Gamma) = \frac{1}{\sqrt{2\pi}R} \int (1+r)\, e^{-r^2/(2R^2)} \times S\left(\Phi/\sqrt{1+r}, \Omega\sqrt{1+r}, \Gamma\right) \mathrm{d}r. \tag{6.47}$$

This extra step is neccessary because the particle trap frequency is not constant, due to a changing intensity gradient around the trap site. The fluctuating intensity gradient changes the trap stiffness and thus the trap frequency. These fluctuations are partly due to the trapping laser power changing over time as the EDFA pump diode current drifts. This effect can be measured by using a monitor photodiode and a tap coupler to measure the optical power in the main fibre. Performing this measurement shows some fluctuation over timescales close to the integration time, however not enough to explain the degree of broadening seen in the PSD. We suggest that the remaining variance in trap frequency is due to vibrations in the setup that shift the relative alignment of the trapping beam and parabolic mirror, moving the intensity maximum and therefore changing the local intensity gradient around the particle. A disadvantage of the parabolic mirror is that it is very susceptible to angular misalignment, making this more of an issue than it would otherwise be using a microscope objective.

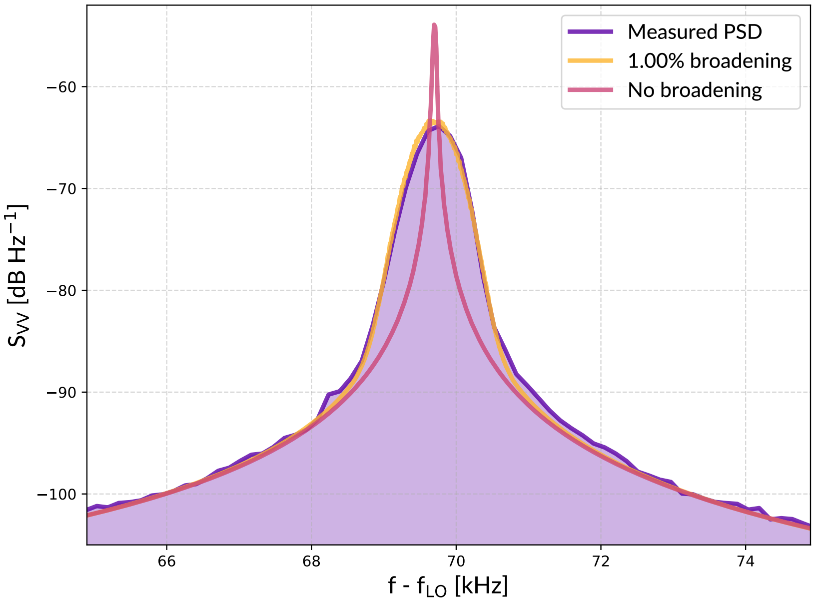

Fig. 6.9. *Comparison of fitted broadened and unbroadened spectra - The unbroadened case is clearly not representative and Gaussian broadening matches the measured lineshape well.*

Figures 6.11 and 6.10 show a representative example of the monitor photodiode signal whilst performing a heterodyne measurement. The time series and power spectrum is given for both the signal from the particle and the monitor photodiode. Figure 6.10 shows that the optical power fluctuates by about half a percent, with a distribution close to Gaussian, hence the use of a Gaussian intensity broadening profile.

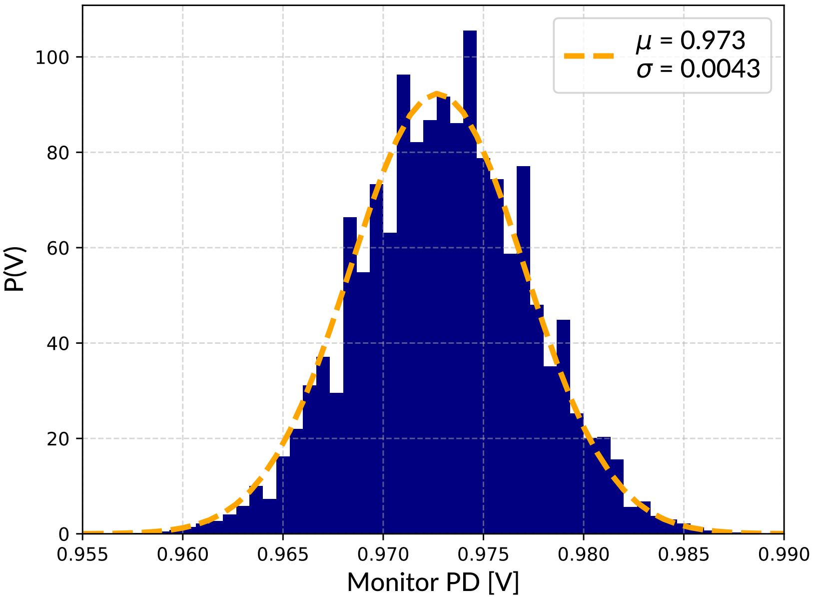

Fig. 6.10. *Histogram of the monitor photodiode signal. Histogram has a $^1/_{e^2}$ width of approximately 0.8% and a Gaussian profile. A Gaussian is fitted to the distribution and superimposed along with the width and mean.*

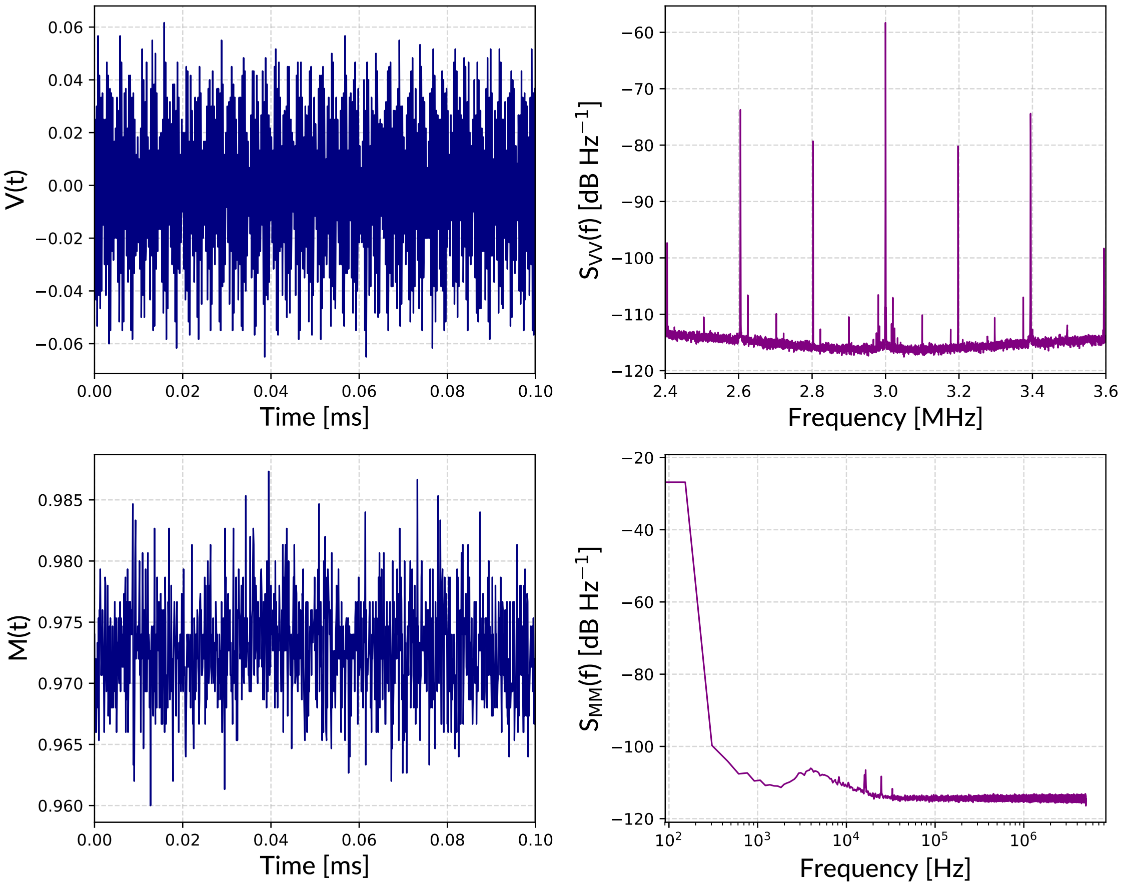

Fig. 6.11. *Monitor photodiode signal characterising optical power fluctuations on timescales of approximately a second. Top: Particle position detection signal and power spectrum. Bottom: Monitor photodiode time trace and power spectrum. Some fluctuations are visible with a slight peak in the power spectrum around 4 kHz. Amplitude of power fluctuations is on the order of 1%.*

§6.4.4. Estimating $\langle x^2 \rangle$ and $^{T_{CoM}}/_m$

In §6.3.2 and §6.3.3 we outlined how we can find the amplitude of the particle oscillation and therefore the temperature to mass ratio using the fit parameters from a Middleton PSD. We found that for our system, the rate of change of phase with respect to distance is $\kappa = 6.85 \times 10^6\ \mathrm{m}^{-1}$. Using a representative fitted value for Φ of 0.35, we get,

$$x_{\mathrm{RMS}} = \frac{\Phi}{\kappa} = \frac{0.35}{6.85 \times 10^6} = 51.1\,\mathrm{nm}. \tag{6.48}$$

This is approximately one particle radius and agrees with values in the literature [72, 74, 94]. We note that we find comparable oscillation amplitude to lower NA systems that use cooling due to the tighter focussing and therefore higher trap stiffness in the z direction.

Although initially we might think to now calculate the centre of mass temperature or the mass of the particle, we are faced with the fact that either calculation would depend on either a measured or assumed value for the other. We can instead calculate the ratio between the two, with the only assumption being that the energy is a single degree of freedom is as we would expect from equipartition. In order to calculate the centre of mass temperature to mass ratio we use equation 6.43 and insert our calculated value for x_{RMS},

$$\frac{T_{\text{CoM}}}{m} = x^2_{\text{RMS}} \times \frac{\Omega^2}{k_B} = \left(51.09 \times 10^{-9}\right)^2 \times \frac{\left(2\pi \times 69.8 \times 10^3\right)^2}{k_B} = 36.4\,\text{K}\,\text{fg}^{-1}. \tag{6.49}$$

Using this ratio we can now investigate what value we get for either T_{CoM} or m when we make a best guess at the other.

We saw in figure 5.4 that the nanoparticles used have radii $r = 50 \pm 4$ nm, and we can use an accepted value for the density of silica of 2650 kg m^{-3} to estimate the volume and mass of a single nanoparticle in equation 6.50.

$$V = \frac{4}{3}\pi r^3 = 5.24 \times 10^{-22}\,\text{m}^3 \tag{6.50}$$

$$m = \rho V = 1.39 \times 10^{-18}\,\text{kg} \tag{6.51}$$

Using this value for particle mass we can calculate T_{CoM} from the ratio of the two.

$$T_{\text{CoM}} = \frac{T_{\text{CoM}}}{m} \times m = 3.64 \times 10^{19} \times 1.39 \times 10^{-18} = 50.5\,\text{K}. \tag{6.52}$$

This result is clearly not correct as the particle centre of mass temperature will not be far below room temperature, particularly as it is positioned at a high intensity focus of a powerful laser. This result is likely due to an inaccurate value for κ, calculated in §6.3.2. The field around the focus is still not well understood and the value for κ relies on the modified wavenumber found using [16, 176], which could be far from representative. This kind of computational method would be interesting to investigate extensions to, as discussed in §7.3. It is also possible that imperfections are present in the mirror, leading to a mishaped focus, and that the trapping beam is slightly misaligned, further distorting the focus.

Another possibility is that the particle mass is not as expected; perhaps due to porosity in the silica particles, or because a particle may have broken up during trapping and so has an effective radius much smaller than expected. This could be investigated by cycling the background gas pressure and tracking the value of $\frac{T_{\text{CoM}}}{m}$ [17], or by calibrating particle motion using its Brownian motion at some intermediate pressure around 10^{-1} mbar [50].

The temperature values calculated are therefore not reliable, but this method is still a useful tool for tracking changes in a particle's dynamics, as will be shown in the next subsection, and at the end of §6.5

§6.4.5. Scanning state parameters

The workflow for extracting thermodynamic parameters is to record the particle position signal, calculate a PSD, fit a Middleton spectum to the PSD and then record the optimum parameters found. Most of this work is done in post-processing and so signal time traces can be taken as often as every 10 seconds at sample rates of 10 MHz and then processed after the experimental run is complete. This enables us to track how the different parameters change over the course of an experiment and plot them as a function of one another.

The two main variables we can change are the background gas pressure, which is proportional to the damping rate, and the optical trapping power, which is proportional to trap frequency squared. Both of these environmental factors will affect the internal temperature of the particle and when the pressure is too low and optical power too high, the particle is lost from the trap. This usually occurs around pressures of about 1×10^{-5} mbar when using approximately 2 W of optical power. Using less optical power can extend this down to 5×10^{-6} mbar for 200 mW of optical power but at this power the EDFA suffers from greater percentage power fluctuations, resulting in more broadening.

The figures in this section show Φ, Γ and RIN as a function of pressure and time for a single dataset. We will discuss the behaviours that can be seen and some conclusions that can be drawn about the particle behaviour. In general, the estimated state parameters are as as expected when calculated by fitting for a particular set of environmental conditions. The values do not depend on the same values as the mass and centre of mass temperature calculations in the previous section and so we need not regard them with the same level of mistrust.

§6.4.5.1. Phase modulation depth, Φ

The phase modulation depth defines by how much the phase of the signal field is modulated, and as κ is constant, it effectively describes the oscillation amplitude of the particle. This is directly related to the centre of mass temperature of the particle, which is in turn weakly coupled to its internal temperature. Figure 6.12 shows a couple of interesting upturns in Φ as pressure decreases, suggesting that as the internal temperature is increased due to a decreased ability to convect heat from the particle, the centre of mass temperature and Φ rise too.

Above approximately 50 mbar it is difficult to obtain a value for Φ as peaks in the PSD are not yet visible and so the sum of the squares of the normalised residuals is not very sensitive to changes in Φ. Below about 3×10^1 mbar, Φ is tracked well, rising sharply at 10^1 mbar. Φ stays relatively constant down to 10^{-1} mbar, at which point the results become noisy due to the low certainty of fit in Γ having a knock-on effect on other fit parameters. There is a slight upturn again in Φ but the ability to resolve this is limited by RIN broadening. It would be interesting to see how this plot continues down to lower pressure if the RIN issue can be improved. The fluctuations in the intensity of the trapping beam could be recorded and used to correct for RIN broadening, however the majority of the broadening effect appears to be caused by fluctuations in alignment that move the trap site over micron-scale distances. This causes the local intensity gradient at the particle to change, and the effect is difficult to record making it difficult to imagine a process for compensating for this in post-processing.

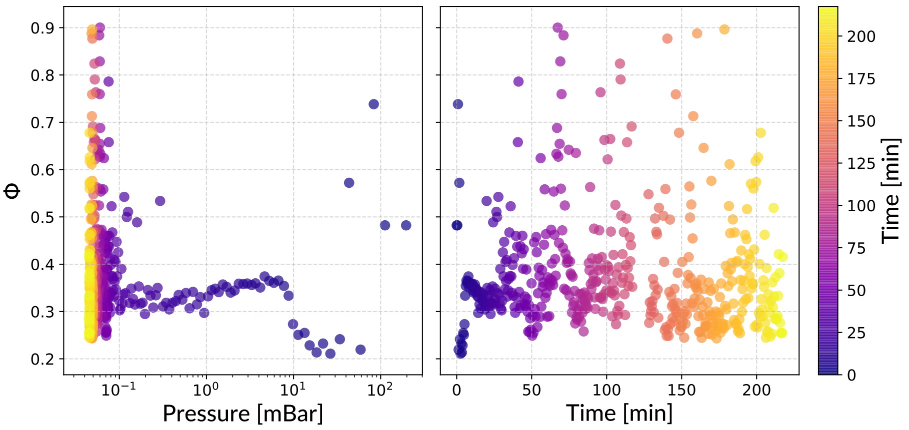

Fig. 6.12. *Behaviour of Φ with pressure and time. Outliers can be seen at high pressure due to fitting insensitivity to Φ at this pressure. Variance of Φ increases below a cut-off pressure, below which RIN dominates over Γ.*

§6.4.5.2. Damping rate

We have already seen the plot of Γ as a function of pressure in §5.4, where we commented on how the uncertainty is low above 10^{-1} mbar but then increases as RIN broadening surpases Stokes broadening. The experimental results for Γ are offset from what might be expected according to Stokes theory, implying the particle radius is slightly less than the manufacturer stated value of 50 nm. Nanoparticle radii are distributed around this nominal value and so some deviation is expected.

Interestingly the path traced out by this plot does not follow the gradient from Stokes drag theory. This is a log-log plot and so a gradient not equal to one implies a nonlinear relationship between pressure and damping rate. A possible explanation for this is that the radius of the particle changes over the course of this experiment, likely due to heating. It is possible that surface impurities are ejected from the nanoparticle as the pressure is decreased, as these impurities would have a higher absorption than that of the silica and so would heat up rapidly. It is also possible that heating the particle causes a kind of annealing-like restructuring of the silica that results in an increased density and decreased radius, decreasing the damping rate. These are surprising results and merit confirmation in further work.

Figure 6.13 also shows Γ as a function of time, in which we can see the particle acting as a pressure sensor. This plot could be used to track the pressure over time via the use of a calibration curve. The increased uncertainty in Γ at low pressure can again be seen in the wide scatter of data points, but most of the points lie along a curve that represents the behaviour of the damping rate. The data points in the low pressure spread area correspond to when the fitting algorithm was unable to accurately determine a value for Γ as Stokes damping was masked by RIN broadening.

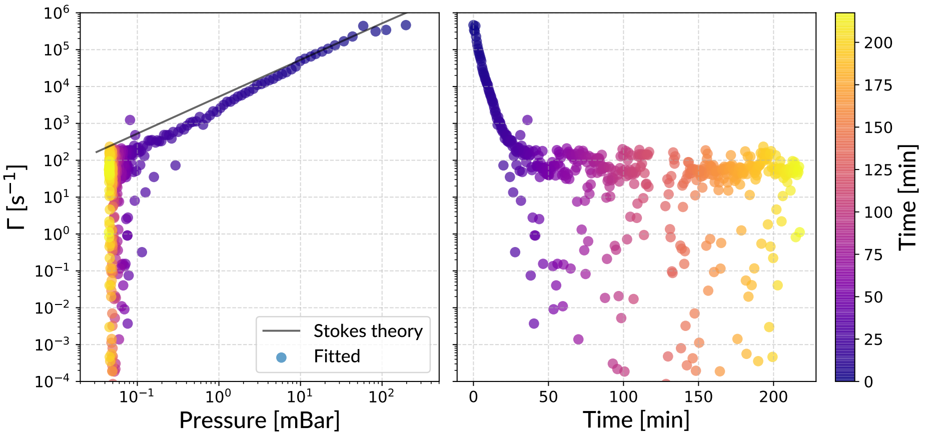

Fig. 6.13. *Behaviour of Γ with pressure and time. The variance of Γ measurements can be seen to increase below the pressure at which RIN broadening begins to dominate over broadening due to background gas collisions. This occurs at about 10^{-1} mbar in a) and 25 minutes in b). The expected relation according to Stokes drag theory is also plotted in a).*

§6.4.5.3. RIN

At high pressure the effects of RIN broadening are masked by the strong Stokes damping; for this reason the fitting results for RIN do not converge at high pressure and we see the results running up against the programmed limits of 0 and 5%. At 3 mbar, Γ is low enough that RIN broadening can be seen and fitting places it at 1.5 % ± 0.5 %. As the pressure decreases, so does the uncertainty on the RIN. The RIN can be seen to be stable at close to 1% for the rest of the experiment. The highly repeatable measurements of the

RIN show that this is a very real effect with a well defined and quantifiable broadening effect.

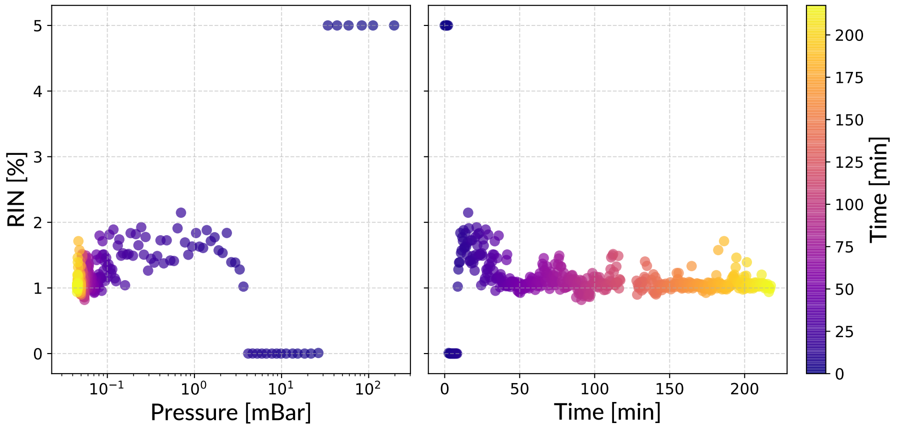

Fig. 6.14. *Behaviour of RIN with pressure and time*

It can be seen that scanning state parameters whilst recording particle position data allows us to fit to, and then track the movement of the system through the parameter space. The method as described currently does allow access to uncertainty information about the points we have plotted on the various graphs in this section, as so we cannot say to what degree we can be confident of the state of the system. At the end of this PhD project a method was touched upon for an alternative method for determining the best estimate of state parameters, as well as providing experimental uncertainties.

§6.5. Whittle Likelihood

Much of this section follows the content of a paper published by the author during the project, and so the section in its entirety should be regarded as referencing [17].

As mentioned in §6.4.1, the distribution of points from a power spectral density estimate, around the theoretical spectrum follows the χ^2 distribution, an asymmetric distribution. Due to this, when fitted using a least squares regression technique the result will be consistently underestimated, as such techniques are trying to place 50% of points above the curve and 50% below, rather than finding the peak, or mode, of the distribution, as is more desirable. In the more common case where points follow a Gaussian distribution, the mean and mode of the distribution are the same; hence the prevalence of least squares as a go-to methodolgy. In our spectral domain problem, this method is asking subtly the wrong question: rather than asking which state parameters put 50% of the points either side of the curve, we should ask which parameters yield the highest value of likelihood for producing the points we have observed.

During the project, investigations into how best to calculate the uncertainties of state parameters fitted using least squares revealed the distinction between the two methods above and led to the following work on likelihood estimation from non-linear measurements.

Likelihood calculation was mentioned at the end of §6.4.1, and it was noted that existing time domain methods don't apply to our system because of the lack of linear measurement. We can however use technique called Whittle's log-likelihood to achieve this task in the frequency domain. The Whittle likelihood

[188] is given by

$$\mathcal{L}\left(\alpha\right)=\sum_{i}\log S\left(\alpha\right)+\frac{\hat{S}}{S\left(\alpha\right)}. \tag{6.53}$$

Here S is the theoretical spectrum, $\hat{S}$ is the estimator of the spectrum, α is the vector of physical parameters taken as inputs to the theoretical spectrum, and i is a counting variable over which we sum each individual frequency at which the power spectrum has been estimated. Using the Whittle likelihood, the probability can be found that the parameters contained in α would produce the measured PSD is given by

$$\mathrm{P}\left(\alpha\mid\hat{S}\right)\propto\exp\left[-\mathcal{L}\left(\alpha\right)\right]. \tag{6.54}$$

The final arrived upon method for finding state parameters of the levitated nanoparticle oscillator in this project was by using the Whittle likelihood as an approximation for the true likelihood (due to it being a spectral domain method). The particle dynamics themselves are well represented by the Whittle likelihood method, however the measurement process is not but we can verify the value numerically. The Whittle likelihood is intended for use on a periodogram (§2.5.1), which is the modulus squared of Fourier transform of the time series data. The method is asymptotically unbiased, but not consistent; meaning it does not suffer from the systematic misestimation issues experienced by the least-squares regression detailed at the end of §6.4.1, but also the variance does not decrease with an increased number of data points. To handle this, periodograms are averaged over using Bartlett's method [184] where an N-length data set is split into a number of M-length segments, windowed by the Tukey-Hanning window [189]. This estimator is χ^2_ν distributed (see figure 6.6), as we expect, where the number of degrees of freedom, ν is related to the number of segments into which we divided the time series data ($\nu={}^{2N}/_{M}$).

The principle advantage offered by using the Whittle likelihood method is that we can now calculate not only the most likely state parameters of the oscillator (already fairly well acheived through least-squares regression) but the uncertainty on those parameter estimates, and therefore draw meaningful physical conclusions from the data. We can map out the probability density function that our physical parameters are given by certain values and thereby find not only the widths of this n-dimensional distribution, but the covariance matrix as well. This can be visualised by attempting to find the most likely values of the physical state parameters $\alpha=[\Phi,\Gamma]$, holding Ω constant, as the trap frequency can be very well defined.

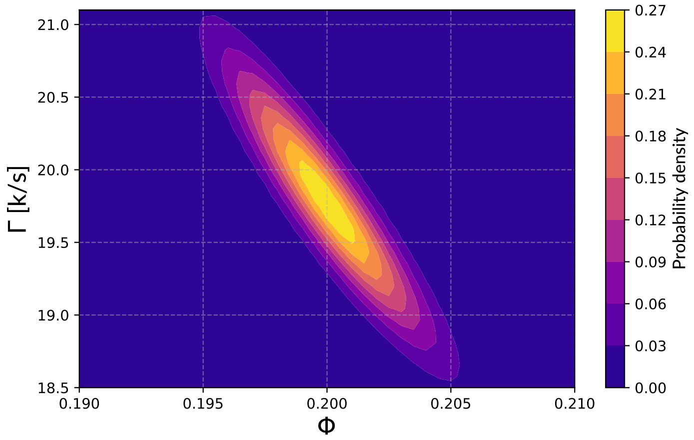

Fig. 6.15. *Probability density over the 2D parameter space for Φ and Γ, found by the Whittle likelihood.*

In order to check the validity of the Whittle likelihood method, We create an ensemble of simulations with state parameters α distributed around some central "true" α_0 position in the parameter space, finding the maximum likelihood estimate (α_{MLE}) in each case. This ensemble estimate of the distribution is then compared to that computed from exp $[-\mathcal{L}(\alpha)]$ directly.

When the validity of the method has been numerically verified through simulation, we can compute the profile likelihood of the 2D parameter space of Φ and Γ. We constrain one of these parameters (say Φ) to some value and then fitting both the interesting parameters (Γ) and other, nuisance parameters such as spectrum noise floor etc. This allows us to calculate the marginal probability, effectively integrating over the nuiscance parameters. Figure 6.16 shows the difference between the marginal probability density, $\mathrm{P}(\Phi) = \int \mathrm{P}(\Phi, \Gamma)\, \mathrm{d}\Gamma$ and simply calculating the probability that a certain parameter set is correct, $\mathrm{P}(\Phi, \Gamma = \Gamma_{\text{MLE}})$. The amount we can vary Φ before the probability falls below a set value is far larger if Γ is also allowed to vary, rather than simply evaluating along the horizontal line $\Gamma = \Gamma_{\text{MLE}}$. This method is designed to account for covariance between state parameters, a property than can have a significant effect on the uncertainty of these parameters and is often neglected in error analysis.

The uncertainty of a certain state parameter can be found the profile likelihood method, tracking how the maximum of the probability distribution changes across many n-1 dimensional cross-sections of the full n-dimensional distribution. This can be thought of as mapping out the height of the "ridge line" seen in figure 6.15, rather than drawing a straight horizontal or vertical line across the space. Example probability distribution functions for each of the physically interesting parameters are shown below.

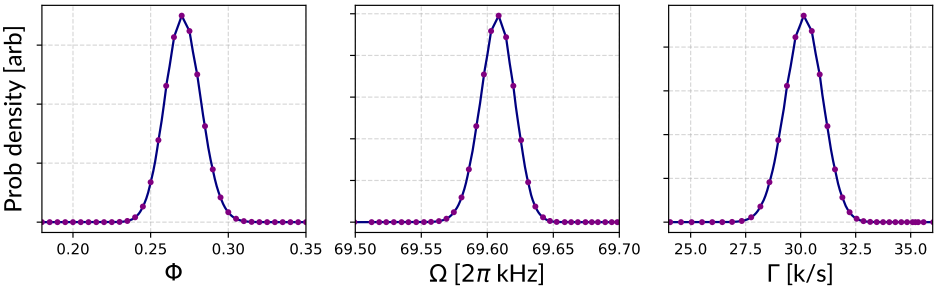

Fig. 6.16. *Individual probability densities for state parameters Φ, Ω and Γ, found from the profile likelihood calculated by holding Φ constant and varying Ω and Γ.*

In general, using the Whittle log-likelihood method to obtain most state parameters gives very similar numerical results to using least-squares regression as in §6.4.2, except in the case of Φ, which was consistently underestimated by LSR. This was determined by simulating an oscillator with known Φ and then using the fitting algorithm to estimate state parameters from the simulated position-time series. The underestimation was likely due to a large covariance between Φ and the other parameters, a systematic source of error that Whittle likelihood is not prone to. Whittle likelihood estimation gave accurate results on the simulated data, leading us to trust the values it yields when used on measured experimental results. The main advantage of Whittle however, is the uncertainty values that it allows us to find. Having these uncertainty values allows us to draw much more reasoned conclusions about the physical behaviour of the nanoparticle oscillator system. The plot below shows a subset of the points from figure 6.12, now with error bars, showing that there is indeed an upturn in Φ as discussed in §6.4.5.1.

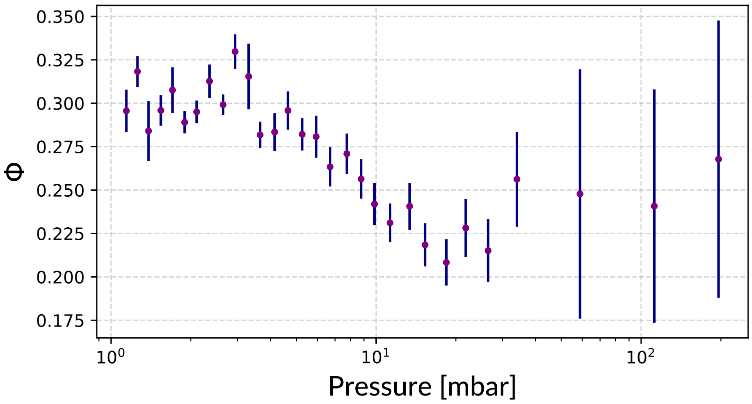

Fig. 6.17. *Whittle likelihood calculation of uncertainties in Φ is used to plot points from figure 6.12, now with error bars, confirming the upturn in Φ with decreasing pressure.*

§6.6. Duffing non-linear Broadening

Up to this point in this project we have been using the approximation that the levitated nanoparticle is trapped in a purely quadratic potential, and therefore its motion is harmonic. In reality the trapping potential cannot possibly be quadratic, as this would represent a case where the value of the potential would tend to infinity with increasing distance from the focus. In the narrow-band regime it becomes imporant to consider the contributions of higher orders of the potential, capturing the difference in shape shown in figure 6.18.

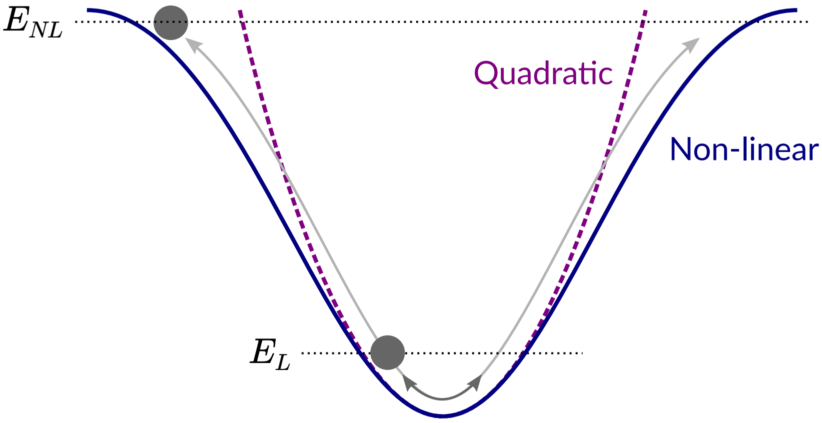

Fig. 6.18. *The forms of the potentials in the quadratic and non-linear case. Particles with different energies explore different spatial extents and so are subject to differing restoring forces. We see here that the higher energy particle oscillates far enough to explore the non-quadratic region and therefore is subject to a non-linear restoring force.*

When the trapped particle has sufficient energy it will oscillate with an amplitude such that it no longer exclusively explores the region of the potential that is well approximated as quadratic, and so the restoring force on the particle deviates from Hooke's law and is non-linear. A particle oscillating in this manner will not be well described by narrow peaks in the frequency domain, as its oscillation is now anharmonic and an extra broadening factor must be applied to the spectrum developed in this chapter.

The degree to which the system exhibits non-linear behaviour is quantified using the non-linear coefficient, ξ, where $\xi = {-2}/{w^2}$ and w is the e^{-2} waist across the focus in the direction in question. In the extended case we now consider, the gradient force on the particle now becomes [72]:

$$\mathbf{F} = -K \left[1 + \sum_{j=x,y,z} \xi_j \mathbf{x}_j^2 \right] \mathbf{x}. \tag{6.55}$$

This leads to the more complete equation of motion (equation 6.56) that can be compared with equation 2.120 for the purely linear case

$$\ddot{\mathbf{x}} + \Gamma \dot{\mathbf{x}} + \Omega^2 \left[1 + \sum_{j=x,y,z} \xi_j \mathbf{x}_j^2 \right] \mathbf{x} = \frac{\mathcal{F}}{m}. \tag{6.56}$$

Γ and the stochastic force, $\mathcal{F}$ (see §2.5.1) are related by the fluctuation-dissipation theorem as discussed previously, and Γ can be thought of as a linear frequency broadening $\Delta\Omega_{\mathrm{L}} = \frac{\Omega}{Q}$ due to thermal excitation from collisions with background gas particles. The amplitude of the particle position fluctuations is a function of the energy and frequency of the oscillator, according to the equipartition theorem; given by $r_{\mathrm{th}} = \sqrt{{2k_B T}/{m\Omega^2}}$.

When using the extended, non-linear description of the system, the particle oscillation frequency is subject to both the linear and an additional, non-lineear frequency shift given by [72]

$$\Delta\Omega_{\mathrm{NL}} = \frac{3}{8} \xi \Omega r_{\mathrm{th}}^2. \tag{6.57}$$

This frequency downshift is visible for large oscillation amplitudes of the particle, and is only visible when Γ is low, as it is otherwise masked by the the damping due to background gas pressure, and the broadening due to RIN. The dominant broadening mechanism can be determined qualitatively using the particle PSD, as each type manifests in a different spectral shape. In this experiment some effects of non-linear broadening are observable around 10^{-3} mbar, but are largely masked by RIN broadening.

The effect of the Duffing non-linearity can be simulated, and gives a line shape as in the figure below.

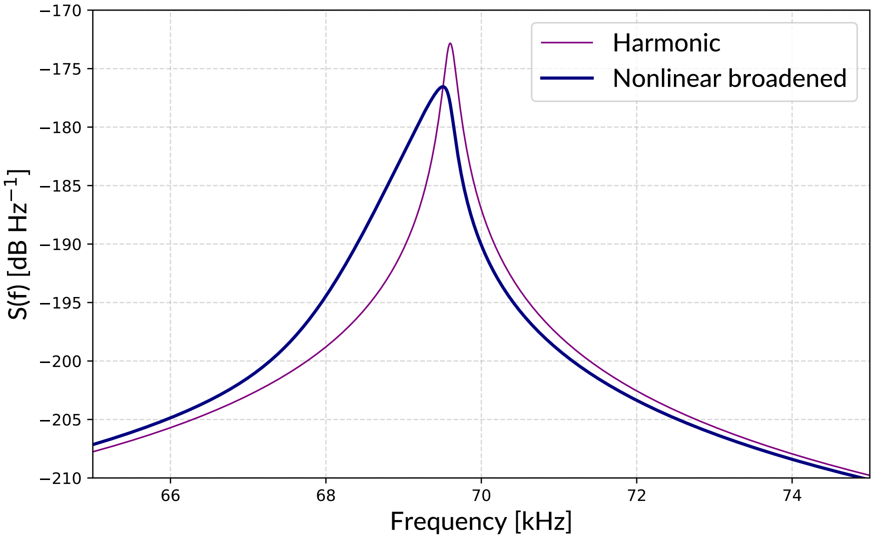

Fig. 6.19. *The effect of broadening due to the Duffing nonlinearity. The characteristic asymettric shape can be seen, as well as the decrease in maximum peak amplitude.*

This spectrum in figure 6.19 is [72]

$$S_{\mathrm{NL}}\left(\Omega\right) = \int \rho\left(E\right) S_{\mathrm{L}}\left(\Omega, E\right) \mathrm{d}E. \tag{6.58}$$

where the non-linear shifted frequencies become $\hat{\Omega}(E) = \Omega + {}^{3\xi}/_{4m\Omega}E$ according to a negative Duffing nonlinearity, and are weighted by the Bolzmann distribution. This is a sensible approach due to the long integration time used when compared with the particle dynamics. The linear PSD, S_{L}, is given by

$$S_{\mathrm{L}}\left(\Omega, E\right) = \frac{E}{\pi m \Omega^2} \frac{\Gamma}{\left(\Omega - \hat{\Omega}\left(E\right)\right)^2 + \left(\frac{\Gamma}{2}\right)^2}. \tag{6.59}$$

As this effect is understood, it would be reasonably simple to include in the spectrum we have developed throughout this chapter, however in our system for the majority of the time the effect is hidden by RIN broadening and so is not included. In future systems with reduced RIN, this would be included in the fitting procedure, as discussed in §7.1.2.

§6.7. Conclusion

In this chapter we have discussed the application of a technique used in RF engineering to use in levitated optomechanics. This technique is used to generate the power spectrum of an oscillator that is phase modulated by a Gaussian random process with a known power spectrum. We started by describing the need for rigorous PSD calculation, and stated a number of problems with the current best approach from the literature. The current technique was described and we highlighted that there are assumptions made that are, by definition, not valid; we also noted that there is an *ad-hoc* marriage of two forms of related power spectra used to obtain parameter estimates.

The Middleton phase modulation spectrum was introduced, and it was shown to produce spectra that agree in form to the accepted spectrum of the damped harmonic oscillator. This method produces a power spectrum of the measured signal as a function of physically intuitable parameters of the experimental system that can be fitted to a measured PSD. From these values we find the oscillation amplitude and the temperature to mass ratio. We can also estimate the mass of the particle and use this to estimate the centre of mass temperature of the particle, although this yeilds confusingly low temperature results at this stage and requires further investigation.

The fitting process can be repeated throughout the course of an experiment in order to track changes in the state of the oscillating particle that occur as the thermodynamic environment changes. In our system this technique is limited by the RIN broadening at low pressure which masks the damping rate due to Stokes drag and increases the uncertainty of fitted thermodynamic parameters. If this can be stabilised then this method should be able to track the particle state down to pressures around 10^{-6} mbar, after which the particle is lost from the trap due to heating.

Towards the end of the project, an interesting new use of an existing likelihood estimation technique was developed, using the frequency-domain Whittle log-likelihood. This can be used as an alternate goodness-of-fit metric for use when fitting to spectra, and can provide the full covariance matrix of the system in order to extract experimental uncertainties that allow us to draw sensible physical conclusions from fitted data.

This technique could be used by other research groups in the levitated optomechanics community. It is applicable to both forward and back scatter experiments, and requires only the appropriate rate of change of phase with particle position. Using heterodyne measurement does not require changing large sections of the experimental system and gives demonstrable advantages in terms of spectral stability. It is our hope that the Middleton expansion spectrum can be used, and improved upon, by other researchers in order to obtain better information about their experimental systems as well.

CHAPTER 7

Future work

The work undertaken during the course of this project has been a roughly even split between constructing the experimental system (chapter 4) and researching and implementing the Middleton spectrum approach to power spectrum estimation (chapter 6). In this chapter we will discuss how the work presented above can be taken forward. There are a number of sensible improvements to the experimental system from which results would greatly benefit. There are also avenues of investigation available that should aid in understanding the particle's environment so that fewer approximations are needed to model the system, and to use it to obtain precise information about the behaviour of the particle.

Alongside improvements to, and continuation of, the pre-existing work, there are a number of interesting potential new directions for research. These are designed to use adapted versions of the existing system to attempt to exceed the current limitations to levitated optomechanical systems. These potential future projects, and the motivation behind them will be discussed in turn.

§7.1. Experimental

First we consider some suggested changes to the existing experimental system. These are designed to address the limitations of the results given in chapter 6, so that the system can be used at lower pressure, with a greater signal to noise ratio.

The major limiting factor on the quality of parameter estimation using a fitted Middleton spectrum is spectral broadening, made up of RIN broadening and non-linear Duffing broadening.

§7.1.1. Intensity stability

The time-changing intensity gradient created by RIN causes the particle trap frequency to fluctuate during measurement and therefore spectral features are distorted. The form of the DHO power spectrum is well known, but the measured spectrum includes this broadening effect and so does not match a spectrum generated from theory. We have attempted to account for this by broading the spectrum with a Gaussian distribution, but the reality is that the intensity gradient distribution seen by the particle over time is not neccessarily Gaussian during the course of the measurement time, and so one cannot expect the measured spectrum to match a broadened theoretical spectrum exactly.

This intensity noise requires stabilisation, so that RIN broadening plays a small role in determining the power spectrum shape in comparison to the more physically interesting parameters Ω, Γ etc. This can be achieved in two ways, corresponding to the two sources of RIN.

The first is to stabilise the laser power entering the trapping objective. This fluctuates for a number of reasons, firstly the output power from the EDFA is not completely constant due to thermal drift in the device and the corresponding pump diode current feedback designed to stabilise this. The EDFA has a mode in which feedback is deactivated, and this should be investigated in conjunction with a higher quality active power stabilisation system. Such a system could use a monitor photodiode on the main beamline to feed back to either an AOM or EOM (electro-optic modulator) in order to attenuate the beam by a varying amount in order to fix the optical power. The second method for stabilising optical power at the trap site is more passive, and involves addressing the thermal drift present in the fibre itself, as well as the fibre circulator. Losses in the circulator convert the optical power into heat, causing thermal expansion in the circulator. This drift alters the power coupling of the device in an unpredictable way and so the optical power transmitted to the trap site changes as the device heats up and cools down. To combat this, other methods of separating the trapping and signal fields should be investigated, be these either a similar device with a greater tolerance for high optical powers, or a different system entirely.

Secondly, the local intensity gradient around the particle trap site is likely to be highly dependent on the angular alignment of the parabolic objective and the incoming trapping beam. This is due to the sensitivity of the parabolic geometry and means that small shifts in alignment translate and distort the intensity maximum in the focal plane of the objective. Angular misalignment can be static, if the system is not setup correctly, or it can be time-varying. Time-varying misalginment is introduced through mechanical vibration of the mirror or collimator and attempts to dampen this should be made in future work.

The methods above should help to reduce RIN, but if the optical power entering the objective is still fluctuating in time it may be appropriate to attempt to measure how this power changes whilst recording particle motion and then use the intensity distribution from the monitor photodiode as the broadening distribution for power spectrum estimation. This should provide a distribution that better reflects the true behaviour of the system at the time in question and will fit better than a “best guess” Gaussian.

§7.1.2. Duffing non-linearity

Duffing non-linearity broadening contrasts with RIN broadening in that it is predictable as it acts on timescales much shorter than the measurement period and is therefore well averaged over. We can therefore calculate the expected non-linear broadening and how it will affect the particle spectrum and apply this modification to the theoretical prediction. This process was not implemented as part of this PhD project but it would be relatively straight-forward to add an extra parameter to the fitting process to determine the Duffing coefficient that produces a spectra best fitting the measured data. This Duffing coefficient allows us to calculate the next term in the Taylor expansion of the trap potential and include its effects on the particle motion, and therfore position and signal collected.

§7.1.3. Loading mechanism

Improving the RIN characteristics of the trap will allow for exploration of the parameter space down to lower pressure, as the interesting physical parameters will not be masked by RIN broadening. When evacuating the chamber in order to reach these pressures, water is desorbed from the chamber walls, making it difficult to reach UHV. Much of this water is introduced by the particle source, as the particles are sonnicated in aqueous solution, with most of the liquid adhereing to the interior surfaces of the chamber. The current nebuliser loading mechanism also requires the frequent opening of a large gate valve between the chamber and atmosphere, by which the naturally occuring moisture and impurities in the air also enter the chamber.

In the future it would be advisable to alter the loading mechanism, either by using a system that backfills the loading chamber with a pure, dry gas such as nitrogen, or by replacing the system altogether. A nitrogen back-filled loading chamber would limit the atmospheric moisture entering the chamber, but water would still be introduced through the nebuliser. An alternative loading mechanism such as laser induced acoustic desorption (LIAD) [190, 191] would completely remove the need to introduce vacuum incompatible substances to the chamber. In LIAD, a preprepared substrate has nanoparticle/nanorods adsorbed or etched on its surface, the back side of which is illuminated with a pulse laser, sending mechanical shockwaves through the substrate that desorb the nanoparticles from the surface. Their trajectories then carry them to the trap site [42]. This process only uses vacuum compatible materials and does not require frequently opening the chamber to atmosphere, and in principle there's no reason this could no be applied to our experiment.

Another approach to the nanoparticle source problem is to use a glass slide with particles adsorbed to the end, excited by a piezoelectric element [22]. The piezo excited the fundamental flexing mode of the glass slide and causes the tip to oscillate rapidly, ejecting nanoparticles from the surface. These particles then fall under the influence of gravity into the trapping region of the setup. This apparatus is vacuum compatible and greatly reduces the frequency with which the chamber must be opened up to atmosphere; it also does not introduce water into the system. Using this system would require a redesign of the chamber as currently there is insufficient volume to support the piezo and glass slide assembly. This technique is used by other research groups to great effect [40, 52, 62, 157].

§7.2. Accessing UHV - Cooling

Currently, our system can repeatably trap nanoparticles down to pressures around 5×10^{-6} mbar. This is determined by the pressure at which trapped particles cannot lose heat to the environment effectively enough to keep their internal temperature below that at which the particle melts or breaks up. When this happens, the particle no longer experiences the correct balance of forces and will be ejected from the trap.

It has been shown [7, 8] that cooling the centre izoof mass motion of the nanoparticle allows particles to be maintained in the trap down to lower pressures than without, as the centre of mass temperature is decreased and this couples to the internal temperature. In order to use our system to explore the UHV pressure regime, and observe the evolution of state parameters, it is likely that active cooling will be required. This can be either parameteric, through the use of a phase lock loop (PLL), or through PID cooling.

§7.2.1. Parametric cooling

Parametric cooling is by far the more popular technique and was used to achieve the state of the art results in the literature [7, 8, 88, 159]. This involves monitoring the particle position and producing a sinusoidal signal at twice the trap frequency with a tunable phase offset. This signal is used to modulate the trap potential depth and with the correct phase relation to particle position, reduces the RMS position amplitude. This is equivalent to cooling the centre of mass motion. This technique requires fast analogue electronics hardware and so is very expensive. This would be the best solution to cool the particle motion but if finances do not allow, it may be possible to use PID cooling instead.

§7.2.2. PID cooling

Towards the end of this project a plan was drawn up for using a PID controller to cool particle motion. This is thought to be achievable by phase modulating a local oscillator at roughly twice the trap frequency using the homodyne signal of the particle position. By mixing the signal $V = \sin(\Omega t)$ (we approximate this to be sinusoidal in this context) with a local oscillator at $\sin(\Omega t + \varphi)$, we can obtain a DC signal. This signal is held constant by the PID controller modulating φ such that the two signal mix and cancel one another. This same phase signal, φ, is fed to another local oscillator that outputs $\sin(2\Omega t + \varphi)$. This signal is used to amplitude modulate the RF signal to an AOM that modulates the intensity of the trapping light. If a sufficiently fast PID controller is tuned correctly, this system should be able to produce a cooling effect on the particle centre of mass motion, albeit not to the same degree as a full PLL. This system requires that the particle trap frequency stay relatively constant such that the phase modulation can compensate for the mismatch. Figure 7.1 gives an overview schematic of the system design.

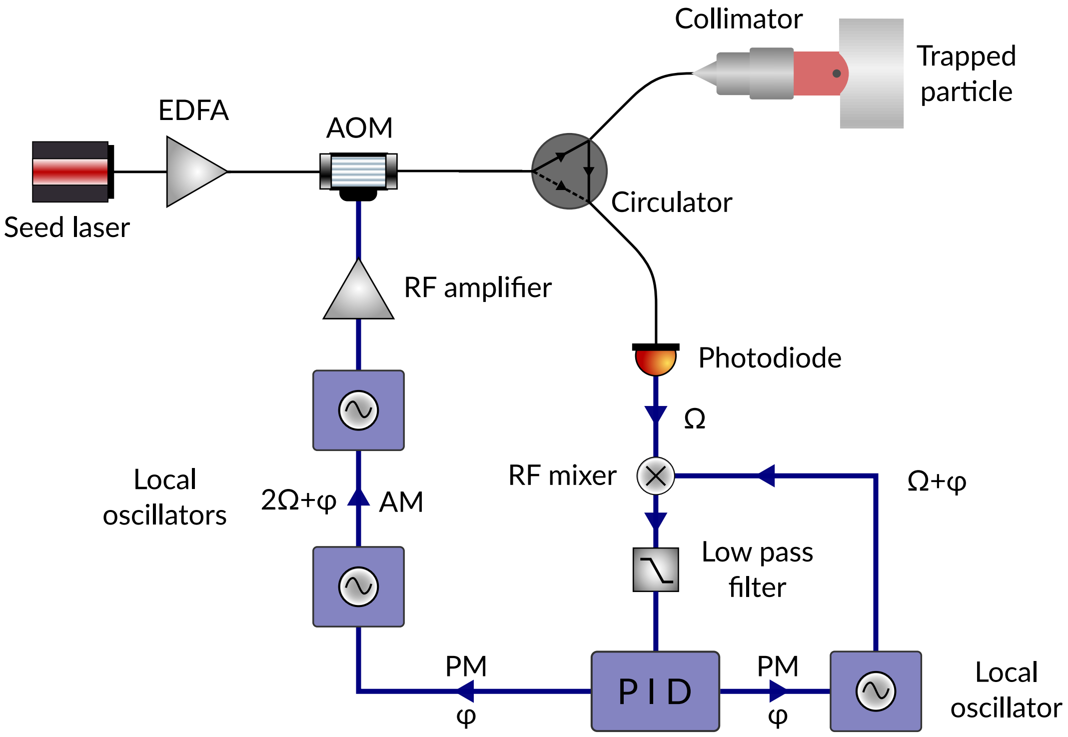

Fig. 7.1. *PID cooling system schematic*

Future work could incorporate the implementation of this system, as the equipment is already available in the lab and, if successful, would allow for interesting further research.

Using either parametric or PID cooling in conjunction with the reduced RIN techniques from §7.1.1 should enable a future system to reach lower pressures than currently achievable, and to fit and investigate the results of applying the Middleton spectrum under these conditions.

§7.3. Understanding the Focal Region

Much of the theoretical understanding of the intensity distribution and focussing behaviour in levitated optomechanics relies on the paraxial Gaussian beam model. In levitated optomechanics, one neccessarily uses a non-paraxial beam to trap and so the assumptions used are quite invalid. It would be highly revealing to understand the intensity distribution around the focus, as well as how it changes with angular misalignment. This can be simulated using the work in references [16,176] using a sum of the surface currents in the mirror and the field they create at any point in space around the focus. This technique allows for the calculation of the effect from a rectangular intensity distribution, from many of which we can create an abitrary illumination profile. It would also be interesting to incorporate the effect of imperfections in the mirror objective geometry into the simulation, as is done with the deep parabola simulation discussed in [166]. These imperfections will distort the focus and thus destabilise and reduce the trap depth; an effect that likely becomes more pronounced with angular misalignment.

This work was started during the course of this project, and initial results were acquired, but requires further time and computation going forward. This work should allow us to calculate the expected beam waist and intensity gradient without relying on the approximations of Gaussian beams. Research of interest to this further work is featured in [167, 192].

§7.4. Parametric State Estimation

Much of the work in this project has been centred around the concept of state estimation, and the techniques used fall under the label "non-parametric state estimation". This is the case because we take a time series, estimate the power spectrum and then attempt to fit to a power spectrum in frequency space, in order to estimate state parameters. In contrast, parametric state estimation reaches these same values directly from the time series, circumventing the need for inexact power spectrum estimation [186].

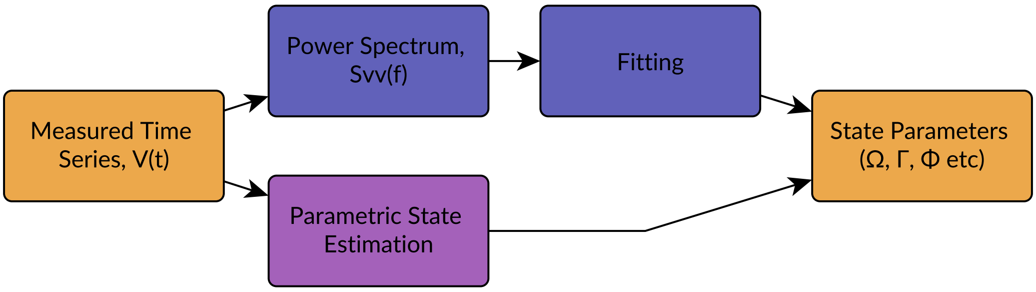

Fig. 7.2. *Parametric vs. non-parametric state estimation*

The problem with parametric methods is that they depend on the linear, auto-regressive nature of the measurement, which is not the case in this experment. The sinusoidal dependence of $V(t)$ on $x(t)$ seems to make these techniques incompatible with this particular experimental architecture, although this is a mature field with much transferable research available from RF engineering and investigating these possibilities merits further attention.

An alternative approach to parametric state estimation might be to train a machine learning (ML) system with simulated position spectra generated from known state parameters. This ML system should be able to then accept a measured signal time series and could deduce the state parameters, given sufficient training on appropriately scaled simulation data. This ML approach should be able to emulate the ability of researchers in the field to look at a time series data and estimate how the particle was behaving, after becoming familiar with a particular experimental system; however qualitative information from the human would be replaced with quantitative state estimates from the ML model.

§7.5. Rayleigh Scatter Suppression

In §1.2.2.1 the state of the art in levitated optomechanics cooling was discussed, and figure 1.8a shows that as pressure decreases, centre of mass temperature encounters a limit. This limit is is due to radiation pressure shot noise (RPSN), the heating effect of the individual momentum kicks experienced by the particle when it scatters trapping light photons. The scattered photons leave the particle with directions distributed by the dipole emission pattern (figure 2.9, equation 2.35), which is symmetric in the z direction. This means the particle centre of mass experiences random momentum kicks and this mechanism can be represented by a heating rate proportional to the scattered laser power and Rayleigh scatter cross-section.

During the course of this project, the idea of a geometry for suppressing this Rayleigh scatter, and therefore the associated heating, was discussed. If built, this could allow the levitated optomechanics community to cool an oscillator to lower phonon occupation number and possibly even to the ground state. The experimental geometry consists of a hemispherical mirror with a radius of a few millimetres at the centre of which a nanoparticle is trapped. The exact mirror radius is manufactured to be close to an integer number of wavelengths of the trapping light and then can be fine tuned by heating. This heating causes thermal expansion of the mirror and allows the radius to be tuned such that scattered light from the particle arrives at the mirror and is retro-reflected, self-interfering and either cancelling or enhancing the scattering process. Ramping the radius of the mirror over a range of a few wavelengths should show a periodic enhancement and suppression of Rayleigh scatter [193]; in a manner similar to that discussed in [194]. A nanoparticle in an optical trap spends mmost of its time about $0.1 \times \lambda$ from it's average position, which could be positioned at the centre of the hemispherical mirror. When tuned to suppress, this method should reduce the effects of heating from RPSN by a factor of $\sim$10 [194]. Figure 7.3 shows the proposed geometry of such a system.

The problem with this idea is that we are suppressing the scatter used to determine the position of the particle, and so we need another method for position measurement. This could be illumination with a second, low power laser, the scatter of which will cause a significantly smaller heating effect than the trapping beam. This scattered light could be collected with a microscope objective and sent to an interferomter in order to determine the particle position. The construction of this setup was beyond the time and cost constraints of this project and so is left for future research. The effects of this kind of tunable supression should be interesting to see, and hopefully could provide a partial solution to the RPSN problem seen across the levitated optomechanics community.

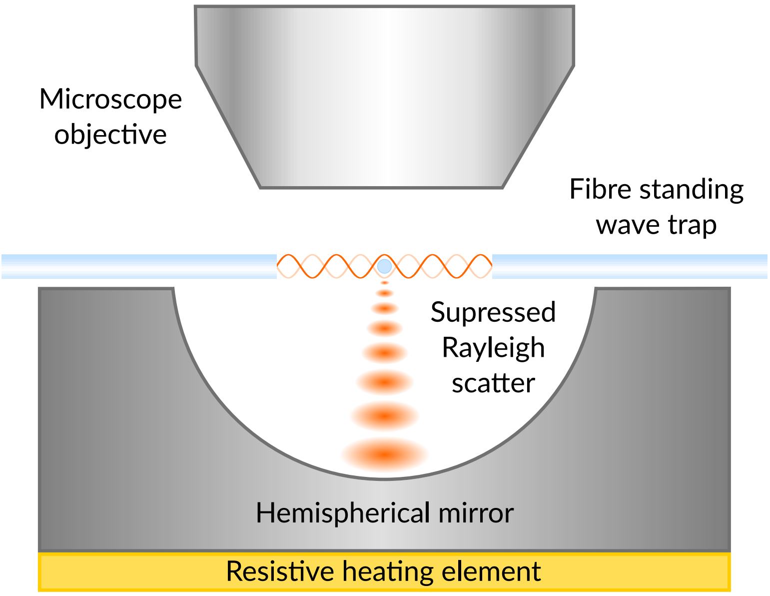

Fig. 7.3. *Rayleigh scatter suppression geometry - A standing wave trap confines the particle in three dimensions at the centre of a hemispherical mirror. Rayleigh scatter is suppressed by the correctly sized mirror, reducing RPSN.*

Doubtless, there are many possible avenues for future research from this system outside those considered in this chapter. The sections above are represent some interesting extensions to this work that could be undertaken by a future student or researcher using the progress made here. In the next and final chapter we give an overview of the progress made towards the objectives of this project and the results that has been discussed in this thesis, as well as looking briefly at what the future is likely to hold for the field of levitated optomechanics.

CHAPTER 8

Conclusion and Outlook

The work herein divides into two parts: the development of the experiment, and the parameter estimation work. In this chapter we will round off the thesis by giving an overview of these two parts and the progress made, making attempts to continually link back to the project goals laid out in §1.4. The thesis will close with a discussion of the future outlook for experiments of this type and the achievements expected in the next few years.

§8.1. Experimental Development

In chapter 4, the experimental setup was described and evaluated. This is a fibre-based, 5 W, 1550 nm optical system that interfaces with a vacuum chamber capable of rapidly reaching pressures of 10^{-6} mbar. The system uses an NA=0.98 parabolic mirror objective to produce a focal waist radius of approximately half a wavelength, in which a 100 nm diameter silica nanoparticle is trapped. The particle oscillates along the optical axis with a frequency of around 100 kHz, and this can be controlled by adjusting the trapping laser power. The setup is designed to maximise the information collected about the motion of the particle in the z direction, and is insensitive to motion in the x or y directions to first order. The oscillating particle phase modulates the trapping light, and Rayleigh scatters this light into the parabolic mirror, where it is collected and coupled back into the optics system. The fibre coupled nature of the optics system means that the majority of the collected signal light is directed to active photodiode area, increasing the signal to noise ratio, and hopefully eventually helping us get closer to the standard quantum limit of position detection.

A fibre-based Mach-Zehnder interferometer was constructed using a fibre circulator, by which phase modulated light is interfered with a reference field in order to produce an oscillating intensity signal at a photodiode. This signal can be used to track the particle motion, although it does not represent a linear measurement of particle position. The setup was designed to incorporate the ability to perform heterodyne measurement in which the phase modulated signal light is interfered with a frequency shifted light source, produced using an AOM. The resultant heterodyne signal is positioned at the difference frequency between the two fields and can be down shifted in order to increase spectral resolution when recorded. The heterodyne signal does not suffer from the loss of information that occurs when using homodyne alternatives, as the spectrum is not centred on 0 Hz when viewed in frequency space, and so does not “fold back” and interfere with itself, changing the spectrum peak amplitudes in the process. For this reason the heterodyne spectrum gives more reliable information on which to perform statistical analysis about the motion of the particle, for use in the parameter estimation research.

The developmental aims outlined in §1.4 have been achieved, and the system performs as was hoped when undertaking this process. Multiple design iterations were used, but the setup as it exists is suitable for performing the research into the more precise state estimation techniques. The setup benefits from a good signal to noise ratio, producing clean spectra that are not cluttered by features not represented in theoretical spectra. The work on the experimental system enabled the state estimation work and allowed for a contribution to the field of levitated optomechanics.

§8.2. Parameter Estimation

Chapter 6 presents a new method for estimating thermodynamic state parameters of an optically trapped nanoparticle, in which the Middleton expansion from RF engineering is applied to produce a power spectrum of position signal measurements from the particle. This technique does not treat the particle position as sinusoidal, as for times longer than the damping time $^1/_\Gamma$, this is not true by definition. Instead the particle is modelled as a stochastic harmonic oscillator, phase modulated by a Gaussian random process with a given power spectrum. We calculate the autocorrelation function of the detector signal and find it to be dependent on a sum of modified Bessel functions, rather than unmodified as has been previously used, although for the experimental parameters of previous systems the difference is small.

The measured intensity signal at our detector is sinusoidally dependent on particle position, and the precise form of the time trace depends on the relative phase between signal and reference fields. Using the methods described, we calculate a power spectral density that depends on intuitable, physical parameters of the system, and that can be fit to a measured power spectrum in order to estimate the state of the particle oscillation.

The calculated spectra show excellent agreement with power spectra estimated from measured position data, and we extract the phase modulation depth, damping rate and trap frequency. Using an equipartition argument we calculated the RMS position amplitude and find it to be consistent with values in the literature. The spectrum generation model was extended to include an arbitrary broadening profile, representing intensity gradient fluctuations in the experimental system that cause the trap frequency to fluctuate and work to broaden spectral features. A Gaussian broadening model was used, however this should be extended in the future to use a measured intensity distribution to better account for these effects.

Using this state estimation technique, the state parameters were tracked as environmental conditions were changed and we observed what we believe to be an upturn in centre of mass temperature as pressure is reduced, however RIN broadening needs to be reduced and these results verified down to lower pressure. We observed an interesting relation between background gas pressure and Stokes damping rate, where damping appeared to decrease non-linearly with pressure. This disagrees with the current model and suggests that the particle radius may have been changing as pressure decreased. This could be due to some form of annealing/tempering process in which the glass restructures on the molecular level and leads to a changed density, or that parts of the nanoparticle or impurities are ejected from, or adhere to the surface, altering the particle radius.

§8.3. Future Outlook

In the future, levitated optomechanics is likely to continue the recent trends, and systems will reach lower and lower phonon occupation numbers. The limits of RPSN are plaguing these kinds of attempts at present, but doubtless this will not continue indefinitely. Just as occurred with more traditional optomechanical resonators such as ring cavities, nano-beams and trampolines, in the near future levitated systems are likely to reach the quantum ground state. At these levels of centre of mass energy they become useful in many sensing applications and are likely to see more application based development. Recently, much levitated optomechanics research has used strong electric fields and charged nanoparticles to investigate various aspects of physics, with the sensing of short-range forces becoming popular. Nanoparticles are likely to continue to be used as probes for surface forces such as the Casimir-Polder force, and for modifications to our understanding of gravity, as well as possible tests of proposed collapse models such as CSL. If levitated optomechanics systems can be cooled to the ground state, its then natural to expect they would then be used to investigate quantum and stochastic thermodynamics. This could further current theoretical and experimental work into fluctuation theorems and help develop a better understanding of how heat behaves on the nano-scale. Rotational optomechanics has opened up an entirely new field of research in the past decade, and this progress with asymmetric nanospheres, and nanorods will surely continue; perhaps these rotational degrees of freedom can also reach low phonon occupation numbers, or alternatively maybe we can take advantage of their ultra-high frequency stability.

Hopefully the work in this thesis is interesting to other researchers, and as a research community we can better understand the subtleties of how best to treat the information with which we calculate how these particles are behaving. Spectrum estimation is a vast research area with many decades of work done in radio frequency signal analysis; perhaps there are even better methods for obtaining information about levitated optomechanics systems, but this needs further work and verification in other experimental setups.

Bibliography

[1] M. Aspelmeyer, T. J. Kippenberg, and F. Marquardt, "Cavity Optomechanics," *Reviews of Modern Physics*, vol. 86, p. 65, mar 2013.

[2] C. Reinhardt, T. Müller, A. Bourassa, and J. C. Sankey, "Ultralow-Noise SiN Trampoline MEMS for Sensing and Optomechanics," vol. 021001, no. April, p. 7, 2015.

[3] Y.-C. Liu, Y.-W. Hu, C. W. Wong, and Y.-F. Xiao, "Review of cavity optomechanical cooling," *Chinese Physics B*, vol. 22, p. 114213, nov 2013.

[4] E. Gavartin, P. Verlot, and T. J. Kippenberg, "A hybrid on-chip optomechanical transducer for ultra-sensitive force measurements," *Nature Nanotechnology*, vol. 7, no. 8, pp. 509–514, 2012.

[5] A. Schliesser, R. Rivière, G. Anetsberger, O. Arcizet, and T. J. Kippenberg, "Resolved-sideband cooling of a micromechanical oscillator," *Nature Physics*, vol. 4, pp. 415–419, apr 2008.

[6] M. Goryachev, D. L. Creedon, E. N. Ivanov, S. Galliou, R. Bourquin, and M. E. Tobar, "Extremely low-loss acoustic phonons in a quartz bulk acoustic wave resonator at millikelvin temperature," *Applied Physics Letters*, vol. 100, no. 24, 2012.

[7] J. Gieseler, B. Deutsch, R. Quidant, and L. Novotny, "Subkelvin Parametric Feedback Cooling of a Laser-Trapped Nanoparticle," *Physical Review Letters*, vol. 109, no. 10, p. 103603, 2012.

[8] V. Jain, J. Gieseler, C. Moritz, C. Dellago, R. Quidant, and L. Novotny, "Direct Measurement of Photon Recoil from a Levitated Nanoparticle," pp. 1–9, 2016.

[9] M. Frimmer, K. Luszcz, S. Ferrero, V. Jain, and L. Novotny, "Controlling the net charge on a nanoparticle optically levitated in vacuum," 2017.

[10] Https://commons.wikimedia.org/wiki/File:GaussianBeamWaist.svg, "Gaussian beam waist."

[11] B. Novotny, Lukas & Hecht, "Principles of Nano-optics," *Textbook*, vol. 1, p. 559, 2006.

[12] P. H. Jones, O. M. Maragò, and G. Volpe, "Optical tweezers: principles and applications," *Cambridge University Press*, vol. 1, p. 541, 2015.

[13] R. Kitamura, L. Pilon, and M. Jonasz, "Optical constants of silica glass from extreme ultraviolet to far infrared at near room temperature," vol. 46, no. 33, 2007.

[14] R.P. Photonics, "Silica Fibers," 2019.

[15] Wolfram, "Ito Process," 2020.

[16] X. Pang, T. D. Visser, and E. Wolf, "Phase anomaly and phase singularities of the field in the focal region of high-numerical aperture systems," *Optics Communications*, vol. 284, no. 24, pp. 5517–5522, 2011.

[17] C. Dawson and J. Bateman, "Spectral analysis and parameter estimation in levitated optomechanics," *Journal of the Optical Society of America B*, vol. 36, no. 6, p. 1565, 2019.

[18] A. Roy, A. B. S. Jing, and M. D. Barrett, "The trapping and detection of single atoms using a spherical mirror," *New Journal of Physics*, vol. 14, 2012.

[19] L. Pinard, C. Michel, B. Sassolas, L. Balzarini, J. Degallaix, J. Dolique, R. Flaminio, D. Forest, M. Granata, B. Lagrange, N. Straniero, J. Teillon, and G. Cagnoli, "The Mirrors Used in the LIGO Interferometers for the First-time Detection of Gravitational Waves," *Optical Interference Coatings 2016*, vol. 56, no. 4, p. MB.3, 2016.

[20] J. Chan, T. P. M. Alegre, A. H. Safavi-Naeini, J. T. Hill, A. Krause, S. Groeblacher, M. Aspelmeyer, and O. Painter, "Laser cooling of a nanomechanical oscillator into its quantum ground state," *Nature*, vol. 478, p. 18, 2011.

[21] J. Vovrosh, M. Rashid, D. Hempston, J. Bateman, and H. Ulbricht, "Controlling the Motion of a Nanoparticle Trapped in Vacuum," *ArXiv*, pp. 1–18, 2016.

[22] A. Ashkin and J. M. Dziedzic, “Optical levitation by radiation pressure,” *Applied Physics Letters*, vol. 19, no. 8, pp. 283–285, 1971.

[23] L. Novotny, “Radiation damping of a polarizable particle,” *Physical Review A*, vol. 96, no. 3, pp. 1–5, 2017.

[24] A. Ashkin, “Acceleration and Trapping of Particles by Radiation Pressure,” *Physical Review Letters*, vol. 24, no. 4, pp. 156–159, 1970.

[25] A. Ashkin and J. M. Dziedzic, “Optical levitation in high vacuum,” *Applied Physics Letters*, vol. 28, no. 6, pp. 333–335, 1976.

[26] A. Ashkin and J. M. Dziedzic, “Feedback stabilization of optically levitated particles,” *Applied Physics Letters*, vol. 30, no. 4, pp. 202–204, 1977.

[27] A. L. Schawlow and C. H. Townes, “Infrared and optical masers,” *Physical Review*, vol. 112, no. 6, pp. 1940–1949, 1958.

[28] H. Tashiro, M. Uchida, and M. Sato-Maeda, “Three-dimensional cell manipulator by means of optical trapping for the specification of cell-to-cell adhesion,” *Opt. Engin.*, vol. 32, no. 11, pp. 2812–2817, 1993.

[29] C. G. Baumann, S. B. Smith, V. A. Bloomfield, and C. Bustamante, “Ionic effects on the elasticity of single DNA molecules,” *Proceedings of the National Academy of Sciences*, vol. 94, no. 12, pp. 6185–6190, 1997.

[30] M. Y. Wu, D. X. Ling, L. Ling, W. Li, and Y. Q. Li, “Stable optical trapping and sensitive characterization of nanostructures using standing-wave Raman tweezers,” *Scientific Reports*, vol. 7, no. January, pp. 1–8, 2017.

[31] Y. Zhang, X. Wu, Y. Wang, S. Zhu, B. Z. Gao, and X. C. Yuan, “Measurement of the microscopic viscosities of microfluids with a dynamic optical tweezers system,” *Laser Physics*, vol. 24, no. 6, 2014.

[32] X.-C. Yao and A. Castro, “Optical trapping microfabrication with electrophoretically delivered particles inside glass capillaries.,” *Optics letters*, vol. 28, no. 15, pp. 1335–7, 2003.

[33] A. Ashkin, J. M. Dziedzic, J. E. Bjorkholm, and S. Chu, “Observation of a single-beam gradient force optical trap for dielectric particles,” *Optics Letters*, vol. 11, no. 5, p. 288, 1986.

[34] A. Ashkin, “Forces of a single-beam gradient laser trap on a dielectric sphere in the ray optics regime,” *Biophysical Journal*, vol. 61, no. 2, pp. 569–582, 1992.

[35] E. Hecht, *Optics*. Pearson, 5th ed., 2016.

[36] R. Omori, T. Kobayashi, and a. Suzuki, “Observation of a single-beam gradient-force optical trap for dielectric particles in air.,” *Optics letters*, vol. 22, no. 11, pp. 816–818, 1997.

[37] M. D. Summers, D. R. Burnham, and D. McGloin, “Trapping solid aerosols with optical tweezers: A comparison between gas and liquid phase optical traps,” *Optics Express*, vol. 16, no. 11, p. 7739, 2008.

[38] T. Li, S. Kheifets, D. Medellin, and M. G. Raizen, “Measurement of the instantaneous velocity of a brownian particle,” *Science*, vol. 328, no. 5986, pp. 1673–1675, 2010.

[39] T. Li, S. Kheifets, and M. G. Raizen, “Millikelvin cooling of an optically trapped microsphere in vacuum,” *Nature Physics*, vol. 7, no. 7, pp. 527–530, 2011.

[40] T. Li, “Fundamental Tests of Physics with Optically Trapped Microspheres,” 2013.

[41] J. Gieseler, *Dynamics of optically levitated nanoparticles in high vacuum*. Phd thesis, ICFO, 2014.

[42] S. Kuhn, G. Wachter, F. F. Wieser, J. Millen, M. Schneider, J. Schalko, U. Schmid, M. Trupke, and M. Arndt, “Nanoparticle detection in an open-access silicon microcavity,” *Applied Physics Letters*, vol. 111, no. 25, 2017.

[43] S. Kuhn, B. A. Stickler, A. Kosloff, F. Patolsky, K. Hornberger, M. Arndt, and J. Millen, “Optically driven ultra-stable nanomechanical rotor,” *Nature Communications*, vol. 8, no. 1, pp. 1–5, 2017.

[44] S. Kuhn, A. Kosloff, B. A. Stickler, F. Patolsky, K. Hornberger, M. Arndt, and J. Millen, “Full rotational control of levitated silicon nanorods,” *Optica*, vol. 4, no. 3, p. 356, 2017.

[45] D. Grass, J. Fesel, S. G. Hofer, N. Kiesel, and M. Aspelmeyer, “Optical trapping and control of nanoparticles inside evacuated hollow core photonic crystal fibers,” 2016.

[46] N. Kiesel, F. Blaser, U. Delić, D. Grass, R. Kaltenbaek, and M. Aspelmeyer, “Cavity cooling of an optically levitated submicron particle.,” *Proceedings of the National Academy of Sciences of the United States of America*, vol. 110, pp. 14180–5, aug 2013.

[47] O. Romero-Isart, A. C. Pflanzer, M. L. Juan, R. Quidant, N. Kiesel, M. Aspelmeyer, and J. I. Cirac, “Optically levitating dielectrics in the quantum regime: Theory and protocols,” *Physical Review A - Atomic, Molecular, and Optical Physics*, vol. 83, no. 1, pp. 1–27, 2011.

[48] J. Millen, P. Z. G. Fonseca, T. Mavrogordatos, T. S. Monteiro, and P. F. Barker, “Cavity cooling a single charged levitated nanosphere,” *Physical Review Letters*, vol. 114, no. 12, 2015.

[49] J. Millen, T. Deesuwan, P. Barker, and J. Anders, “Nanoscale temperature measurements using non-equilibrium Brownian dynamics of a levitated nanosphere,” *Nature Nanotechnology*, vol. 9, no. 6, pp. 425–9, 2014.

[50] M. G. Genoni, J. Zhang, J. Millen, P. F. Barker, and A. Serafini, “Quantum cooling and squeezing of a levitating nanosphere via time-continuous measurements,” *New Journal of Physics*, vol. 17, no. 7, p. 73019, 2015.

[51] G. A. T. Pender, P. F. Barker, F. Marquardt, J. Millen, and T. S. Monteiro, “Optomechanical cooling of levitated spheres with doubly resonant fields,” *Physical Review A*, vol. 85, no. 2, p. 021802, 2012.

[52] P. Z. G. Fonseca, E. B. Aranas, J. Millen, T. S. Monteiro, and P. F. Barker, “Nonlinear dynamics and millikelvin cavity-cooling of levitated nanoparticles,” pp. 1–5, 2015.

[53] A. T. Anishur Rahman, A. C. Frangeskou, P. F. Barker, and G. W. Morley, “An analytical model for the detection of levitated nanoparticles in optomechanics,” *Review of Scientific Instruments*, vol. 89, no. 2, pp. 1–10, 2018.

[54] P. F. Barker and M. N. Shneider, “Cavity cooling of an optically trapped nanoparticle,” *Physical Review A - Atomic, Molecular, and Optical Physics*, vol. 81, feb 2010.

[55] T. S. Monteiro, J. Millen, G. A. T. Pender, F. Marquardt, D. Chang, and P. F. Barker, “Dynamics of levitated nanospheres: Towards the strong coupling regime,” *New Journal of Physics*, vol. 15, no. 1, p. 015001, 2013.

[56] E. B. Aranas, P. G. Z. Fonseca, P. F. Barker, and T. S. Monteiro, “Towards detection of the quantum limit with slowly modulated optomechanics,” vol. 0, pp. 1–5, 2016.

[57] A. Arvanitaki and A. A. Geraci, “Resonantly Detecting Axion-Mediated Forces with Nuclear Magnetic Resonance,” *Physical Review Letters*, vol. 113, no. 16, pp. 1–5, 2014.

[58] G. Ranjit, M. Cunningham, K. Casey, and A. A. Geraci, “Zeptonewton force sensing with nanospheres in an optical lattice,” *Physical Review A - Atomic, Molecular, and Optical Physics*, vol. 93, no. 5, pp. 1–5, 2016.

[59] A. Arvanitaki and A. A. Geraci, “Detecting high-frequency gravitational waves with optically levitated sensors,” *Physical Review Letters*, vol. 110, no. 7, pp. 1–5, 2013.

[60] Z.-Q. Yin, A. A. Geraci, and T. Li, “Optomechanics of Levitated Dielectric Particles,” *International Journal of Modern Physics B*, vol. 27, no. 26, p. 1330018, 2013.

[61] A. Geraci and H. Goldman, “Sensing Short-Range Forces with a Nanosphere Matter-Wave Interferometer,” 2014.

[62] G. Ranjit, D. P. Atherton, J. H. Stutz, M. Cunningham, and A. A. Geraci, “Attonewton force detection using microspheres in a dual-beam optical trap in high vacuum,” *Physical Review A*, vol. 91, p. 051805, 2015.

[63] A. A. Geraci, S. B. Papp, and J. Kitching, “Short-range force detection using optically cooled levitated microspheres,” *Physical Review Letters*, vol. 105, no. 10, pp. 1–4, 2010.

[64] A. A. Geraci, S. J. Smullin, D. M. Weld, J. Chiaverini, and A. Kapitulnik, “Improved constraints on non-Newtonian forces at 10 microns,” *Physical Review D - Particles, Fields, Gravitation and Cosmology*, vol. 78, no. 2, pp. 1–12, 2008.

[65] Z. Q. Yin, T. Li, X. Zhang, and L. M. Duan, “Large quantum superpositions of a levitated nanodiamond through spin-optomechanical coupling,” *Physical Review A - Atomic, Molecular, and Optical Physics*, vol. 88, no. 3, pp. 1–6, 2013.

[66] T. M. Hoang, Y. Ma, J. Ahn, J. Bang, F. Robicheaux, Z.-Q. Yin, and T. Li, “Torsional optomechanics of a levitated nonspherical nanoparticle,” *ArXiv e-prints*, pp. 1–5, 2016.

[67] J. Millen and A. Xuereb, “Perspective on quantum thermodynamics,” *New Journal of Physics*, vol. 18, no. 1, p. 011002, 2016.

[68] J. Gieseler and J. Millen, “Levitated Nanoparticles for Microscopic Thermodynamics — A Review,” *Entropy*, pp. 1–23, 2018.

[69] D. Goldwater, B. A. Stickler, K. Hornberger, and J. Millen, “Levitated electromechanics: all-electrical cooling of charged nano- and micro-particles,” 2018.

[70] B. Stickler, B. Papendell, S. Kuhn, B. Schrinski, J. Millen, M. Arndt, and K. Hornberger, “Probing macroscopic quantum superpositions with nanorotors,” *New Journal of Physics*, pp. 0–10, 2018.

[71] P. Mestres, J. Berthelot, M. Spasenović, J. Gieseler, L. Novotny, and R. Quidant, “Long distance manipulation of a levitated nanoparticle in high vacuum,” *ArXiv e-prints*, pp. 1–12, 2015.

[72] J. Gieseler, L. Novotny, and R. Quidant, “Thermal nonlinearities in a nanomechanical oscillator,” *Nat Phys*, vol. 9, no. 12, pp. 806–810, 2013.

[73] J. Gieseler, R. Quidant, C. Dellago, and L. Novotny, “Dynamic relaxation of a levitated nanoparticle from a non-equilibrium steady state,” *Nature Nanotechnology*, vol. 9, no. 5, pp. 358–364, 2014.

[74] F. Ricci, R. A. Rica, M. Spasenovic, J. Gieseler, L. Rondin, L. Novotny, and R. Quidant, “Optically levitated nanoparticle as a model system for stochastic bistable dynamics,” *Nature Communications*, vol. 8, no. May, pp. 1–7, 2017.

[75] J. Gieseler, M. Spasenović, L. Novotny, and R. Quidant, “Nonlinear mode coupling and synchronization of a vacuum-trapped nanoparticle,” *Physical Review Letters*, vol. 112, no. 10, pp. 1–5, 2014.

[76] L. P. Neukirch, J. Gieseler, R. Quidant, L. Novotny, and A. Nick Vamivakas, “Observation of nitrogen vacancy photoluminescence from an optically levitated nanodiamond.,” *Optics letters*, vol. 38, pp. 2976–9, aug 2013.

[77] P. Mestres, J. Berthelot, M. Spasenović, J. Gieseler, L. Novotny, and R. Quidant, “Cooling and manipulation of a levitated nanoparticle with an optical fiber trap,” *Applied Physics Letters*, vol. 107, no. 15, 2015.

[78] M. Frimmer, J. Gieseler, T. Ihn, and L. Novotny, “A levitated nanoparticle as a classical two-level atom,” vol. 34, no. 6, pp. 52–57, 2017.

[79] D. Hempston, J. Vovrosh, M. Toroš, G. Winstone, M. Rashid, and H. Ulbricht, “Force sensing with an optically levitated charged nanoparticle,” *Applied Physics Letters*, vol. 111, no. 13, pp. 1–5, 2017.

[80] A. Setter, M. Toroš, J. F. Ralph, and H. Ulbricht, “Real-time Kalman filter: Cooling of an optically levitated nanoparticle,” *Physical Review A*, vol. 97, no. 3, pp. 1–8, 2018.

[81] M. Rashid and H. Ulbricht, “Wigner Reconstruction in Levitated Optomechanics,” *ArXiv e-prints*, pp. 1–5, 2017.

[82] M. Rashid, T. Tufarelli, J. Bateman, J. Vovrosh, D. Hempston, M. S. Kim, and H. Ulbricht, “Experimental Realization of a Thermal Squeezed State of Levitated Optomechanics,” *Physical Review Letters*, vol. 117, no. 27, pp. 1–5, 2016.

[83] J. Bateman, I. McHardy, A. Merle, T. R. Morris, and H. Ulbricht, “On the Existence of Low-Mass Dark Matter and its Direct Detection,” *Scientific Reports*, vol. 5, p. 8058, 2015.

[84] J. Bateman, S. Nimmrichter, K. Hornberger, and H. Ulbricht, “Near-field interferometry of a free-falling nanoparticle from a point-like source,” *Nature Communications*, vol. 5, 2014.

[85] C. Wan, M. Scala, G. W. Morley, A. A. Rahman, H. Ulbricht, J. Bateman, P. F. Barker, S. Bose, and M. S. Kim, “Free Nano-Object Ramsey Interferometry for Large Quantum Superpositions,” *Physical Review Letters*, vol. 117, no. 14, pp. 1–6, 2016.

[86] A. Großardt, J. Bateman, H. Ulbricht, and A. Bassi, “Effects of Newtonian gravitational self-interaction in harmonically trapped quantum systems,” *Scientific Reports*, vol. 6, pp. 1–16, 2016.

[87] A. Xuereb, H. Ulbricht, and M. Paternostro, “Macroscopicity in an optomechanical matter-wave interferometer,” *Optics Communications*, vol. 337, pp. 53–56, 2014.

[88] J. Vovrosh, M. Rashid, D. Hempston, J. Bateman, M. Paternostro, and H. Ulbricht, “Parametric feedback cooling of levitated optomechanics in a parabolic mirror trap,” *Journal of the Optical Society of America B*, vol. 34, no. 7, p. 1421, 2017.

[89] A. Sawadsky, H. Kaufer, R. M. Nia, S. P. Tarabrin, F. Y. Khalili, K. Hammerer, and R. Schnabel, “Observation of generalized optomechanical coupling and cooling on cavity resonance,” *Physical Review Letters*, vol. 114, no. 4, pp. 1–5, 2015.

[90] B. Rodenburg, L. P. Neukirch, A. N. Vamivakas, and M. Bhattacharya, “Quantum model of cooling and force sensing with an optically trapped nanoparticle,” *Optica*, vol. 3, no. 3, p. 318, 2016.

[91] F. Marquardt and S. Girvin, “Optomechanics,” *Physics*, vol. 2, p. 40, may 2009.

[92] F. Marquardt, A. A. Clerk, and S. M. Girvin, “Quantum Theory of Optomechanical Cooling,” *ArXiv e-prints*, vol. 2008, p. 12, mar 2008.

[93] E. Hebestreit, M. Frimmer, R. Reimann, and L. Novotny, “Sensing Static Forces with Free-Falling Nanoparticles,” *Physical Review Letters*, vol. 121, no. 6, pp. 1–5, 2018.

[94] G. Winstone, M. Rademacher, R. Bennett, S. Buhmann, and H. Ulbricht, “Direct measurement of short-range forces with a levitated nanoparticle,” *ArXiv e-prints*, pp. 1–12, 2017.

[95] R. Diehl, E. Hebestreit, R. Reimann, F. Tebbenjohanns, M. Frimmer, and L. Novotny, “Optical levitation and feedback cooling of a nanoparticle at subwavelength distances from a membrane,” *Physical Review A*, vol. 98, no. 1, pp. 1–6, 2018.

[96] Y. Arita, M. Mazilu, and K. Dholakia, “Laser-induced rotation and cooling of a trapped microgyroscope in vacuum,” *Nature Communications*, vol. 4, pp. 1–7, 2013.

[97] R. Reimann, M. Doderer, E. Hebestreit, R. Diehl, M. Frimmer, D. Windey, F. Tebbenjohanns, and L. Novotny, “GHz Rotation of an Optically Trapped Nanoparticle in Vacuum,” pp. 1–5, 2018.

[98] S. M. Barnett, “Optical angular-momentum flux,” *Journal of Optics B: Quantum and Semiclassical Optics*, vol. 4, no. 2, pp. S7–S16, 2002.

[99] D. Serrano, J. Karlsson, A. Fossati, A. Ferrier, and P. Goldner, “All-optical control of long-lived nuclear spins in rare-earth doped nanoparticles,” *Nature Communications*, vol. 9, no. 1, pp. 1–7, 2018.

[100] H. S. Knowles, D. M. Kara, and M. Atatüre, “Controlling a nuclear spin in a nanodiamond,” *Physical Review B*, vol. 96, no. 11, pp. 1–6, 2017.

[101] S. Dhomkar, J. Henshaw, H. Jayakumar, and C. A. Meriles, “Long-term data storage in diamond,” *Science Advances*, vol. 2, no. 10, pp. e1600911–e1600911, 2016.

[102] V. R. Horowitz, B. J. Alemán, D. J. Christle, A. N. Cleland, and D. D. Awschalom, “Electron spin resonance of nitrogen-vacancy centers in optically trapped nanodiamonds.,” *Proceedings of the National Academy of Sciences of the United States of America*, vol. 109, pp. 13493–7, aug 2012.

[103] R. M. Pettit, L. P. Neukirch, Y. Zhang, and A. Nick Vamivakas, “Coherent control of a single nitrogen-vacancy center spin in optically levitated nanodiamond,” *Journal of the Optical Society of America B*, vol. 34, no. 6, p. C31, 2017.

[104] A. C. Frangeskou, A. T. Rahman, L. Gines, S. Mandal, O. A. Williams, P. F. Barker, and G. W. Morley, “Pure nanodiamonds for levitated optomechanics in vacuum,” *New Journal of Physics*, vol. 20, no. 4, 2018.

[105] Materialscientist, “Model of nitrogen-vacancy center in diamond.”

[106] A. A. Geraci, S. B. Papp, and J. Kitching, “Short-range force detection using optically cooled levitated microspheres,” *Physical Review Letters*, vol. 105, no. 10, pp. 3–6, 2010.

[107] S. Nimmrichter, K. Hornberger, and K. Hammerer, “Optomechanical sensing of spontaneous wave-function collapse,” *Physical Review Letters*, vol. 113, no. 2, pp. 1–5, 2014.

[108] A. Bassi, K. Lochan, S. Satin, T. P. Singh, and H. Ulbricht, "Models of wave-function collapse, underlying theories, and experimental tests," *Reviews of Modern Physics*, vol. 85, no. 2, pp. 471–527, 2013.

[109] G. C. Ghirardi, P. Pearle, and A. Rimini, "Markov processes in Hilbert space and continuous spontaneous localization of systems of identical particles," *Physical Review A*, vol. 42, no. 1, pp. 78–89, 1990.

[110] I. A. Martínez, E. Roldán, L. Dinis, D. Petrov, J. M. Parrondo, and R. A. Rica, "Brownian Carnot engine," *Nature Physics*, vol. 12, no. 1, pp. 67–70, 2016.

[111] M. Diez-Silva, M. Dao, J. Han, C.-T. Lim, and S. Suresh, "Shape and Biomechanical Characteristics of Human Red Blood Cells in Health and Disease," *MRS Bulletin*, vol. 35, no. 05, pp. 382–388, 2010.

[112] J. C. Slater, "Atomic radii in crystals," *The Journal of Chemical Physics*, vol. 41, no. 10, pp. 3199–3204, 1964.

[113] M. Arndt, O. Nairz, J. Vos-Andreae, C. Keller, G. Van Der Zouw, and A. Zellinger, "Wave-particle duality of C60 molecules," *Nature*, vol. 401, no. 6754, pp. 680–682, 1999.

[114] S. Gerlich, S. Eibenberger, M. Tomandl, S. Nimmrichter, K. Hornberger, P. J. Fagan, J. Tüxen, M. Mayor, and M. Arndt, "Quantum interference of large organic molecules," *Nature Communications*, vol. 2, no. 1, 2011.

[115] C. Brand, S. Eibenberger, U. Sezer, and M. Arndt, "Matter-wave physics with nanoparticles and biomolecules," *ArXiv e-prints*, pp. 1–27, 2017.

[116] R. Kaltenbaek, M. Aspelmeyer, P. F. Barker, A. Bassi, J. Bateman, K. Bongs, S. Bose, C. Braxmaier, C. Brukner, B. Christophe, M. Chwalla, P. F. Cohadon, A. M. Cruise, C. Curceanu, K. Dholakia, L. Diósi, K. Döringshoff, W. Ertmer, J. Gieseler, N. Gürlebeck, G. Hechenblaikner, A. Heidmann, S. Herrmann, S. Hossenfelder, U. Johann, N. Kiesel, M. Kim, C. Lämmerzahl, A. Lambrecht, M. Mazilu, G. J. Milburn, H. Müller, L. Novotny, M. Paternostro, A. Peters, I. Pikovski, A. P. Zanoni, E. M. Rasel, S. Reynaud, C. J. Riedel, M. Rodrigues, L. Rondin, A. Roura, W. P. Schleich, J. Schmiedmayer, T. Schuldt, K. C. Schwab, M. Tajmar, G. M. Tino, H. Ulbricht, R. Ursin, and V. Vedral, "Macroscopic quantum resonators (MAQRO): 2015 update," *EPJ Quantum Technology*, vol. 3, no. 1, 2016.

[117] L. Diósi, "Testing spontaneous wave-function collapse models on classical mechanical oscillators," *Physical Review Letters*, vol. 114, no. 5, pp. 1–5, 2015.

[118] A. Smirne and A. Bassi, "Dissipative Continuous Spontaneous Localization (CSL) model," *Scientific Reports*, vol. 5, pp. 1–9, 2015.

[119] M. Carlesso, M. Paternostro, H. Ulbricht, A. Vinante, and A. Bassi, "Non-interferometric test of the continuous spontaneous localization model based on rotational optomechanics," *New Journal of Physics*, 2018.

[120] ESA, "Assessment of a Quantum Physics Payload Platform QPPF," Tech. Rep. CDF-183(C), 2018.

[121] A. A. Geraci, S. B. Papp, and J. Kitching, "Short-range force detection using optically cooled levitated microspheres," *Physical Review Letters*, vol. 105, no. 10, pp. 1–4, 2010.

[122] Y. Bidel, O. Carraz, R. Charrière, M. Cadoret, N. Zahzam, and A. Bresson, "Compact cold atom gravimeter for field applications," *Applied Physics Letters*, vol. 102, no. 14, pp. 0–4, 2013.

[123] UQuans, "Absolute Quantum Gravimeter," tech. rep.

[124] S. Abend, M. Gebbe, M. Gersemann, H. Ahlers, H. Müntinga, E. Giese, N. Gaaloul, C. Schubert, C. Lämmerzahl, W. Ertmer, W. P. Schleich, and E. M. Rasel, "Atom-chip fountain gravimeter," *Physical Review Letters*, vol. 117, no. 20, pp. 1–7, 2016.

[125] C. V. Rammeloo, *Optimisation of a Compact Cold-Atoms Interferometer for Gravimetry*. PhD thesis, University of Birmingham, 2018.

[126] L. Zhu, *A cold atoms gravimeter for use in absolute gravity comparisons*. PhD thesis, University of Birmingham, 2018.

[127] J. I. Malcolm, *Construction of a portable platform for cold atom interferometry*. PhD thesis, University of Birmingham, 2015.

[128] S. A. Beresnev, V. G. Chernyak, and G. A. Fomyagin, “Motion of a spherical particle in a rarefied gas. Part 2. Drag and thermal polarization,” *Journal of Fluid Mechanics*, vol. 219, no. -1, p. 405, 1990.

[129] Pfeiffer, “The Vacuum Technology Know How Book,” 2013.

[130] G. Winstone, R. Bennett, M. Rademacher, M. Rashid, S. Buhmann, and H. Ulbricht, “Direct measurement of the electrostatic image force of a levitated charged nanoparticle close to a surface,” *Physical Review A*, vol. 98, no. 5, p. 053831, 2018.

[131] J. Horodecki Michałand Oppenheim, “Fundamental limitations for quantum and nanoscale thermodynamics,” *Nature Communications*, vol. 4, no. May, pp. 1–6, 2013.

[132] J. Roßnagel, S. T. Dawkins, K. N. Tolazzi, O. Abah, E. Lutz, F. Schmidt-Kaler, and K. Singer, “A single-atom heat engine,” *Science*, vol. 352, no. 6283, pp. 325–329, 2016.

[133] J. Roßnagel, O. Abah, F. Schmidt-Kaler, K. Singer, and E. Lutz, “Nanoscale heat engine beyond the carnot limit,” *Physical Review Letters*, vol. 112, no. 3, pp. 1–5, 2014.

[134] F. Altintas, A. Ü. Hardal, and Ö. E. MüstecapIIoglu, “Quantum correlated heat engine with spin squeezing,” *Physical Review E - Statistical, Nonlinear, and Soft Matter Physics*, vol. 90, no. 3, pp. 1–9, 2014.

[135] V. Blickle and C. Bechinger, “Realization of a micrometre-sized stochastic heat engine,” *Nature Physics*, vol. 8, no. 2, pp. 143–146, 2012.

[136] D. Janzing, “On the computational power of molecular heat engines,” *Journal of Statistical Physics*, vol. 122, no. 3, pp. 531–556, 2006.

[137] S. Li, Q. Jiang, S. Liu, Y. Zhang, Y. Tian, C. Song, J. Wang, Y. Zou, G. J. Anderson, J.-y. Y. Han, Y. Chang, Y. Liu, C. Zhang, L. Chen, G. Zhou, G. Nie, H. Yan, B. Ding, and Y. Zhao, “A DNA nanorobot functions as a cancer therapeutic in response to a molecular trigger in vivo,” *Nature Biotechnology*, vol. 36, no. 3, pp. 258–264, 2018.

[138] V. García-López, F. Chen, L. G. Nilewski, G. Duret, A. Aliyan, A. B. Kolomeisky, J. T. Robinson, G. Wang, R. Pal, and J. M. Tour, “Molecular machines open cell membranes,” *Nature*, vol. 548, no. 7669, pp. 567–572, 2017.

[139] D. Dermatas, T. Mpouras, and I. Panagiotakis, “Application of Nanotechnology for waste management: Challenges and limitations,” *Waste Management and Research*, vol. 36, no. 3, pp. 197–199, 2018.

[140] A. Cavalcanti, B. Shirinzadeh, M. Zhang, and L. C. Kretly, “Nanorobot hardware architecture for medical defense,” *Sensors*, vol. 8, no. 5, pp. 2932–2958, 2008.

[141] Saha, M. Saha, and Saha, “Nanomedicine: Promising Tiny Machine for the Healthcare in Future-A Review,” *Oman Medical Journal*, vol. 24, no. 4, pp. 242–247, 2009.

[142] A. Ghosh and P. Fischer, “Controlled Propulsion of Artificial Magnetic Nanostructured Propellers 2009,” *Nano*, pp. 7–9, 2009.

[143] U. Seifert, “Stochastic thermodynamics, fluctuation theorems and molecular machines,” *Reports on Progress in Physics*, vol. 75, no. 12, 2012.

[144] M. Campisi, J. Pekola, and R. Fazio, “Nonequilibrium fluctuations in quantum heat engines: Theory, example, and possible solid state experiments,” *New Journal of Physics*, vol. 17, pp. 1–14, 2015.

[145] M. H. Partovi, “Quantum Thermodynamics,” *Physics Letters A*, vol. 137, no. 9, pp. 3–7, 1989.

[146] Anthony E Siegman, *Lasers*. Mill Valley, California: University Science Books, 1986.

[147] A. P. Kiselev, “Electromagnetic field in a neighborhood of a focus,” *Journal of Soviet Mathematics*, vol. 11, no. 5, pp. 744–752, 1979.

[148] J. A. Stratton and L. J. Chu, “Diffraction theory of electromagnetic waves,” *Physical Review*, vol. 56, no. 1, pp. 99–107, 1939.

[149] J. S. Lee, T. L. Song, J. K. Du, and J. G. Yook, “Near-field to far-field transformation based on stratton-chu fomula for EMC measurements,” *IEEE Antennas and Propagation Society, AP-S International Symposium (Digest)*, pp. 606–607, 2013.

[150] W. Hsu and R. Barakat, "Stratton–Chu vectorial diffraction of electromagnetic fields by apertures with application to small-Fresnel-number systems," *Journal of the Optical Society of America A*, vol. 11, no. 2, p. 623, 1994.

[151] M. T. H. Reid, S. Johnson, and J. Feist, "SCUFF-EM," 2019.

[152] M. Mahamdeh, C. Pérez Campos, and E. Schäffer, "Under-filling trapping objectives optimizes the use of the available laser power in optical tweezers," *Optics Express*, vol. 19, no. 12, p. 11759, 2011.

[153] H. Minkowski, "Die Grundgleichungen fur die elektromagnetischen Vorgange in bewegten Korpern," *Mathematische Annalen*, vol. 68, no. 4, pp. 472–525, 1910.

[154] E. A. Hinds and S. M. Barnett, "Momentum exchange between light and a single atom: Abraham or Minkowski?," *Physical Review Letters*, vol. 102, no. 5, pp. 1–4, 2009.

[155] M. Mansuripur, "Resolution of the Abraham–Minkowski controversy," *Optics Communications*, vol. 283, pp. 1997–2005, may 2010.

[156] R. Grimm, M. Weidemüller, and Y. B. Ovchinnikov, "Optical Dipole Traps for Neutral Atoms," *Advances in Atomic, Molecular and Optical Physics*, vol. 42, no. C, pp. 95–170, 2000.

[157] D. W. Hempston, *Force detection in levitated optomechanics.* PhD thesis, University of Southampton, 2017.

[158] J. Gieseler, B. Deutsch, R. Quidant, L. Novotny, I.-i. D. C. Fotoniques, and M. T. Park, "Supplementary Information for Sub-Kelvin Parametric Feedback Cooling of a Laser-Trapped Nanoparticle," *Phys. Rev. Lett.*, vol. 109, p. 103603, 2012.

[159] J. Vovrosh, *Parametric feedback cooling and squeezing of optically levitated Particles.* PhD thesis, University of Southampton, 2017.

[160] S. Ten, "Ultra Low-loss Optical Fiber Technology," *Optical Fiber Communication Conference 2016*, pp. 8–10, 2016.

[161] R. Kubo, "The fluctuation-dissipation theorem," *Reports on Progress in Physics*, vol. 29, no. 1, p. 306, 1966.

[162] P. D. Welch, "The Use of Fast Fourier Transform for the Estimation of Power Spectra: A Method Based on Time Averaging Over Short, Modified Periodograms," *IEEE Transactions on Audio and Electroacoustics*, vol. 15, no. 2, pp. 70–73, 1967.

[163] S. Engelberg, *Digital Signal Processing: An Experimental Approach.* 2008.

[164] Corning Inc., "Corning ®SMF- 28 ®Ultra Optical Fiber," no. November, 2014.

[165] P. Jayarajan, P. G. Kuppusamy, T. V. Sundararajan, M. R. Thiyagupriyadharsan, Z. AhamedYasar, R. Maheswar, and I. S. Amiri, "Analysis of temperature based power spectrum in EDFA and YDFA with different pump power for THz applications," *Results in Physics*, vol. 10, no. April, pp. 160–163, 2018.

[166] V. Salakhutdinov, M. Sondermann, L. Carbone, E. Giacobino, A. Bramati, and G. Leuchs, "Optical trapping of nanoparticles by full solid-angle focusing," *Optica*, vol. 3, no. 11, p. 1181, 2016.

[167] L. Alber, M. Fischer, M. Bader, K. Mantel, M. Sondermann, and G. Leuchs, "Focusing characteristics of a 4 pi parabolic mirror light-matter interface," *Journal of the European Optical Society*, vol. 13, no. 1, 2017.

[168] Corning Inc., "Single Fiber Fusion Splicing Application Note," no. June, 2009.

[169] A. A. Clerk, M. H. Devoret, S. M. Girvin, F. Marquardt, and R. J. Schoelkopf, "Introduction to quantum noise, measurement, and amplification," *Reviews of Modern Physics*, vol. 82, no. 2, pp. 1155–1208, 2010.

[170] C. M. Caves, "Quantum limits on noise in linear amplifiers," *Physical Review D*, vol. 26, no. 8, pp. 1817–1839, 1982.

[171] G. P. Agrawal, *Fiber-Optic Communications Systems, Third Edition.*, vol. 6. 2002.

[172] C. Dawson, "Echo," 2018.

[173] L3erdnik, “Arago Shadow,” 2018.

[174] E. D. Palik, *Handbook of Optical Constants of Solids.* Academic Press, 1985.

[175] B. Richards and E. Wolf, “Electromagnetic diffraction in optical systems, II. Structure of the image field in an aplanatic system,” *Proceedings of the Royal Society of London. Series A. Mathematical and Physical Sciences*, vol. 253, no. 1274, pp. 358–379, 1959.

[176] A. Boivin and E. Wolf, “Electromagnetic Field in the Neighborhood of the Focus of a Coherent Beam,” *Physical Review*, vol. 138, no. 6, 1965.

[177] W. Stöber, A. Fink, and E. Bohn, “Controlled growth of monodisperse silica spheres in the micron size range,” *Journal of Colloid and Interface Science*, vol. 26, pp. 62–69, jan 1968.

[178] C. P. Blakemore, A. D. Rider, S. Roy, A. Fieguth, A. Kawasaki, N. Priel, and G. Gratta, “Precision mass and density measurement of individual optically levitated microspheres,” *Physical Review Applied*, vol. 12, no. 2, pp. 1–5, 2019.

[179] C. Dawson and J. Bateman, “Spectral analysis and parameter estimation in levitated optomechanics,” *ArXiv*, no. March, pp. 1–9, 2019.

[180] D. Middleton, “The distribution of energy in randomly modulated waves,” no. March, 1951.

[181] N. Abramson, “Bandwidth and Spectra of Phase-and-Frequency-Modulated Waves,” *IEEE Transactions on Communications Systems*, vol. 11, no. 4, pp. 407–414, 1963.

[182] P. Brochard, T. Sudmeyer, and S. Schilt, “Power Spectrum Computation for an Arbitrary Phase Noise Using Middleton’s Convolution Series: Implementation Guideline and Experimental Illustration,” *IEEE Transactions on Ultrasonics, Ferroelectrics, and Frequency Control*, vol. 64, no. 11, pp. 1766–1775, 2017.

[183] A. Godone, S. Micalizio, and F. Levi, “RF spectrum of a carrier with a random phase modulation of arbitrary slope,” *Metrologia*, vol. 45, no. 3, pp. 313–324, 2008.

[184] L. H. Koopmans, *Spectral Analysis of Time Series.* Academic Press, 1995.

[185] C. M. Hurvich and K. I. Beltrao, “Asymptotics for the Low-Frequency Ordinates of the Periodogram of a Long-Memory Time Series,” *Journal of Time Series Analysis*, vol. 14, no. September, pp. 1–54, 1993.

[186] R. Singh, D. Ghosh, and R. Adhikari, “Fast Bayesian inference of the multivariate Ornstein-Uhlenbeck process,” *Physical Review E*, vol. 98, no. 1, pp. 1–10, 2018.

[187] D. Sivia and J. Skilling, “Data Analysis: A Bayesian Tutorial,” *Technometrics*, vol. 40, no. 2, p. 155, 1998.

[188] P. Whittle, “Tests of Fit in Time Series,” *Biometrika*, vol. 39, no. 3-4, pp. 309–318, 1952.

[189] F. J. Harris, “On the Use of Windows for Harmonic Analysis with the Discrete Fourier Transform,” *Proceedings of the IEEE*, vol. 66, no. 1, p. 51, 1978.

[190] A. R. Dow, A. M. Wittrig, and H. I. Kenttämaa, “Laser-Induced Acoustic Desorption Mass Spectrometry,” *European Journal of Mass Spectrometry*, vol. 18, no. 2, pp. 77–92, 2012.

[191] P. Asenbaum, S. Kuhn, S. Nimmrichter, U. Sezer, and M. Arndt, “Cavity cooling of free silicon nanoparticles in high vacuum.,” *Nature communications*, vol. 4, p. 2743, jan 2013.

[192] S. W. Bahk, P. Rousseau, T. A. Planchon, V. Chvykov, G. Kalintchenko, A. Maksimchuk, G. A. Mourou, and V. Yanovsky, “Characterization of focal field formed by a large numerical aperture paraboloidal mirror and generation of ultra-high intensity (10 22 W/cm 2),” *Applied Physics B: Lasers and Optics*, vol. 80, no. 7, pp. 823–832, 2005.

[193] M. Motsch, M. Zeppenfeld, P. W. Pinkse, and G. Rempe, “Cavity-enhanced Rayleigh scattering,” *New Journal of Physics*, vol. 12, 2010.

[194] G. Hétet, L. Slodicka, A. Glätzle, M. Hennrich, and R. Blatt, “QED with a spherical mirror,” *Physical Review A - Atomic, Molecular, and Optical Physics*, vol. 82, no. 6, pp. 1–12, 2010.